

Heteromultivalent Virus-mimetic Nanoparticles for Specific Mesangial Cell Targeting

Dissertation to obtain the Degree of Doctor of Natural Sciences
(Dr. rer. nat.)

From the Faculty of Chemistry and Pharmacy
University of Regensburg



Presented by
Sara Maslanka Figueroa
from Ourense (Spain)

March 2020

Sara Maslanka Figueroa

**Heteromultivalent Virus-mimetic Nanoparticles for Specific
Mesangial Cell Targeting**

Heteromultivalent Virus-mimetic Nanoparticles for Specific Mesangial Cell Targeting

Dissertation to obtain the Degree of Doctor of Natural Sciences
(Dr. rer. nat.)

From the Faculty of Chemistry and Pharmacy
University of Regensburg



Presented by
Sara Maslanka Figueroa
from Ourense (Spain)

March 2020

This work was carried out from April 2016 until March 2020 at the Department of Pharmaceutical Technology of the University of Regensburg.

The thesis was prepared under supervision of Prof. Dr. Achim Göpferich.

Doctoral application submitted on: 16.03.2020

Date of examination: 27.05.2020

Examination board:

Chairman: Prof. Dr. Jens Schlossmann

1st Expert: Prof. Dr. Achim Göpferich

2nd Expert: Prof. Dr. Frank Schweda

3rd Examiner: Prof. Dr. Miriam Breunig

To my family

*For the things we have to learn before we can do them, we
learn by doing them*

Aristotle (384 - 322 BC)

Table of contents

Chapter 1	Introduction What nanoparticles can learn from viruses: viral mimicry in synthetic targeted therapeutic nanoparticles.....	9
Chapter 2	Goals of the Thesis.....	53
Chapter 3	Influenza A virus mimetic nanoparticles trigger selective cell uptake	59
Chapter 4	The effect of ligand mobility on the cellular interaction of multivalent nanoparticles	93
Chapter 5	Nanoparticles mimicking viral cell recognition strategies are superior transporters into mesangial cells	131
Chapter 6	Thermodynamic, spatial and methodological considerations for the manufacturing of therapeutic polymer nanoparticles	171
Chapter 7	Summary and Conclusion	207
Appendix	Abbreviations	215
	Curriculum Vitae	219
	List of Publications	221
	Acknowledgements	223
	Statement in Lieu of an Oath	225

Chapter 1

What nanoparticles can learn from viruses: Viral mimicry in synthetic targeted therapeutic nanoparticles

Abstract

Viruses are nanomaterials with a number of properties that surpass those of many synthetic nanoparticles (NPs) for biomedical applications. They possess a rigorously ordered structure, come in a variety of shapes, and present unique surface elements, such as spikes. These attributes facilitate propitious biodistributions, the crossing of complex biological barriers and an enhanced cellular interplay. More so, due to an orchestrated sequence of interactions of their stringently arranged particle corona with cellular surface receptors they effectively infect their host cells with utmost specificity, while at the same time evading the immune system. Furthermore, their efficacy is improved by their response to stimuli and ability to spread from cell to cell. Over the years, great efforts have been made to mimic distinct viral traits to improve nanomaterial design. However, a closer look at the literature reveals that no systematic evaluation of the impact of viral mimicry on nanotherapeutic targeting strategies exists. In this review, we elucidate the impact of viral properties on fundamental advances in targeted nanomaterial design. We give a comprehensive overview of the developed formulations and identify critical considerations for their fruitful implementation. More so, we discuss the advantages and future perspectives of a virus-mimetic nanomaterial design and try to elucidate if viral mimicry holds the key for better NP targeting.

1 Introduction

Nanomaterials used for the targeted therapy or diagnosis of diseases face several obstacles upon administration. When particles infiltrate biological media they are immediately subjected to the adsorption of proteins on their surfaces, the protein corona [1], affecting not only their stability [2] but also their toxicity [3], targeting abilities [4] and clearance [5], and thus, limiting their efficacy. Additionally, depending on their intended application and route of administration they have to overcome complex biological barriers [6]. Examples for this are the blood-brain barrier (BBB) in cerebral diseases or the mucus and epithelial barrier faced after oral administration. More so, nanomaterials are required to specifically identify their targets among myriads of cells to fulfil their therapeutic objective and avoid deleterious side effects. Furthermore, the cellular membrane is an additional impediment that limits nanoparticles (NPs) from reaching intracellular compartments. Even once this, apparently final, obstacle is overcome particles are required to escape from endocytic vesicles to release their cargo or further disseminate to distinct organelles.

Viruses in contrast, are also nanosized particles that are exceptional at overcoming these impediments. To perpetuate their life cycle they are able to cross difficult biological barriers, evade immune-mediated clearance and specifically recognize and invade their host cells [7]. Subsequently they are able to disseminate from one cell to another. Several distinct viral traits have been identified as the reason for these abilities, such as their morphologies, surface characteristics (i.e, roughness, glycosylation, charge), stimuli responsiveness, and their interactions with cellular receptors (Table I). Therefore, over the years, scientist have been deeply invested on imitating these properties and their effects to improve the performance of nanomaterials. Despite virus-based delivery systems, such as viral vectors or virus-like particles also holding great biomedical potential, they are still associated with considerable safety burdens [8, 9]. Thereby, synthetic NPs appear as safer and more versatile option. They additionally facilitate the incorporation of multiple different cargos for a broad spectrum of applications and have clear advantages regarding production, storage and reproducibility [10].

In this review we give an overview of the viral traits adopted in targeted nanomaterial design to improve NPs' efficiency. Starting with simple structural characteristics and ligand display, and ending with more complex attributes, such as the sequential interaction with surface receptors, stimuli responsiveness or cell to cell spreading. We critically examine the advances that viral mimicry has enabled for targeted nanotherapy and outline pivotal design parameters that must be considered for a rational NP optimization. More so, we discuss the latest trends and outline future perspectives for the virus-like nanomaterial design.

Chapter 1: What Nanoparticles can Learn from Viruses

Table I. Viral characteristics associated with overcoming obstacles in biological media

Obstacle	Viral trait to success
Biodistribution	Shape
Biological Barriers	Shape Surface properties (roughness, zwitterionic) Specific receptor binding
Immune response	Glycosylation
Protein corona	Zwitterionic surface
Cell membrane	Shape Surface properties (roughness, glycosylation) Receptor-mediated interaction
Endosomal escape	Surface (spikes) Stimuli responsiveness
Cell specificity	Sequential ligand presentation

2 Structural Characteristics

2.1 Morphology

Viruses are nanosized entities of about 20-200 nm (being the 400 nm Mimivirus the largest one described to date [11]). There is little research on the effects that size has on the viral life cycle. However, it is known that is related to the length of the genome the virus is enclosing [12]. This can be also related to nanomaterials, as there are spatial constrictions that determine their cargo loading [13]. However, a nanomaterial's size is a fundamental parameter determining its suitability for concrete applications. For example, for the extravasation to specific tissues, the NP size must be under a (patho)physiologically determined cutoff [14, 15]. More so, the particle size determines the blood residence, clearance [16-18], and interaction with the immune system [19-21].

Viruses come in various shapes and forms, such as polyhedral, rod-like, or filamentous, which bestow them with distinct biodistribution and targeting properties [22]. For example, it has been shown that the filamentous form of the Influenza virus has a higher specific infectivity than their spherical virion counterparts [23]. Mimicking this morphology with synthetic NPs resulted in a prolonged circulation time after injection [24] and a specific lung vasculature targeting [25]. A rod shape is associated with higher virus diffusion rates in tumor tissue [26], and can be mimicked with synthetic NPs by techniques such as the co-assembly of polyanions and artificial virus capsid proteins [27], the condensation of DNA and block copolymers [28], or the seeded growth synthesis of gold NPs [29]. A polyhedral virus shape has been linked to a high targeting specificity [30], a very sought after property for targeted NPs. However, despite the influence that a NP's geometry has on its blood residence biodistribution and cellular uptake [31], most therapeutic NPs still are designed in a

spherical shape, as their straight forward preparation is of advantage [14]. Nevertheless, the new accessible methodologies that are being developed to achieve a higher variety of shapes, such as the use of self-folding polymers to produce polyhedral particles [32], provide new platforms that may ease future particle shape optimization.

2.2 Surface properties

The surface of viruses is crucial for the infection process, as it determines its interaction with the surrounding medium and distribution to specific compartments, such as the central nervous system [33]. The mimicking of viral surface properties can enhance the cellular interaction of synthetic NPs. Especially the characteristic surface roughness of spiked enveloped viruses is usually associated to a higher infectivity and cellular internalization [34].

Interestingly the same effects of increased targeting and cell penetrability were seen when spikes were introduced on the surface of NPs. This has been demonstrated with inorganic materials, such as silica- [35] or Au@Ag- [36] NPs but also with fluorinated peptide dendrimer-based polymer vectors [37] and carrier free polyethyleneimine (PEI)/DNA nanosystems [38]. In all cases a higher cellular endocytosis and enhanced cargo delivery was observed, indicating that surface roughness is a highly important design parameter leading to the success of nanomaterials.

More so, it was recently linked to a quicker NP-cell interaction [39]. Mesoporous silica nanospheres surrounded by spike-forming mesoporous nanotubes were able to strongly interact with their target cells after only 5 minute incubation, in contrast to non-functionalized spherical particles, which required extensive cell contact [39]. Furthermore, the spikes changed the particle internalization route from a clathrin-mediated endocytosis for non-functionalized particles, to a combination of caveole-mediated endocytosis and macropinocytosis. Synthetic spikes can also be constituted by targeting ligands themselves, as it was shown by the formulations developed by Liu *et al.* [40] and Xu *et al.* [41]. The former developed lentivirus mimicking NPs displaying Zn-dipicolylamine analogue-spikes, a zinc coordinative ligand with high affinity to phosphate moieties on cell membranes [40]. The latter, imitated coated viruses, such as influenza or herpesvirus (HV), by displaying transferrin (TF) spikes on the surface of their liposome-DNA complexes [41]. In both cases the spikes were able to bind the cell membrane and mediate internalization. Additionally, spikes conferred endosomal escape abilities or a higher *in vivo* stability and gene transfer, respectively, compared to non-functionalized particles.

Chapter 1: What Nanoparticles can Learn from Viruses

A typical viral characteristic is surface glycosylation [42]. In some cases, such as for the influenza virus, glycosylation is essential to enhance cellular internalization [43] and in others, such as for the human immunodeficiency virus (HIV) [44], it is crucial for immune evasion. For synthetic NPs there seems to be contradictory evidence regarding the influence of glycosylation on immune activation, and it is often viewed as an obstacle for the generation of an adequate immune response. However, Tokatlian *et. al* [45] recently highlighted that adjusting the NP immunogen glycosylation is critical for vaccine design, as they demonstrated that deglycosylation significantly affects antibody response. Mannose presentation on self-assembling ovalbumin carrying NPs was also associated with a higher *in vivo* immune response compared to non-glycosylated NPs [46]. Regarding the efficiency of NP-cell interactions, glycosylation is generally considered an improvement in NP design. Pinnapireddy *et al.* [47] mimicked enveloped viruses with glycosylated anionic liposomes prepared from lipids found in the envelopes of HIV and herpes simplex virus (HSV). The formulation, intended for gene delivery, achieved an increased particle internalization through lectin receptors [48]. Also, the addition of mannose to cationic albumin NPs allowed for an enhanced brain targeting and *in vivo* glioma treatment [49]. As for viruses, which require an optimal glycosylation balance that “shields” from the immune system but still allows efficient receptor binding [50], it is reasonable to believe that NP surface glycosylation needs to be exactly tailored for each formulation in accordance with its physicochemical characteristics and intended application.

Once particles enter biological media, they are subjected to protein adsorption and the formation of a protein corona. For viruses, several host factors indispensable for infectivity can attach to their surface, like Apo-E lipoprotein for hepatitis C virus (HCV) [51]. A recent study that evaluated the protein corona formation on respiratory syncytial virus and HSV type-1 when incubated with different bodily fluids showed that the surface properties of the virus were responsible for determining the enrichment with different corona elements [52]. Additionally, the fluid from which the proteins proceeded, determined the corona composition, which in turn affected the viral infectivity. However, viral and NP corona may be quite different, due to the diverging surface compositions. More so, viral particles may be overall subjected to a lesser protein corona formation. In this regard, Pitek *et al.* [53] discovered that after plasma incubation, virus particles derived from the tobacco mosaic virus bound 6-times less protein than synthetic NPs. The authors associated this with the display of positive and negative charge patches on the viral particles in combination with hydrophobic and hydrophilic domains. Recently, our group also showed that zwitterionic polymeric NPs adsorbed less protein when incubated in serum compared to positive, negative or uncharged particles, as it provides less domains allowing for hydrophobic or electrostatic interactions [2]. This is in accordance to previous studies

that demonstrated that the protein binding suppression of such materials is due to their ability to electrostatically bind great amounts of water molecules [54–56]. Therefore, in addition to the typically implemented strategies used to suppress protein corona formation, such as PEG coating, an adjustment of the surface charge of particles, imitating the charged but neutral viral surface, should be considered. Furthermore, a virus-like exploitation of the protein corona may enhance the targeting abilities of NPs [57].

Close mimicking of the viral surface has also been extremely useful to achieve mucus-penetration. Surface characteristics that allow viral particles to overcome the mucus barrier are a charged but neutral surface and a hydrophilic nature. It has been demonstrated that particles that hold these features are able to overcome the mucus barrier [58, 59], making them appropriate vehicles for oral [60] and vaginal drug administration [61]. However, the combination of these surface properties with a virus-like active targeting has been shown to further increase the penetrability of nanomaterials, which is especially interesting for the oral insulin delivery. Liu *et al.* [62] were able to overcome the mucus barrier with polyelectrolyte complexes mimicking the viral envelope, composed of polysaccharides, peptides and lipids, with L-Phenylalanine-functionalized chitosan polymers. The authors found that functionalized polymers yielded a 2-fold higher bioavailability than non-modified particles. Zhu *et al.* [63] demonstrated that active targeting can be used to surmount not only the mucus- but also the epithelial absorption barrier. They functionalized insulin carriers with poly(ethylene glycol) (PEG)-shielded poly-arginine which was able to mediate epithelial cell penetration and produce hypoglycemia *in vivo*. They further demonstrated the particle safety [64] and expanded on their mimicry concept implementing the densely charged but neutral surface of viruses [65]. In this manner the NPs displayed the distinct viral attributes needed to overcome not one, but two barriers.

Viruses are meticulously built systems in that every component holds an exact function. This promotes their paramount goal of delivering their genetic content into host cells. More so, the success of this endeavor strictly depends on a perfect interworking of all constituents. Size, shape and surface properties are apparently simple elements of particle design. However, they can have enormous influence on a particle's cellular interaction and biodistribution [66]. Mimicking the viral morphology and surface characteristics can lead to faster and greater NP-cell interactions and even bestow barrier penetration abilities. Therefore, the structural replica of a virus must be considered the first step when trying to achieve viral traits on synthetic NPs (Figure 1).

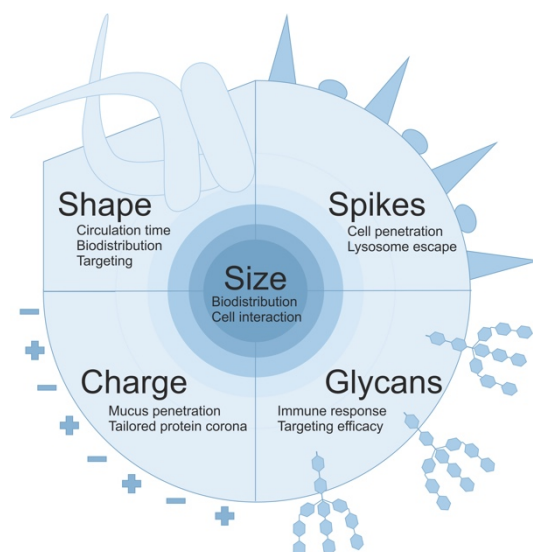


Figure 1. Structural viral properties and their effects on synthetic NP design.

3 Ligand display and cell recognition

3.1 Multivalent display of ligands

One of the viral attributes that has had the most impact on the field of targeted nanomaterials is the multivalent ligand display. Viruses present numerous copies of the same ligand on their surface, which allows them to interact with receptors on the cellular surface (Figure 2). This specific interaction with host cells is an essential and obligatory element of the viral life cycle as it enables the delivery of their genetic content [67]. It is broadly accepted that mimicking the viral multivalent ligand display improves a NP's target cell-recognition. Generally, the tethering of ligands to the NP surface is associated with an affinity loss of the individual ligands, which is compensated by the binding of several receptors simultaneously [68]. This has led to enhanced targeting through avidities in the nano- [69] or even picomolar range [70]. Multivalent NPs have been used to target G protein-coupled receptors (GPCRs) [69, 71, 72], integrins [73, 74] and lectin receptors [75] with ligands such as peptides or proteins, aptamers and small molecules [76]. But, even though the virus-like ligand display seems like an easy enough concept to be reproduced with synthetic materials, it noteworthy that several distinct parameters play an influence on the success of a multivalent NP. One of the most relevant ones is ligand density, which is frequently neglected in nanomaterial design. In their excellent recent review Alkilany *et al.* [77] calculated the number of ligands displayed by viruses on their surface. Depending on the virus, they obtained a range between 7-659 ligands per virus particle. Interestingly, this number is usually greatly exceeded in synthetic NPs, where sometimes thousands

of molecules are tethered to a single NP. More so, results show that the optimal ligand density is a unique characteristic for each formulation. In some cases, a minimum threshold needs to be surpassed to induce targeting effects. For example, for folate-functionalized NPs, a ligand density over 10% was needed in order to exceed the internalization of non-targeted particles [78]. In other cases, an optimum ligand density may exist, its alteration leading to a decrease in targeting. Fakhari *et al.* [79] demonstrated that a medium (50%) cLABL density on poly(lactic-co-glycolic acid) (PLGA) NPs achieved the optimum targeting of ICAM-1 expressing cells. Lower or higher ligand densities resulted in a poor particle uptake. Similarly, Elias *et al.* [80] found that an intermediate ligand density was optimal for targeting purposes using antibodies against HER2/neu, overexpressed in cancer cells. Generally, decreases in targeting with higher grafting densities are explained by a steric hindrance of the ligands and decreased ligand mobility [81]. This may disrupt interaction with the receptors to a point where their internalization is impeded. Another scenario is presented when a targeting plateau is reached above a certain ligand density. Poon *et al.* [82] showed that low ligand densities (20% folate density) were ideal for their system and higher functionalization did not enhance targeting. Lastly, there are systems where an increase in ligand number results in a continuous enhancement of NP targeting efficiency, which is frequently detected for RGD-ligands [83, 84]. Therefore, it is essential to carefully and individually adjust the number of ligands on the particle corona for each system.

An additional factor to be considered for the multivalent NP design is the ligand conformation. Viruses often display ligands with defined conformations and regular spacings. This is the case of adenovirus, which presents RGD clusters [85] on five penton base proteins with a 5.7 nm spacing [86], indispensable for viral infection [87]. RGD ligands are also one of the most used candidates for targeting purposes, as integrins are expressed in both tumor- and tumor endothelial cells [73]. Using adenovirus physical structure as a guide, Ng *et al.* [88] studied the influence of the ligand clustering on the targeting efficiency. RGD ligands were tethered to Au NPs to generate clusters, which were subsequently attached to PEI polyplexes. The cluster-presenting particles achieved a 5.4- or 35- fold increase in gene transfer in cells expressing low and high integrin densities, respectively, compared to non-modified polyplexes, showing a higher sensitivity to receptor density. This selectivity towards cells expressing high target receptor levels is fundamental for the design of nanomaterials which base their targeting principle on receptor overexpression by specific cells in a diseased state. The clustering principle has also been applied to folate molecules [82, 89] with similar results, demonstrating that it is a promising approach to optimize ligand presentation.

Chapter 1: What Nanoparticles can Learn from Viruses

The interactions of ligands with their targets may also be defined by the length of the linkers used to tether them to the particle surface. First, it may increase or decrease the particle size, which highly influences the cellular interaction [14]. Second, it can alter the ligand disposition, which can be spaced out or tightly grouped by using longer or shorter tethers, respectively [83]. Thirdly, it can influence the ligand mobility on the particle surface, which has a tremendous influence on the cellular internalization of a NP [81].

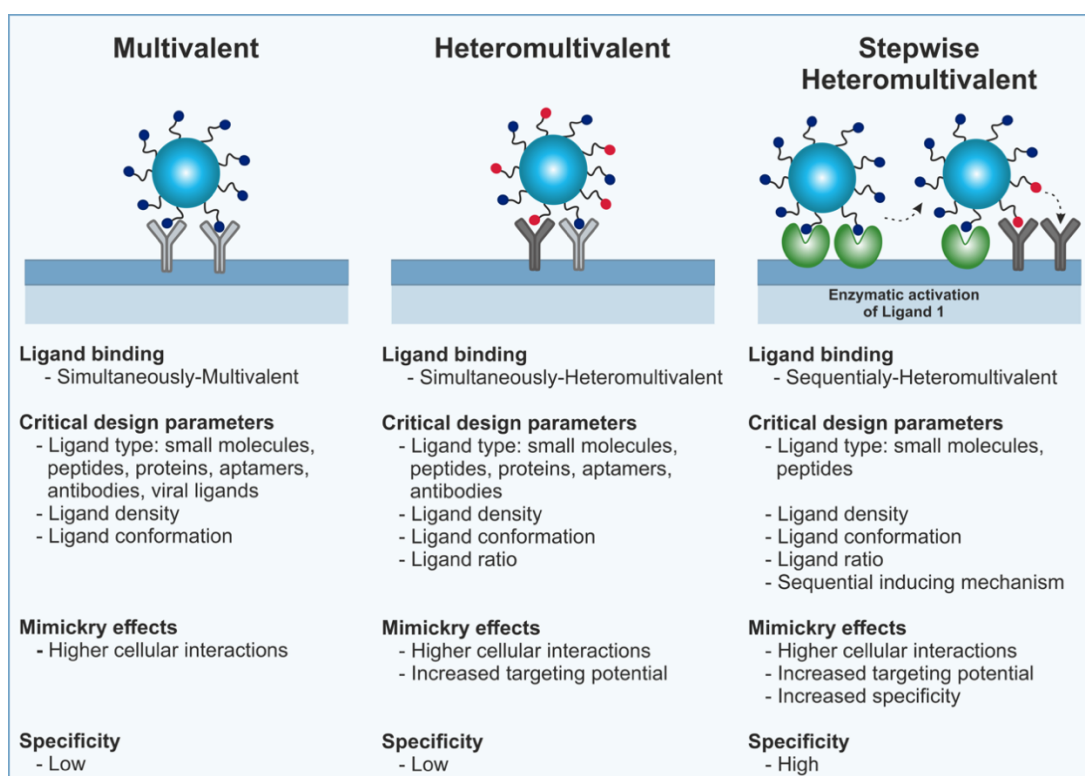


Figure 2. Comparison of virus-mimetic ligand presentation approaches on synthetic NPs.

It is generally accepted that the virus-like multivalent ligand display enhances the particles overall avidity and targeting capabilities. Nevertheless, it does not increase the nanomaterials overall specificity, which is indispensable for therapeutic applications of such materials. Despite generally addressing disease-related overexpressed receptors, they are often also prevalent in “healthy” off-target tissues, which leads to poor material bioavailabilities and deleterious side effects. One of the elements that can negatively impact the specificity of multivalent NPs is the elevated number of ligands displayed on their corona, which is usually higher than the one presented by viruses [77]. *In vivo* this may additionally cause a particle stealth loss and increased protein corona formation, which also hinder targeting. More so, a very precise control over NP design features besides ligand density, such as linker length

and ligand conformation, is crucial to achieve optimal effects. Altogether, a multivalent ligand display seems to be a prerequisite but not sufficient to effectively imitate the viral target cell recognition.

3.2 Multivalent display of virus-derived ligands

A frequently used design approach to mimic the viral targeting principles is the decoration of NPs with natural viral surface “ligands”, like attachment factors, cell penetrating peptides, fusion-proteins, and antigen-derived peptides. Viral surface antigens tethered to NPs are mainly of interest in the field of vaccine development which will not be addressed here, as they are outside of the scope of this review and have extensively been reviewed elsewhere [90, 91]. In this section, we will focus on systems displaying viral surface molecules seeking an increase in target cell recognition for drug delivery, with diagnostic or therapeutic purposes.

During the initial phases of cell entry, viruses make use of attachment factors that anchor them to the host cell membrane. Despite it being a low-affinity binding, it is of importance in the viral cycle, as it aids receptor recruitment [92]. Furthermore, its inhibition can suppress the infection process [93]. Almost three decades ago, Rubas *et al.* [94] discovered that modifying liposomes with the reovirus M cell attachment protein $\sigma 1$ increased by 10-fold their cellular uptake *in vitro* compared to non-targeted formulations. Also, the recent identification of a new heparin-binding domain, pre-S1(30-42), of hepatitis B virus (HBV) involved in initial virus attachment enabled the development of virus-mimicking liposomes for the specific identification of human hepatic cells [95]. Interestingly, particles functionalized with the attachment peptide were able to deliver doxorubicin (DOX) to hepatic cells more efficiently than liposomes functionalized with the peptide associated with viral targeting, i.e., pre-S1(2-47) [96], corroborating the immensely important role of attachment in viral infectivity.

Viral surface antigens can also be used for the targeting of specific cell types. Somiya and Kuroda [97] developed a HBV-mimetic nanocapsule using the hepatitis B surface antigen L protein for specific drug delivery to human hepatocytes. To overcome the elicitation of an immune response resulting from the repeated administration of viral antigens on the surface of NPs, they made use of an additional viral trait, this is, the ability to mutate [98]. To that end, the Gln-292 and Gly-302 were substituted with Arg, suppressing the immunogenicity of the formulation [99], which is indispensable for repeated administrations.

Additionally, viral surface ligands can be used to overcome barriers which normally present a huge difficulty for nanocarriers, such as the BBB. In this regard, a small peptide derived from the rabies virus (RABV) glycoprotein (RVG), RVG29, that

Chapter 1: What Nanoparticles can Learn from Viruses

interacts with high specificity with the cell entry-mediating neuronal nicotinic acetylcholine receptor, was used by several authors as targeting entity to enable BBB crossing. It was coupled to polymeric PEG-poly(lactic acid) (PLA) NPs to increase the BBB penetration of deferoxamine, an iron chelator used to protect against oxidative damage [100]. A higher BBB crossing of the drug enabled by this formulation prevented neuron damage and neurobehavioral deficits in mice with no systemic adverse effects. RGV29 was also grafted onto calcified calcium carbonate- and DOX-containing polymeric PLGA NPs to address brain tumors. After ligand-mediated uptake, the calcium carbonate contained in the particles generated carbon dioxide gas upon acidification, increasing DOX release, and achieving tumor size suppression in a mouse model. Lee *et al.* [29] also used RVG29 to develop a nanoformulation for the treatment of brain tumors based on silica-coated gold nanorods.

During infection, viruses present different proteins and peptides that aid cell penetration. Several cell penetrating peptides (CPPs) used in active targeting are derived from viral capsids [101], such as the HIV [102] and the Brome mosaic virus [103]. One of the most commonly used CPPs is probably the HIV derived trans-activating transcriptor (TAT) peptide [104]. It has been used to decorate the surface of several different nanomaterials, such as silica- [105, 106], magnetic- [107, 108], Au- [109, 110], lipid- [111, 112], and polymeric NPs [113, 114], amongst many others, to accomplish cell or nucleus penetration and BBB-crossing for diagnostic and therapeutic purposes.

Lastly, ligands inducing viral fusion can also be grafted onto NP. Gao *et al.* [115] functionalized parainfluenza virus envelope-mimicking fusiogenic vesicles with hemagglutinin-neuraminidase protein and the viral fusion protein, which bind sialic acid-containing receptors and initiate fusion, respectively. After fusion, the molecular beacons contained in the NP target miRNAs and generate a quantifiable fluorescence signal, which can be applied in exosome mRNA detection and cancer diagnosis. Wang *et al.* [36], took advantage of a phage fusion protein, pVIII, and prepared phage-mimetic rod-shaped NPs self-assembled from Ag@Au nanorods for specific targeting and photothermal therapy. The fusion proteins allowed for a specific colorectal carcinoma cancer cell targeting and ablation. Interestingly, the assembly of the phage proteins on the NP surface was achieved through electrostatic interactions, a coupling which is usually mediated by covalent bonds. However, this allowed the pVIII protein to maintain its natural conformation and orientate itself outwards, facilitating targeting.

Taken all together these results show that by isolating viral ligands and displaying them on NPs we are not only able to enhance important NP characteristics, such as

targeting, penetration, and barrier crossing, but also shed some light on their involvement during viral infection.

3.3 Heteromultivalent ligand display

The virus-like multivalent display of tethered ligands on NPs highly increases their targeting abilities. However, the cellular interplay of viruses is usually mediated by more than a single ligand. Therefore, as an approach to increase the specificity and targeting capacity of multivalent systems, heteromultivalent NPs, displaying different types of ligands on their surface, were developed (Figure 2). They more closely mimic viruses, which require several recognition molecules for host-cell identification. For example, the HCV depends on the co-expression of four proteins (SR-B1, CD81, claudin-1, and occludin) to mediate cell entry [67]. This concept's increase in cell specificity is based on the fact that the probability of more than one cell expressing the same receptors decreases with the number of receptors that are addressed. More so, by using an additional set of ligands, the targeting capacity of heteromultivalent particles should be enhanced compared to multivalent NPs. Heteromultivalently binding NPs have been extensively investigated over the past years [116]. They find mostly application in cancer [117], and vascular pathologies [118, 119], characterized by a concomitant spatiotemporal upregulation of several surface receptors, such as the TF receptor (TfR) [120], folate receptor (FR) [121], epidermal growth factor receptor (EGFR) [122], integrins [123], and selectins [124]. Like for multivalent systems, antibodies, small molecules, and peptides [125], are mainly used as targeting moieties. An overview of different formulations developed over the past years is depicted in Table II.

Table II. Heteromultivalent NP formulations

NP	Ligands	Targets	LD and/or LR	<i>In vivo</i>	Therapy	Ref.
Liposome	Ab (1)	CD19	-	yes	DOX/VI	[126]
	Ab (2)	CD20				
Liposome	Antibody NGR peptides	GD ₂ AN	-	yes	DOX	[127]
Liposome	Ab (1)	CD19	50% of each ligand	no	DOX	[128]
	Ab (2)	CD20				
Liposome	Ab FA	EGFR FR	3 Ab molecules + 200 folate molecules per NP	no	DOX	[129]
Liposome	Ab (1)	ICAM	1:1 ligand ratio	no	-	[130]
	Ab (2)	ELAM				
Liposome	Ab (1)	ICAM	-	no	-	[131]
	Ab (2)	E-selectin				
Liposome	Peptide (1) Peptide (2)	$\alpha\text{v}\beta\text{3}$ integrin Galectin-1	-	no	-	[132]

Chapter 1: What Nanoparticles can Learn from Viruses

Liposome	Ab (1) Ab (2)	VCAM1 E-selectin	1:1 ligand ratio	no	-	[124]
Liposome	Peptide (1) Peptide (2)	$\alpha\text{v}\beta\text{3}$ integrin Galectin-1	-	yes	-	[133]
Liposome	Ab fragment (1) Ab fragment (2)	EGFR CEA	-	no	-	[134]
Liposome	Peptide (1) Peptide (2)	P-selectin $\alpha\text{v}\beta\text{3}$ integrin	-	yes	-	[135]
Liposome	Peptide cRGDfc	EGFR $\alpha\text{v}\beta\text{3}$ integrin	1:1 ligand ratio	yes	DOX	[136]
PEI	B6	TfR	-	no	-	[10]
Polyplex	RGD-motif	Integrin	-	no	-	[121]
Au NPs	Ab (1) Ab (2)	FR EGFR	-	no	-	[121]
Au NPs	FA Glucose	FR GR	-	no	DOX	[137]
Au NPs	Peptide (1) Peptide (2)	EGFR TfR	-	yes	Phtalocyanine 4	[138]
PEG-PAMAM	TF WGA	TfR Endothelium	-	no	DOX	[139]
Polymer NPs	c(RGDfK) TF	$\alpha\text{v}\beta\text{3}$ integrin TfR	-	no	PTX	[120]
PEG-PLGA NPs	FA HA	FA Receptor CD44	5:2 ligand ratio	yes	-	[140]
QDs	GE11 c(RGDfK)	EGFR $\alpha\text{v}\beta\text{3}$ integrin	-	no	siRNA + ON	[122]
Silica NPs	cRGD ATWLPRR peptide	$\alpha\text{v}\beta\text{3}$ integrin Neuropilin 1	-	yes	-	[141]
Nanographene oxide	Folate cRGD	FR $\alpha\text{v}\beta\text{3}$ integrin	1:1 ligand ratio	yes	Photothermal therapy	[142]
DNA Nanoclaw	Ab (1) Ab (2) Ab (3)	EpCAM EGFR HER-2	-	no	DNA	[143]
Liposome/Silica NPs	Peptide (1) Peptide (2) Peptide (3) Peptide (4)	P-selectin $\alpha\text{v}\beta\text{3}$ integrin EGFR Fibronectin	500 ligands of each type	yes	-	[144]

LD: Ligand density; LR: Ligand ratio; Ab: Antibody; ON: Oligonucleotides; WGA: wheat germ agglutinin

It is essential to note that as for multivalent systems, there are several factors that can determine the cellular outcome of a heteromultivalent system, such as ligand density, ligand ratio and ligand arrangement. However, for most published formulations there is a lack of information regarding these parameters (Table II). As they have enormous influence on the establishment of receptor interactions [77, 145], it should come as no surprise that heteromultivalent NPs frequently achieve only moderate improvements, regarding targeting and specificity, compared to “simple” multivalent systems [120, 139]. The addition of a second ligand type increases the complexity of the system and

does not equal the rise in number of a single ligand. Furthermore, excessive particle functionalization can propitiate targeting ability loss [128] and off-target interactions [146]. A higher functionalization is usually associated with a higher avidity of the particle system. However, a high avidity attachment to the cell surface is not always positive seen from the viral perspective. It can hinder virus diffusion through the cell membrane and reduce the chances to find the cell entry mediating receptor [147]. More so, the number of interactions between viruses and their receptors are limited. Delguste *et al.* showed that only 2 or 3 simultaneous interactions occurred between HIV and glycosaminoglycans [147]. This is something that should be considered when designing functionalized particles.

Ligand arrangement on the particle surface can also determine the enhancement, or lack thereof, in particle internalization through a heteromultivalent system. Dissipative particle dynamics stimulations showed that length mismatch or interactions between ligands can impede dual ligand binding [148]. When Liu *et al.* systematically evaluated the influence of ligand ratio and tether length of hyaluronic acid (HA) and folic acid (FA) presenting NPs [140], they saw that a precise formulation achieved maximum selectivity. A 1:5 HA:FA ratio resulted in maximum binding to double positive cancer cells with minimum binding to cells expressing only one of the targeted receptors. More so, HA had to be tethered to a longer 7k PEG chain, than the 5k PEG chain used to link FA, to achieve selectivity. This sheds light to the complexity of the formulations and the need for a systematic review of every design parameter. Additionally, the nature of the ligand coupling can also influence targeting abilities. It has been demonstrated that non-specific ligand attachment during linkage is a fact that frequently occurs. Unfortunately, non-covalently bound ligands can be exchanged in biologic fluids by new peptides and proteins, which hinder targeting [149].

As for multivalent systems[81], ligand availability also plays an important role in the efficacy of heteromultivalent particles. Considering this, Wang *et al.* [143] proposed magnetic DNA “nanoclaws” for the early cancer diagnosis through detection of circulating tumor cells. They achieved a flexible claw morphology by rolling circle amplification and hybridation of DNA probes. The magnetic nanoclaws were able to capture target cells in a mixture with off-target cells with a 95% efficiency and 85% purity due to the high availability of the displayed antibodies, contrary to spherical control NPs. This was confirmed with clinical samples, demonstrating that a simple ligand surface attachment is insufficient to exploit the potential of heteromultivalency.

The exact definition of the expression patterns of the targeted receptors is also an element that can enable an optimal particle design. Gunawan *et al.* [124, 130, 131] carried out several studies with immunoliposomes functionalized with antibodies targeting ICAM and E-selectin on activated endothelial cells. The formulation was

Chapter 1: What Nanoparticles can Learn from Viruses

optimized to achieve a cooperative effect of the two ligands with a 1:1 ratio when lipid rafts were present on the cells [131]. However, the maximum binding of the final NPs varied tremendously with the transient expression of the targets. Also, Levine and Kokkoli [123] demonstrated that PEGylated liposomes targeting two different cancer biomarkers, integrin $\alpha_5\beta_1$ and $\alpha_6\beta_4$, with equal ligand numbers achieved enhanced binding to cells with equal and high receptor expressions, but not to cells with different expression patterns. These results can be an obstacle for the clinical translation of such systems, due to the individuality of each disease and patient. Nevertheless, the disease biomarker variability, especially in tumors and metastasis, can also open new applications for heteromultivalent NPs. By targeting more than one receptor, the temporarily downregulation of one of them can be overcome by binding to the second one [135, 136]. In this context, Peiris *et al.* [144] demonstrated that metastasis targeting can be improved by functionalizing particles with up to four different ligands. The authors found that in a triple-negative breast cancer model two-ligand particles produced highly variable results depending on the animal while four-ligand particles achieved consistent results with 7% of the initial dose reaching even in subclinical metastasis.

A disadvantage of adding targeting capabilities is that it can complicate a system's design to a high extent making its clinical translation difficult [150], as the ligand dynamics can highly differ from its single-ligand counterparts. In combination, ligands can hold different roles than when they are separately presented. This was demonstrated by Nie *et al.* [10] when functionalizing PEI polyplexes with B6 and a RGD-motif to target the tumoral TfR and integrins, respectively. Even though the authors aimed for a synergistic ligand effect they discovered that it was not additive. RGD, a targeting ligand known to cause NP internalization, mediated cellular attachment whereas B6 binding resulted in particle uptake. These results shed light on the different dynamic that the combination of two ligands can generate, which often does not equal the sum of the individual effects. More so, they can result contradictory. A recent study combining two ligands promoting anti-angiogenic and antitumoral activity, showed a paradoxical stimulation of cell survival due to the activation of an additional pathway when both ligands bound simultaneously [141].

Lastly, it has to be taken into account that due to the complexity of heteromultivalent systems, *in vitro* results often do not correlate with *in vivo* findings. This was the case for PEGylated liposomes developed for tumor angiogenesis imaging targeting integrin $\alpha_v\beta_3$ and galectin-1 with RGD and galectin-1-specific angixin, respectively [132]. Even though the dual targeted formulations showed a superior targeting *in vitro* than single-ligand formulations, both particle types showed similar tumor accumulations. Additionally, they differed in their distribution, being the heteromultivalent

formulations found in the tumor endothelium and the single-targeted liposomes in the vessel lumen [133]. Sawant *et al.* [151] also detected that *in vivo* their TF- and 2C5 monoclonal antibody-functionalized NPs showed little improvement in targeting efficiency compared to single-ligand formulations. Furthermore, it is noteworthy that for the majority heteromultivalent systems there are no *in vivo* studies available (Table II).

Taken all together, these results demonstrate that the virus mimicking heteromultivalency is a promising concept. However, every detail of the particle design (ligand density, ligand ratio, ligand arrangement) and its application (target expression levels, pattern variations) must be systematically studied and combined to achieve the sought-after targeting and specificity goals.

3.4 Stepwise heteromultivalent ligand display

Even though (hetero)multivalent display of ligands on a particle surface has been extensively investigated over the past years for the development targeted nanomaterials it has yet failed to achieve the desired results. Particles still lack specificity and targeting abilities. Compared to the 0.7% of the initial dose of non-functionalized nanomaterials that reaches a tumor, implementation of targeted recognition strategies elevates this value only to 0.9% [152]. This becomes even more discouraging when the actual dose that is internalized by the tumor cells, 0.0014%, is quantified [153]. Despite being virus-inspired, (hetero)multivalent approaches fail to completely mimic the viral host cell recognition process, which is decidedly more complex [7, 92]. Viruses not only bind heteromultivalently distinct membrane receptors, but they do so in a sequential manner [92]. Examples for this are the HIV type 1 binding consecutively to the CD4 and the chemokine receptor [154] or adenoviruses attaching to the coxsackie and adenovirus receptor (CAR) and integrins [155, 156]. As the presentation of ligands by heteromultivalent NPs is simultaneous, any cell expressing either of the target receptors is able to bind the particles. The independent binding of different tissues by each ligand was demonstrated for RGD and TF targeted polyplexes intended for the treatment of choroidal neovascularization [157] and for p-selectin and $\alpha\beta3$ integrin targeting NPs used for breast cancer treatment [135]. Overall, this translates into a poor particle specificity and target accumulation. This shortcoming of nanomaterials can be surmounted by a stepwise heteromultivalent approach with a virus-like sequential ligand presentation (Figure 2). In some studies, different ligands are coupled to a NPs surface for its sequential presentation, in that one of them enables cellular targeting, and the second one directs the particle to intracellular compartments, such as mitochondria [158] or the nucleus [159]. Nevertheless, the ligands are ubiquitously present on the particle surface and

Chapter 1: What Nanoparticles can Learn from Viruses

therefore cannot decrease nonspecific particle accumulation. Our group recently showed, that mimicking the stepwise host cell recognition of influenza A viruses highly increases the target cell specificity of nanomaterials [70]. Influenza A viruses display hemagglutinin on their envelope, which requires activation by an enzyme on the host cell membrane before binding to sialic acid, which triggers cell uptake [160]. To mimic this enzyme-mediated recognition, angiotensin-I (Ang-I) was coupled to biocompatible PEG-PLA block copolymer NPs with a PLGA-stabilized core [161]. Ang-I probed the target cells for the presence of angiotensin converting enzyme (ACE), which upon binding cleaved the two last amino acids, releasing angiotensin-II (Ang-II). The interaction of Ang-II with the Gq-coupled receptor angiotensin-II type 1 receptor (AT1R), as an agonist triggered endocytosis [162]. This principle was designed to identify with high specificity mesangial cells, as they play a crucial role in the development of diabetic nephropathy [163]. This renal complication is suffered by 50% of the 425 million diabetic patients worldwide [164] and lacks specific treatment options. The translation of the influenza A recognition principle enabled synthetic NPs to specifically identify mesangial cells in co-culture mixtures where they made up only 10%.

Furthermore, we improved the system incorporating an additional viral cell recognition step, the initial cell attachment (Chapter 5). As discussed above, viruses often attach to the host-cell surface to increase the viral concentration and initiate receptor recruitment. It does not mediate internalization of the virus particle, but it has been shown to be a decisive step during the infection process [93]. In order to mimic the attachment while still maintaining specificity, an antagonist for the AT1R, losartan carboxylic acid (EXP3174), was coupled to the particles. EXP3174 decorated NPs were previously shown to attach to the cell membrane, but not mediate internalization [68, 165]. The close mimicking of the viral host cell recognition, through a first attachment, followed by an enzymatic activation and concluded by an agonist-receptor binding (Figure 3A) enabled a 5- or 15-fold higher accumulation of particles in mesangial cells *in vivo* than NPs lacking the attachment principle or any viral traits, respectively (Figure 3B).

As there are a plethora of ectoenzymes available, this design principle can be expanded to other cell types involved in the development of diseases. These results demonstrate that apparently minor steps in the virus host-cell recognition strategy play crucial roles in their infectivity. Furthermore, their translation onto synthetic nanomaterials, increases extraordinarily their specificity and targeting capabilities and open new research paths to further improve nanomaterial design.

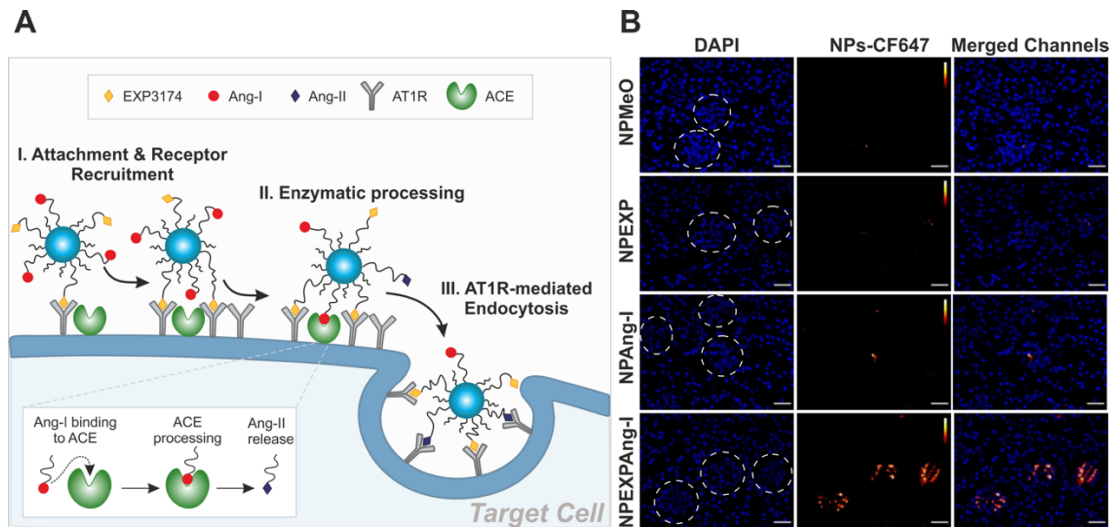


Figure 3. Virus mimetic cell recognition strategies. (A) Illustration of the initial receptor attachment and sequential target cell recognition and internalization of virus-mimetic NPs (NPEXPAng-I). (B) *In vivo* glomerular distribution and mesangial cell targeting. NPs mimicking the viral cell attachment and multistep recognition (NPEXPAng-I) show a high glomerular accumulation. Elimination of the attachment-mediating ligand reduces the targeting potential (NPAng-I). Control particles with no ligand (NPMcO) or only able to attach (NPEXP) show no glomerular localization. (Chapter 5).

4 Stimuli responsiveness

Viruses have evolved to respond to external stimuli, such as enzymes, reduction, or changes in the pH value, during their infection process [7]. This stimuli-responsiveness has been implemented on the newer generation of nanocarriers as it enables exploiting the specific disease environment to achieve a more effective and specific targeting. Particles can be designed to switch their surface charge, unmask active targeting ligands or shed their coating in response to pH variations, redox- or enzyme activity. Following this trend in recent years nanocarriers have been becoming more complex and “smarter” by incorporating multiple stimuli responsive elements. More so, such systems may allow for a higher control of the particle fate after administration (Figure 4). Despite stimuli-responsive nanomaterials being reviewed in the past [166], due to the high number of publications in this field over the last 3 years we will give a brief overview and discuss the newest systems that aim to mimic viral behavior or traits.

4.1 Single stimuli-responsive systems

The pathological characteristics of therapeutically relevant tissues can be used to increase the targeting efficiency of nanocarriers. Enzyme-responsive systems that target enzymes linked to a specific disease are an example of this [167]. The enzymes

Chapter 1: What Nanoparticles can Learn from Viruses

most commonly addressed are the matrix metalloproteinases (MMPs) [168], which can be found in the extracellular tumor medium. They have been used to unveil PEG-shielded ligands protected during circulation [169–174], or to induce a NP morphology change [175–178], increasing the targeting potential of NPs. Other enzymes, such as legumain, which is upregulated in tumors in correlation with their malignancy [179], have also been targeted to unveil shielded ligands, like TAT[180], in a site-specific manner. Enzymes associated with drug-resistant bacterial strains, such as Penicillin G amidase and β -lactamase [181] or *P. aeruginosa* elastase [182], can also be used as targets to achieve a selective delivery of antimicrobial agents. More so, enzyme-responsive systems have long been adopted for the controlled delivery of drugs [40, 114, 171, 183].

As an alternative approach to enzymes, linkers or tethers with pH-responsive functionalities can be introduced in the particle design, to shield ligands during blood circulation, and increase their targeting once an acidic environment is reached [184–186]. Furthermore, pH-responsiveness can be used to initiate cargo release [187–189] in acidic intracellular compartments or tumor milieus [190]. More so, it can be adopted to mimic the viral trait of endosomal escape [191, 192] which is mediated by membrane fusion or disruption, for enveloped and non-enveloped viruses [193], respectively. The endolysosomal escape of non-enveloped viruses was mimicked by Song *et al.* [194] with NPs prepared from pH-sensitive hydrazone bond-containing polyurethane. After target-specific cell internalization, upon exposure to acidic pH the particles underwent charge reversal, core exposure and induced endosome rupture. This viral trait has also been implemented in synthetic nanomaterials through additional mechanisms, such as membrane fusion, osmotic disruption, particle swelling and membrane destabilization [195] or the incorporation of viral and viral-mimetic peptide sequences related to endosomal escape [196, 197].

Lastly, Redox-responsive systems show great potential as drug delivery systems [198] in disease with elevated reactive oxygen species (ROS), such as cancer [199, 200]. They can be used to induce a site-specific drug release, as shown by Jian *et al.* [201]. The authors emulated the viral capability of overcoming barriers, such as the BBB, with virus-sized polymerosomes encapsulating the toxin saporin, which is highly degradable *in vivo*. The particles were functionalized with angiopep-2, a high affinity ligand towards the low-density lipoprotein receptor-related protein-1 (LRP-1). Due to their redox responsiveness, upon reaching intracellular environments the particles were able to release their payload. After administration in glioblastoma-bearing mice particles were able to accumulate at the target through LRP-1-mediated BBB transcytosis and increase survival rate through tumor inhibition.

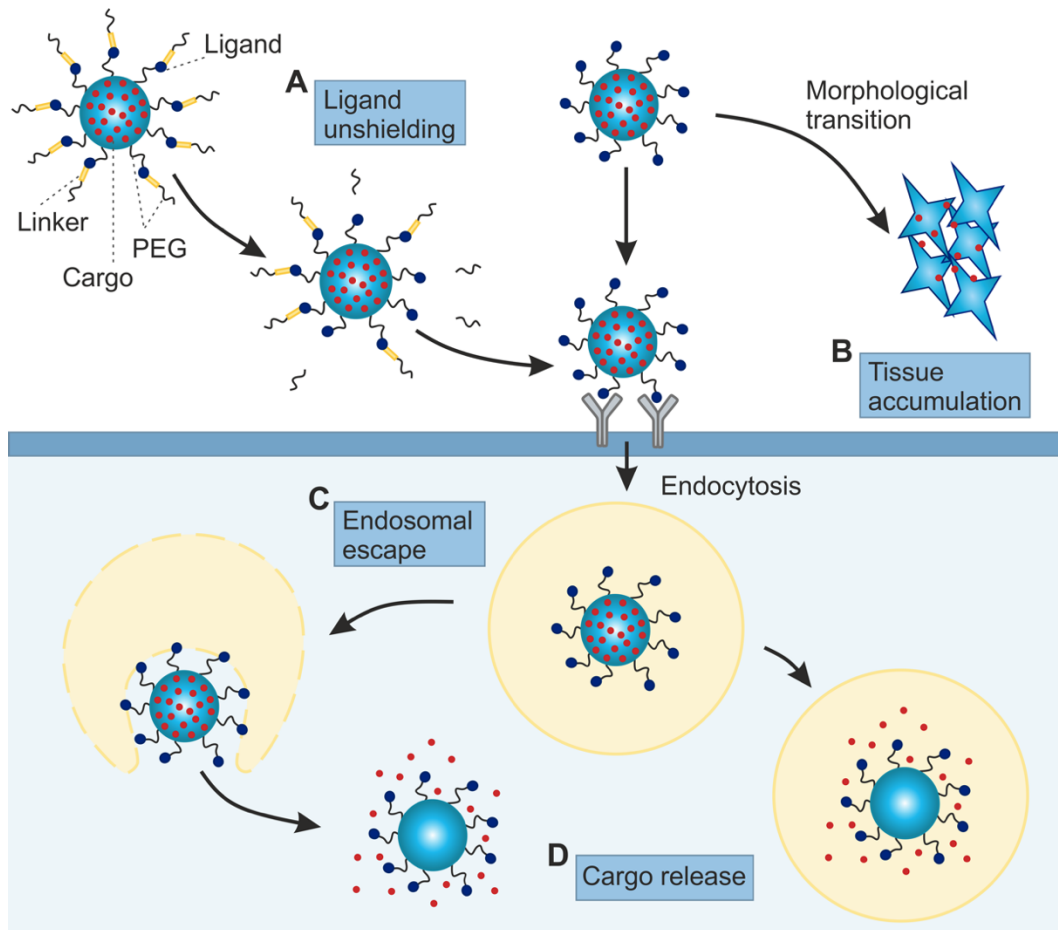


Figure 4. Effects of stimuli responsiveness in targeted virus-mimetic NPs. A) NPs with PEG protected ligands are subjected to ligand unshielding through enzymatic, pH or redox-responsive linker cleavage at the target site. B) NPs undergo morphological transition due to specific enzymatic processing or temperature variation and accumulate in a specific tissue, such as sites of bacterial infection or tumors. C) After NP cellular uptake, endosomal escape is triggered by pH mediated membrane disruption D) Cargo release from NPs is initiated after response to pH, redox-, or enzymatic stimuli in different intracellular compartments.

4.2 Multiresponsive systems

Particles that respond to a single stimulus hold great advantages regarding targeting efficiency. However, in recent years nanomaterials are being designed so that they respond to a combination of stimuli. These multiresponsive systems allow to mimic the continuous changes that viruses undergo during their infection cycle. They also enable targeting a higher variety of diseases with increased specificity. More so, they provide a more precise control of particle fate upon administration.

Some systems present sequential responsiveness to the same type of stimuli, as for example, the multiple targeting of both extracellular and intracellular enzymes. Han *et al.* [171] used this concept and achieved specific tumor targeting, through un-shielding of a PEGylated ligand by MMP-9 and controlled drug by cathepsin-B, present in the tumor environment and lysosomes, respectively. Another approach is the dual redox-responsiveness, which was employed by He *et al.* [202] to increase delivery of nucleic acids to tumor cell with polyplexes that, like viruses, are subject to sequential unshielding and unpacking steps: first after cellular attachment or internalization, and second to enable genome release after endosomal escape.

Other systems are responsive to a combination of different stimuli. The association of MMP- and reactive oxygen species (ROS)-responsiveness enabled Daniel *et al.* [203] to use amphiphilic polymer NPs in inflammatory diseases, such as myocardial infarction, arthritis, ischemia and atherosclerosis, where both are upregulated. With this design approach they achieved specific targeting of ischemic skeletal muscle [204], avoiding off-targeting of healthy muscle and regulating macrophage internalization [205]. The increase in NP specificity achieved by multiresponsive systems has the potential to reduce therapy-associated toxicity. Zhang *et al.* [206] developed a polycaprolacton and PEG delivery system connected by redox-responsive azo bonds that were disintegrated by azoreductase after sialic acid-mediated internalization in hepatocellular carcinoma cells. Camptothecin release due to disulfide bond breakage was triggered in the presence of high concentrations of glutathione [206]. A combination of active targeting with the two-step stimuli-responsive drug release achieved a good *in vivo* targeting with an efficient tumor therapy. Similarly, Li *et al.* [207] developed NPs composed of hydroxyethyl starch (HES) coupled to paclitaxel (PTX) through a redox-sensitive disulfide bond. During circulation particles underwent a size reduction due to HES degradation by α -amylase, which promoted their extravasation to tumors. The cleavage of the disulfide bond in high redox potential tumor environments unloaded the particles cargo.

Stimuli responsive NPs enable increased targeting specificity and site-controlled drug release. Additionally, when combining responses to multiple stimuli the sequential transformation viruses suffer during their infection process can be mimicked. Furthermore, due to the myriad of developed materials with transversal application, the therapy options for difficultly targeted diseases are broadened.

5 Cell to cell spreading

A fundament for the perpetuation of the viral cycle is their ability to replicate and spread from cell to cell [208]. The former may not be (to date) possible, but bestowing

NPs with the latter may allow to lower dosages and enforce valuable properties in applications, such as cancer treatment. Several years ago, Lee *et al.* [209] developed a virus mimetic delivery vehicle capable of disseminating from cell to cell. It consisted on a core-shell nanogel loaded with DOX. The poly(l-histidine-co- phenylalanine) core was covered by a PEG shell, linked to bovine serum albumin (BSA) molecules. To achieve a specific targeting to tumor cells, folate molecules were conjugated to the BSA. Upon subjection of the nanogels to different pH values, they were able to shrink and expand due to their pH sensitive core, varying between 55 nm at pH 7.4 and 355 nm at pH 6.4. After “infection” of the target cells, DOX-mediated apoptosis was induced, and the nanogels were released in to the medium ready to target the next cell. This DOX apoptosis-derived approach to induce cell spreading was also used by Cui *et al.* [210]. They additionally enhanced the penetration in tumors by NP hyaluronidase release under acidic tumor conditions, which is able to cleave HA in the extracellular matrix and reduces the NP size. However, a limitation of this infective mechanism is the amount of DOX loaded in the nanocarriers, since it is responsible for cell death and NP release. Fang *et al.* [211] developed magneto-responsive nanocapsules composed of an iron oxide core and a tumor targeting lactoferrin shell. The anti-cancer drug-loaded NPs were able to release therapeutic agents whilst concomitantly producing intense heat after an external high frequency magnetic field was applied. Particles were released after cell death and migrated to neighboring cells. With this dual treatment mechanism, the need of a drug-induced effect for particle spreading is minimized. Another option to achieve particle spreading was shown by Zhang *et al.* who developed a DOX carrier system composed of dendritic peptides, which under acidic pH conditions revealed arginine rich domains that induced membrane-braking activity [187]. The problem can be further evaded when the NPs are able to bind to the cell cytoskeleton in order to disseminate to neighboring cells, as was shown recently by Dalmau-Mena *et al.* [212]. Their approach was based on the how viruses bind to the microtubule motor to disseminate and replicate. Gold NPs were modified with viral peptides that bind dynein, a microtubule motor which is used for transport by several viruses [213]. Internalized particles were able to move through the cytosol after dynein binding and progress to neighboring cells through cell projections, reducing the particle loss to extracellular compartments.

Overall mimicking the viral transmission shows great potential, especially in the field of oncology where the therapy would enormously benefit from the dose reductions enabled by these technologies. Nevertheless, an improvement of the specificity of the targeting mechanisms would pose a great advantage, as it would facilitate a much wider range of applications. Meanwhile, local therapy seems to be the ideal use of such “infective” NPs, reducing the risk of off target effects.

6 Towards an artificial virus?

A comprehensive examination of the viral characteristics has promoted the design of particles that mimic different aspects of a virus' natural behavior. Already implementing single viral traits has improved several aspects of nanomaterials' performance. However, even though this fundamental research has considerably advanced our knowledge and has provided the foundations for particle optimization, a holistic approach may hold more promise. The combination of structural features, such as shape and surface properties, with ligand mediated cell recognition and stimuli responsiveness has recently led to the development of formulations that are almost an exact synthetic replica of viruses. In publications such as the one by Lee *et al.* [29] we can see that this provides huge advantages regarding targeting capability. In their work they prepared a synthetic duplicate of the RABV by exactly matching its size, shape and surface glycoprotein. Silica-coated gold nanorods, with elongated morphology equal to the RABV were chosen to increase the cellular receptor interaction. Their close imitation of the RABV properties enabled a virus-like *in vivo* behavior which could suppress brain tumors after irradiation. Due to their viral surface ligands the particles interact with the virus-used targeted receptors, but the perfect combination with an exact virus-like shape and size potentiates its effect. Also the work published by Mable *et al.* [214] were the morphology and pH-responsiveness of the Dengue virus (DV) was mimicked with copolymer vesicles points towards the same conclusions. By imitating the framboidal morphology the DV adopts upon transition from the 28°C mosquito vector to the 37°C human host [215] and its additional pH-induced transformation that allows for endosomal escape, they were able to address SR-B1 overexpressing triple-negative breast cancer cells for which there are currently no targeted therapies. More so, their formulation did not accumulate in healthy or SR-B1-negative cells. The authors attributed the targeting specificity to a combination of the ligand and the Dengue-mimicking rough surface, which was associated with higher targeting efficiency through membrane deformation [214].

Therefore, the holistic implementation of viral properties on NPs to create an "artificial virus" may aid increase the therapies' specificity and effectivity, as individual traits seem insufficient to achieve these goals. We can probably look forward to formulations further implementing multiple viral traits to achieve the perfect "synthetic virus", which may surmount the alarming low specificity and target cell accumulation that nanomaterials achieve up to date [152, 153].

An important question in this regard is if there will be a single universal "artificial virus formulation" only subjected to slight modifications depending on the application, or if viruses will be mimicked in accordance with their natural targets. The latter is a frequently used approach. For example, for brain targeting the RABV is often

used as a model [29, 100], for its capability of crossing the difficult BBB. Another example is the addressing of hepatic cells with particles imitating the HBV [95–97]. However, to expand the applicability to therapeutically relevant cells not naturally addressed by viruses the first approach may be a better fit. This is reinforced by the focus on high tunability of the formulations being developed. Indisputably, due to disease individuality an exact tailoring of the formulation is essential. More so, the cargo selection can also play a role on the chosen formulation. Whether the intent is delivery of genes, small molecule drugs or proteins or it requires external irradiation, such as for photothermal therapy, the systems composition and therefore characteristics will have to change.

Last but not least, the feasibility of the clinical translation of these systems is overcast by substantial uncertainty. An encouraging element in this direction is the effort that numerous researches make to use safe, non-toxic and FDA-approved materials for their developed formulations. However, the complexity that the formulations reach with increasing number of viral traits added may pose an obstacle for clinical application. Therefore, additional comprehensive research is needed in an exciting field where only the pillars have been set.

7 Conclusion

The implementation of viral features on NPs is a conquerable endeavor that has substantially influenced and improved the design of therapeutic nanomaterials. Future investigations in the formulation field incorporating viral traits using a more holistic approach may solve the specificity and accumulation problems NPs face up to date. Overall, it is reasonable to say that viruses can be considered as a great source of inspiration for nanomaterial design with enormous potential in the field of targeted drug delivery.

References

- [1] Rahman M, Laurent S, Tawil N, et al. Nanoparticle and Protein Corona. In: *Protein-Nanoparticle Interactions*, pp. 21–44.
- [2] Abstiens K, Maslanka Figueroa S, Gregoritz M, et al. Interaction of functionalized nanoparticles with serum proteins and its impact on colloidal stability and cargo leaching. *Soft Matter* 2019; 15: 709–720.
- [3] Lee YK, Choi E-J, Webster TJ, et al. Effect of the protein corona on nanoparticles for modulating cytotoxicity and immunotoxicity. *Int J Nanomedicine* 2015; 10: 97–113.
- [4] Mirshafiee V, Mahmoudi M, Lou K, et al. Protein corona significantly reduces active targeting yield. *Chem Commun* 2013; 49: 2557.
- [5] Karmali PP, Simberg D. Interactions of nanoparticles with plasma proteins: Implication on clearance and toxicity of drug delivery systems. *Expert Opin Drug Deliv* 2011; 8: 343–357.
- [6] Meng H, Leong W, Leong KW, et al. Walking the line: The fate of nanomaterials at biological barriers. *Biomaterials* 2018; 174: 41–53.
- [7] Marsh M, Helenius A. Virus Entry: Open Sesame. *Cell* 2006; 124: 729–740.
- [8] Dunbar CE, High KA, Joung JK, et al. Gene therapy comes of age. *Science* 2018; 359: eaan4672.
- [9] Li SD, Huang L. Non-viral is superior to viral gene delivery. *J Control Release* 2007; 123: 181–183.
- [10] Nie Y, Schaffert D, Rödl W, et al. Dual-targeted polyplexes: One step towards a synthetic virus for cancer gene therapy. *J Control Release* 2011; 152: 127–134.
- [11] Raoult D, Audic S, Robert C, et al. The 1.2-megabase genome sequence of Mimivirus. *Science* 2004; 306: 1344–50.
- [12] Cui J, Schlub TE, Holmes EC. An allometric relationship between the genome length and virion volume of viruses. *J Virol* 2014; 88: 6403–10.
- [13] Maslanka Figueroa S, Fleischmann D, Beck S, et al. Thermodynamic, Spatial and Methodological Considerations for the Manufacturing of Therapeutic Polymer Nanoparticles. *Pharm Res* 2020; 37: 59.
- [14] Albanese A, Tang PS, Chan WCW. The Effect of Nanoparticle Size, Shape, and Surface Chemistry on Biological Systems. *Annu Rev Biomed Eng* 2012; 14: 1–16.
- [15] Hang C, Choi J, Zuckerman JE, et al. Targeting kidney mesangium by

- nanoparticles of defined size. *Proc Natl Acad Sci U S A* 2011; 108: 6656–6661.
- [16] Soo Choi H, Liu W, Misra P, et al. Renal clearance of quantum dots. *Nat Biotechnol* 2007; 25: 1165–1170.
- [17] Zhou C, Long M, Qin Y, et al. Luminescent Gold Nanoparticles with Efficient Renal Clearance. *Angew Chemie* 2011; 123: 3226–3230.
- [18] Zuckerman JE, Davis ME. Targeting Therapeutics to the Glomerulus With Nanoparticles. *Adv Chronic Kidney Dis* 2013; 20: 500–507.
- [19] Blanco E, Shen H, Ferrari M. Principles of nanoparticle design for overcoming biological barriers to drug delivery. *Nat Biotechnol* 2015; 33: 941–951.
- [20] Bachmann MF, Jennings GT. Vaccine delivery: a matter of size, geometry, kinetics and molecular patterns. *Nat Rev Immunol* 2010; 10: 787–796.
- [21] Manolova V, Flace A, Bauer M, et al. Nanoparticles target distinct dendritic cell populations according to their size. *Eur J Immunol* 2008; 38: 1404–1413.
- [22] Lico C, Giardullo P, Mancuso M, et al. A biodistribution study of two differently shaped plant virus nanoparticles reveals new peculiar traits. *Colloids Surfaces B Biointerfaces* 2016; 148: 431–439.
- [23] Roberts PC, Compans RW. Host cell dependence of viral morphology. *Proc Natl Acad Sci* 1998; 95: 5746–5751.
- [24] Geng Y, Dalhaimer P, Cai S, et al. Shape effects of filaments versus spherical particles in flow and drug delivery. *Nat Nanotechnol* 2007; 2: 249–255.
- [25] Mahmud A, Discher DE. Lung vascular targeting through inhalation delivery: Insight from filamentous viruses and other shapes. *IUBMB Life* 2011; 63: 607–612.
- [26] Lee KL, Hubbard LC, Hern S, et al. Shape matters: the diffusion rates of TMV rods and CPMV icosahedrons in a spheroid model of extracellular matrix are distinct. *Biomater Sci* 2013; 1: 581.
- [27] Hernandez-Garcia A, Cohen Stuart MA, de Vries R. Templated co-assembly into nanorods of polyanions and artificial virus capsid proteins. *Soft Matter* 2018; 14: 132–139.
- [28] Jiang X, Qu W, Pan D, et al. Plasmid-Templated Shape Control of Condensed DNA-Block Copolymer Nanoparticles. *Adv Mater* 2013; 25: 227–232.
- [29] Lee C, Hwang HS, Lee S, et al. Rabies Virus-Inspired Silica-Coated Gold Nanorods as a Photothermal Therapeutic Platform for Treating Brain Tumors. *Adv Mater* 2017; 29: 1605563.

Chapter 1: What Nanoparticles can learn from viruses

- [30] Andersson S. The Structure of Virus Capsids. *Zeitschrift für Anorg und Allg Chemie* 2008; 634: 2161–2170.
- [31] Truong NP, Whittaker MR, Mak CW, et al. The importance of nanoparticle shape in cancer drug delivery. *Expert Opin Drug Deliv* 2015; 12: 129–142.
- [32] Fernandes R, Gracias DH. Self-folding polymeric containers for encapsulation and delivery of drugs. *Adv Drug Deliv Rev* 2012; 64: 1579–1589.
- [33] Chen MY, Hoffer A, Morrison PF, et al. Surface properties, more than size, limiting convective distribution of virus-sized particles and viruses in the central nervous system. *J Neurosurg* 2005; 103: 311–319.
- [34] Banerjee N, Mukhopadhyay S. Viral glycoproteins: biological role and application in diagnosis. *Virusdisease* 2016; 27: 1–11.
- [35] Niu Y, Yu M, Hartono SB, et al. Nanoparticles Mimicking Viral Surface Topography for Enhanced Cellular Delivery. *Adv Mater* 2013; 25: 6233–6237.
- [36] Wang F, Liu P, Sun L, et al. Bio-mimetic Nanostructure Self-assembled from Au@Ag Heterogeneous Nanorods and Phage Fusion Proteins for Targeted Tumor Optical Detection and Photothermal Therapy. *Sci Rep* 2015; 4: 6808.
- [37] Cai X, Jin R, Wang J, et al. Bioreducible Fluorinated Peptide Dendrimers Capable of Circumventing Various Physiological Barriers for Highly Efficient and Safe Gene Delivery. *ACS Appl Mater Interfaces* 2016; 8: 5821–5832.
- [38] Sun X, Li M, Yang Y, et al. Carrier-free nanodrug-based virus-surface-mimicking nanosystems for efficient drug/gene co-delivery. *Biomater Sci* 2018; 6: 3300–3308.
- [39] Wang W, Wang P, Tang X, et al. Facile Synthesis of Uniform Virus-like Mesoporous Silica Nanoparticles for Enhanced Cellular Internalization. *ACS Cent Sci* 2018; 15: 839–846.
- [40] Liu S, Yang J, Jia H, et al. Virus Spike and Membrane-Lytic Mimicking Nanoparticles for High Cell Binding and Superior Endosomal Escape. *ACS Appl Mater Interfaces* 2018; 10: 23630–23637.
- [41] Xu L, Frederik P, Pirolo KF, et al. Self-Assembly of a Virus-Mimicking Nanostructure System for Efficient Tumor-Targeted Gene Delivery. *Hum Gene Ther* 2002; 13: 469–481.
- [42] Vigerust DJ, Shepherd VL. Virus glycosylation: role in virulence and immune interactions. *Trends Microbiol* 2007; 15: 211–218.
- [43] Klenk H-D, Wagner R, Heuer D, et al. Importance of hemagglutinin

- glycosylation for the biological functions of influenza virus. *Virus Res* 2001; 82: 73–75.
- [44] Fenouillet E, Gluckman JC, Bahraoui E. Role of N-linked glycans of envelope glycoproteins in infectivity of human immunodeficiency virus type 1. *J Virol* 1990; 64: 2841–8.
- [45] Tokatlian T, Read BJ, Jones CA, et al. Innate immune recognition of glycans targets HIV nanoparticle immunogens to germinal centers. *Science (80-)* 2019; 363: 649–654.
- [46] Li L, Zheng T, Wang T, et al. Virus Envelope-Like Self-Assembled Nanoparticles Based on α -CD/PEG for Antigens Targeting to Dendritic Cells. *J Biomed Nanotechnol* 2017; 13: 1490–1499.
- [47] Pinnapireddy S, Raafat El Assy M, Schlote P, et al. Glycosylated Artificial Virus-Like Hybrid Vectors for Advanced Gene Delivery. *Polymers (Basel)* 2019; 11: 243.
- [48] Jain K, Kesharwani P, Gupta U, et al. A review of glycosylated carriers for drug delivery. *Biomaterials* 2012; 33: 4166–4186.
- [49] Byeon HJ, Thao LQ, Lee S, et al. Doxorubicin-loaded nanoparticles consisted of cationic- and mannose-modified-albumins for dual-targeting in brain tumors. *J Control Release* 2016; 225: 301–313.
- [50] Tate M, Job E, Deng Y-M, et al. Playing Hide and Seek: How Glycosylation of the Influenza Virus Hemagglutinin Can Modulate the Immune Response to Infection. *Viruses* 2014; 6: 1294–1316.
- [51] Chang K-S, Jiang J, Cai Z, et al. Human apolipoprotein e is required for infectivity and production of hepatitis C virus in cell culture. *J Virol* 2007; 81: 13783–93.
- [52] Ezzat K, Pernemalm M, Pålsson S, et al. The viral protein corona directs viral pathogenesis and amyloid aggregation. *Nat Commun* 2019; 10: 2331.
- [53] Pitek AS, Wen AM, Shukla S, et al. The Protein Corona of Plant Virus Nanoparticles Influences their Dispersion Properties, Cellular Interactions, and in Vivo Fates. *Small* 2016; 12: 1758–1769.
- [54] Leng C, Hung H-C, Sun S, et al. Probing the Surface Hydration of Nonfouling Zwitterionic and PEG Materials in Contact with Proteins. *ACS Appl Mater Interfaces* 2015; 7: 16881–16888.
- [55] Ashraf S, Park J, Bichelberger MA, et al. Zwitterionic surface coating of quantum dots reduces protein adsorption and cellular uptake. *Nanoscale* 2016; 8: 17794–17800.

Chapter 1: What Nanoparticles can learn from viruses

- [56] Shengfu Chen, Jie Zheng, Lingyan Li A, et al. Strong Resistance of Phosphorylcholine Self-Assembled Monolayers to Protein Adsorption: Insights into Nonfouling Properties of Zwitterionic Materials. *J Am Chem Soc* 2005; 125: 14474–14478.
- [57] Maiolo D, Del Pino P, Metrangolo P, et al. Nanomedicine delivery: Does protein corona route to the target or off road? *Nanomedicine* 2015; 10: 3231–3247.
- [58] Witten J, Samad T, Ribbeck K. Selective permeability of mucus barriers. *Curr Opin Biotechnol* 2018; 52: 124–133.
- [59] Lai SK, Elizabeth O’hanlon D, Harrold S, et al. Rapid transport of large polymeric nanoparticles in fresh undiluted human mucus. *Proc Natl Acad Sci* 2007; 104: 1482–1487.
- [60] Ensign LM, Cone R, Hanes J. Oral drug delivery with polymeric nanoparticles: The gastrointestinal mucus barriers. *Adv Drug Deliv Rev* 2012; 64: 557–570.
- [61] Ensign LM, Tang BC, Wang Y-Y, et al. Mucus-penetrating nanoparticles for vaginal drug delivery protect against herpes simplex virus. *Sci Transl Med* 2012; 4: 138ra79.
- [62] Liu C, Xu H, Sun Y, et al. Design of Virus-Mimicking Polyelectrolyte Complexes for Enhanced Oral Insulin Delivery. *J Pharm Sci* 2019; 1–8.
- [63] Zhu X, Wu J, Shan W, et al. Sub-50 nm Nanoparticles with Biomimetic Surfaces to Sequentially Overcome the Mucosal Diffusion Barrier and the Epithelial Absorption Barrier. *Adv Funct Mater* 2016; 26: 2728–2738.
- [64] Shan W, Cui Y, Liu M, et al. Systematic evaluation of the toxicity and biodistribution of virus mimicking mucus-penetrating DLPC-NPs as oral drug delivery system. *Int J Pharm* 2017; 530: 89–98.
- [65] Wu J, Zheng Y, Liu M, et al. Biomimetic Viruslike and Charge Reversible Nanoparticles to Sequentially Overcome Mucus and Epithelial Barriers for Oral Insulin Delivery. *ACS Appl Mater Interfaces* 2018; 10: 9916–9928.
- [66] Verma A, Stellacci F. Effect of Surface Properties on Nanoparticle-Cell Interactions. *Small* 2010; 6: 12–21.
- [67] Grove J, Marsh M. The cell biology of receptor-mediated virus entry. *J Cell Biol* 2011; 195: 1071–82.
- [68] Hennig R, Pollinger K, Vesper A, et al. Nanoparticle multivalency counterbalances the ligand affinity loss upon PEGylation. *J Control Release* 2014; 194: 20–27.

- [69] Hild W, Pollinger K, Caporale A, et al. G protein-coupled receptors function as logic gates for nanoparticle binding and cell uptake. *Proc Natl Acad Sci U S A* 2010; 107: 10667–72.
- [70] Maslanka Figueroa S, Veser A, Abstiens K, et al. Influenza A virus mimetic nanoparticles trigger selective cell uptake. *Proc Natl Acad Sci* 2019; 116: 9831–9836.
- [71] Dreaden EC, Gryder BE, Austin LA, et al. Antiandrogen Gold Nanoparticles Dual-Target and Overcome Treatment Resistance in Hormone-Insensitive Prostate Cancer Cells. *Bioconjug Chem* 2012; 23: 1507–1512.
- [72] Hennig R, Veser A, Kirchhof S, et al. Branched Polymer–Drug Conjugates for Multivalent Blockade of Angiotensin II Receptors. *Mol Pharm* 2015; 12: 3292–3302.
- [73] Danhier F, Le Breton A, Pr at V. RGD-Based Strategies To Target Alpha(v) Beta(3) Integrin in Cancer Therapy and Diagnosis. *Mol Pharm* 2012; 9: 2961–2973.
- [74] Lim EH, Danthi N, Bednarski M, et al. Integrin $\alpha\beta3$ -targeted molecular imaging and therapy in angiogenesis. *Nanomedicine Nanotechnology, Biol Med* 2005; 1: 110–114.
- [75] Lepenies B, Lee J, Sonkaria S. Targeting C-type lectin receptors with multivalent carbohydrate ligands. *Adv Drug Deliv Rev* 2013; 65: 1271–1281.
- [76] Yoo J, Park C, Yi G, et al. Active Targeting Strategies Using Biological Ligands for Nanoparticle Drug Delivery Systems. *Cancers (Basel)* 2019; 11: 640.
- [77] Alkilany AM, Zhu L, Weller H, et al. Ligand density on nanoparticles: A parameter with critical impact on nanomedicine. *Adv Drug Deliv Rev* 2019; 143: 22–36.
- [78] Saeed AO, Magnusson JP, Moradi E, et al. Modular Construction of Multifunctional Bioresponsive Cell-Targeted Nanoparticles for Gene Delivery. *Bioconjug Chem* 2011; 22: 156–168.
- [79] Fakhari A, Baoum A, Siahaan TJ, et al. Controlling ligand surface density optimizes nanoparticle binding to ICAM-1. *J Pharm Sci* 2011; 100: 1045–56.
- [80] Elias DR, Poloukhine A, Popik V, et al. Effect of ligand density, receptor density, and nanoparticle size on cell targeting. *Nanomedicine* 2013; 9: 194–201.
- [81] Maslanka Figueroa S, Fleischmann D, Beck S, et al. The Effect of Ligand Mobility on the Cellular Interaction of Multivalent Nanoparticles. *Macromol Biosci* 2020; 20: 1900427.

Chapter 1: What Nanoparticles can learn from viruses

- [82] Poon Z, Chen S, Engler AC, et al. Ligand-Clustered “Patchy” Nanoparticles for Modulated Cellular Uptake and In Vivo Tumor Targeting. *Angew Chemie Int Ed* 2010; 49: 7266–7270.
- [83] Abstiens K, Gregoritz M, Goepferich AM. Ligand Density and Linker Length are Critical Factors for Multivalent Nanoparticle–Receptor Interactions. *Appl Mater Interfaces* 2019; 11: 1311–1320.
- [84] Chen H, Paholak H, Ito M, et al. ‘Living’ PEGylation on gold nanoparticles to optimize cancer cell uptake by controlling targeting ligand and charge densities. *Nanotechnology* 2013; 24: 355101.
- [85] Stewart PL, Chiu CY, Huang S, et al. Cryo-EM visualization of an exposed RGD epitope on adenovirus that escapes antibody neutralization. *EMBO J* 1997; 16: 1189–1198.
- [86] Chiu CY, Mathias P, Nemerow GR, et al. Structure of Adenovirus Complexed with Its Internalization Receptor, $\alpha\beta 5$ Integrin. *J Virol* 1999; 73: 6759–6768.
- [87] Goldman MJ, Wilson JM. Expression of alpha v beta 5 integrin is necessary for efficient adenovirus-mediated gene transfer in the human airway. *J Virol* 1995; 69: 5951–8.
- [88] Ng QK, Sutton MK, Soonsawad P, et al. Engineering Clustered Ligand Binding Into Nonviral Vectors: $\alpha\beta 3$ Targeting as an Example. *Mol Ther* 2009; 17: 828–836.
- [89] Moradi E, Vllasaliu D, Garnett M, et al. Ligand density and clustering effects on endocytosis of folate modified nanoparticles. *RSC Adv* 2012; 2: 3025.
- [90] Zhou J, Kroll A V., Holay M, et al. Biomimetic Nanotechnology toward Personalized Vaccines. *Adv Mater* 2019; 1901255.
- [91] Chattopadhyay S, Chen J-Y, Chen H-W, et al. Nanoparticle Vaccines Adopting Virus-like Features for Enhanced Immune Potentiation. *Nanotheranostics* 2017; 1: 244–260.
- [92] Boulant S, Stanifer M, Lozach P-Y. Dynamics of virus-receptor interactions in virus binding, signaling, and endocytosis. *Viruses* 2015; 7: 2794–815.
- [93] Jones JC, Turpin EA, Bultmann H, et al. Inhibition of Influenza Virus Infection by a Novel Antiviral Peptide That Targets Viral Attachment to Cells. *J Virol* 2006; 80: 11960–11967.
- [94] Rubas W, Banerjea AC, Gallati H, et al. Incorporation of the reovirus M cell attachment protein into small unilamellar vesicles: incorporation efficiency and binding capability to L929 cells in vitro. *J Microencapsul* 1990; 7: 385–395.

- [95] Liu Q, Somiya M, Iijima M, et al. A hepatitis B virus-derived human hepatic cell-specific heparin-binding peptide: identification and application to a drug delivery system. *Biomater Sci* 2019; 7: 322–335.
- [96] Zhang X, Zhang Q, Peng Q, et al. Hepatitis B virus preS1-derived lipopeptide functionalized liposomes for targeting of hepatic cells. *Biomaterials* 2014; 35: 6130–6141.
- [97] Somiya M, Kuroda S. Development of a virus-mimicking nanocarrier for drug delivery systems: The bio-nanocapsule. *Adv Drug Deliv Rev* 2015; 95: 77–89.
- [98] Finlay BB, McFadden G. Anti-Immunology: Evasion of the Host Immune System by Bacterial and Viral Pathogens. *Cell* 2006; 124: 767–782.
- [99] Jung J, Somiya M, Jeong SY, et al. Low immunogenic bio-nanocapsule based on hepatitis B virus escape mutants. *Nanomedicine Nanotechnology, Biol Med* 2018; 14: 595–600.
- [100] You L, Wang J, Liu T, et al. Targeted Brain Delivery of Rabies Virus Glycoprotein 29-Modified Deferoxamine-Loaded Nanoparticles Reverses Functional Deficits in Parkinsonian Mice. *ACS Nano* 2018; 12: 4123–4139.
- [101] Koren E, Torchilin VP. Cell-penetrating peptides: breaking through to the other side. *Trends Mol Med* 2012; 18: 385–393.
- [102] Fawell S, Seery J, Daikh Y, et al. Tat-mediated delivery of heterologous proteins into cells. *Proc Natl Acad Sci U S A* 1994; 91: 664–8.
- [103] Qi X, Droste T, Kao CC. Cell-Penetrating Peptides Derived from Viral Capsid Proteins. *Mol Plant-Microbe Interact* 2011; 24: 25–36.
- [104] Torchilin VP. Tat peptide-mediated intracellular delivery of pharmaceutical nanocarriers. *Adv Drug Deliv Rev* 2008; 60: 548–558.
- [105] Santra S, Yang H, Dutta D, et al. TAT conjugated, FITC doped silica nanoparticles for bioimaging applications. *Chem Commun* 2004; 0: 2810.
- [106] Pan L, He Q, Liu J, et al. Nuclear-Targeted Drug Delivery of TAT Peptide-Conjugated Monodisperse Mesoporous Silica Nanoparticles. *J Am Chem Soc* 2012; 134: 5722–5725.
- [107] Lewin M, Carlesso N, Tung C-H, et al. Tat peptide-derivatized magnetic nanoparticles allow in vivo tracking and recovery of progenitor cells. *Nat Biotechnol* 2000; 18: 410–414.
- [108] Wunderbaldinger P, Josephson L, Weissleder R. Tat Peptide Directs Enhanced Clearance and Hepatic Permeability of Magnetic Nanoparticles. *Bioconjug Chem*

Chapter 1: What Nanoparticles can learn from viruses

- 2002; 13: 264–268.
- [109] de la Fuente JM, Berry CC. Tat Peptide as an Efficient Molecule To Translocate Gold Nanoparticles into the Cell Nucleus. *Bioconjug Chem* 2005; 16: 1176–1180.
- [110] Phan MD, Kim H, Lee S, et al. HIV Peptide-Mediated Binding Behaviors of Nanoparticles on a Lipid Membrane. *Langmuir* 2017; 33: 2590–2595.
- [111] Liu L, Guo K, Lu J, et al. Biologically active core/shell nanoparticles self-assembled from cholesterol-terminated PEG–TAT for drug delivery across the blood–brain barrier. *Biomaterials* 2008; 29: 1509–1517.
- [112] Liu, Yang; Wang, Hao; Kamei, Ken-ichiro; Yan, Ming; Chen, Kuan-Ju; Yun, Qinghua; Shi, Linqi; Lu, Yunfeng; Tseng H-R. Delivery of Intact Transcription Factor by Using Self-Assembled Supramolecular Nanoparticles. *Angew Chemie* 2011; 123: 3114–3118.
- [113] Rao KS, Reddy MK, Horning JL, et al. TAT-conjugated nanoparticles for the CNS delivery of anti-HIV drugs. *Biomaterials* 2008; 29: 4429–4438.
- [114] Xiong X-B, Lavasanifar A. Traceable Multifunctional Micellar Nanocarriers for Cancer-Targeted Co-delivery of MDR-1 siRNA and Doxorubicin. *ACS Nano* 2011; 5: 5202–5213.
- [115] Gao X, Li S, Ding F, et al. Rapid Detection of Exosomal MicroRNAs Using Virus-Mimicking Fusogenic Vesicles. *Angew Chemie - Int Ed* 2019; 58: 8719–8723.
- [116] Modery-Pawlowski CL, Sen Gupta A. Heteromultivalent ligand-decoration for actively targeted nanomedicine. *Biomaterials* 2014; 35: 2568–2579.
- [117] Gao H. Perspectives on Dual Targeting Delivery Systems for Brain Tumors. *J Neuroimmune Pharmacol* 2017; 12: 6–16.
- [118] Gupta A Sen. Nanomedicine approaches in vascular disease: A review. *Nanomedicine Nanotechnology, Biol Med* 2011; 7: 763–779.
- [119] Liu Y, Chen Q, Xu M, et al. Single peptide ligand-functionalized uniform hollow mesoporous silica nanoparticles achieving dual-targeting drug delivery to tumor cells and angiogenic blood vessel cells. *Int J Nanomedicine* 2015; 10: 1855–1867.
- [120] Xu Q, Liu Y, Su S, et al. Anti-tumor activity of paclitaxel through dual-targeting carrier of cyclic RGD and transferrin conjugated hyperbranched copolymer nanoparticles. *Biomaterials* 2012; 33: 1627–1639.
- [121] Bhattacharyya S, Khan JA, Curran GL, et al. Efficient delivery of gold nanoparticles by dual receptor targeting. *Adv Mater* 2011; 23: 5034–5038.

- [122] Zhang M-Z, Li C, Fang B-Y, et al. High transfection efficiency of quantum dot-antisense oligonucleotide nanoparticles in cancer cells through dual-receptor synergistic targeting. *Nanotechnology* 2014; 25: 255102.
- [123] Levine RM, Kokkoli E. Dual-ligand $\alpha 5\beta 1$ and $\alpha 6\beta 4$ integrin targeting enhances gene delivery and selectivity to cancer cells. *J Control Release* 2017; 251: 24–36.
- [124] Gunawan RC, Almeda D, Auguste DT. Complementary targeting of liposomes to IL-1 α and TNF- α activated endothelial cells via the transient expression of VCAM1 and E-selectin. *Biomaterials* 2011; 32: 9848–9853.
- [125] Shadidi M, Sioud M. Selective targeting of cancer cells using synthetic peptides. *Drug Resist Updat* 2003; 6: 363–371.
- [126] Sapra P, Allen TM. Improved Outcome When B-Cell Lymphoma Is Treated with Combinations of Immunoliposomal Anticancer Drugs Targeted to Both the CD19 and CD20 Epitopes. *Clin Cancer Res* 2004; 10: 2530–2537.
- [127] Pastorino F, Chiara B, Di Paolo D, et al. Targeting Liposomal Chemotherapy via Both Tumor Cell-Specific and Tumor Vasculature-Specific Ligands Potentiates Therapeutic Efficacy. *Cancer Res* 2006; 66: 10073–10082.
- [128] Laginha K, Mumbengegwi D, Allen T. Liposomes targeted via two different antibodies: Assay, B-cell binding and cytotoxicity. *Biochim Biophys Acta - Biomembr* 2005; 1711: 25–32.
- [129] Saul JM, Annapragada A V., Bellamkonda R V. A dual-ligand approach for enhancing targeting selectivity of therapeutic nanocarriers. *J Control Release* 2006; 114: 277–287.
- [130] Gunawan RC, Auguste DT. The role of antibody synergy and membrane fluidity in the vascular targeting of immunoliposomes. *Biomaterials* 2010; 31: 900–907.
- [131] Gunawan RC, Auguste DT. Immunoliposomes That Target Endothelium In Vitro Are Dependent on Lipid Raft Formation. *Mol Pharm* 2010; 7: 1569–1575.
- [132] Kluza E, van der Schaft DWJ, Hautvast PAI, et al. Synergistic Targeting of $\alpha v\beta 3$ Integrin and Galectin-1 with Heteromultivalent Paramagnetic Liposomes for Combined MR Imaging and Treatment of Angiogenesis. *Nano Lett* 2010; 10: 52–58.
- [133] Kluza E, Jacobs I, Hectors SJCG, et al. Dual-targeting of $\alpha v\beta 3$ and galectin-1 improves the specificity of paramagnetic/fluorescent liposomes to tumor endothelium in vivo. *J Control Release* 2012; 158: 207–214.
- [134] Mack K, R ger R, Fellermeier S, et al. Dual Targeting of Tumor Cells with

Chapter 1: What Nanoparticles can learn from viruses

- Bispecific Single-Chain Fv-Immunoliposomes. *Antibodies* 2012; 1: 199–214.
- [135] Doolittle E, Peiris PM, Doron G, et al. Spatiotemporal Targeting of a Dual-Ligand Nanoparticle to Cancer Metastasis. *ACS Nano* 2015; 9: 8012–8021.
- [136] Covarrubias G, He F, Raghunathan S, et al. Effective treatment of cancer metastasis using a dual-ligand nanoparticle. *PLoS One* 2019; 14: e0220474.
- [137] Li X, Zhou H, Yang L, et al. Enhancement of cell recognition in vitro by dual-ligand cancer targeting gold nanoparticles. *Biomaterials* 2011; 32: 2540–2545.
- [138] Dixit S, Miller K, Zhu Y, et al. Dual Receptor-Targeted Theranostic Nanoparticles for Localized Delivery and Activation of Photodynamic Therapy Drug in Glioblastomas. *Mol Pharm* 2015; 12: 3250–3260.
- [139] He H, Li Y, Jia X-R, et al. PEGylated Poly(amidoamine) dendrimer-based dual-targeting carrier for treating brain tumors. *Biomaterials* 2011; 32: 478–487.
- [140] Liu Y, Hui Y, Ran R, et al. Synergetic Combinations of Dual-Targeting Ligands for Enhanced In Vitro and In Vivo Tumor Targeting. *Adv Healthc Mater* 2018; 7: 1800106.
- [141] Jia T, Choi J, Ciccione J, et al. Heteromultivalent targeting of integrin $\alpha\beta3$ and neuropilin 1 promotes cell survival via the activation of the IGF-1/insulin receptors. *Biomaterials* 2018; 155: 64–79.
- [142] Jang C, Lee JH, Sahu A, et al. The synergistic effect of folate and RGD dual ligand of nanographene oxide on tumor targeting and photothermal therapy in vivo. *Nanoscale* 2015; 7: 18584–18594.
- [143] Wang Z, Qin W, Zhuang J, et al. Virus-Mimicking Cell Capture Using Heterovalency Magnetic DNA Nanoclaws. *ACS Appl Mater Interfaces* 2019; 11: 12244–12252.
- [144] Peiris PM, He F, Covarrubias G, et al. Precise targeting of cancer metastasis using multi-ligand nanoparticles incorporating four different ligands. *Nanoscale* 2018; 10: 6861–6871.
- [145] Tjandra KC, Thordarson P. Multivalency in Drug Delivery—When Is It Too Much of a Good Thing? *Bioconjug Chem* 2019; 30: 503–514.
- [146] Angioletti-Uberti S. Exploiting Receptor Competition to Enhance Nanoparticle Binding Selectivity. *Phys Rev Lett* 2017; 118: 1–5.
- [147] Delguste M, Zeippen C, Machiels B, et al. Multivalent binding of herpesvirus to living cells is tightly regulated during infection. *Sci Adv*; 4, <http://advances.sciencemag.org/> (2018, accessed 30 September 2019).

- [148] Xia QS, Ding HM, Ma YQ. Can dual-ligand targeting enhance cellular uptake of nanoparticles? *Nanoscale* 2017; 9: 8982–8989.
- [149] Cristina M, Giudice L, Meder F, et al. Constructing bifunctional nanoparticles for dual targeting: improved grafting and surface recognition assessment of multiple ligand nanoparticles. *Nanoscale* 2016; 8: 16969.
- [150] Cheng Z, Zaki A Al, Hui JZ, et al. Multifunctional Nanoparticles: Cost Versus Benefit of Adding Targeting and Imaging Capabilities. *Science (80-)* 2012; 338: 903–910.
- [151] Sawant RR, Jhaveri AM, Koshkaryev A, et al. The effect of dual ligand-targeted micelles on the delivery and efficacy of poorly soluble drug for cancer therapy. *J Drug Target* 2013; 21: 630–638.
- [152] Wilhelm S, Tavares AJ, Dai Q, et al. Analysis of nanoparticle delivery to tumours. *Nat Rev Mater* 2016; 1: 1–12.
- [153] Dai Q, Wilhelm S, Ding D, et al. Quantifying the Ligand-Coated Nanoparticle Delivery to Cancer Cells in Solid Tumors. *ACS Nano* 2018; 12: 8423–8435.
- [154] Berger EA, Murphy PM, Farber JM. Chemokine receptors as HIV-1 coreceptors: Roles in Viral Entry, Tropism, and Disease. *Annu Rev Immunol* 1999; 17: 657–700.
- [155] Li E, Stupack D, Bokoch GM, et al. Adenovirus Endocytosis Requires Actin Cytoskeleton Reorganization Mediated by Rho Family GTPases. *J Virol* 1998; 72: 8806–8812.
- [156] Nemerow GR, Stewart PL. Role of alpha(v) integrins in adenovirus cell entry and gene delivery. *Microbiol Mol Biol Rev* 1999; 63: 725–34.
- [157] Singh SR, Grossniklaus HE, Kang SJ, et al. Intravenous transferrin, RGD peptide and dual-targeted nanoparticles enhance anti-VEGF intrareceptor gene delivery to laser-induced CNV. *Gene Ther* 2009; 16: 645–659.
- [158] Chan MS, Liu LS, Leung HM, et al. Cancer-Cell-Specific Mitochondria-Targeted Drug Delivery by Dual-Ligand-Functionalized Nanodiamonds Circumvent Drug Resistance. *ACS Appl Mater Interfaces* 2017; 9: 11780–11789.
- [159] Chen D, Li B, Cai S, et al. Dual targeting luminescent gold nanoclusters for tumor imaging and deep tissue therapy. *Biomaterials* 2016; 100: 1–16.
- [160] Peitsch C, Klenk H-D, Garten W, et al. Activation of influenza A viruses by host proteases from swine airway epithelium. *J Virol* 2014; 88: 282–91.
- [161] Owen SC, Chan DPY, Shoichet MS. Polymeric micelle stability. *Nano Today* 2012;

Chapter 1: What Nanoparticles can learn from viruses

7: 53–65.

- [162] Bkaily G, Sleiman S, Stephan J, et al. Angiotensin II AT 1 receptor internalization, translocation and de novo synthesis modulate cytosolic and nuclear calcium in human vascular smooth muscle cells. *Can J Physiol Pharmacol* 2003; 81: 274–287.
- [163] Nguyen TQ, Goldschmeding R. The Mesangial Cell in Diabetic Nephropathy. In: *Diabetic Nephropathy*. Springer International Publishing, 2019, pp. 143–151.
- [164] International Diabetes Federation. IDF Diabetes Atlas. *IDF Diabetes Atlas, 8th Ed* 2017; 1–150.
- [165] Hennig R, Ohlmann A, Staffel J, et al. Multivalent nanoparticles bind the retinal and choroidal vasculature. *J Control Release* 2015; 220: 265–274.
- [166] Wang S, Huang P, Chen X. Stimuli-Responsive Programmed Specific Targeting in Nanomedicine. *ACS Nano* 2016; 10: 2991–2994.
- [167] Yao Q, Kou L, Tu Y, et al. MMP-Responsive ‘Smart’ Drug Delivery and Tumor Targeting. *Trends Pharmacol Sci* 2018; 39: 766–781.
- [168] Malemud CJ. Matrix metalloproteinases (MMPs) in health and disease: an overview. *Front Biosci* 2006; 11: 1696–1701.
- [169] Zhu L, Kate P, Torchilin VP. Matrix Metalloprotease 2-Responsive Multifunctional Liposomal Nanocarrier for Enhanced Tumor Targeting. *ACS Nano* 2012; 6: 3491–3498.
- [170] Zhu L, Wang T, Perche F, et al. Enhanced anticancer activity of nanopreparation containing an MMP2-sensitive PEG-drug conjugate and cell-penetrating moiety. *Proc Natl Acad Sci* 2013; 110: 17047–17052.
- [171] Han H, Valdepérez D, Jin Q, et al. Dual Enzymatic Reaction-Assisted Gemcitabine Delivery Systems for Programmed Pancreatic Cancer Therapy. *ACS Nano* 2017; 11: 1281–1291.
- [172] Li H, Miteva M, Kirkbride KC, et al. Dual MMP7-Proximity-Activated and Folate Receptor-Targeted Nanoparticles for siRNA Delivery. *Biomacromolecules* 2015; 16: 192–201.
- [173] Magnusson JP, Fernández-Trillo F, Sicilia G, et al. Programmed assembly of polymer-DNA conjugate nanoparticles with optical readout and sequence-specific activation of biorecognition. *Nanoscale* 2014; 6: 2368–2374.
- [174] Guo F, Wu J, Wu W, et al. PEGylated self-assembled enzyme-responsive nanoparticles for effective targeted therapy against lung tumors. *J*

- Nanobiotechnol* 2018; 16: 57.
- [175] Callmann CE, Barback C V., Thompson MP, et al. Therapeutic Enzyme-Responsive Nanoparticles for Targeted Delivery and Accumulation in Tumors. *Adv Mater* 2015; 27: 4611–4615.
- [176] Chien M-P, Thompson MP, Barback C V., et al. Enzyme-Directed Assembly of a Nanoparticle Probe in Tumor Tissue. *Adv Mater* 2013; 25: 3599–3604.
- [177] Nguyen MM, Carlini AS, Chien M-P, et al. Enzyme-Responsive Nanoparticles for Targeted Accumulation and Prolonged Retention in Heart Tissue after Myocardial Infarction. *Adv Mater* 2015; 27: 5547–5552.
- [178] Proetto MT, Callmann CE, Cliff J, et al. Tumor Retention of Enzyme-Responsive Pt(II) Drug-Loaded Nanoparticles Imaged by Nanoscale Secondary Ion Mass Spectrometry and Fluorescence Microscopy. *ACS Cent Sci* 2018; 4: 1477–1484.
- [179] Liu C, Sun C, Huang H, et al. Overexpression of Legumain in Tumors Is Significant for Invasion/Metastasis and a Candidate Enzymatic Target for Prodrug Therapy. *Cancer Res* 2003; 63: 2957–2964.
- [180] Liu Z, Xiong M, Gong J, et al. Legumain protease-activated TAT-liposome cargo for targeting tumours and their microenvironment. *Nat Commun* 2014; 5: 4280.
- [181] Li Y, Liu G, Wang X, et al. Enzyme-Responsive Polymeric Vesicles for Bacterial-Strain-Selective Delivery of Antimicrobial Agents. *Angew Chemie* 2016; 128: 1792–1796.
- [182] Insua I, Lamas E, Zhang Z, et al. Enzyme-responsive polyion complex (PIC) nanoparticles for the targeted delivery of antimicrobial polymers. *Polym Chem* 2016; 7: 2684.
- [183] Hu Q, Katti PS, Gu Z. Enzyme-responsive nanomaterials for controlled drug delivery. *Nanoscale* 2014; 6: 12273–12286.
- [184] Vivès E, Schmidt J, Pèlerin A. Cell-penetrating and cell-targeting peptides in drug delivery. *Biochim Biophys Acta - Rev Cancer* 2008; 1786: 126–138.
- [185] Li Z-Y, Liu Y, Hu J-J, et al. Stepwise-Acid-Active Multifunctional Mesoporous Silica Nanoparticles for Tumor-Specific Nucleus-Targeted Drug Delivery. *ACS Appl Mater Interfaces* 2014; 6: 14568–14575.
- [186] Zhang Z, Zhang X, Xu X, et al. Virus-Inspired Mimics Based on Dendritic Lipopeptides for Efficient Tumor-Specific Infection and Systemic Drug Delivery. *Adv Funct Mater* 2015; 25: 5250–5260.
- [187] Zhang X, Xu X, Li Y, et al. Virion-Like Membrane-Breaking Nanoparticles with

Chapter 1: What Nanoparticles can learn from viruses

- Tumor-Activated Cell-and-Tissue Dual-Penetration Conquer Impermeable Cancer. *Adv Mater* 2018; 30: 1707240.
- [188] Jiang L, Liang Y, Huo Q, et al. Viral capsids mimicking based on pH-sensitive biodegradable polymeric micelles for efficient anticancer drug delivery. *J Biomed Nanotechnol* 2018; 14: 1409–1419.
- [189] Xu M, Chen Y, Banerjee P, et al. Dendritic Cells Targeting and pH-Responsive Multi-layered Nanocomplexes for Smart Delivery of DNA Vaccines. *AAPS PharmSciTech* 2017; 18: 2618–2625.
- [190] Gao H, Cheng T, Liu J, et al. Self-Regulated Multifunctional Collaboration of Targeted Nanocarriers for Enhanced Tumor Therapy. *Biomacromolecules* 2014; 15: 18.
- [191] Wannasarit S, Wang S, Figueiredo P, et al. A Virus-Mimicking pH-Responsive Acetalated Dextran-Based Membrane-Active Polymeric Nanoparticle for Intracellular Delivery of Antitumor Therapeutics. *Adv Funct Mater* 2019; 1905352: 1–14.
- [192] Sasaki K, Kogure K, Chaki S, et al. An artificial virus-like nano carrier system: enhanced endosomal escape of nanoparticles via synergistic action of pH-sensitive fusogenic peptide derivatives. *Anal Bioanal Chem* 2008; 391: 2717–2727.
- [193] Mudhakar D, Harashima H. Learning from the Viral Journey: How to Enter Cells and How to Overcome Intracellular Barriers to Reach the Nucleus. *AAPS J* 2009; 11: 65.
- [194] Song N, Zhou L, Li J, et al. Inspired by nonenveloped viruses escaping from endo-lysosomes: a pH-sensitive polyurethane micelle for effective intracellular trafficking. *Nanoscale* 2016; 8: 7711–7722.
- [195] Smith SA, Selby LI, Johnston APR, et al. The Endosomal Escape of Nanoparticles: Toward More Efficient Cellular Delivery. *Bioconjug Chem* 2018; acs.bioconjugchem.8b00732.
- [196] Plank C, Oberhauser B, Mechtler K, et al. The Influence of Endosome-disruptive Peptides on Gene Transfer Using Synthetic Virus-like Gene Transfer Systems. 1994; 269: 12918–12924.
- [197] Cho YW, Kim J-D, Park K. Polycation gene delivery systems: escape from endosomes to cytosol. *J Pharm Pharmacol* 2003; 55: 721–734.
- [198] McCarley RL. Redox-Responsive Delivery Systems. *Annu Rev Anal Chem* 2012; 5: 391–411.
- [199] Szatrowski TP, Nathan CF. Production of large amounts of hydrogen peroxide

- by human tumor cells. *Cancer Res* 1991; 51: 794–8.
- [200] Guo X, Cheng Y, Zhao X, et al. Advances in redox-responsive drug delivery systems of tumor microenvironment. *J Nanobiotechnology* 2018; 16: 74.
- [201] Jiang Y, Yang W, Zhang J, et al. Protein Toxin Chaperoned by LRP-1-Targeted Virus-Mimicking Vesicles Induces High-Efficiency Glioblastoma Therapy In Vivo. *Adv Mater* 2018; 30: 1–7.
- [202] He Y, Nie Y, Cheng G, et al. Viral Mimicking Ternary Polyplexes: A Reduction-Controlled Hierarchical Unpacking Vector for Gene Delivery. *Adv Mater* 2014; 26: 1534–1540.
- [203] Daniel KB, Callmann CE, Gianneschi NC, et al. Dual-responsive nanoparticles release cargo upon exposure to matrix metalloproteinase and reactive oxygen species †. *Chem Commun* 2016; 52: 2126.
- [204] Ungerleider JL, Kammeyer JK, Braden RL, et al. Enzyme-targeted nanoparticles for delivery to ischemic skeletal muscle. *Polym Chem* 2017; 8: 5212–5219.
- [205] Adamiak L, Touve MA, Leguyader CLM, et al. Peptide Brush Polymers and Nanoparticles with Enzyme-Regulated Structure and Charge for Inducing or Evading Macrophage Cell Uptake. *ACS Nano* 2017; 11: 9877–9888.
- [206] Zhang L, Wang Y, Zhang X, et al. Enzyme and Redox Dual-Triggered Intracellular Release from Actively Targeted Polymeric Micelles. *ACS Appl Mater Interfaces* 2017; 9: 3388–3399.
- [207] Li Y, Hu H, Zhou Q, et al. α -Amylase- and Redox-Responsive Nanoparticles for Tumor-Targeted Drug Delivery. *ACS Appl Mater Interfaces* 2017; 9: 19215–19230.
- [208] Mothes W, Sherer NM, Jin J, et al. Virus Cell-to-Cell Transmission. *J Virol* 2010; 84: 8360–8368.
- [209] Lee ES, Kim D, Youn YS, et al. A Virus-Mimetic Nanogel Vehicle. *Angew Chemie* 2008; 120: 2452–2455.
- [210] Cui T, Yan Z, Qin H, et al. A Sequential Target-Responsive Nanocarrier with Enhanced Tumor Penetration and Neighboring Effect In Vivo. *Small* 2019; 1903323.
- [211] Fang J-H, Lee Y-T, Chiang W-H, et al. Magneto-responsive Virus-Mimetic Nanocapsules with Dual Heat-Triggered Sequential-Infected Multiple Drug-Delivery Approach for Combinatorial Tumor Therapy. *Small* 2015; 11: 2417–2428.
- [212] Dalmau-Mena I, del Pino P, Pelaz B, et al. Nanoparticles engineered to bind

Chapter 1: What Nanoparticles can learn from viruses

cellular motors for efficient delivery. *J Nanobiotechnology* 2018; 16: 33.

- [213] Martínez-Moreno M, Navarro-Lérida I, Roncal F, et al. Recognition of novel viral sequences that associate with the dynein light chain LC8 identified through a pepscan technique. *FEBS Lett* 2003; 544: 262–267.
- [214] Mable CJ, Canton I, Mykhaylyk OO, et al. Targeting triple-negative breast cancer cells using Dengue virus-mimicking pH-responsive framboidal triblock copolymer vesicles. *Chem Sci* 2019; 10: 4811–4821.
- [215] Rey FA. Two hosts, two structures. *Nature* 2013; 497: 443–444.

Chapter 2

Goals of the Thesis

Targeted nanomaterials are powerful platforms for biomedical applications. If designed correctly they have the potential to fulfill the ultimate requirements of an optimal treatment: the effective delivery of therapeutic agents to specific cells/tissues and the evasion of deleterious side effects. Among them, polymeric nanoparticles (NPs) appear highly promising, as they are biocompatible and biodegradable, precisely tunable, and able to incorporate diverse cargos for therapeutic or diagnostic purposes. More so, they can be easily functionalized with ligands, such as small molecules, peptides or antibodies to increase their interaction with distinct cells. These targeting moieties are generally selected for their high affinity towards cell surface receptors overexpressed in diseased states. To counteract the affinity loss derived from tethering ligands to the particle surface, an elevated number of ligands is coupled to each NP. This promotes the multivalent binding of several receptors simultaneously, highly increasing the overall avidity of the particles. This virus-derived design concept has broadly been implemented on different materials to address various therapeutically-relevant receptor families.

Nevertheless, up to date targeted nanotherapies still fail to effectively fulfill their anticipated outcomes. This can be partially attributed to a lack of *in vitro* and *in vivo* target-cell specificity due to the ubiquitous presence of the addressed receptors. More so, an incomplete knowledge of the parameters governing multivalent interactions often results in a futile NP-design that yields inconsistent results. Additionally, when particles are administered to a living organism, they faced a very environment full of obstacles, such as biological barriers, flow conditions, or the adsorption of proteins, that hinder their targeting abilities and lead to insufficient particle accumulation at the target site. Furthermore, due to a limited awareness of the parameters that determine cargo loading on nanomaterials, the encapsulation of certain highly promising drugs is still challenging. Altogether, this translates into disappointing therapeutic outcomes due to an unexploited potential of targeted nanomaterials.

The goal of this work was to develop a polymeric nanoscale therapeutic system, focusing on overcoming these issues, for the specific recognition of mesangial cells, as they are highly relevant therapeutic targets due to their significant involvement in the development of diabetic nephropathy.

Despite virus-like multivalent ligand display having made considerable advances at increasing NP interactions with cells, it has remained unsuccessful at enhancing the target cell-specificity in a polycellular environment. A fundamental reason is the failure to accurately mimic the viral host-cell recognition strategy and to implement its

Chapter 2: Goals of the Thesis

intricate multistep nature. Therefore, to bestow nanomaterials with the virus-like ability of unequivocally distinguishing between target and off-target cells, particles carrying out a stepwise cellular recognition were designed (**Chapter 3**). Influenza A virus, which requires enzymatic activation by the target cell prior to attaining cell entry, served as a model. Angiotensin-I (Ang-I), a peptide cleavable by cell membrane-bound angiotensin converting enzyme (ACE) to angiotensin-II, was used as a proligand. After ACE activation, interaction of particle-bound angiotensin-II with the Ang-II type 1 receptor (AT1R), triggers cellular uptake. Both targets, ACE and AT1R, were selected due to their overexpression in mesangial cells under diabetic conditions. The particles were characterized for their physicochemical characteristics and their avidity for the targets was investigated through enzyme kinetic assays and intracellular calcium measurements. Additionally, the feasibility of a sequential mesangial-cell recognition was assessed. Subsequently, the target-cell specificity in a complex *in vitro* setting was elucidated by confocal laser scanning microscopy and flow cytometry.

NP functionalization is usually attained by tethering ligands to their surface with linkers, such as poly(ethylene glycol) (PEG). However, the repercussion that simple particle design features have on the multivalent interactions are frequently vastly underestimated. In **Chapter 4**, ligand-functionalized particles with hetero- and homogeneous PEG shells were formulated in order to assess the effect of ligand mobility on the NP avidity and the particle fate after cell contact. More so, the superiority of ligand mobility over functionalization degree was investigated.

As nanoformulations are generally optimized *in vitro*, when they are administered *in vivo* the outcomes diverge tremendously or are even paradoxical. One of the reasons being that the latter conditions are immensely more complex, and thus, decrease the targeting abilities of NPs. Therefore, in **Chapter 5**, NPs with an enhanced *in vivo* mesangial cell recognition strategy were designed. Using again viruses as a blueprint, their initial step of cellular attachment was mimicked, as it serves the purposes of increasing the particle concentration at the host surface and promoting subsequent recognition steps. EXP3174, an AT1R antagonist, was selected as a ligand to mediate attachment. In combination with the previously established Influenza A virus-mimetic specific targeting, the cellular recognition was a three-step process. The interaction of the tethered ligands and the particles avidity for the addressed receptors were assessed. Flow cytometry and confocal microcopy were used to elucidate particle specificity and cellular interaction *in vitro*. More so, the targeting ability and *in vivo*

mesangial cell-accumulation was investigated through immunohistochemistry and fluorescence microscopy methods.

To obtain NPs of therapeutic value, they must be loaded with drugs different approaches. The antifibrotic drug pirfenidone (PFD), is a highly interesting candidate for the treatment of mesangial cells in the context of diabetic nephropathy. However, due to its water solubility and lack of ionizable groups, its encapsulation through nanoprecipitation can be challenging. In **Chapter 6** the parameters for loading PFD in polymeric NPs through nanoprecipitation were evaluated. The compatibility of PFD with the particle-forming polymers was assessed through thermodynamic prediction parameters. More so, the influence of the nanoprecipitation technique (bulk vs microfluidic manufacturing) on the drug loading and cellular interaction was determined. Additionally, spatial constrictions on the PFD incorporation were elucidated. Furthermore, the effects of co-encapsulating an additional drug molecule on the PFD loading and release were assessed.

Chapter 3

Influenza A virus mimetic nanoparticles trigger selective cell uptake

Published in *Proceedings of the National Academy of Science*

2019, 116 (20), 9831-9836

This chapter was published as: S. Maslanka Figueroa, A. Vesper, K. Abstiens, D. Fleischmann, S. Beck and A. Goepferich, *Proc. Natl. Acad. Sci* 2019, 116 (20), 9831-9836, doi:10.1073/pnas.1902563116.

Abstract

Poor target cell specificity is currently a major shortcoming of nanoparticles (NPs) used for biomedical applications. It causes significant material loss to off-target sites and poor availability at the intended delivery site. To overcome this limitation, we designed particles that identify cells in a virus-like manner. As a blueprint, we chose a mechanism typical of influenza A virus particles in which ectoenzymatic hemagglutinin activation by target cells is a mandatory prerequisite for binding to a secondary target structure that finally confirms cell identity and allows for uptake of the virus. We developed NPs that probe mesangial cells for the presence of angiotensin-converting enzyme on their surface using angiotensin I (Ang-I) as a proligand. This initial interaction enzymatically transforms Ang-I to a secondary ligand angiotensin II (Ang-II) that has the potential to bind in a second stage to Ang-II type-1 receptor (AT1R). The presence of the receptor confirms the target cell identity and triggers NP uptake *via* endocytosis. Our virus-mimetic NPs showed outstanding target-cell affinity with picomolar avidities and were able to selectively identify these cells in the presence of 90% off-target cells that carried only the AT1R. Our results demonstrate that the design of virus-mimetic cell interactive NPs is a valuable strategy to enhance NP specificity for therapeutic and diagnostic applications. Our set of primary and secondary targets is particularly suited for the identification of mesangial cells that play a pivotal role in diabetic nephropathy, one of the leading causes of renal failure, for which currently no treatment exists.

1 Introduction

Nanomaterials are valuable tools in the field of drug delivery as they can target cells with high specificity, avoiding the side effects of conventional drug administration [1]. NPs with the ability to bind to distinct target structures on cell surfaces are particularly valuable [2]. However, various publications have raised doubts about the efficacy of cell targeting, including the meta-analysis published by Wilhelm *et al.* which screened 10 years of preclinical *in vivo* cancer therapy data. Their analysis revealed that the presence of a target cell-specific ligand on a NP surface gave only a modest increase in the percentage of the dose that entered solid tumors with a value of 0.9% compared to 0.7% for NPs without any cell recognition mechanism [3]. Even though the authors identified a number of factors that could be responsible for the low uptake values, they concluded that poor cell recognition was particularly decisive and that the development of better strategies for target cell identification is a significant need.

In fact, a plethora of strategies have been explored to improve the ability of NPs to recognize a target cell with sufficient specificity. Progress has been made especially in the understanding of multivalent ligand-receptor interactions and their contribution to the avidity of a particular nanomaterial for cells that carry the respective receptor [4]. Thus, we know that a NP equipped with highly specific ligands tethered to its surface can achieve nanomolar avidity for the target cell [5]. In this case, the multivalent binding [6] compensates for the affinity loss stemming from the massive structural changes to the ligands when they are attached to linkers or tethering molecules such as poly(ethylene glycol) (PEG) [7]. The mechanism has been well documented in the literature for several nanomaterials [8–10] binding to G protein-coupled receptors (GPCRs) [5, 11, 12] or integrins [13]. However, high avidity is a necessary but not sufficient prerequisite for identifying target cells. A fundamental problem that cannot be overcome with “simple” multivalent particles is the lack of specificity. Since there may be more cell types in the organism that carry the receptor chosen for targeting, this can increase the odds of particles binding to off-target sites [14].

In attempts to overcome poor specificity, heteromultivalency [15] has frequently been explored. This strategy takes advantage of the fact that targeting multiple receptors decreases the chance that off-target cells carry the same set of receptors. However, when NPs carried several different types of ligands rather than only one for more precise target cell identification, the increases in specificity were modest. Because the ligands are presented simultaneously by the nanomaterials, any cell expressing either of the respective receptors will bind the particles and interfere with them.

Chapter 3: Influenza A Virus Mimetic Nanoparticles Trigger Selective Cell Uptake

To overcome this limitation, we developed NPs that interact with cells in a virus-like manner [16]. In contrast to simple hetero-multivalently binding NPs, viral cell attachment and entry is a complex sequential process of two or more stages [17]. Adenoviruses, for example, reveal their ligand for integrin binding that triggers cell uptake only after first binding to the coxsackie adenovirus receptor [18]. Our approach to increase target cell specificity by using more than one target site for cell identification was inspired by Influenza A virus which requires enzymatic activation of hemagglutinin, a pro-ligand glycoprotein in the viral envelope. Once activated, the ligand binds to cell surface sialic acid, triggering cell uptake [19].

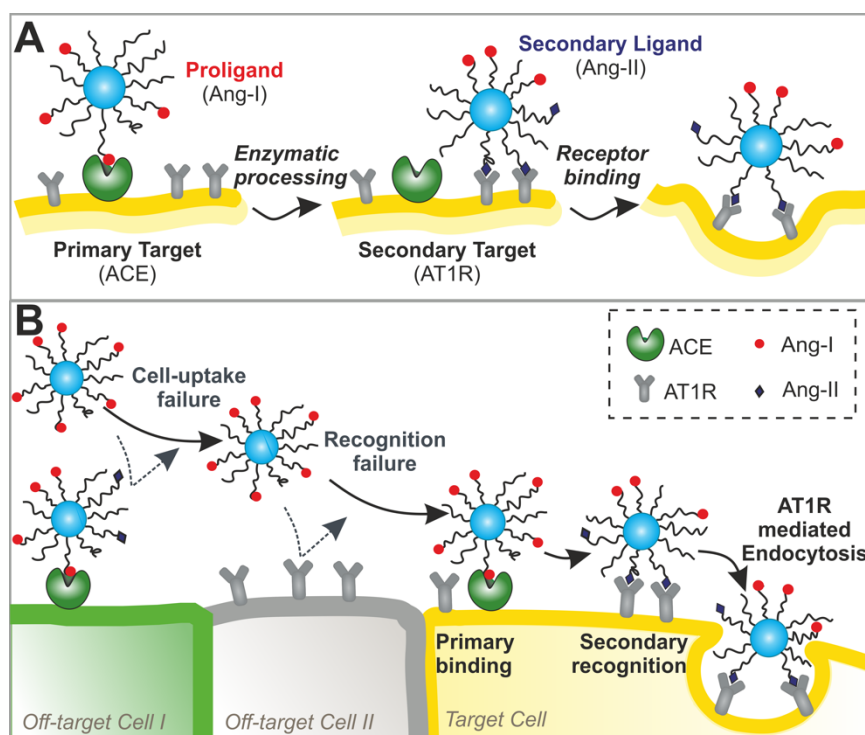


Figure 1. Illustration of the concept of hetero-multivalent interactive target cell identification by virus-mimetic NPs. (A) Target cell-specific recognition and internalization make up a sequential two-stage process. During the first stage, Ang-I binds to ACE, the primary target on the cell surface with high affinity ($K_m = 19 \mu\text{M}$) [20]. The subsequent cleavage reaction produces Ang-II, the secondary ligand. During the secondary recognition stage, Ang-II binds to the secondary target AT1R. As a receptor agonist, it triggers endocytosis of the NP upon receptor binding [21]. (B) NPs fail to recognize off-target cells that carry only the primary (Off-target Cell I) or secondary (Off-target Cell II) target receptor.

We aimed to use this principle to engineer NPs with high specificity for mesangial cells, which play a pivotal role in the development of diabetic nephropathy [22]. We designed NPs with a surface-immobilized substrate to an enzyme located on the target cell membrane, specifically the proligand Ang-I which we expected to be “visible” to cells bearing the primary target, angiotensin converting enzyme (ACE) (Figure 1A). The subsequent enzymatic reaction cleaves the dipeptide His-Leu from Ang-I

converting it to Ang-II, the secondary active ligand. Ang-II can then bind to the AT1R present on the target cell. As an agonist, it triggers receptor mediated endocytosis [21]. If NPs come into contact with off-target cells expressing only one of the two target receptors, ACE or AT1R, the NPs will either be activated but not internalized or they will not be able to bind the cell at all (Figure 1B).

2 Materials and Methods

2.1 Materials

Lysine N-modified Angiotensin-I (Lys-Ang-I) and Ang-II (Lys-Ang-II) (purity >98%) were purchased from Genscript (Piscataway, NJ, USA). Ang-I and Ang-II were purchased from Bachem (Bubendorf, Switzerland). Valsartan was purchased from Santa Cruz Biotechnology (Dallas, TX, USA). O-aminobenzoic acid-phenylalanyl-arginine-lysine (2,4-dinitrophenyl)-proline (Abz-FRK(Dnp)-P) was purchased from Enzo Life Sciences (Farmingdale, NY, USA). Carboxylic acid terminated PEG was obtained from JenKem Technology USA Inc. (Allen, TX, USA). All other chemicals were obtained from Sigma Aldrich (Taufkirchen, Germany) in analytical grade. Ultrapure water, which was obtained from a Milli-Q water purification system (Millipore, Billerica, MA, USA), was used for NP and buffer preparation. The buffers used for NP modification were 0.1 M 2-(N-morpholino) ethanesulfonic acid (MES) buffer at pH 6, and Dulbecco's phosphate buffered saline (DPBS) at pH 7.4, containing 1.5 mM KH_2PO_4 , 2.7 mM KCl, 8 mM Na_2HPO_4 and 138 mM NaCl. The assay buffer used for ACE activity quantification was a 0.1 M Tris buffer with 50 mM NaCl and 10 μM ZnCl_2 at pH 7.

2.2 Cell culture

Rat mesangial cells (rMCs) were a kind gift from Armin Buschauer (Department of Pharmaceutical/Medicinal chemistry II, University Regensburg, Germany). NCI-H295R and HeLa cells were purchased from ATCC (CRL-2128 and CCL-2, respectively). All three cell lines were cultured in RPMI1640 medium containing 10% fetal bovine serum (FBS) (Biowest, Nuaille, France), supplemented with insulin-transferrin-selenium (Life Technologies, Carlsbad, CA, USA) and 100 nM hydrocortisone. HK-2 cells were purchased from ATCC (CRL-2190) and maintained in DMEM-F12 (1:1) medium supplemented with 10% FBS.

Chapter 3: Influenza A Virus Mimetic Nanoparticles Trigger Selective Cell Uptake

2.3 Polymer synthesis and NP preparation

To synthesize block copolymers with different functional groups at the end of the PEG chain, we used commercially obtained carboxylic acid- or methoxy-terminated PEG as macroinitiators for ring-opening polymerization of cyclic lactide using 1,8-diazabicyclo[5.4.0]undec-7-ene (DBU) as catalyst after Qian et. al [23] with slight modifications, as previously described by our group [24]. Resulting block copolymers were a 10kDa poly(lactic acid) (PLA) with a carboxylic acid-terminated 2kDa or 5kDa PEG chain or a methoxy-terminated 5kDa PEG chain. The respective $^1\text{H-NMR}$ spectra are shown in Figure S6.

To detect NPs *in vitro*, the carboxylic acid-terminated poly(lactic-co-glycolic acid) (PLGA) (13.4 kDa) in the hydrophobic core was labelled with two different fluorescent dyes [25], CF647-amine (for FACS) and tetramethylrhodamine (TAMRA)-amine (for confocal laser scanning microscopy (CLSM)) prior to NP preparation using 4-(4,6-Dimethoxy-1,3,5-triazin-2-yl)-4-methylmorpholinium chloride (DMTMM) as a coupling agent, as previously reported by our group [26]. Briefly, amine functionalized CF647 or TAMRA dyes were coupled to carboxylic acid terminated PLGA using DMTMM as a linker. PLGA was used in a 5-fold excess so that not all the polymer was labelled. The fluorescent PLGA was purified from non-coupled dye through dialysis over 24 h.

For NP preparation, PEG-PLA block copolymers were mixed with 13.4 kDa PLGA in acetonitrile (ACN) at a set 70/30 mass ratio and a final concentration of 10 mg mL⁻¹. Polymer solutions were used to manufacture NPs *via* bulk precipitation by adding them dropwise under stirring water to a final concentration of 1 mg mL⁻¹. NP formulations were agitated for 2 h until the organic solvent was completely evaporated and then concentrated by ultracentrifugation using a 100 kDa molecular weight cut-off Microsep advance centrifugal device (Pall corporation, Port Washington, NY, USA) at 959 g for 15 minutes.

NP-COOH were modified with Lys-Ang-I or Lys-Ang-II using 1-Ethyl-3-(3-dimethylaminopropyl)carbodiimide (EDC) and N-Hydroxysuccinimide (NHS) chemistry. NPs (0.3 μmol PEG) were activated with EDC (10 mM) in presence of NHS (80 mM) in MES buffer (100 mM, pH 6). After 30 minutes of activation, 2-mercaptoethanol was added in excess (45 μmol) to quench the reaction over a period of 15 minutes. Subsequently, either Lys-AngI or Lys-AngII was added to the activated NPs (0.45 μmol), and the pH was raised by the addition of DPBS (pH 7.4). After 2 h of gentle stirring, angiotensin-modified NPs were purified by dialysis against 4 L water using a 6-8 kDa molecular weight cut-off regenerated cellulose dialysis membrane (Spectrum Laboratories, Inc, Rancho Dominguez, CA, USA) over 18 h (with medium change after 0.5, 1, 2, 3, 4, and 6 h), followed by ultracentrifugation using a 100 kDa

molecular weight cut-off Microsep advance centrifugal device (Pall corporation, Port Washington, NY, USA) at 959 *g* for 15 minutes.

2.4 NP characterization

NP size was measured using a Malvern ZetaSizer Nano ZS (Malvern Instruments GmbH, Lappersdorf, Germany) with a 633 He-Ne Laser at a 173° backscatter angle, using a micro cuvette. The electrophoretic mobility (ξ -potential) of the NPs was measured with a Malvern ZetaSizer Nano ZS using a folded capillary cell. Both measurements were conducted at 25 °C in 10% DPBS.

The PEG concentration of the NP solutions was determined using a colorimetric iodine complexing assay adapted from Childs [27], as previously described [26]. The absorbance was measured using a FLUOstar Omega microplate reader (BMG Labtech, Ortenberg, Germany). Angiotensin peptide concentration was determined fluorometrically using an LS-5S fluorescence plate reader (Perkin Elmer, Waltham, MA, USA) by measuring the arginine content using 9,10-phenanthrenequinone [26, 28].

2.5 Intracellular calcium mobilization assay

The affinity of NP-bound Ang-II towards the AT1R was investigated using a ratiometric Fura-2 Ca²⁺ chelator method as previously described by our group [7]. Samples used in the assay were Ang-II dilutions to test the functionality of the AT1R on the tested cells (Figure S2B), and Ang-II-functionalized NPs (NPAng-II) to investigate the affinity of NP-bound angiotensin-II towards the AT1R (Figure 2). In addition, Ang-I-functionalized NPs (NPAng-I) enzymatically activated to NPAng-II by a soluble form of ACE were used to confirm the occurrence of enzymatic processing (Figure 3). A stock solution of NPAng-I with a concentration of 10 μ M Ang-I was incubated with 0.1 μ M rabbit lung ACE (Sigma Aldrich, Taufkirchen, Germany) for 2 h at 37 °C. To inhibit the conversion of NPAng-I to NPAng-II by the soluble enzyme form, samples were also incubated in the presence of 20 μ M captopril. To inhibit also ACE on the membrane of rMCs during the measurements, the cells were additionally pre-incubated with 5 mM captopril in PBS for 15 minutes. As a control, unmodified NPMeO were used. Inhibition of the intracellular calcium mobilization of activated NPs was performed by the addition of 20 μ M valsartan after the incubation period. NPs were then used as agonist samples in an intracellular calcium mobilization assay, as described above. A student's t-test was performed using GraphPad Prism to assess statistical significance.

Chapter 3: Influenza A Virus Mimetic Nanoparticles Trigger Selective Cell Uptake

2.6 Flow cytometry

To investigate the sequential two-stage interaction of virus-mimetic NPs with target cells, rMCs and HK-2 cells were seeded into 24-well plates at densities of 30,000 and 50,000 cells per well, respectively, and incubated for 48 h. NP solutions were prepared at a concentration of 0.7 mg NP mL⁻¹ in Leibovitz medium (LM) supplemented with 0.1% bovine serum albumin (BSA). After washing the cells with DPBS, the pre-warmed NPs were pipetted onto them and incubated for 45 minutes at 37 °C. To confirm uptake specificity, cells were incubated with 1 mM captopril and/or valsartan for 15 minutes prior to NP addition. To assess the target-cell specificity of the NPs, rMCs stained with 10 µM CellTracker™ green (CTG) dye (Thermo Fisher Scientific, Waltham, MA, USA) for 30 minutes at 37 °C in serum-free RPMI1640 were seeded in 24-well plates in co-culture together with NCI-H295R or HeLa cells at densities of 10,000 and 75,000, respectively, and incubated for 48 h. NP solutions at 0.02 mg mL⁻¹ in LM with 0.1% BSA were subsequently added and left on the cells for 45 minutes at 37 °C. In both experiments, the NP solutions were discarded after the incubation time and the cells washed thoroughly with DPBS, trypsinized, and centrifuged (2x, 200 g, 5 minutes, 4 °C). Finally, the cells were resuspended in DPBS, and their fluorescence was analyzed with a FACS Calibur flow cytometer (Becton Dickinson, Franklin Lakes, NJ, USA). NP fluorescence was excited at 633 nm and the emission was recorded using a 661/16 nm bandpass filter. rMC fluorescence was excited at 488 nm and recorded using a 530/30 bandpass filter. FACS results were analyzed using Flowing software 2.5.1 (Turku Centre for Biotechnology, Finland). The population of viable cells and, in the co-culture experiments, the stained rMCs and non-fluorescent HeLa or NCI-H295R cells were gated. The geometric mean of the NP-associated fluorescence was analyzed. A student's t-test was performed using GraphPad Prism to assess statistical significance.

2.7 CLSM

To investigate the sequential two-stage interaction of virus-mimetic NPs with target cells, rMCs and HK-2 cells were seeded into 8-well µ-slides (Ibidi, Planegg, Germany) at 10,000 cells per well and incubated for 24 h. Cells were washed with DPBS and incubated for 45 minutes at 37 °C with pre-warmed NP solutions at concentrations of 0.7 mg mL⁻¹ in LM supplemented with 0.1% BSA. For uptake inhibition, cells were incubated 15 minutes prior to NP addition with 1 mM captopril and/or valsartan. For NP target-cell specificity experiments, CTG-stained rMCs (10 µM, 30 minutes, 37 °C) were seeded in co-culture together with CellTracker™ deep red (CTDR)-stained HeLa or NCI-H295R cells (25 µM, 30 minutes, 37 °C) in 8-well µ-slides at densities of 2,000 and 10,000 cells per well, respectively, and incubated for 24 h. Cells were washed with DPBS and incubated for 45 minutes with 0.2 mg mL⁻¹ NPs in LM with 0.1% BSA. After

the incubation period, the NP solutions were discarded, and the cells were washed thoroughly with DPBS. LM was added before viewing the cells under a microscope. Images of live cells were acquired with a Zeiss Axiovert 200 microscope with a LSM 510 laser-scanning device using a 63x Plan-Apochromat (NA 1.4) objective, and AIM 4.2 software (Zeiss, Jena, Germany). NP-associated fluorescence was excited with a 543 nm He-Ne laser and recorded with a 560-615 bandpass filter. rMC and HeLa or NCI-H295R fluorescence was excited with a 488 Argon or a 633 nm He/Ne Laser and recorded with a 560-615 bandpass and a 650 longpass filter, respectively. The focal plane was set at 1.1 μm .

3 Results and Discussion

3.1 Development of virus-mimetic NPs

For the development of our virus-mimetic NPs, we relied on well-known polymers recognized for their biocompatibility and high reproducibility of particle manufacture. For NP synthesis, PEG-PLA [23] block copolymers were stabilized against disassembly in cell culture medium with hydrophobic PLGA cores [29]. The combination of both polymers offers the possibility of integrating favorable traits regarding drug encapsulation, targeting ability and controlled drug release [30, 31] without the size increase PEG-PLA NPs undergo when stabilization is achieved by increasing the PLA molecular weight [32]. We coupled lysine N-modified Ang-I and Ang-II to NPs bearing carboxylic acid modified PEG chains on their surface (NP-COOH) such that between 15 and 25% of PEG chains per particle were modified (Figure S1A and S1C). Using copolymers with different PEG chain lengths allowed for preparation of NPs with different sizes (Figure S1B). This is useful because size has been found to be an important parameter affecting NP-cell interactions [26, 33]. The angiotensin-modified NPs we prepared were 50 nm (NP₂₁₀Ang-I/II) and 80 nm (NP₅₁₀Ang-I/II) in size with narrow particle size distributions (polydispersity index (PDI) 0.1-0.2) (Figure S1B).

3.2 Interaction with the AT1R

First, we investigated whether Ang-II decorated NPs were able to bind to the AT1R and meet this fundamental prerequisite for the concept of enzymatic ligand activation. Since the AT1R is a Gq-coupled receptor [34], its response to agonist binding can be followed *via* cytosolic calcium measurements. To this end, we incubated AT1R-positive rMCs (Figure S2 and S3) with Ang-II-positive NPs. The resulting intracellular calcium increase with rising particle concentration is in line with the ability of Ang-II to mediate calcium mobilization (Figure S2B) and confirms that the secondary ligand

Chapter 3: Influenza A Virus Mimetic Nanoparticles Trigger Selective Cell Uptake

bound to its target receptor (Figure 2). NP₂₁₀Ang-II and NP₅₁₀Ang-II yielded similar results, indicating that NP size was of minor significance. NPs decorated with the pro-ligand Ang-I, in contrast, were not able to bind the AT1R. Likewise, ligand-free control methoxy-ended particles (NPMeO) did not cause any calcium influx. Overall, the results confirmed that NPs carrying the secondary ligand Ang-II in their particle corona are able to bind to target cells *via* the AT1R, the designated secondary target in this two-stage binding concept, with high avidity that yielded EC₅₀ values in the picomolar range.

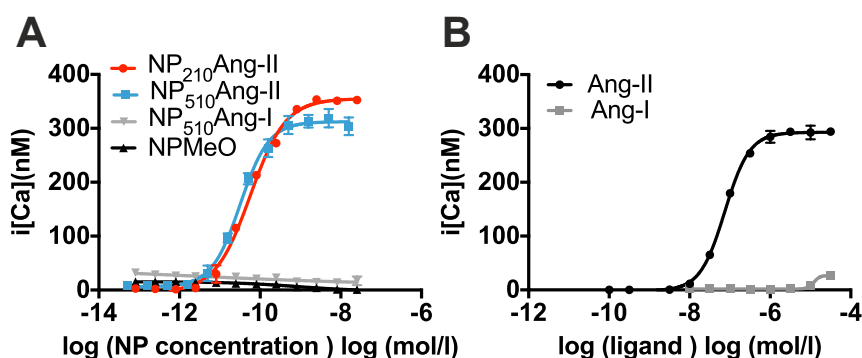


Figure 2. AT1R interaction with angiotensin-labeled NPs. (A) Interaction of secondary ligand-modified NPs (Ang-II) with the secondary target (AT1R) on rMCs as measured by intracellular calcium levels. 50 nm NP₂₁₀Ang-II and 80 nm NP₅₁₀Ang-II particles bind to the AT1R of target cells with similar avidities of 53.7 ± 6.4 pM and 30.7 ± 3.8 pM, respectively. The ligand-free control particles (NPMeO) and Ang-I modified particles (NP₅₁₀Ang-I) did not interact with the receptor. (B) AT1R stimulation by angiotensin peptides as measured by calcium mobilization assay in rMCs. Increasing concentrations of Ang-II produce increasing intracellular calcium concentrations. Only at the highest Ang-I concentrations applied (10 and 30 μ M) could low levels of intracellular calcium be measured, which is a result of Ang-I activation by ACE on the cell membrane during the experiments (see Figure S4). Results represent mean \pm SD ($n = 3$).

3.3 Interaction with ACE

After confirming that Ang-II-modified particles bind to the secondary target receptor, we were intrigued to know if the NP-bound Ang-I could bind to ACE as the primary target structure and if it would be converted to the secondary ligand Ang-II. In these experiments, soluble enzyme served as a surrogate for enzyme immobilized on the target cell surface. We incubated Ang-I-modified NPs with 0.1 μ M rabbit lung ACE and tested again for AT1R activation in rMCs. Figure 3 shows that enzyme-incubated NPAng-I yielded a high intracellular calcium signal from which we concluded that the NPs must have bound to the ACE and that Ang-I in the particle corona must have been converted to Ang-II. The affinity of the interaction between NP-bound Ang-I and ACE was of the same order of magnitude as that for the free substrate (K_m of 8.1 ± 2.4 μ M and 1.4 ± 0.3 μ M for NP₂₁₀Ang-I and NP₅₁₀Ang-I, respectively (Figure S5)). In control

experiments, we showed that receptor activation can be completely suppressed by blocking it with valsartan, a highly affine AT1R antagonist ($K_d = 1.44$ nM) [35]. This proves that the signal must have been NP-triggered, confirming that the NPs had bound to the receptor. When the enzyme was inhibited by captopril ($pK_i = 9.40$) [36] the signal dropped back to background levels indicating a failed enzymatic reaction. Due to the rapidness of the enzymatic conversion we also blocked the cell-membrane bound enzyme on the cells during the measurements to avoid conversion by the cells themselves (see Figure S4).

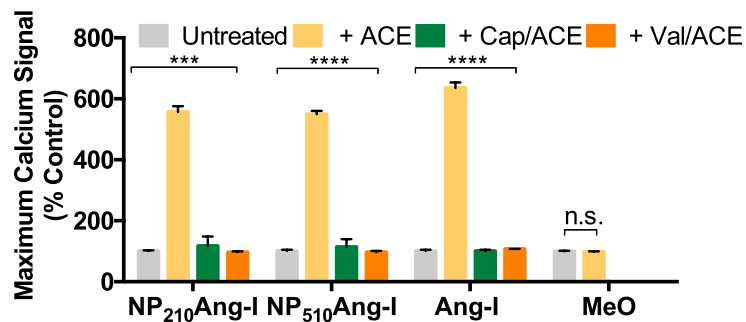


Figure 3. Enzymatic activation of NPs by soluble ACE. Incubation of NP₂₁₀Ang-I or NP₅₁₀Ang-I with 0.1 μ M rabbit lung ACE transformed the NPs to AT1R activating NPAng-II, as shown by the increase in intracellular calcium concentration (yellow bar). Ang-I served as a positive control. In the absence of ACE neither Ang-I decorated NPs nor Ang-I could activate the AT1R (grey bar) similarly to the ligand-free NPMEO. The addition of captopril (Cap) inhibited the Ang-II formation (green bar), and the AT1R antagonist valsartan (Val) blocked the receptor directly (orange bar). Results represent mean \pm SD ($n = 3$ measurements, levels of statistical significance are indicated as *** $p \leq 0.001$ and **** $p \leq 0.0001$ compared to ACE treated samples). n.s., non-significant.

3.4 Cellular uptake in target cells

After NP binding to the primary and secondary target molecules was confirmed, we tested the interaction of the two-stage virus-mimetic NPs with cells. AT1R- and ACE-expressing rMCs and HK-2 cells (Figure S2) were incubated with NPs carrying the pro-ligand (Ang-I) and investigated for particle uptake. Internalization of NP₅₁₀Ang-I and NP₂₁₀Ang-I after pro-ligand activation by cell membrane-bound ACE was observed in both rMCs and HK-2 cells (Figure 4A-D). It was shown that both ACE activation and AT1R binding were necessary by adding either captopril, an ACE inhibitor of the primary target, or valsartan, an antagonist of the secondary target. The fluorescence intensities measured in these control experiments were comparable to the ones obtained for the ligand-free NPMEO, which shows that the NPAng-I first recognizes and binds ACE on the cell membrane, activating a number of pro-ligand Ang-I

Chapter 3: Influenza A Virus Mimetic Nanoparticles Trigger Selective Cell Uptake

molecules and transforming them to the secondary ligand Ang-II. The newly created NP_{Ang-II} then binds to the secondary target AT1R, triggering receptor-mediated internalization. In rMCs (Figure 4C) and HK-2 cells (Figure 4D), the smaller NP₂₁₀Ang-I were taken up in higher amounts than their larger counterparts, NP₅₁₀Ang-I. This demonstrates a size-dependent interaction between NPs and their target molecules and opens interesting new possibilities for NP optimization.

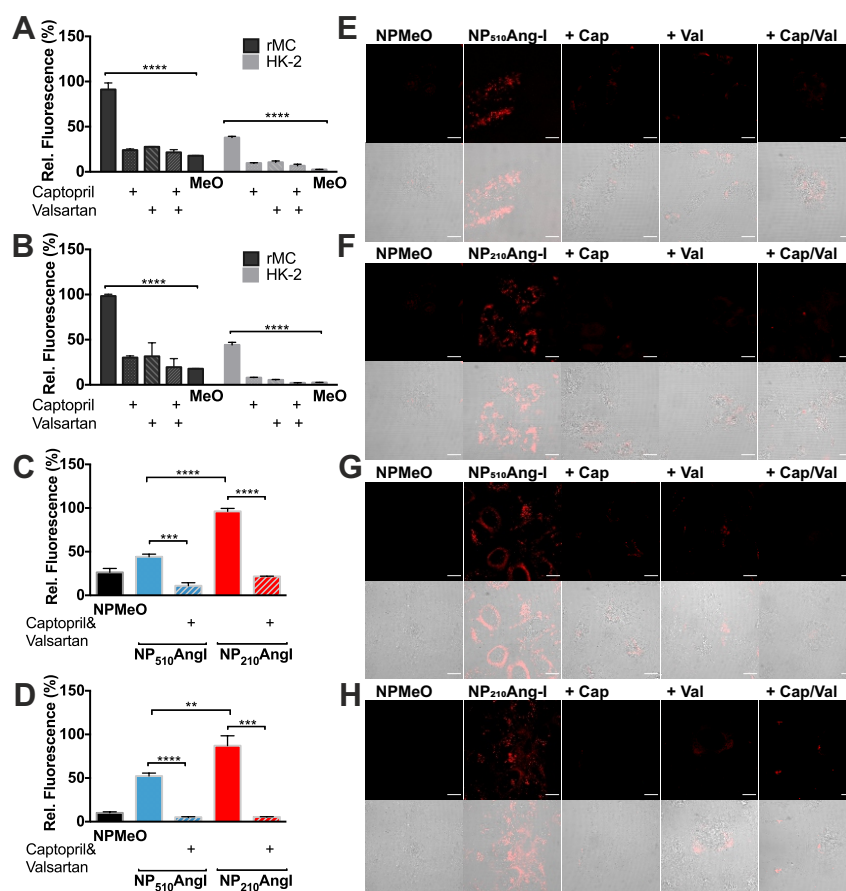


Figure 4. Sequential two-stage interaction by virus-mimetic NPs with primary and secondary receptor positive rMCs and HK-2 cells as shown by flow cytometry (A-D) and CLSM (E-H) (A) NP₅₁₀Ang-I and (B) NP₂₁₀Ang-I were internalized by both cell types compared to the negative control (NPMEO). NP uptake was shown to be size dependent. Incubation of (C) rMCs and (D) HK-2 cells with either NP₂₁₀Ang-I or NP₅₁₀Ang-I showed that the smaller NPs were taken up in significantly higher amounts by both cell lines. Results represent mean \pm SD (n = 3, levels of statistical significance are indicated as **p \leq 0.01, ***p \leq 0.001 and ****p \leq 0.0001). CLSM images were taken after incubating (E)/(F) rMCs and (G)/(H) HK-2 cells with (F)/(H) NP₂₁₀Ang-I and (E)/(G) NP₅₁₀Ang-I. Fluorescence indicating NP uptake can be seen in cells incubated with NP_{Ang-I}, compared to the weak uptake in cells receiving non-targeted NPMEO. In both experiments, NP-uptake could be inhibited by 1 mM captopril and/or valsartan. Scale bar 10 μ m.

To confirm these results, the interaction of the cells with the NPs was investigated by CLSM (Figure 4 E-H). NP-associated fluorescence was observed in rMCs and HK-2 cells incubated with NP₂₁₀Ang-I and NP₅₁₀Ang-I (Figure 4E/F and Figure G/H, respectively). Cells incubated with ligand-free NPMeO show considerably less NP-associated fluorescence. Again, NP uptake could be completely suppressed by adding captopril and/or valsartan.

3.5 Target cell-specificity of influenza virus mimetic NPs

To assess the target-cell specificity of the virus-mimetic NPs, we investigated their interaction with cell lines that have different expression patterns of the target molecules (Figure 5). In contrast to rMCs and HK-2 cells, NCI-H295R cells lack the primary recognition molecule, ACE (Figure S2 and S3) and carry only the secondary target receptor AT1R. Our virus-mimetic NPs showed the highest uptake rates in rMCs and HK-2 cells and only moderate uptake in NCI-H295R cells. This moderate uptake was comparable to that of ligand-free NPMeO control particles and is due to the base level of nonspecific cellular uptake of NPs [37].

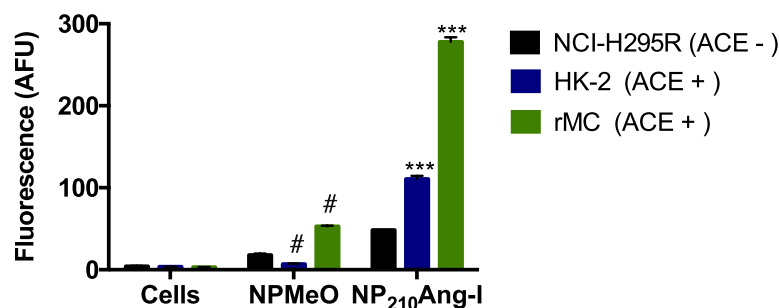


Figure 5. Target-cell specificity of virus-mimetic NPs investigated in different cell lines using flow cytometry. Virus-mimetic NPs were internalized in ACE- and AT1R-positive rMCs and HK-2 cells serving as target cells. Only moderate uptake comparable to the negative control particles (NPMeO) was detected in NCI-H295R cells, which served as off-target cells and carried only the secondary receptor. There was a correlation between the cellular ACE activity and cell binding/uptake, as rMCs have the highest enzymatic activity. Results represent mean \pm SD ($n = 3$, levels of statistical significance are indicated as *** $p \leq 0.001$ compared to untargeted NPMeO, and # $p \leq 0.01$ compared to untreated cells). AFU: arbitrary fluorescence units.

These results confirm the high specificity of our interactive NPs, as their uptake in NCI-H295R cells, which carry only one of two mandatory recognition structures, is as low as for non-targeted NPMeO. Furthermore, there is a strong correlation between the enzymatic activity of the different cell types and the NP-targeting ability. rMCs, which had the highest ACE activity (Figure S2 and S3) also had the highest particle uptake. This demonstrates that even better targeting specificity can be achieved when

Chapter 3: Influenza A Virus Mimetic Nanoparticles Trigger Selective Cell Uptake

ACE expression is increased, making these NPs a promising tool for the treatment of diseases that present with overexpressed ACE levels, as in the case of mesangial cells in diabetic nephropathy [38, 39] or Alzheimer’s disease [40].

In a final set of experiments, we investigated whether our virus-mimetic NPs would be able to distinguish between target and off-target cells when presented with both of them simultaneously. To this end, we co-cultured rMCs together with AT1R-positive but ACE-negative HeLa or NCI-295R cells. To better distinguish between cell types, we marked rMCs fluorescently with CTG (rMCs-CTG). For CLSM images, off-target cells were marked with a different fluorescent label, and all cell nuclei were stained for better visualization. After incubating the co-cultures with virus-mimetic NP₂₁₀Ang-I, we examined NP uptake using CLSM (Figure 6A) and flow cytometry (Figure 6B-C).

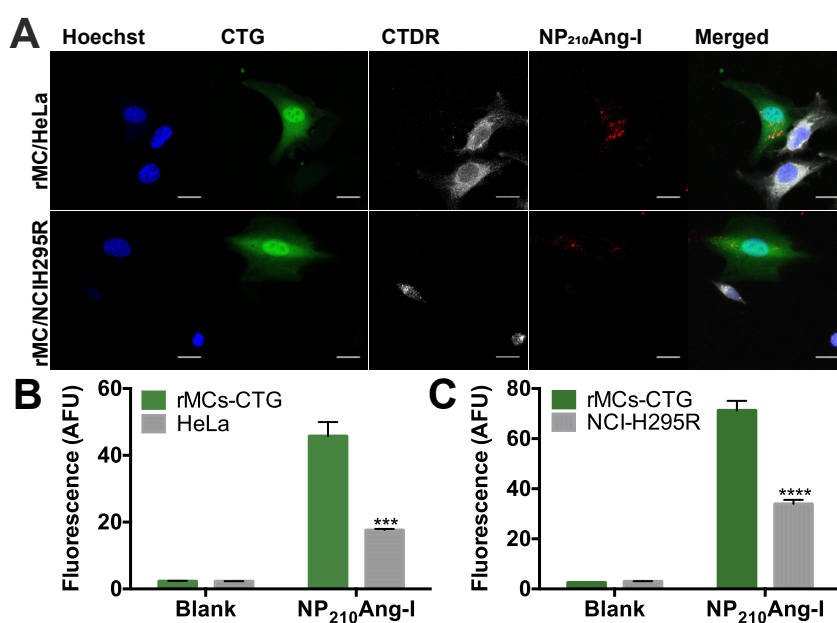


Figure 6. Target cell specificity of virus-mimetic NPs when presented to co-cultures of target- and off-target cells. (A) CLSM images of green-stained fluorescent rMCs (green) and deep red-stained off-target HeLa or NCI-H295R cells (white). Cells were additionally stained with Hoechst 33258 for nuclei visualization. NP₂₁₀Ang-I-associated red fluorescence could only be detected in rMCs, demonstrating the high selectivity of virus-mimetic NPs. Co-culture flow cytometry analysis of (B) rMCs with HeLa cells or (C) rMCs with NCI-H295R in the presence or absence of virus-mimetic NPs corroborated the results. Results represent mean \pm SD ($n = 3$ measurements, levels of statistical significance are indicated as *** $p \leq 0.001$ and **** $p \leq 0.0001$ compared to rMCs-CTG). AFU: arbitrary fluorescence units. Scale bar 20 μ m.

In both experiments, we observed remarkable selectivity. CLSM images revealed that NP-associated red fluorescence was strongly co-localized with the green fluorescence of target rMCs, but not with off-target HeLa or NCI-H295R cells. Flow cytometry confirmed the microscopy results. We found that NPs were not only taken up in significantly higher amounts by rMCs, but this specificity was achieved in an

environment with 10-fold more off-target cells than target cells. Comparable results were obtained for two different off-target cell types. While both carry only the secondary target molecule responsible for NP-uptake, NCI-H295R cells display over 100-fold higher receptor expression than HeLa cells, as shown previously by our group [41], proving that AT1R expression on off-target cells is not of concern for the exceptional specificity of virus-mimetic NPs.

4 Conclusion

In recent years, the investigation into the concept of viral-mimetic, enzyme-responsive NPs has been limited. In most cases, extracellular enzymes such as matrix metalloproteinases (MMPs) [42–45] or proteases [46] were targeted to unveil active NPs that could then interact with tumor cells. Surprisingly, virus-mimetic ectoenzymatic activation following receptor-mediated endocytosis has never been explored. Our work shows that it is possible to design NPs that interact with target cells in a manner similar to the Influenza A virus, using a sequential, interactive two-stage process. Ang-I-decorated copolymer NPs made the initial target cell contact by binding to ACE *via* the proligand Ang-I (Figure 3). As a result of this primary binding process, the NPs were enzymatically activated to unveil Ang-II, the secondary ligand. Ang-II prompts the second stage of binding in which the AT1R is the target receptor (Figure 2). NP binding triggers cell uptake by receptor mediated endocytosis (Figure 4). Our study of the interaction of such NPs with cells carrying only one of the two target structures showed that the presence of both receptors is a *sine qua non* for cell uptake that significantly increases target cell specificity. Moreover, we found a correlation between primary target (ACE) expression and cell uptake. rMCs, which express higher levels of ACE than HK-2 cells, took up significantly more NPs (Figure 5). This makes such materials a promising tool for the treatment of diseases in which an enzyme is overexpressed, as in the case of mesangial cells during diabetic nephropathy [39]. In this instance, it is beneficial that NPs have been reported by multiple groups to enter the mesangium, which is a prerequisite for a nanotherapeutic intervention [47].

In cell co-cultures, particles were able to distinguish target cells that carried both the primary and secondary targets (rMCs of HK-2) from off-target cells that carried only the secondary target (HeLa- and NCI-H295R cells) (Figure 6). Our particles exclusively bound to target cells. This sheds light on the mechanism of the NP-cell interaction. Particles that had been enzymatically activated by ACE and, therefore carried Ang-II in their corona did not bind to neighboring off-target cells despite their 10-fold higher prevalence. NPs seemed to remain bound to the cells that they initially made contact

Chapter 3: Influenza A Virus Mimetic Nanoparticles Trigger Selective Cell Uptake

with *via* their primary target ligand Ang-I. The low K_m value for the enzymatic conversion of Ang-I by ACE, reflecting the high affinity of the NP-bound substrate/enzyme interaction, can provide some explanation for this phenomenon (Figure S5). It is reasonable to assume that the particles are subject to multivalent interactions such that several Ang-I molecules on one NP interact simultaneously with several cell membrane-bound ACE molecules. The kinetics of these parallel interactions significantly hinder the dissociation of NPs from the cell surface while continuously increasing the number of Ang-II molecules in the particle corona. This increases the density of Ang-II in the cleft between particle and cell surface rapidly enough to bind neighboring AT1Rs. Alternatively, the particles, since they are completely substrate-covered, could undergo a rotation on the cell surface until AT1R binding. In both cases, the continuous creation of secondary ligand increasing the avidity for the secondary receptor to EC_{50} values in the 30-50 pM range (for purely Ang-II covered NPs) (Figure 2) could explain why particles cannot move freely and bind to neighboring off-target cells. Overall, our data shows that despite the clean-cut design principles that we used for translating the natural mechanism of influenza A virus-cell interaction to synthetic, therapeutic NPs, the detailed mechanism of NP-cell interaction will need to be further elucidated in future studies.

A critical, forward-looking question is whether our particles are limited to the model enzyme receptor combination we chose. A look at the literature reveals that there are a plethora of well-known ectoenzymes [48, 49]. These could be used to cleave peptide sequences on NPs masking not only natural peptidic but also non-peptidic synthetic receptor ligands, which have enhanced stability in biological environments and concomitantly, a high affinity for a secondary cell surface target of choice. This would increase the number of potential target cells, besides mesangial cells, for our model particles, expanding the applicability and versatility of our concept significantly.

References

- [1] Allen TM, Cullis PR. Drug delivery systems: entering the mainstream. *Science* 2004; 303: 1818–22.
- [2] Mout R, Moyano DF, Rana S, et al. Surface functionalization of nanoparticles for nanomedicine. *Chem Soc Rev* 2012; 41: 2539.
- [3] Wilhelm S, Tavares AJ, Dai Q, et al. Analysis of nanoparticle delivery to tumours. *Nat Rev Mater* 2016; 1: 1–12.
- [4] Peer D, Karp JM, Hong S, et al. Nanocarriers as an emerging platform for cancer therapy. *Nat Nanotechnol* 2007; 2: 751–760.
- [5] Hild W, Pollinger K, Caporale A, et al. G protein-coupled receptors function as logic gates for nanoparticle binding and cell uptake. *Proc Natl Acad Sci U S A* 2010; 107: 10667–72.
- [6] Mammen M, Choi SK, Whitesides GM. Polyvalent interactions in biological systems: Implications for design and use of multivalent ligands and inhibitors. *Angew Chemie - Int Ed* 1998; 37: 2754–2794.
- [7] Hennig R, Pollinger K, Vesper A, et al. Nanoparticle multivalency counterbalances the ligand affinity loss upon PEGylation. *J Control Release* 2014; 194: 20–27.
- [8] Fasting C, Schalley CA, Weber M, et al. Multivalency as a Chemical Organization and Action Principle. *Angew Chemie Int Ed* 2012; 51: 10472–10498.
- [9] Silpe JE, Sumit M, Thomas TP, et al. Avidity Modulation of Folate-Targeted Multivalent Dendrimers for Evaluating Biophysical Models of Cancer Targeting Nanoparticles. *ACS Chem Biol* 2013; 8: 2063–2071.
- [10] Wang S, Dormidontova EE. Nanoparticle targeting using multivalent ligands: computer modeling. *Soft Matter* 2011; 7: 4435.
- [11] Dreaden EC, Gryder BE, Austin LA, et al. Antiandrogen Gold Nanoparticles Dual-Target and Overcome Treatment Resistance in Hormone-Insensitive Prostate Cancer Cells. *Bioconjug Chem* 2012; 23: 1507–1512.
- [12] Hennig R, Vesper A, Kirchhof S, et al. Branched Polymer–Drug Conjugates for Multivalent Blockade of Angiotensin II Receptors. *Mol Pharm* 2015; 12: 3292–3302.
- [13] Kluza E, van der Schaft DWJ, Hautvast PAI, et al. Synergistic Targeting of $\alpha_v\beta_3$ Integrin and Galectin-1 with Heteromultivalent Paramagnetic Liposomes for Combined MR Imaging and Treatment of Angiogenesis. *Nano Lett* 2010; 10: 52–

Chapter 3: Influenza A Virus Mimetic Nanoparticles Trigger Selective Cell Uptake

58.

- [14] Cheng Z, Zaki A Al, Hui JZ, et al. Multifunctional Nanoparticles: Cost Versus Benefit of Adding Targeting and Imaging Capabilities. *Science* (80-) 2012; 338: 903–910.
- [15] Modery-Pawlowski CL, Sen Gupta A. Heteromultivalent ligand-decoration for actively targeted nanomedicine. *Biomaterials* 2014; 35: 2568–2579.
- [16] Marsh M, Helenius A. Virus Entry: Open Sesame. *Cell* 2006; 124: 729–740.
- [17] Boulant S, Stanifer M, Lozach P-Y. Dynamics of virus-receptor interactions in virus binding, signaling, and endocytosis. *Viruses* 2015; 7: 2794–815.
- [18] Grove J, Marsh M. The cell biology of receptor-mediated virus entry. *J Cell Biol* 2011; 195: 1071–82.
- [19] Peitsch C, Klenk H-D, Garten W, et al. Activation of influenza A viruses by host proteases from swine airway epithelium. *J Virol* 2014; 88: 282–91.
- [20] Rice GI, Thomas DA, Grant PJ, et al. Evaluation of angiotensin-converting enzyme (ACE), its homologue ACE2 and neprilysin in angiotensin peptide metabolism. *Biochem J* 2004; 383: 45–51.
- [21] Bkaily G, Sleiman S, Stephan J, et al. Angiotensin II AT 1 receptor internalization, translocation and de novo synthesis modulate cytosolic and nuclear calcium in human vascular smooth muscle cells. *Can J Physiol Pharmacol* 2003; 81: 274–287.
- [22] Qian Y, Feldman E, Pennathur S, et al. From fibrosis to sclerosis: mechanisms of glomerulosclerosis in diabetic nephropathy. *Diabetes* 2008; 57: 1439–45.
- [23] Qian H, Wohl AR, Crow JT, et al. A Strategy for Control of “Random” Copolymerization of Lactide and Glycolide: Application to Synthesis of PEG- b -PLGA Block Polymers Having Narrow Dispersity. *Macromolecules* 2011; 44: 7132–7140.
- [24] Abstiens K, Maslanka Figueroa S, Gregoritz M, et al. Interaction of functionalized nanoparticles with serum proteins and its impact on colloidal stability and cargo leaching. *Soft Matter* 2019; 15: 709–720.
- [25] Valencia PM, Hanewich-Hollatz MH, Gao W, et al. Effects of ligands with different water solubilities on self-assembly and properties of targeted nanoparticles. *Biomaterials* 2011; 32: 6226–6233.
- [26] Abstiens K, Gregoritz M, Goepferich AM. Ligand Density and Linker Length are Critical Factors for Multivalent Nanoparticle–Receptor Interactions. *Appl*

- Mater Interfaces* 2019; 11: 1311–1320.
- [27] Childs CE. The determination of polyethylene glycol in gamma globulin solutions. *Microchem J* 1975; 20: 190–192.
- [28] Smith RE, MacQuarrie R. A sensitive fluorometric method for the determination of arginine using 9,10-phenanthrenequinone. *Anal Biochem* 1978; 90: 246–255.
- [29] Owen SC, Chan DPY, Shoichet MS. Polymeric micelle stability. *Nano Today* 2012; 7: 53–65.
- [30] Xiao RZ, Zeng ZW, Zhou GL, et al. Recent advances in PEG-PLA block copolymer nanoparticles. *Int J Nanomedicine* 2010; 5: 1057–65.
- [31] Makadia HK, Siegel SJ, Makadia HK, et al. Poly Lactic-co-Glycolic Acid (PLGA) as Biodegradable Controlled Drug Delivery Carrier. *Polymers (Basel)* 2011; 3: 1377–1397.
- [32] Yang ZL, Li XR, Yang KW, et al. Amphotericin B-loaded poly(ethylene glycol)-poly(lactide) micelles: Preparation, freeze-drying, and in vitro release. *J Biomed Mater Res Part A* 2008; 85A: 539–546.
- [33] Jiang W, Kim BYS, Rutka JT, et al. Nanoparticle-mediated cellular response is size-dependent. *Nat Nanotechnol* 2008; 3: 145–150.
- [34] de Gasparo M, Catt KJ, Inagami T, et al. International Union of Pharmacology. XIII. The angiotensin II receptors. *Pharmacol Rev* 2000; 52: 415–472.
- [35] de Gasparo M, Whitebread S. Binding of valsartan to mammalian angiotensin AT1 receptors. *Regul Pept* 1995; 59: 303–311.
- [36] Bevilacqua M, Vago T, Rogolino A, et al. Affinity of angiotensin I-converting enzyme (ACE) inhibitors for N- and C-binding sites of human ACE is different in heart, lung, arteries, and veins. *J Cardiovasc Pharmacol* 1996; 28: 494–9.
- [37] Huang X, Teng X, Chen D, et al. The effect of the shape of mesoporous silica nanoparticles on cellular uptake and cell function. *Biomaterials* 2010; 31: 438–448.
- [38] Cristovam PC, Arnoni CP, de Andrade MCC, et al. ACE-Dependent and Chymase-Dependent Angiotensin II Generation in Normal and Glucose-Stimulated Human Mesangial Cells. *Exp Biol Med* 2008; 233: 1035–1043.
- [39] Vidotti DB, Casarini DE, Cristovam PC, et al. High glucose concentration stimulates intracellular renin activity and angiotensin II generation in rat mesangial cells. *Am J Physiol Physiol* 2004; 286: F1039–F1045.
- [40] Ohrui T, Tomita N, Sato-Nakagawa T, et al. Effects of brain-penetrating ACE inhibitors on Alzheimer disease progression. *Neurology* 2004; 63: 1324–5.

Chapter 3: Influenza A Virus Mimetic Nanoparticles Trigger Selective Cell Uptake

- [41] Hennig R, Ohlmann A, Staffel J, et al. Multivalent nanoparticles bind the retinal and choroidal vasculature. *J Control Release* 2015; 220: 265–274.
- [42] Callmann CE, Barback C V., Thompson MP, et al. Therapeutic Enzyme-Responsive Nanoparticles for Targeted Delivery and Accumulation in Tumors. *Adv Mater* 2015; 27: 4611–4615.
- [43] Nguyen MM, Carlini AS, Chien M-P, et al. Enzyme-Responsive Nanoparticles for Targeted Accumulation and Prolonged Retention in Heart Tissue after Myocardial Infarction. *Adv Mater* 2015; 27: 5547–5552.
- [44] Han H, Valdepérez D, Jin Q, et al. Dual Enzymatic Reaction-Assisted Gemcitabine Delivery Systems for Programmed Pancreatic Cancer Therapy. *ACS Nano* 2017; 11: 1281–1291.
- [45] Guo F, Wu J, Wu W, et al. PEGylated self-assembled enzyme-responsive nanoparticles for effective targeted therapy against lung tumors. *J Nanobiotechnol* 2018; 16: 57.
- [46] Adamiak L, Touve MA, Leguyader CLM, et al. Peptide Brush Polymers and Nanoparticles with Enzyme-Regulated Structure and Charge for Inducing or Evading Macrophage Cell Uptake. *ACS Nano* 2017; 11: 9877–9888.
- [47] Hang C, Choi J, Zuckerman JE, et al. Targeting kidney mesangium by nanoparticles of defined size. *Proc Natl Acad Sci U S A* 2011; 108: 6656–6661.
- [48] Alexander SP, Fabbro D, Kelly E, et al. The Concise Guide to PHARMACOLOGY 2015/16: Enzymes. *Br J Pharmacol* 2015; 172: 6024–6109.
- [49] Kreutzberg GW, Reddington M, Zimmermann H. *Cellular Biology of Ectoenzymes: Proceedings of the International Erwin-Riesch-Symposium on Ectoenzymes May 1984*. Springer Berlin Heidelberg, 1986.

Chapter 3 - Supporting Information

Influenza A Virus Mimetic Nanoparticles Trigger Selective Cell Uptake

1 Supplementary Materials

1.1 Characterization of cells for AT1R and ACE expression

rMCs and HK-2 cells were chosen as an *in vitro* model to test the virus-mimetic NPs as both express ACE and AT1R on their cell membrane according to the literature [1–3]. First, we confirmed the prevalence of the primary (ACE) and secondary (AT1R) target structure by reverse transcription polymerase chain reaction (RT-PCR) (Figure S2A and Table S1). To this end, cells were cultured in T-25 culture flasks (Corning, Corning, NY, USA) until subconfluent. Then the cellular RNA was isolated with an additional DNase digestion, using the peqGOLD total RNA kit and the peqGOLD DNase I Digest Kit (Peqlab Biotechnologie GmbH, Erlangen, Germany), as indicated by the manufacturer. Concentration and purity of the obtained RNA was measured with the Nanodrop 1000 Spectrophotometer (Thermo Fisher Scientific, Waltham, MA, USA). The single stranded cDNA was synthesized from 0.7 µg RNA, which was reverse transcribed with the peqGOLD cDNA Synthesis Kit H Minus (Peqlab Biotechnologie GmbH, Erlangen, Germany). For double stranded cDNA synthesis and amplification PCR was conducted using a LifeECO Thermal Cycler (Biozym Scientific GmbH, Hess. Oldendorf, Germany) and peqGOLD Taq-DNA-Polymerase “all inclusive” (Peqlab Biotechnologie GmbH, Erlangen, Germany). Primer sequences used were obtained from literature and are depicted in Table S1. PCR was run for 40 cycles with each 30 s denaturation at 94 °C, 60 s annealing at the indicated annealing temperatures (Table S1), and 30 s extension at 72 °C. Obtained products were visualized under UV illumination in a 2% agarose gel stained with ethidium bromide. Results can be seen in Figure S2A.

Since mRNA levels do not always correlate with protein levels [4] a ratiometric intracellular calcium mobilization assay was performed to confirm the presence of functional AT1R. As Gq-coupled receptor [5], its activation by an agonist such as Ang-II triggers calcium influx into the cell cytosol (Figure S2B).

To determine the ACE activity of the different cell types we used o-aminobenzoic acid-phenylalanyl-arginine-lysine (2,4-dinitrophenyl)-proline (Abz-FRK(Dnp)-P), an internally quenched peptide substrate that can be hydrolyzed by the cell membrane-bound ACE at the Arg-Lys(Dnp) bond [6], adapting methods described by Sabatini *et al.* [7] and Carmona *et al.* [8]. To this end, cells were seeded at a density of 135,000 cells per well, 100,000 cells per well, or 200,000 cells per well, respectively in a Corning CellBIND 96-well, flat, black, microplate (Corning, Corning, NY, USA), and incubated for 1h at 37 °C, 5% CO₂. Cells were washed with assay buffer prior to incubating them in the same buffer supplemented with 10 µM of the ACE substrate Abz-FRK(Dnp)-P. For ACE activity inhibition, cells were additionally incubated with 2.5 µM Captopril for 5 minutes previous to substrate addition. Variation of fluorescence over time was

Chapter 3: Influenza A Virus Mimetic Nanoparticles Trigger Selective Cell Uptake

recorded at different time points using a LS-5S fluorescence plate reader (Perkin Elmer, Waltham, MA, USA) at λ_{ex} = 320 nm and λ_{em} = 420 nm (Figure S3). To determine the protein content of each well, cells were firstly lysed with M-PER Mammalian Protein Extraction Reagent (Thermo Fisher Scientific, Waltham, MA, USA) and then the total protein content of the lysate was quantified [9]. ACE activity was expressed as pmol of hydrolyzed substrate per minute and per μ g of protein (Figure S2C). Student's t-test was performed using GraphPad Prism in order to assess statistical significance.

To confirm that also Ang-I, the proligand, could be cleaved by ACE positive cells, rMCs were seeded in T-75 culture flasks (Corning, Corning, NY, USA) and incubated until subconfluent. The cells were washed with DPBS and 10 ml phenol red-free RPMI1640 medium, supplemented with 100 μ M Ang-I was added. For ACE inhibition, cells were pre-incubated in the same medium, supplemented with 1 mM Captopril for 15 minutes prior to angiotensin-I addition. At different time points, 100 μ L samples were taken from the supernatant and stored at -20 °C until they were used as AT1R agonist sample solutions in an intracellular calcium mobilization assay, as described in the main text (Figure S2D).

1.2 Micheaelis-Menten kinetics of soluble ACE using Ang-I, NP₂₁₀Ang-I and NP₅₁₀Ang-I as substrates

In order to determine the Michaelis-Menten constant (K_m) for the hydrolysis of NP-bound Ang-I, NP samples were diluted to concentrations ranging between 30 nM and 300 μ M ligand. The samples were incubated with 15 nM rabbit lung ACE (Sigma Aldrich, Taufkirchen, Germany) for 5, 15, 30, 60, 90, or 120 minutes before they were used in a calcium mobilization assay with AT1R- positive rMCs. The increases in intracellular calcium concentration over the incubation time with the enzyme were recorded. To inhibit the enzymatic conversion, 20 μ M captopril was pre-incubated for 15 minutes with the ACE. In order to convert the calcium signal obtained (nM) to hydrolyzed substrate (pmol), a dilution series ranging between 1 nM and 300 μ M Ang-II were used as agonists in the calcium mobilization assay. The signal produced by 300 μ M Ang-II was correlated with the amount of Ang-II used in the AT1R stimulation, and this value was adopted for further calculations. The velocity (pmol minute^{-1}) of the reaction at 5 minutes incubation time was plotted against the substrate concentration (μ M) for the determination of K_m (Figure S4) with GraphPad Prism. The feasibility of this assay was confirmed by the fact that the K_m value obtained for non-bound Ang-I matched the described literature values for this peptide [10].

2 Nanoparticle characterization

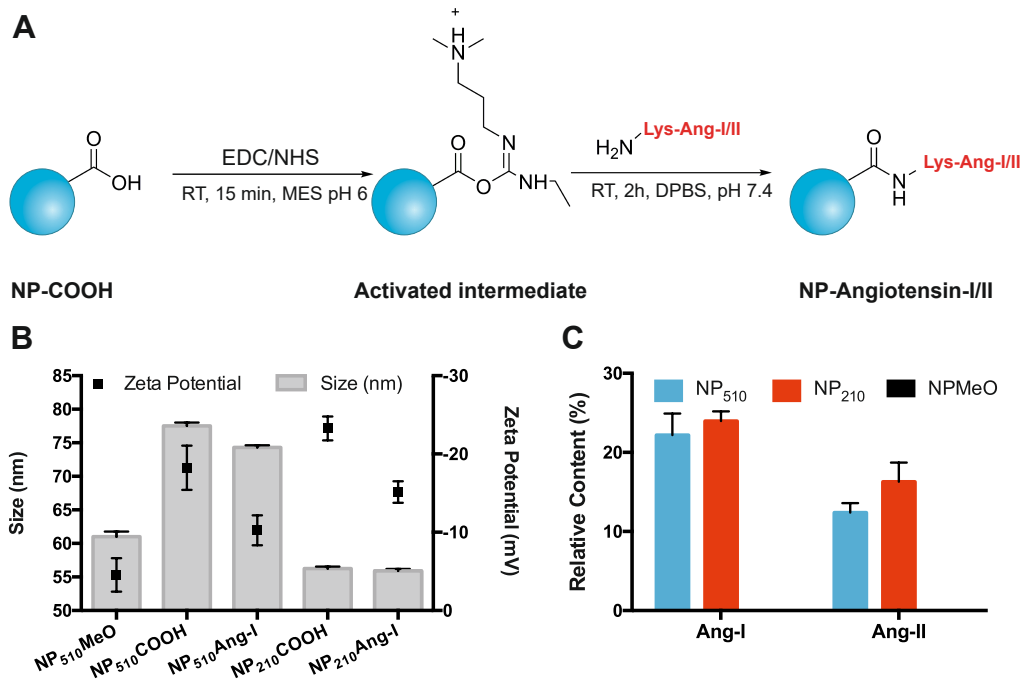


Figure S1. NPs carrying angiotensin derivatives. (A) Reaction scheme of the ligand coupling reaction. NP-COOH are activated using EDC to an amine reactive o-acylisourea intermediate stabilized by NHS that reacts with the amino group of lysine attached to the N-terminal end of the angiotensin peptides. (B) NP size, size distribution (PDI) and zeta potential before and after ligand conjugation. (C) Quantification of ligand modified PEG chains. Ligand free NPMEO served as negative control. Results represent mean \pm SD of $n = 3$ measurements.

3 Cell line characterization

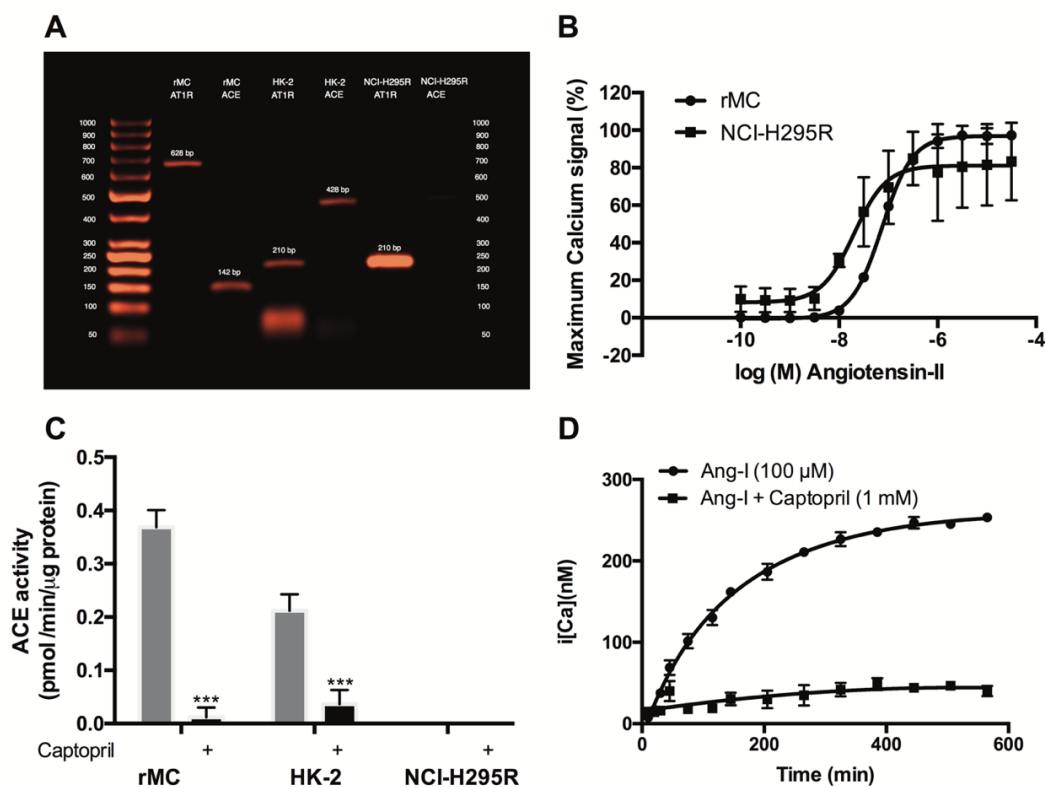


Figure S2. Characterization of cells for AT1R and ACE expression. (A) RT-PCR results in a 2% agarose gel stained with ethidium bromide. Expected bands for AT1R expression (628 and 210 bp) and ACE (142 and 428 bp) can be seen for rMCs and HK-2 cells. Only AT1R mRNA could be found in NCI-H295R cells (210 bp). (B) Intracellular calcium mobilization after AT1R stimulation in rMCs and NCI-H295R cells. The receptor was stimulated with different concentrations of Ang-II, after the cells had been loaded with Fura-2 dye. Increases in cytosolic calcium concentration could be measured with rising agonist concentrations. (C) ACE activity of rMCs, HK-2 and NCI-H295R cells using 10 μM Abz-FRK(Dnp)-P as a substrate. rMCs showed a higher substrate conversion rate than HK-2 cells. No enzymatic activity could be measured for NCI-H295R cells, confirming the previously obtained PCR results. Enzymatic hydrolysis of the substrate could be completely inhibited by addition of 2.5 μM captopril. See also Figure S3. Levels of statistical significance are indicated as *** $p \leq 0.001$. (D) Enzymatic conversion of Ang-I by rMCs. Cells were incubated with 100 μM Ang-I, and supernatants were analyzed in a calcium mobilization assay. Cell conversion of Ang-I to Ang-II was shown by the increase of intracellular calcium concentration upon AT1R stimulation by Ang-II. Inhibition of the signal rise over time could be achieved by preincubating the cells with 1 mM captopril. Results represent mean \pm SD of $n = 3$ measurements.

4 ACE activity measurement

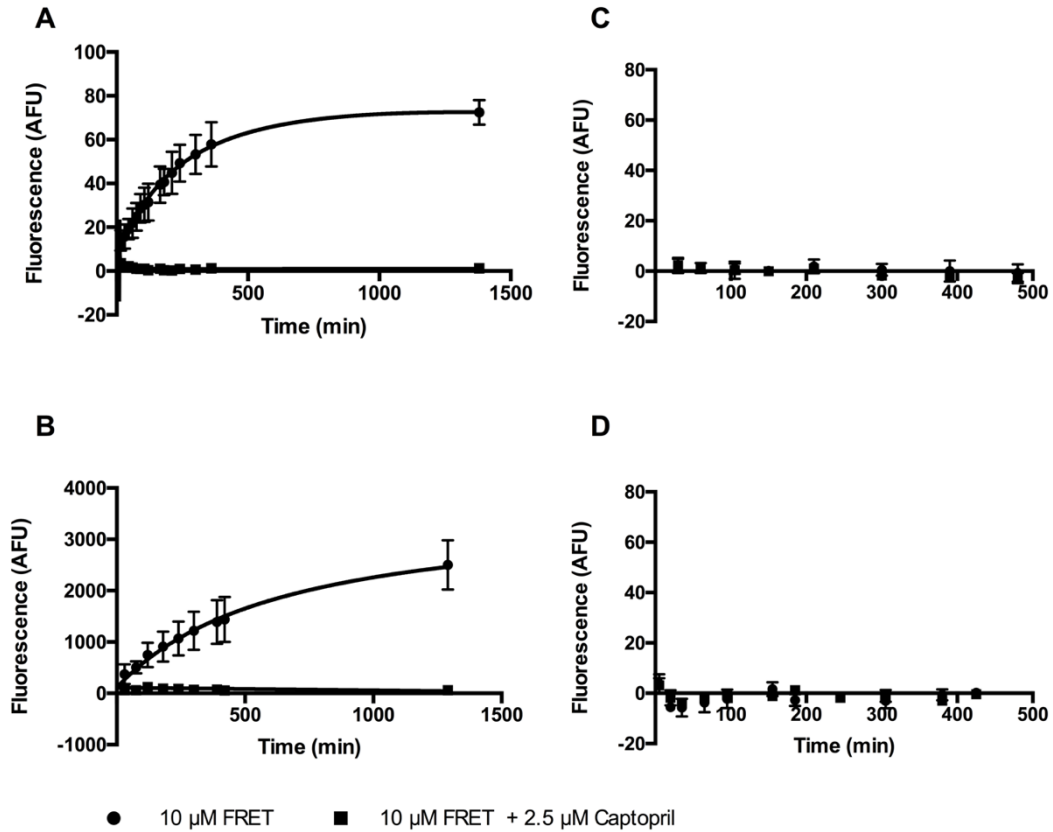


Figure S3. ACE activity measurement using a specific FRET substrate. Abz-FRK(Dnp)-P hydrolysis by (A) rMCs, (B) HK-2 cells, (C) NCI-H295R cells and (D) washing buffer. Increases in fluorescence due to enzymatic splitting of the substrate by cell membrane-bound ACE. rMCs and HK-2 cells are able to hydrolyze the substrate, but not NCI-H295R cells. Specificity of the substrate is shown by the lack of fluorescence increase when 2.5 μ M captopril was added. Additionally, the buffer used to wash the cells prior to substrate addition was not able to activate the fluorogenic substrate, indicating that the cells themselves and not serum remnants were responsible for the enzymatic activity. Results represent mean \pm SD of $n = 3$ measurements.

5 Time-dependent calcium signal

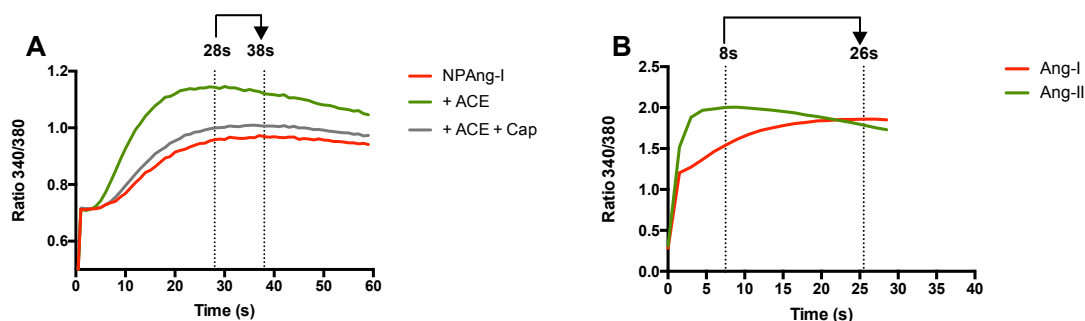


Figure S4. Calcium assay showing the response of cells to Ang-I and Ang-II. Ang-I to Ang-II conversion during AT1R stimulation measurements of particle-bound ligand (A) or free ligand (B) followed by Fura-2 intracellular calcium measurement in ACE expressing rMCs. As a ratiometric assay the maximum ratio between the 340 and 380 nm excited and 540 nm recorded fluorescence is examined [11]. As an agonist for the receptor, Ang-II produces a fast response with maximum ratios after 8 seconds of stimulation. When Ang-I is used the signal increases gradually with a delayed maximum at 26 s, which can be explained by a continuous conversion of Ang-I to Ang-II by the cell membrane-bound ACE (see Figure S2 and S3) (B). This response is also seen for particles with tethered ligands (A). NPAng-I pre-incubated with 0.1 μ M, which reflects the presence of soluble enzyme in cell culture, show a maximum ratio after 28 seconds. The signal cannot be completely suppressed by the presence of 20 μ M Captopril (Cap) but is only delayed to 38 seconds. This suggests that there is a second source of enzyme, which is the ACE in on the cell membranes which can only be silenced when the cells are incubated separately with 5 mM captopril prior to the experiment. Differences between the free and particle-bound ligands are due to an incomplete enzymatic activation of Ang-I to Ang-II on the particle corona and to differences in conversion rates and affinities towards the receptor.

6 Michaelis-Menten kinetics

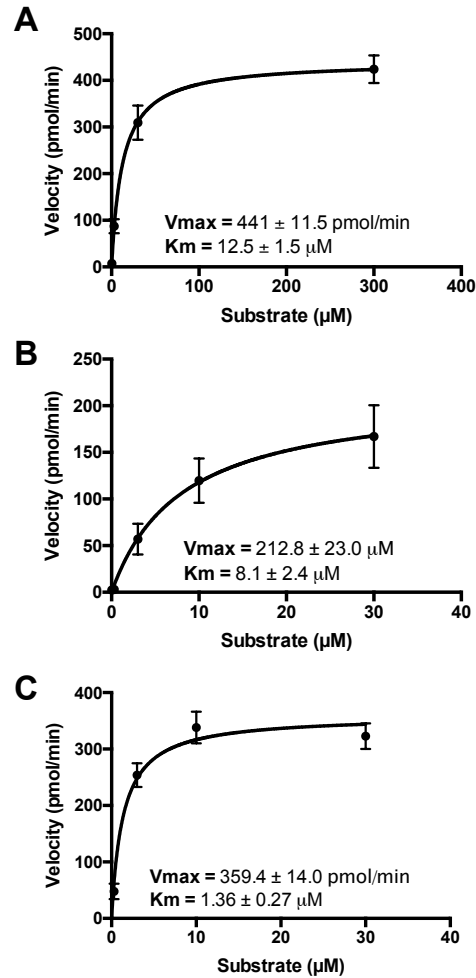


Figure S5. Michaelis-Menten kinetics of soluble ACE. (A) Ang-I, (B) NP₂₁₀Ang-I and (C) NP₅₁₀Ang-I were used as substrates. Dilutions of NP-bound and non-bound Ang-I were incubated with 15 nM rabbit lung ACE. The hydrolysis product was quantified with an intracellular calcium mobilization assay using AT1R positive rMCs. Michaelis-Menten constant obtained for NP-bound ligand (K_{m} of 8.1 ± 2.4 μM and 1.4 ± 0.3 μM for NP₂₁₀Ang-I and NP₅₁₀Ang-I, respectively) were lower than the value obtained for free Ang-I (12.5 ± 1.5 μM). Results represent mean \pm SD of $n = 3$ measurements.

7 Polymer characterization

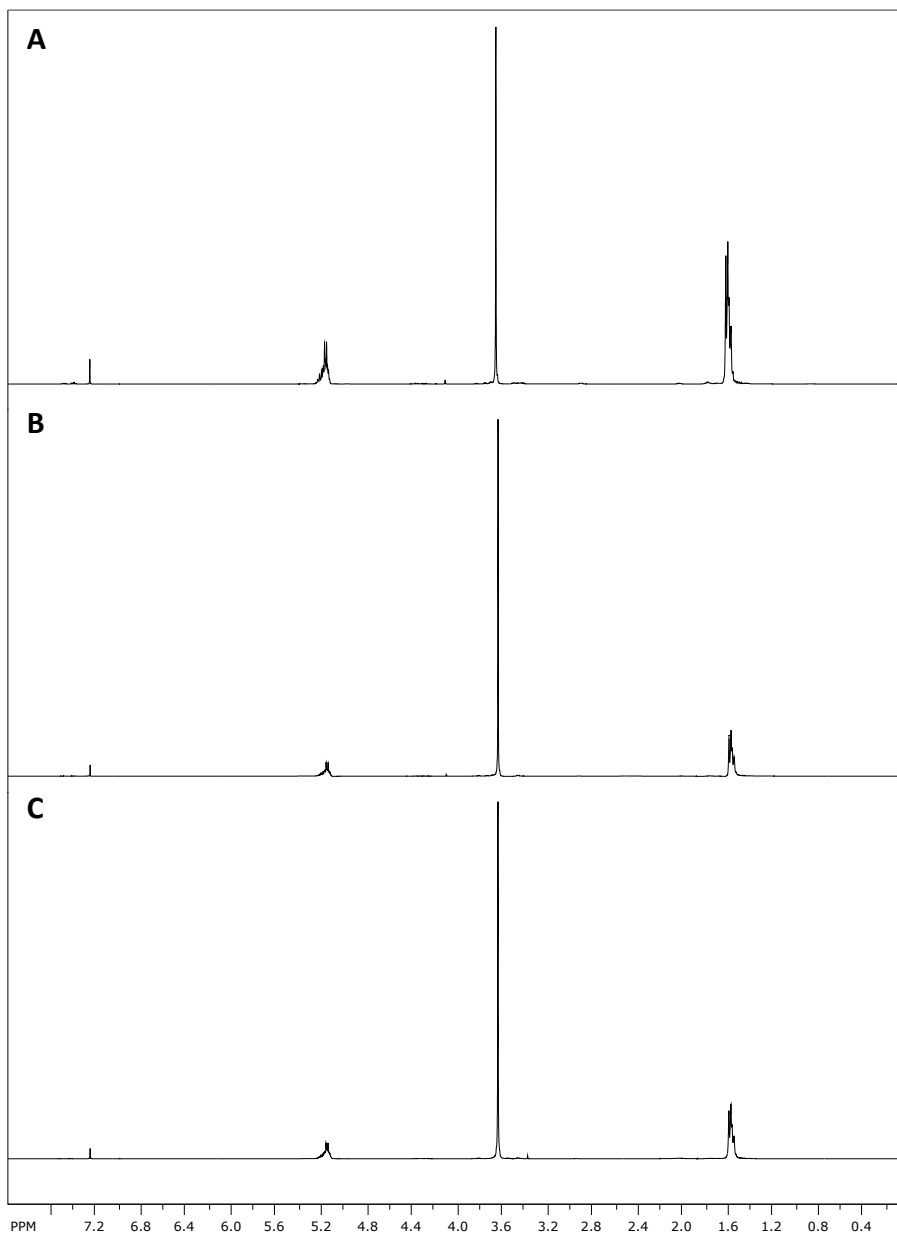


Figure S6. ¹H-NMR (CDCl₃, 300 MHz) spectra of PEG-PLA block copolymers. 10kDa PLA attached to carboxylic acid-terminated 2kDa (A) or 5kDa (B) PEG and methoxy-terminated 5kDa PEG (C). δ (ppm): 1.58 ppm (-C(CH₃)H-), 3.39 ppm (H₃COCH₂CH₂-), 3.65 ppm (-OCH₂CH₂-), 4.21 ppm (-OCH₂CH₂-O(CO)-), 5.16 ppm (-C(CH₃)H-), 7.26 ppm (solvent peak).

8 Primers used in PCR

Table S1

Product	Primer sequence	S/AS	Lenght (bp)	Ta (°C)	Reference
AT1R human	GGC CAG TGT TTT TCT TTT GAA TTT AGC AC	S	210	57	[12]
	TGA ACA ATA GCC AGG TAT CGA TCA ATG C	AS			
ACE human	GGT GGT GTG GAA CGA GTA TG TCG GGT AAA ACT GGA GGA TG	S AS	428	52	[12]
AT1R rat	TTG GAA ACA GCT TGG TGG TGA T CCA GAA AAG AAG AAG AAA AGC AC	S AS	628	52	[13]
ACE rat	TCC TGC TAG ACA TGG AGA CGA CAG CTC TTC CAC ACC CAA AG	S AS	142	54	[14]

Ta: Annealing temperature, S: sense, AS: antisense

9 References

- [1] Cristovam PC, Arnoni CP, de Andrade MCC, et al. ACE-Dependent and Chymase-Dependent Angiotensin II Generation in Normal and Glucose-Stimulated Human Mesangial Cells. *Exp Biol Med* 2008; 233: 1035–1043.
- [2] Vidotti DB, Casarini DE, Cristovam PC, et al. High glucose concentration stimulates intracellular renin activity and angiotensin II generation in rat mesangial cells. *Am J Physiol Physiol* 2004; 286: F1039–F1045.
- [3] Ni J, Ma K-L, Wang C-X, et al. Activation of renin-angiotensin system is involved in dyslipidemia-mediated renal injuries in apolipoprotein E knockout mice and HK-2 cells. *Lipids Health Dis* 2013; 12: 49.
- [4] Maier T, Güell M, Serrano L. Correlation of mRNA and protein in complex biological samples. *FEBS Lett* 2009; 583: 3966–3973.
- [5] de Gasparo M, Catt KJ, Inagami T, et al. International Union of Pharmacology. XIII. The angiotensin II receptors. *Pharmacol Rev* 2000; 52: 415–472.
- [6] Mauricio C. Araujo, Robson L. Melo, Maria Helena Cesari, et al. Peptidase Specificity Characterization of C- and N-Terminal Catalytic Sites of Angiotensin I-Converting Enzyme†. *Biochemistry* 2000; 29: 8519–8525.

Chapter 3: Influenza A Virus Mimetic Nanoparticles Trigger Selective Cell Uptake

- [7] Sabatini RA, Bersanetti PA, Farias SL, et al. Determination of angiotensin I-converting enzyme activity in cell culture using fluorescence resonance energy transfer peptides. *Anal Biochem* 2007; 363: 255-262.
- [8] Carmona AK, Schwager SL, Juliano MA, et al. A continuous fluorescence resonance energy transfer angiotensin I-converting enzyme assay. *Nat Protoc* 2006; 1: 1971-1976.
- [9] Bradford MM. A rapid and sensitive method for the quantitation of microgram quantities of protein utilizing the principle of protein-dye binding. *Anal Biochem* 1976; 72: 248-254.
- [10] Rice GI, Thomas DA, Grant PJ, et al. Evaluation of angiotensin-converting enzyme (ACE), its homologue ACE2 and neprilysin in angiotensin peptide metabolism. *Biochem J* 2004; 383: 45-51.
- [11] Grynkiewicz G, Poenie M, Tsien RY. A New Generation of Ca²⁺ Indicators with Greatly Improved Fluorescence Properties*. *J Biol Chem* 1985; 260: 3440-3450.
- [12] Liebau MC, Lang D, Böhm J, et al. Functional expression of the renin-angiotensin system in human podocytes. *Am J Physiol Physiol* 2006; 290: F710-F719.
- [13] Chouinard RF, Meek RL, Cooney SK, et al. Effects of amino acids and glucose on mesangial cell aminopeptidase a and angiotensin receptors. *Kidney Int* 2002; 61: 106-109.
- [14] Klimas J, Olvedy M, Ochodnicka-Mackovicova K, et al. Perinatally administered losartan augments renal ACE2 expression but not cardiac or renal Mas receptor in spontaneously hypertensive rats. *J Cell Mol Med* 2015; 19: 1965-1974.

Chapter 4

The Effect of Ligand Mobility on the Cellular Interaction of Multivalent Nanoparticles

Published in *Macromolecular Bioscience*

2020, 20 (2), 1900427

This chapter was published as: S. Maslanka Figueroa, D. Fleischmann, S. Beck and A. Goepferich, *Macromol. Biosci.* 2020, 20 (2), 1900427, doi:10.1002/mabi.201900427

Abstract

Multivalent nanoparticle binding to cells can be of picomolar avidity making such interactions almost as intense as those seen with antibodies. However, reducing nanoparticle (NP) design exclusively to avidity optimization by the choice of ligand and its surface density does not sufficiently account for controlling and understanding cell-particle interactions. Cell uptake, for example, is of paramount significance for a plethora of biomedical applications and does not exclusively depend on the intensity of multivalency. In this study we show that the mobility of ligands tethered to particle surfaces has a substantial impact on particle fate upon binding. Nanoparticles carrying angiotensin-II (Ang-II) tethered to highly mobile 5kDa long poly(ethylene glycol) (PEG) chains separated by ligand-free 2kDa short PEG chains show a superior accumulation in angiotensin-II receptor type 1 (AT1R) positive cells. In contrast, when ligand mobility is constrained by densely packing the NP surface with 5kDa PEG chains only, cell uptake decreases by 50%. Remarkably, irrespective of ligand mobility and density both particle types have similar EC50 values in the 1-3 nM range. These findings demonstrate that ligand mobility on the NP corona is an indispensable attribute to be considered in particle design to achieve optimal cell uptake *via* multivalent interactions.

1 Introduction

Nanoparticles (NPs) are considered ideal candidates for drug delivery because they are able to convey their cargo to a desired site of action, thus avoiding the deleterious consequences of off-target effects [1]. To achieve specific NP-cell interactions, particle surfaces are usually functionalized with ligands that are able to recognize distinct cellular structures. To counterbalance the affinity loss derived from the tethering of ligands to linkers [2], numerous ligand molecules are coupled to a single NP to enable the simultaneous recognition of several receptor molecules on the cell membrane. This multivalent binding highly increases the nanomaterial's overall avidity [3], which is why over the last years the research focus has been set on improving this trait. Still, targeted nanomaterials fail to achieve optimal results and studies deliver highly variable outcomes. This can mainly be attributed to an incomplete understanding of the influence that distinct particle design features have on multivalent interactions and, therefore, the particle's fate after binding. Additionally, adjustment of one particle attribute usually correlates with modifications of several other characteristics, which highly influences the outcome at cellular level. Therefore, a profound understanding of the parameters affecting multivalent binding is needed to improve NP design.

There are several factors that are known to influence a nanomaterial's multivalent binding, and thus the targeting capacity of NPs, such as particle size and receptor- or ligand density [4, 5]. The latter not only determines the ability of a NP to bind to the target cell surface, but also the thermodynamic feasibility of cellular uptake [6] and its precise pathway [7]. Still, there are several other elements that contribute to the thermodynamic favorability of a multivalent interaction, among which flexibility was noted to be crucial by several publications [8, 9]. In their seminal theoretical paper, Kitov and Bundle highlight that the flexibility of a system significantly increases the number of ways in which bonds can be formed in a multivalent interaction which, in turn, supports binding [10]. More so, they predict the compensation of the entropy loss derived from a binding by an increase in possible conformations and a reduced steric burden [10]. Therefore, a higher flexibility in a particle system that allows for a higher ligand mobility could enhance cellular interaction. However, ligand mobility on the particle corona is not sufficiently taken into consideration in particle design. Furthermore, the interplay between ligand mobility and ligand density is not yet completely understood.

NPs are commonly shielded by polymers, such as poly(ethylene glycol) (PEG), which, beside acting as a tether for ligands, enable prolonged circulation times [11] and reduce plasma protein absorption [12]. To achieve those effects, a high polymer surface density is usually required [13], which restrains the flexibility of the system and the

Chapter 4: The Effect of Ligand Mobility on the Cellular Interaction

ligand mobility. Generally, the polymers comprising the NP corona are kept homogeneous in terms of length, i.e. molecular weight, and the multivalent interactions are to some extent length-dependent [14]. For example, it was demonstrated that decreasing the overall PEG length can increase the uptake of liposomes [15] and polymer NPs [16]. However, these adjustments in polymer composition can reduce the overall particle PEG covering. Concomitantly, they tremendously alter particle size, which is a key factor determining NP-cell interactions [17], making it difficult to discern which parameter contributed to the targeting increase. Therefore, the goal of this study was to investigate the effect of ligand mobility whilst maintaining a high PEG density and producing minor particle size variations. For our purposes we decided to design NPs with heterogeneous surface polymer compositions, a design choice sparsely represented in the literature [15, 18–21]. To date, this concept is loosely associated with higher targeting efficiency or improved ligand binding and density control, but a deeper understanding of how it affects ligand mobility is required.

For our systematic investigation on the impact of ligand mobility on multivalent targeting particles, we relied on polymer NPs as a scaffold, consisting of PEG-poly(lactic acid)(PLA) and poly(lactic-co-glycolic acid) (PLGA). We considered them highly suited for this study as their ligand mobility can be tailored by adjusting the polymer composition. More so, they are biocompatible and biodegradable and are fitted for the use as drug carriers. To endow particles with targeting capacities we used angiotensin derivative ligands, which we previously used for highly specific cell identification [22], and sought to further improve the system by adjusting its flexibility. To that end, we coupled angiotensin-I (Ang-I) or angiotensin-II (Ang-II), targeting cell membrane-bound angiotensin converting enzyme (ACE) or angiotensin-II type 1 receptor (AT1R), respectively, to long PEG_{5k}-PLA_{10k} chains and kept the remaining non-modified polymers (NMPs) shorter by using a PEG_{2k}-PLA_{10k} to allow higher conformational freedom to the ligand-carrying polymers (LMPs) (Figure 1A). We compared this “flexible” NP-design with particles carrying NMPs of the same length as the LMPs, representing the conventional NP formulations. Additionally, we manufactured particles with increasing ligand densities to investigate if higher targeting capability (more ligands) would compensate for the associated mobility loss. The resulting NP formulations were characterized in terms of size, surface charge, and ligand content. Their ligand affinity and particle avidity towards their respective targets were evaluated, and their cellular interaction regarding targeting efficiency, uptake specificity, and cellular distribution was analyzed. Lastly, the polymer conformation on the particle corona and the distance between ligands was estimated.

2 Materials and Methods

2.1 Materials

Carboxylic acid end-functionalized hydroxyl-PEG with molecular weights of 2000 (COOH-PEG_{2k}-OH) and 5000 Da (COOH-PEG_{5k}-OH) were obtained from JenKem Technology USA Inc. (Allen, TX, USA). Lysine N-modified Angiotensin-I (Lys-Ang-I) and Ang-II (Lys-Ang-II) (purity > 98%) were purchased from Genscript (Piscataway, NJ, USA). EXP3174 was purchased from Santa Cruz Biotechnology (Dallas, TX, USA). Fura-2AM was purchased from Life Technologies (Carlsbad, CA, USA). CellMask™ deep red plasma membrane stain (CMDR), and Pierce BCA assay kit were purchased from Thermo Fisher Scientific (Waltham, MA, USA). ACE from rabbit lung and all other reagents in analytical grade were obtained from Sigma Aldrich (Taufkirchen, Germany). Ultrapure water was obtained from a Milli-Q water purification system (Millipore, Billerica, MA, USA).

2.2 Cell culture

Rat mesangial cells (rMCs) were kindly gifted by Prof. Dr. Armin Kurtz (Institute of Physiology, University of Regensburg, Germany). They were cultured in RPMI1640 medium with 10% fetal bovine serum (FBS) (Biowest, Nuaille, France) supplemented with insulin-transferrin-selenium (Life Technologies, Carlsbad, CA, USA) and 100 nM hydrocortisone. The characterization of the cells for their AT1R and ACE expression was previously shown by our group [22].

2.3 Polymer synthesis and ligand coupling

PEG-PLA block-copolymers were synthesized *via* ring opening polymerization of cyclic lactide after Qian *et. al.* [23] with slight modifications described previously by our group [24]. COOH-PEG-OH was used as a macroinitiator and 1,8-diazabicyclo[5.4.0]undec-7-ene (DBU) as a catalyst. Resulting polymers were 10kDa PLA with either a 2kDa or 5kDa carboxylic acid terminated PEG chain (COOH-PEG_{2k}-PLA_{10k} or COOH-PEG_{5k}-PLA_{10k}, respectively) [22].

To synthesize Ang-I/II-PEG_{5k}-PLA_{10k}, COOH-PEG_{5k}-PLA_{10k} (14 μmol) was activated with 1-Ethyl-3-(3-dimethylaminopropyl)carbodiimide (EDC) and N-Hydroxysuccinimide (NHS) (350 μmol) in N,N-Dimethylformamide (DMF) for 2 h under stirring. Afterwards, 2-Mercaptoethanol (863 μmol) was added to quench the reaction for 20 minutes. Either Lys-Ang-I or Lys-Ang-II ligand (17 μmol) were dissolved in DMF with N,N-Diisopropylethylamine (DIPEA) (66 μmol), added

Chapter 4: The Effect of Ligand Mobility on the Cellular Interaction

dropwise to the activated polymer, and left to stir for 48 h. The resulting polymer was diluted in Millipore water so that the DMF content was lower than 10% (v/v) and dialyzed using a 6-8 kDa molecular weight cut-off regenerated cellulose dialysis membrane (Spectrum Laboratories, Inc, Rancho Dominguez, CA, USA) for 24 h (with medium change after 30 minutes, 2, and 6 h) to remove uncoupled ligand and reagents. To determine the degree of ligand modification, polymer micelles were created by precipitating acetonitrile (ACN)-dissolved polymer in Millipore water under stirring to a final concentration of 1 mg mL⁻¹. After the complete evaporation of the organic phase, a Pierce BCA assay, following the manufacturer's instructions, and an iodine complexing colorimetric assay [25], as we previously described [16], were performed to quantify the ligand and PEG concentration, respectively (Figure S1).

2.4 NP preparation

For preparation of block copolymer NPs, 10 mg mL⁻¹ of either COOH-PEG_{2k}-PLA_{10k} or COOH-PEG_{5k}-PLA_{10k} (for NP_{2/510} or NP_{5/510}, respectively) and PLGA_{13.4k} were mixed in ACN at a 70:30 mass ratio. NPs were prepared *via* bulk nanoprecipitation under vigorous stirring in 10% Dulbecco's Phosphate Buffered Saline (DPBS) (v/v) (pH 7.4) to a final concentration of 1 mg mL⁻¹. The NPs were left stirring for 3 hours until the organic solvent was completely evaporated. Afterwards, they were concentrated using a 30kDa molecular weight cut-off Microsep advance centrifugal device (Pall Corporation, Port Washington, NY, USA) at 959 g for 20 minutes. For particles with different ligand densities, the unmodified carboxylic acid-ended polymers were replaced by varying amounts of Ang-I/II-PEG_{5k}-PLA_{10k}, keeping the molar ratio of PEG chains to PLGA constant. For fluorescently-labelled NPs, a CF647- (for flow cytometry analysis) or tetramethylrhodamine (TAMRA)- (for CLSM experiments) covalently labelled PLGA, synthesized as described before by our group [16], was used for NP preparation.

2.5 NP characterization

Size and ξ -potential of all NP formulations were measured using a Malvern ZetaSizer Nano ZS (Malvern Instruments GmbH, Lappersdorf, Germany) with a 633 nm He-Ne laser at a backscatter angle of 173°. Size was measured in disposable microcuvettes (Brand, Wertheim, Germany). Electrophoretic mobility was measured using a folded capillary cell (Malvern, Herrenberg, Germany) with a set measurement position at 4.65 mm. Data was recorded using the Malvern Zetasizer software 7.11 (Malvern Instruments, Worcestershire, United Kingdom). All samples were measured at 25 °C in 10% (v/v) DPBS (pH 7.4). PEG concentration in NPs was quantified using a

colorimetric iodine complexing assay [25] and correlated with the exact gravimetric NP content determined through lyophilization, as previously described by our group [16]. The molar NP concentration was calculated using Equation (1), where m is the NP mass determined through the iodine assay, ρ_{NP} is the density of the NPs (1.25 g cm^{-3}) [26], dh is the hydrodynamic diameter of the NPs measured by DLS, N_A is the Avogadro number and V is the volume of the NP samples.

$$PNC = \frac{m}{\rho_{NP} \frac{4}{3} \pi \left(\frac{dh}{2}\right)^3} \times \frac{1}{N_A V} \quad (1)$$

Ligand content on NPs was quantified using a BCA assay, using Lys-Ang-I and Lys-Ang-II as standards, following the manufacturer's instructions, and normalized to the molar PEG concentration to obtain the ligand density. Absorbance measurements were performed with a FLUOstar Omega microplate reader (BMG Labtech, Ortenber, Germany).

2.6 Intracellular calcium measurements

To quantify the AT1R response to the different NP formulations, a ratiometric Fura-2 Ca^{2+} chelator method [27] was used as previously described by our group [2]. In short, a rMC-suspension was incubated in Leibovitz medium (LM) supplemented with $5 \mu\text{M}$ Fura-2AM, 0.05% Pluronic F-127, and 2.5 mM Probenecid (1 hour, light protected, 50 rpm). The cells were washed with DPBS by centrifugation (2x, 200 g, 5 minutes) and adjusted to a count of either 2 or 1 million cells mL^{-1} (for IC50 or EC50 measurements, respectively) in LM with 2.5 mM Probenecid. To determine EC50 values (short stimulation) cells (90,000 cells) were injected on top of the samples ($10 \mu\text{L}$, 1 nM to 300 μM ligand concentration) and the resulting signal recorded immediately for 30 seconds per well using a FLUOstar Omega microplate reader. Filters used for excitation were 340/20 nm and 380/20 nm, and the emission was recorded with a 510/20 nm bandpass filter. To determine IC50 values (long stimulation), samples ($10 \mu\text{L}$, 1 nM to 300 μM ligand concentration) were incubated with 90,000 cells in a half-area microplate plate for 30 minutes. Afterwards, an Ang-II solution ($45 \mu\text{L}$, 300 nM) was injected on top of the samples and the calcium influx was measured as described above. 0.1% Triton-X 100 or 0.1% Triton-X 100 with 45 mM ethylene glycol-bis(2-aminoethylether)-N,N,N',N'-tetraacetic acid (EGTA) were used as control solutions to determine the maximal and minimal signal ratio (R_{max} and R_{min}). The intracellular calcium concentrations were calculated with an assumed K_d value of 255 nM for the Fura-2-calcium complex, after Grynkiewicz [27]. The maximum calcium signal (%) was plotted against the molar NP concentration, calculated after Equation (1), to allow

Chapter 4: The Effect of Ligand Mobility on the Cellular Interaction

comparison between formulations. Statistical significance was assessed by a Student's t test using GraphPad Prism 6.0 (GraphPad Software Inc. La Jolla, CA, USA).

2.7 Enzyme kinetic measurements

The Michaelis-Menten kinetics of the soluble form of ACE were determined using Ang-I bearing NP formulations as the substrate. To that end, the different NP formulations (ligand concentrations 10-200 μM) were incubated with rabbit lung ACE (18 μM) for different time periods (5, 15, 30, 60, 90 and 120 minutes). The conversion over time of Ang-I to Ang-II on the particle corona was quantified by measuring the intracellular calcium influx generated by the AT1R stimulation by the hydrolyzed substrate, as described above. A range of known concentrations of Ang-II (1 nM-300 μM) were used as control samples in the assay to convert the measured calcium concentration (nM) to pmol of product. The velocity of the reaction (pmol minutes^{-1}) at 15 minutes incubation time was plotted against the substrate concentration used in the assay to determine the Michaelis-Menten constant (K_m) using GraphPad Prism 6.0. The catalytic constant (K_{cat}) was determined and the specificity constant (K_{cat}/K_m) used to compare different substrates for one enzyme. A Student's t test was performed with GraphPad Prism 6.0 to assess statistical significance.

2.8 Flow cytometry

To determine the uptake rates of the different NP formulations *via* flow cytometry, rMCs were seeded in 24-well plates (30,000 cells per well) and incubated over 48 hours. Afterwards, they were incubated for 45 minutes with CF647-labelled NP solutions (20 $\mu\text{g mL}^{-1}$) in LM supplemented with 0.1% BSA. To inhibit the NP uptake, the cells were pre-incubated with either EXP3174 (1 mM) or chlorpromazine, genistein or cytochalasin D (25 μM) in LM for 30 minutes prior to NP addition. Next, the cells were washed with DPBS, trypsinized and washed through centrifugation with DPBS (2x, 200 g, 5 minutes, 4 °C). Lastly, the NP-associated cell fluorescence was analyzed using a CyFlow Space flow cytometer (Sysmex Partec GmbH, Goerlitz, Germany) with FloMax software. A 638 nm red diode laser was used to excite, and a 675/30 bandpass filter was used to record fluorescence. Data was analyzed using Flowing software (Turku Centre for Biotechnology, Finland). The population of viable cells was gated, and the fluorescence geometrical mean was evaluated. GraphPad Prism 6.0 was used to assess statistical significance through a Student's t-test.

2.9 Confocal laser scanning microscopy (CLSM) analysis

To analyze NP uptake using CLSM, rMCs were seeded into 8-well Nunc™ Lab Tech™ II Chamber Slide™ systems (Thermo Fisher Scientific, Waltham, MA, USA) (10,000 cells per well) and left to attach for 24 hours. After that, the cells were washed with DPBS and incubated with TAMRA-labelled NPs (20 µg mL⁻¹) in LM supplemented with 0.1% BSA for 45 minutes. After the incubation period, the NP solutions were discarded, and the cells were washed with DPBS and stained fluorescently with CMDR (1x) for 5 minutes before fixing them with 4% paraformaldehyde in DPBS (10 minutes, r.t.). To inhibit the NP uptake, the cells were pretreated with EXP3174 (1 mM) in LM with 0.1% BSA for 30 minutes prior to NP addition. Images were acquired with AIM4.2 software (Zeiss, Jena, Germany) using a Zeiss Axiovert 200 microscope with an LSM 510 laser-scanning device using a 63x Plan-Apochromat (NA 1.4) objective. Fluorescence was excited with 543 nm and 633 nm He-Ne lasers and recorded with a 560-615 bandpass and a 650 longpass filter (for NP and cell fluorescence, respectively). The focal plane was set at 1.5 µm.

2.10 Calculation of the distance between PEG chains (D , D_s and ds)

The surface (S) that each PEG chain occupies on the NP was calculated after Gref *et al.* [12] using Equation (2) where M_{PEG} is the molecular weight of the PEG chains and f is the mass fraction of PEG in the blends of PEG-PLA. Subsequently the distance between PEG chains was determined through Equation (3), assuming that S is a circular area [28], and a homogeneous polymer distribution. The parameters used for the calculations are listed in Table S2. The R_F was calculated as an indicator of the arrangement of the PEG chains on the NP surface with Equation (4) where the length of a PEG monomer is $\alpha = 0.35$ nm and the number of monomers in one molecule (N) was determined by dividing the molecular weight of the PEG by the monomer molecular weight of 44 g mol⁻¹.

$$S = \frac{6 M_{PEG}}{dh N_A f \rho_{NP}} \quad (2)$$

$$D = 2 \left(\frac{S}{\pi} \right)^{\frac{1}{2}} \quad (3)$$

$$R_F = \alpha N^{\frac{3}{5}} \quad (4)$$

3 Results and Discussion

3.1 Ligand decorated NPs

Chapter 4: The Effect of Ligand Mobility on the Cellular Interaction

To study the effect of ligand mobility on the NP-cell interactions, we chose polymeric PEG-PLA NPs with a PLGA-stabilized hydrophobic core, to avoid size increases resulting from a stabilization with high molecular weight PLA [29]. Such NPs are well-known for their biocompatibility and high versatility, as the particle composition can be precisely tailored by combining different PEG-PLA block copolymers (Figure 1A). Additionally, they are readily prepared *via* bulk nanoprecipitation of organic polymer solutions in aqueous medium.

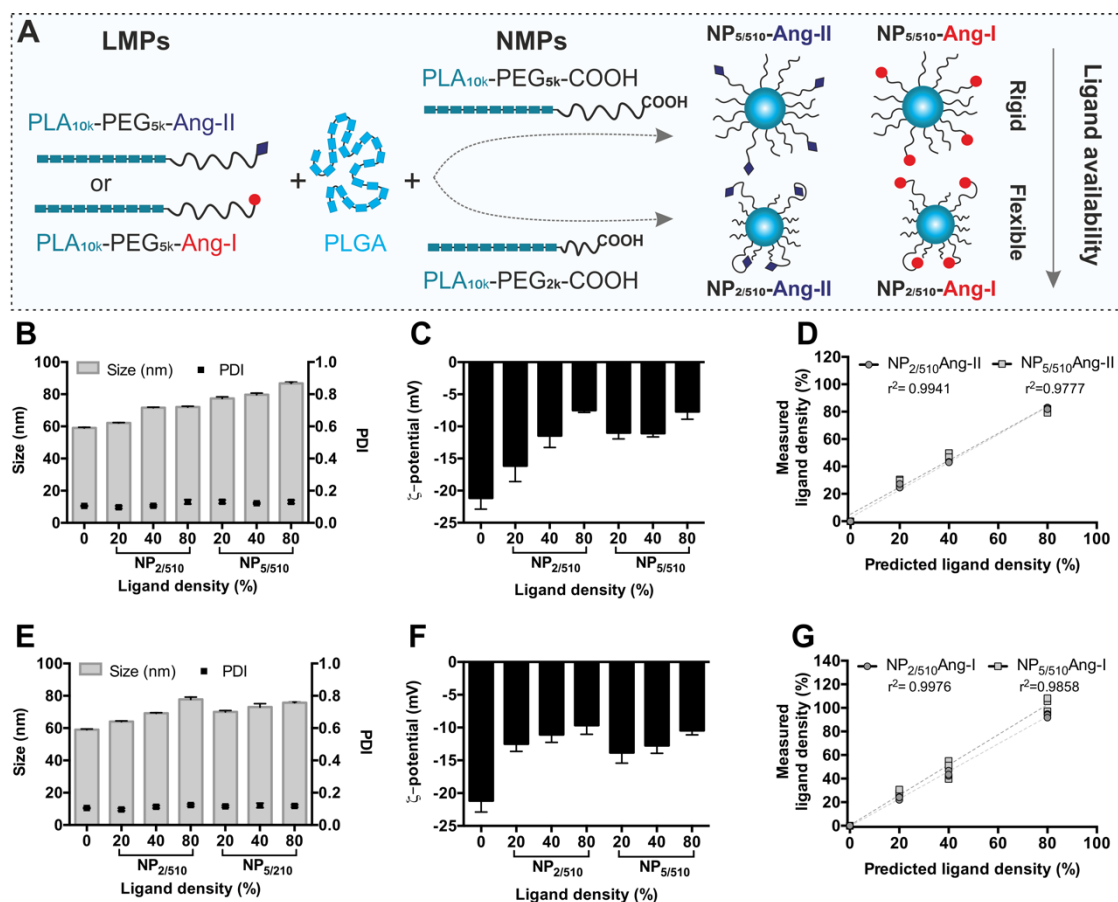


Figure 1. (A) Composition and characterization of (B)-(D) Ang-II and (E)-(G) Ang-I targeted NP formulations. Hydrodynamic diameter measured by (B), (E) DLS, (C), (F) ζ -potential, and (D), (G) correlation of the measured normalized molar ligand content and the predicted ligand density. Results are presented as mean \pm SD of at least $n = 3$ measurements.

We covalently coupled ligands to longer carboxylic acid-terminated PEG_{5k}-PLA_{10k} copolymers prior to NP preparation (Figure S1), which allows for precise control of the ligand density on the NP corona. NMPs were either the same length as the LMPs with carboxylic acid-ended PEG_{5k}-PLA_{10k} (COOH-PEG_{5k}-PLA_{10k}) or a shorter COOH-PEG_{2k}-PLA_{10k} to create NPs with homo- or heterogeneous polymer shells (NP_{5/510} or NP_{2/510}, respectively) with varying ligand densities (Figure S2). To impart specific recognition ability to our NPs, we chose to use two peptidic ligands that target a

receptor and/or a cell membrane-bound enzyme, Ang-II and Ang-I, respectively. Ang-II is known for its high-affinity to the AT1R [30], which upon binding is responsible for receptor-mediated endocytosis [31]. Ang-I is a substrate for ACE [32], which we recently used to develop highly specific virus-mimetic NPs [22]. The binding of Ang-I-decorated NPs to the cell membrane-bound ACE results in the excision of the last two amino acids of the peptide, generating Ang-II-carrying NPs that are internalized through AT1R-mediated endocytosis. To minimize any possible interference on the NP-cell interaction [33], the polymers were chosen to keep the particles in a narrow size range (60-80 nm) (Figure 1B and 1E). The resulting particles carried a negative surface charge that decreased in absolute value with increasing ligand content on the particle surface (Figure 1C and 1F) due to decreasing numbers of carboxylic acid-terminated NMPs. Creating NPs with negative surface charges is a great method of avoiding non-specific attachment to the negative cell membrane. To evaluate the effect of ligand density on the particle-cell interaction, NPs with low (20%), medium (40%) and high (80%) ligand densities were prepared. Since polymer-ligand coupling occurred prior to particle preparation, the predicted ligand density correlated well with the actual ligand density measured after particle preparation (Figure 1D and 1G).

3.2 AT1R-binding of Ang-II carrying NPs

To determine the effect that ligand mobility exerts on the AT1R interaction and the NP's overall avidity, NP_{2/510} and NP_{5/510} functionalized with Ang-II (NP_{2/510}Ang-II and NP_{5/510}Ang-II, respectively) carrying 20, 40, or 80% ligand densities were prepared. The affinities of the particle-bound ligands and avidities of the resulting formulations towards the AT1R after a short NP-cell contact were evaluated using a calcium mobilization assay (Figure 2) with AT1R-expressing rMCs [22], as previously described by our group [22, 34]. Under normal conditions, rMCs express high levels of the AT1R, of about $1,185 \pm 83$ fmol mg⁻¹ protein [35]. The stimulation of the Gq-coupled AT1R by an agonist results in a cytosolic Ca⁺² influx that is measured by this assay [31]. It is known that the binding of ligands to polymers like PEG reduces their affinity towards their target receptor [2] (Figure S3A). Interestingly, the coupling of Ang-II to COOH-PEG_{5k}-PLA_{10k} resulted in even higher affinity loss than that measured for the PEGylated form. However, this is compensated through an avidity gain of NPs prepared from the aforementioned polymer (Figure S3B), as they enable multivalent binding of the ligands to the cell membrane-bound receptors. The avidity of the particles (determined through the EC₅₀ values obtained based on particle concentration (PNC-EC₅₀)), was in the same nanomolar range for both particle types (Figure 2). However, there were notable differences between the two formulations regarding the effect of ligand density. While the avidity of NP_{2/510} significantly

Chapter 4: The Effect of Ligand Mobility on the Cellular Interaction

increased with higher functionalization (Figure 2A), it remained constant for NP_{5/510} (Figure 2B), even though the number of ligands per NP increased with the ligand density in both particle types (Figure S4). This suggests that the rigid composition due to long NMPs of NP_{5/510} hinders subsequent ligand-receptor interactions with increasing numbers of available ligands. This is reinforced by the fact that the overall affinity of the particle-bound ligands (LC-EC50) remained equal independent of the NP composition (Figure 2C and 2D). As the only parameter affecting multivalency varied between the formulations is the ligand mobility, the differences in avidity of NP_{2/510} is most likely a result of the shorter NMPs.

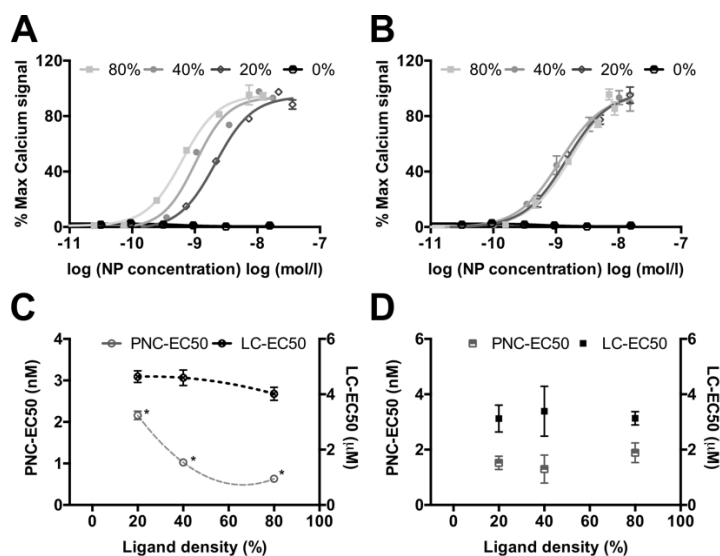


Figure 2. AT1R stimulation by Ang-II decorated NPs in rMCs. Maximum intracellular calcium response of (A) NP_{2/510}Ang-II and (B) NP_{5/510}Ang-II with different ligand densities. Particle avidity and ligand affinity of (C) NP_{2/510}Ang-II and (D) NP_{5/510}Ang-II. PNC-EC50 (EC50 values calculated based on NP concentration); LC-EC50 (EC50 values calculated based on particle-bound ligand concentration). Results are presented as mean \pm SD of at least $n = 3$ measurements. The data in c) are fitted with a second-order polynomial. Levels of statistical significance are indicated as * $p < 0.001$ comparing PNC-EC50 values at different ligand densities.

However, in these experiments the NP-cell contact is very brief (under 1 minute). As NPs are much larger than free ligands, they experience diminished diffusion, and thus require an extended presentation time to effectively interact with their targets. To investigate NP-cell interactions over a longer timescale, specifically how the avidity of NP_{2/510}Ang-II for the AT1R is affected, we extended the incubation period of the NPs with cells to 30 minutes (Figure 3) and determined the NP avidity (PNC-IC50) (Figure 3A) and the particle-bound ligand affinity (LC-IC50) (Figure 3B). After extensive NP-cell contact, the avidity of NP_{2/510}Ang-II increased (Figure 3A). However, this increase was only significant for particles with low (20%) ligand densities, i.e. highest ligand mobilities (Figure 3A). The particle-bound ligands also displayed increased affinities (IC50) for the AT1R compared to the ones obtained after a short stimulation (EC50)

(Figure 3B) and the highest increase was also seen for NP_{2/510} at low ligand densities (20%) (Figure 3B). These results indicate that a higher ligand mobility leads to a slower NP-cell interaction which can be explained by a lower number of ligands on the particle corona [6], which necessitate extra time to execute binding. Additionally, reversible entrapment of the ligands in the polymer chains may occur [36], impairing rapid ligand-receptor interactions. This phenomenon is more probable in NPs with low grafting densities [37] and long polymer chains [38]. The slower interactions of flexible particles may show potential benefits *in vivo* where NPs face extensive circulation times and, more importantly, off-target cells. As the selectivity of a multivalent system can be increased if initial binding is impeded by a repulsive factor [9], the delayed initial binding of particles with high ligand mobility (NP_{2/510} 20% ligand) (Figure 2 and 3) may be an alternative to the suggested approach of adding sterically hindering polymer chains [39]. Additionally, the inclusion of extra polymers, which can hinder the subsequent targeting efficiency, would be circumvented by this design. However, this needs to be further investigated in future experiments.

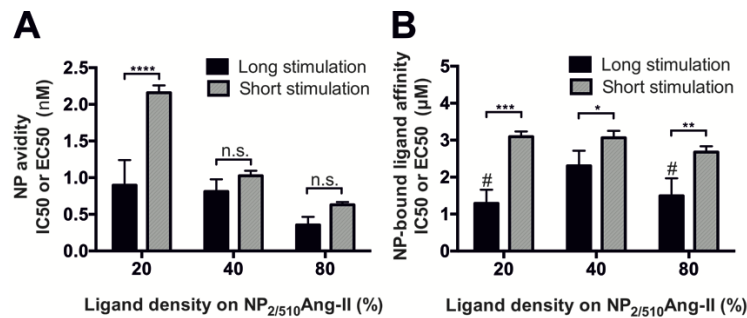


Figure 3. Influence of the AT1R stimulation period on the (A) particle avidity (B) and particle-bound ligand affinity of NP_{2/510}Ang-II. A short (1 minute) direct stimulation of rMCs with the particles yields a dose response curve where the EC50 values can be calculated. By pre-incubating the cells with the NPs (30 minutes) and treating them afterwards with free Ang-II, the IC50 values can be determined. Results are presented as mean \pm SD of at least $n = 3$ measurements. Levels of statistical significance are indicated as * $p \leq 0.05$, ** $p \leq 0.01$, *** $p \leq 0.001$, and **** $p \leq 0.0001$, and # $p \leq 0.05$ compared to particle-bound ligand affinity at 40% ligand density n.s.: non-significant.

3.3 ACE kinetics using Ang-I decorated NPs as substrates

To explore the effect of ligand availability on the multivalent binding abilities towards an alternative target, we selected Ang-I-decorated NPs that interact with the cell membrane-bound ACE [22]. NPs with 20, 40, or 80% Ang-I modified PEG_{5k}-PLA_{10k} were prepared, with particle coronas made up of either short COOH-PEG_{2k}-PLA_{10k} or long COOH-PEG_{5k}-PLA_{10k} NMPs (NP_{2/510}Ang-I and NP_{5/510}Ang-I, respectively). Soluble ACE obtained from rabbit lung served as a surrogate for the cell membrane-bound form of the enzyme to determine the Michaelis-Menten kinetics for the different

Chapter 4: The Effect of Ligand Mobility on the Cellular Interaction

particles (Figure 4). The Michaelis-Menten constant (K_m) was calculated based on the ligand (Figure 4A and 4B) and particle concentrations (Figure 4C and 4D) for the different NP formulations (Table S1). Additionally, the catalysis constant (K_{cat}) was determined to calculate the specificity constant (K_{cat}/K_m), which is useful in comparing different substrates for the same enzyme [40] (Figure 4E and 4F). The substrate that yields the highest specificity constant is considered the best substrate for the enzyme. At all ligand densities, the K_{cat}/K_m values for NP_{2/510} were significantly higher than those for NP_{5/510}, for both ligand- (Figure 4E) and NP concentration-based (Figure 4F) calculations. This suggests that the ligands on their surface are better accessible to the enzyme, which can be attributed to the shorter NMPs. For both NP_{2/510} and NP_{5/510}, the affinity for the enzyme increases with higher ligand density, probably due to a higher number of ligand molecules on the NP surface (Figure S4) that are able to bind more enzyme molecules. Nevertheless, because a soluble form of ACE was used for the experiments, the ligand-enzyme interaction is not spatially constrained as it would be with the cell membrane-bound enzyme and cannot fully illustrate the multivalent binding on a cellular surface.

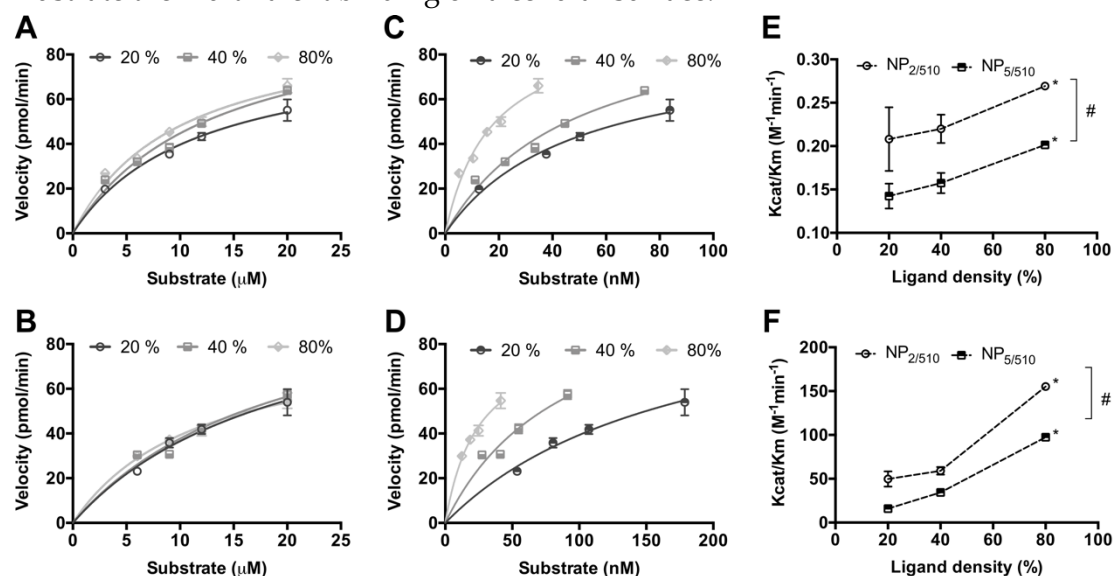


Figure 4. Michaelis-Menten kinetics of Ang-I decorated NPs. Enzyme kinetics calculated based on ligand concentrations of (A) NP_{2/510}Ang-I and (B) NP_{5/510}Ang-I, or NP concentrations of (C) NP_{2/510}Ang-I and (D) NP_{5/510}Ang-I at different ligand densities. Specificity constant (K_{cat}/K_m) of NP_{2/510} and NP_{5/510} calculated with the (E) ligand- or (F) NP concentration-based K_m . Results are presented as mean \pm SD of at least $n = 3$ measurements. Levels of statistical significance are indicated as * $p \leq 0.05$ comparing NPs with 80% ligand density to NPs with 20 or 40% ligand density and # $p \leq 0.005$ comparing NP_{2/510} and NP_{5/510}.

3.4 Cellular internalization of AT1R-targeting NPs

To determine the influence of ligand mobility at a cellular level we performed uptake experiments (Figure 5) analyzed *via* flow cytometry (Figure 5A) and CLSM (Figure 5B). rMCs, positive for AT1R expression, were used as target cells [22]. Considerable differences could be detected between Ang-II decorated NP_{2/510} and NP_{5/510}. In agreement with our previous experiments, uptake was noticeably dependent on ligand density for NP_{2/510}. However, lower ligand densities (20%) resulted in much better cellular internalization than medium- (40%) or high (80%) ligand densities, differing from what would be expected by the AT1R-avidity measurements performed at short stimulation periods (Figure 2). These divergencies can be explained by the fact that for NP uptake the cells are incubated for longer time periods (45 minutes) with the NPs. As can be seen for the avidity measurements after a long stimulation (Figure 3), the avidity of the particles evens out at all ligand densities. Additionally, it can be attributed to differences in experimental setup, as uptake experiments are performed with adherent cells, mimicking physiological conditions, and for the avidity measurements cells must be placed in suspension. Under such non-restrictive conformational conditions, receptor interactions at higher ligand densities may be favored.

NP_{5/510}-associated fluorescence was independent of the degree of functionalization, mirroring the AT1R avidity measured by the intracellular calcium assay described above. This indicates that a lower ligand mobility constrains the ligand-receptor interaction. When rMCs were incubated with an AT1R antagonist, losartan carboxylic acid (EXP3174), for 30 minutes, we observed significant suppression of uptake which suggests specificity. Overall, NP_{2/510} were taken up to a much higher extent than NP_{5/510}, demonstrating that shorter 2k NMPs that enhance the ligand mobility facilitate the NP-cell interaction. It points towards a better receptor binding, as higher internalization rates are usually related to enhanced multivalent binding [41]. With 80% ligand density, the uptake of NP_{2/510} matches that of NP_{5/510}, as the particles assimilate, and the ligands lose mobility due to an increase in long LMPs. At 80% ligand density, 80% of the PEG on the particle surface is long 5k PEG, and only the remaining 20% is the shorter 2k for NP_{2/510} or longer 5k PEG for NP_{5/510}. With this polymer composition, it seems that the favorable effects of shorter NMPs are lost, as there are majority of longer polymer chains hindering the ligand binding. These results highlight the importance of ligand mobility to obtain satisfactory cellular interaction. Contrary to common assumptions that increasing the degree of functionalization increases the targeting potential of NPs, here we demonstrate that the amount of ligand present on the surface is not as important as its mobility, i.e., the conformational flexibility that allows it to interact with the target receptors. Similar effects were

Chapter 4: The Effect of Ligand Mobility on the Cellular Interaction

described by Poon, *et al.* for folate-functionalized particles. They noticed that increasing the surface coverage over the optimal 20% lead to less efficient NP uptake [42]. Furthermore, an increase in ligand density usually reduces the targeting potential due to enhanced serum protein adsorption resulting from covering the PEG shield with ligands. Minimizing protein corona formation is essential to preserve the specific targeting abilities of nanomaterials [43] and avoid their clearance by macrophages [44]. For our formulations, significantly higher serum protein adsorption was observed for rigid NP_{5/510} compared to flexible NP_{2/510} (Figure S5). This seems to corroborate our assumption that LMPs on flexible particles can assume a partially folded conformation, which initially may shield the ligand. This trend is enhanced with lower particle functionalization.

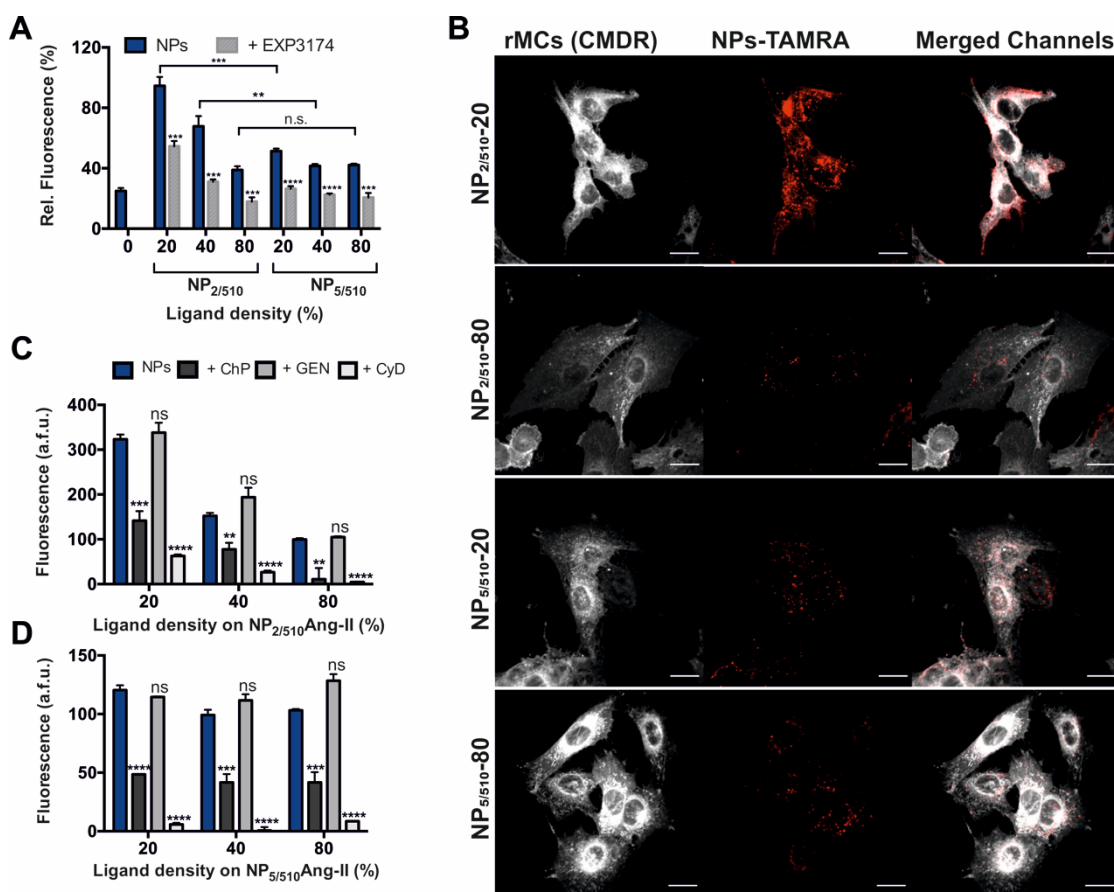


Figure 5. Cellular internalization of NP_{2/510}Ang-II and NP_{5/510}Ang-II in rMCs. (A) Uptake of NPs with different ligand densities and uptake inhibition by free EXP3174 analyzed by flow cytometry. (B) Uptake of NP_{2/510}Ang-II and NP_{5/510}Ang-II with 20 or 80% ligand density analyzed by CLSM (Scale bar 20 μ m). Internalization inhibition of (C) NP_{2/510}Ang-II and (D) NP_{5/510}Ang-II by chlorpromazine (ChP), genistein (GEN) or cytochalasin D (CyD). Results are presented as mean \pm SD of at least $n=3$ measurements. Levels of statistical significance are indicated as ** $p \leq 0.005$, *** $p \leq 0.0005$, and **** $p \leq 0.0001$. n.s.: non-significant.

Intracellular localization of the NPs was confirmed by CLSM analysis (Figure 5B). For microscopy experiments, only particles with low (20%) and high (80%) ligand densities were investigated. NPs with medium (40%) ligand density were not examined because minor differences between particle types are difficult to discern by this method. The results mirrored those obtained by flow cytometry. The highest NP-associated fluorescence was seen for NP_{2/510} with 20% ligand on the surface. At 80% ligand density, uptake of NP_{2/510} is comparable to that of NP_{5/510}, which shows no dependency with the ligand density. The uptake could be inhibited by EXP3174 treatment of cells prior to NP addition (Figure S6).

To investigate if ligand mobility influences the internalization pathway of Ang-II functionalized NPs, we performed uptake inhibition studies by pre-incubating the cells with either chlorpromazine, genistein, or cytochalasin D (clathrin, caveole or actin polymerization inhibitors, respectively) prior to NP addition. As shown in Figure 5C and 5D, adding chlorpromazine significantly inhibited uptake of Ang-II carrying NPs by about 60-80%. This level of inhibition was similar to that caused by EXP3174, indicating that particles are mainly taken up by specific clathrin-mediated endocytosis. We previously found the same uptake pathway for Ang-II decorated quantum dots [34]. Genistein did not affect NP uptake, indicating that it is not caveolae-mediated. As expected, Cytochalasin D caused the highest uptake inhibition, as it is able to inhibit both non-specific particle uptake as well as interfere with other endocytic routes like clathrin-mediated endocytosis by disrupting the cell cytoskeleton [45, 46]. Regarding the internalization route, no differences could be detected between the different formulations, indicating that increased ligand mobility just enhances the multivalent binding of the receptor, without changing the natural endocytic route.

3.5 Cellular internalization of Ang-I decorated NPs

To determine the influence of ligand mobility on the uptake of enzyme targeting particles, we also determined the cellular uptake of ACE-targeting Ang-I decorated NPs (NP_{2/510}Ang-I and NP_{5/510}Ang-I) (Figure 6), *via* flow cytometry (Figure 6A) and CLSM (Figure 6B) in rMCs [22]. Ang-I is a substrate for ACE and when it is located on the particle corona it binds to the enzyme on the cell membrane. This results in the production of Ang-II on the particle surface and the NPs can then be internalized by AT1R-mediated endocytosis [22]. Interestingly, the uptake results for Ang-I decorated NPs mirrored the results for Ang-II decorated NPs. Higher uptake was obtained for NP_{2/510} compared to NP_{5/510}, which decreased with increasing ligand density. The specificity of uptake *via* the AT1R was proven by the significant suppression observed after addition of captopril, an ACE inhibitor (Figure 6A). The similarity between the uptake of Ang-I and Ang-II decorated NPs indicates that the initial conversion of Ang-

Chapter 4: The Effect of Ligand Mobility on the Cellular Interaction

I on the particle surface is not a limiting factor for particle internalization. Furthermore, when comparing the uptake kinetics of Ang-I and Ang-II decorated NPs, equivalent results were obtained (Figure 6C and 6D). Because the enzymatic conversion of Ang-I to Ang-II occurs rapidly on the rMC surface ($2 \text{ pmol minute}^{-1}$) [22], it does not limit cellular uptake as much as multivalent AT1R binding. Under these experimental conditions, the Ang-I on the particle surface is converted to Ang-II in less than 1 minute by the cells. With a 45-minute incubation period, this leaves the particles enough time to interact with the AT1R. Additionally, the higher uptake of Ang-I modified NP_{2/510} is favored by the higher affinity of the ligands to the enzyme (Figure 4), which keeps them at the cell surface facilitating subsequent receptor binding. Equivalent results were obtained by CLSM analysis (Figure 6B and Figure S7), which confirmed intracellular localization of NPs.

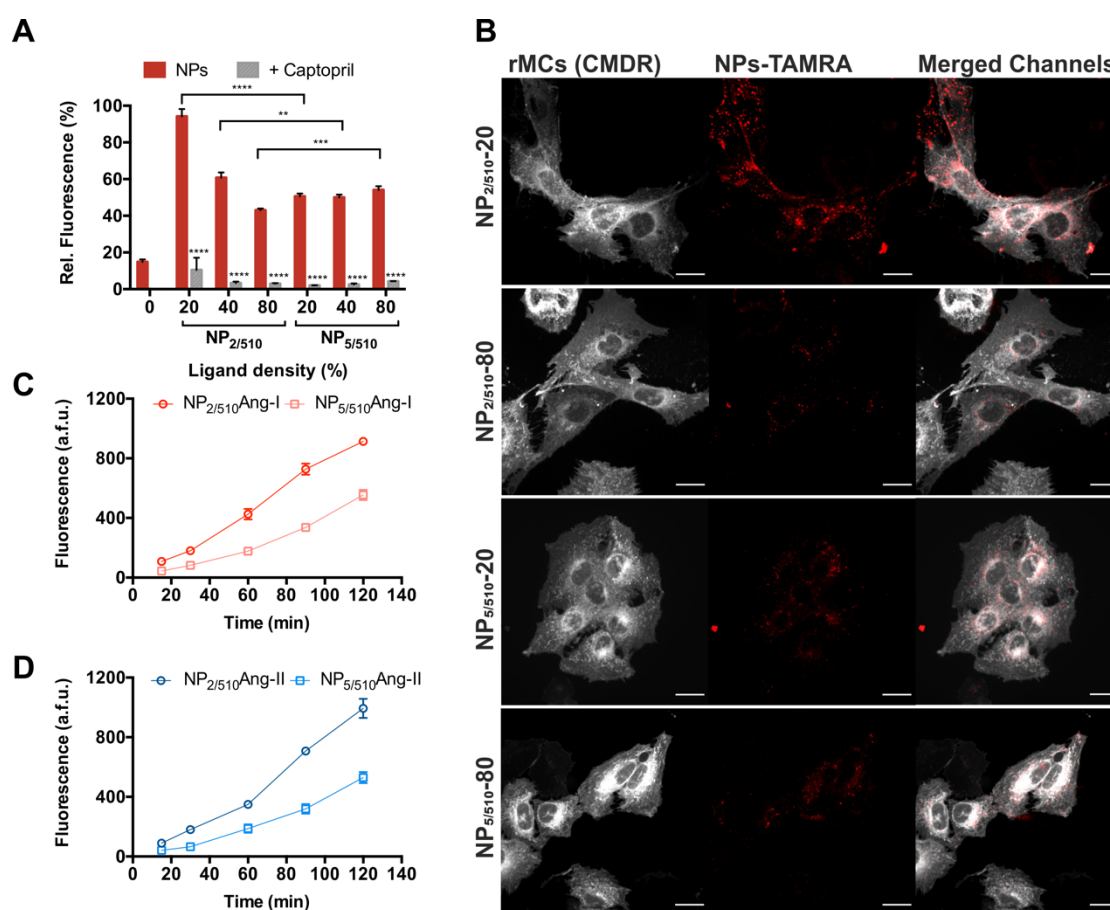


Figure 6. Cellular internalization of NP_{2/510}Ang-I and NP_{5/510}Ang-I in rMCs. (A) Cellular uptake of NPs with different ligand densities and internalization inhibition by 1 mM captopril analyzed by flow cytometry. (B) Uptake of NP_{2/510}Ang-I and NP_{5/510}Ang-I with 20 or 80% ligand density analyzed by CLSM (Scale bar 20 μm). Internalization kinetics of (C) Ang-I or (D) Ang-II functionalized NP_{2/510} and NP_{5/510} with 20% ligand density. Results are presented as mean \pm SD of at least n=3 measurements. Levels of statistical significance are indicated as ** $p \leq 0.005$, *** $p \leq 0.0005$ and **** $p \leq 0.0001$.

3.6 Polymer distribution on the NP shell: Conformational considerations and distance between PEG chains.

To explain the differences between the NP formulations regarding interaction with their targets, we estimated the distance between the PEG chains on the particle corona. The theoretical distance between the polymer chains on a particle corona for a known NP diameter and polymer molecular weight can be calculated assuming that all the PEG from the PEG-PLA block-copolymer migrates to the outer NP shell and the PLA blocks are anchored in the core [12] (please refer to the experimental section for an exact explanation of the calculation). In this way we determined the distance between NMPs (ds), LMPs (D), and LMPs and the next same-length polymer (Ds) (Figure 7 and Table S2). The ds values for NP_{2/510} and NP_{5/510} are comparable, as the total polymer in both formulations is the same and increases with the ligand density (Figure 7B). D also follows the same trend for the two NP formulations, with decreasing distances at higher LMP content (Figure 7C). Nevertheless, when Ds is calculated, significant differences between the two NP species are detected (Figure 7D). For NP_{5/510}, Ds remains constant, independent of the amount of ligand that the particles carry, because all the polymer chains are exactly the same length. For NP_{2/510}, there is a significant decrease in Ds as more, longer LMP chains are added to the formulation. Furthermore, there is a significantly higher Ds for all ligand densities compared to NP_{5/510}, due to the shorter NMPs. This indicates that the ligands have higher mobility freedom and are less sterically hindered on NP_{2/510} than on NP_{5/510}. As the particles assimilate to NP_{5/510} at higher ligand densities this distance diminishes, and the particles become more rigid. Depending on the size of the target receptor or enzyme, the distance between ligands can highly influence the outcome of an interaction, as not all ligands may be able to bind. According to Erickson, the approximate radius of a protein in nm can be calculated assuming a spherical shape and an average specific volume of 0.73 cm³ g⁻¹ [47]. The AT1R is a protein composed of 359 amino acids with a molecular weight of approximately 41 kDa [48]. The ACE has a molecular weight of 112 kDa [49]. Under the aforementioned assumptions, the diameters of the AT1R and ACE would be approximately 4.6 and 6.4 nm, respectively. According to this, only the flexible particles (NP_{2/510}) with low ligand density would be able to bind several targets in a multivalent manner (Figure 7D). At higher degrees of functionalization, the distance between consecutive ligands is smaller than the one between targets, leading to inefficient binding where some ligands may lose their targeting capacity and sterically hinder each other. For rigid NPs (NP_{5/510}), the long NMPs can also limit the LMP mobility and prevent the ligands from interacting with their targets. This explains the superior NP-cell interaction displayed by NP_{2/510} (Figure 5 and 6), where the ligands have a higher conformational freedom to bind their targets, a trait conferred by the shorter NMPs. To further confirm the arrangement of the PEG chains on the

Chapter 4: The Effect of Ligand Mobility on the Cellular Interaction

particle surface, the Flory radius (R_F) was calculated. If the distance between polymer chains is greater than R_F , the polymers assume a folded mushroom configuration. When R_F is greater than the distance between polymer chains, they adopt an extended brush conformation [36]. The R_F values calculated for the 2k and 5k PEGs were 3.60 and 6.06 nm. For all NP formulations, the distances between the PEG chains on the particle surface were less than the R_F (Figure S8), suggesting a brush conformation. For the low ligand density $NP_{2/510}$ the distance between LMPs is over the R_F value of 2k PEG but under that for 5k PEG. Taken all together, this can explain the higher mobility and flexibility of the LMPs at lower ligand densities in $NP_{2/510}$, for which there could be a partially folded configuration that would make interactions of such particles slower but more efficient regarding binding and its subsequent cellular uptake.

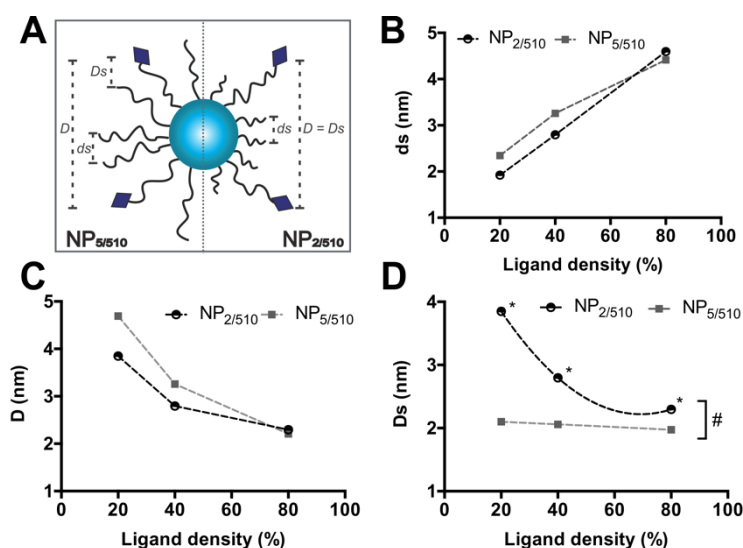


Figure 7. Distance between polymer chains on the NP corona at different ligand densities. (A) Schematic representation of the distance among polymer chains on $NP_{2/510}$ and $NP_{5/510}$. (B) Distance ds between NMPs, (C) distance D between ligand-modified polymer chains and (D) distance Ds between ligand-modified polymer and the same length PEG chains. Results are presented as mean \pm SD of at least $n = 3$ calculations derived from at least $n = 3$ independent size measurements. The data in (D) were fitted with a second-order polynomial. Levels of statistical significance are indicated as $*p \leq 0.0001$ comparing $NP_{2/510}$ with 20, 40, and 80% ligand densities and $\#p \leq 0.0001$ comparing $NP_{2/510}$ and $NP_{5/510}$ at different ligand densities.

4 Conclusions

The establishment of multivalent interactions between NPs and their target cells is a complex multifactorial process. Different particle attributes, such as size or ligand-type and density [5] are essential for determining the binding avidity. However, our

work suggests that a high particle avidity for the targeted receptors does not unequivocally predict a particle's fate after binding.

In this study, we demonstrated that by tailoring the polymer composition on the particle corona, the ligand mobility, and in turn the cellular uptake of NPs can be modulated. By combining polymers of different lengths, we were able to design particles with high polymer density, which is essential for stealth properties [50], while still preserving the mobility of the tethered ligands. We showed that flexible particles (NP_{2/510}) with the highest ligand mobility (at 20% ligand density) even though partially subjected to ligand shrouding have analogous avidities for their targets to their rigid counterparts (NP_{5/510}) which present more surface-available but sterically hindered ligands. More so, after extensive cellular contact the interactions with the targets are facilitated and thus, the particles' avidities and particle-bound ligand affinities significantly increased. Furthermore, flexible particles experience increased cellular uptake due to the optimal distance between targeting entities along with a higher ligand mobility. Interestingly, increasing the ligand density did not result in higher targeting ability of the NPs, due to a sterically hindered, inefficient target binding. Thus, it is advisable to avoid overloading NPs with ligands, which can potentially lead to less selective binding [8, 9], and instead adjust the ligand mobility. The initial ligand shrouding should be further investigated, as it may have the potential to reduce initial binding, a strategy suggested to increase particle selectivity [9, 39]. In this regard, the relationship of the formulation's avidity and binding with the receptor density would need to be elucidated. It is reasonable to believe that higher receptor densities may lead to increased cellular interactions. A phenomenon that becomes more important for formulations with more flexible coronae, since the likelihood of binding increases [8].

Taken together, our results show that designing of multivalently-binding NPs is an intricate process which necessitates finding a balance between several particle attributes. Among them, we show that the ligand mobility, which can be increased by adjusting the polymer corona composition and the number of targeting entities on the particle surface, needs to be considered to achieve optimal interactions at the cellular level.

References

- [1] Allen TM, Cullis PR. Drug delivery systems: entering the mainstream. *Science* 2004; 303: 1818–22.
- [2] Hennig R, Pollinger K, Veser A, et al. Nanoparticle multivalency counterbalances the ligand affinity loss upon PEGylation. *J Control Release* 2014; 194: 20–27.
- [3] Hong S, Leroueil PR, Majoros IJ, et al. The Binding Avidity of a Nanoparticle-Based Multivalent Targeted Drug Delivery Platform. *Chem Biol* 2007; 14: 107–115.
- [4] Elias DR, Poloukhine A, Popik V, et al. Effect of ligand density, receptor density, and nanoparticle size on cell targeting. *Nanomedicine* 2013; 9: 194–201.
- [5] Alkilany AM, Zhu L, Weller H, et al. Ligand density on nanoparticles: A parameter with critical impact on nanomedicine. *Adv Drug Deliv Rev* 2019; 143: 22–36.
- [6] Yuan H, Zhang S. Effects of particle size and ligand density on the kinetics of receptor-mediated endocytosis of nanoparticles. *Appl Phys Lett* 2010; 96: 033704.
- [7] Dalal C, Saha A, Jana NR. Nanoparticle Multivalency Directed Shifting of Cellular Uptake Mechanism. *J Phys Chem C* 2016; 120: 6778–6786.
- [8] Tjandra KC, Thordarson P. Multivalency in Drug Delivery—When Is It Too Much of a Good Thing? *Bioconjug Chem* 2019; 30: 503–514.
- [9] Curk T, Dobnikar J, Frenkel D. Design principles for super selectivity using multivalent interactions. In: *Multivalency: Concepts, Research and Applications*. Hoboken, NJ: Wiley, pp. 75–102.
- [10] Kitov* PI, Bundle DR. On the Nature of the Multivalency Effect: A Thermodynamic Model. *J Am Chem Soc* 2003; 125: 16271–16284.
- [11] Klibanov AL, Maruyama K, Torchilin VP, et al. Amphipathic polyethyleneglycols effectively prolong the circulation time of liposomes. *FEBS Lett* 1990; 268: 235–237.
- [12] Gref R, Lück M, Quellec P, et al. ‘Stealth’ corona-core nanoparticles surface modified by polyethylene glycol (PEG): influences of the corona (PEG chain length and surface density) and of the core composition on phagocytic uptake and plasma protein adsorption. *Colloids Surfaces B Biointerfaces* 2000; 18: 301–313.
- [13] Owens Iii DE, Peppas NA. Opsonization, biodistribution, and pharmacokinetics of polymeric nanoparticles. *Int J Pharm* 2006; 307: 93–102.

-
- [14] Cruz LJ, Tacke P, Fokkink R, et al. The influence of PEG chain length and targeting moiety on antibody-mediated delivery of nanoparticle vaccines to human dendritic cells. *Biomaterials* 2011; 32: 6791–6803.
- [15] Stefanick JF, Ashley JD, Kiziltepe T, et al. A Systematic Analysis of Peptide Linker Length and Liposomal Polyethylene Glycol Coating on Cellular Uptake of Peptide-Targeted Liposomes. *ACS Nano* 2013; 7: 2935–2947.
- [16] Abstiens K, Gregoritz M, Goepferich AM. Ligand Density and Linker Length are Critical Factors for Multivalent Nanoparticle–Receptor Interactions. *Appl Mater Interfaces* 2019; 11: 1311–1320.
- [17] Jiang W, Kim BYS, Rutka JT, et al. Nanoparticle-mediated cellular response is size-dependent. *Nat Nanotechnol* 2008; 3: 145–150.
- [18] Liu Y, Li K, Pan J, et al. Folic acid conjugated nanoparticles of mixed lipid monolayer shell and biodegradable polymer core for targeted delivery of Docetaxel. *Biomaterials* 2009; 31: 330–338.
- [19] Gref R, Couvreur P, Barratt G, et al. Surface-engineered nanoparticles for multiple ligand coupling. *Biomaterials* 2003; 24: 4529–4537.
- [20] Zhao P, Wang H, Yu M, et al. Paclitaxel loaded folic acid targeted nanoparticles of mixed lipid-shell and polymer-core: In vitro and in vivo evaluation. *Eur J Pharm Biopharm* 2012; 81: 248–256.
- [21] Rungta A, Natarajan B, Neely T, et al. Grafting Bimodal Polymer Brushes on Nanoparticles Using Controlled Radical Polymerization. *Macromolecules* 2012; 45: 9303–9311.
- [22] Maslanka Figueroa S, Veser A, Abstiens K, et al. Influenza A virus mimetic nanoparticles trigger selective cell uptake. *Proc Natl Acad Sci* 2019; 116: 9831–9836.
- [23] Qian H, Wohl AR, Crow JT, et al. A Strategy for Control of “Random” Copolymerization of Lactide and Glycolide: Application to Synthesis of PEG-*b*-PLGA Block Polymers Having Narrow Dispersity. *Macromolecules* 2011; 44: 7132–7140.
- [24] Abstiens K, Maslanka Figueroa S, Gregoritz M, et al. Interaction of functionalized nanoparticles with serum proteins and its impact on colloidal stability and cargo leaching. *Soft Matter* 2019; 15: 709–720.
- [25] Childs CE. The determination of polyethylene glycol in gamma globulin solutions. *Microchem J* 1975; 20: 190–192.
- [26] Rabanel J-M, Faivre J, Tehrani SF, et al. Effect of the Polymer Architecture on

Chapter 4: The Effect of Ligand Mobility on the Cellular Interaction

- the Structural and Biophysical Properties of PEG-PLA Nanoparticles. *ACS Appl Mater Interfaces* 2015; 7: 10374–10385.
- [27] Grynkiewicz G, Poenie M, Tsien RY. A New Generation of Ca²⁺ Indicators with Greatly Improved Fluorescence Properties*. *J Biol Chem* 1985; 260: 3440–3450.
- [28] Damodaran VB, Fee CJ, Ruckh T, et al. Conformational Studies of Covalently Grafted Poly(ethylene glycol) on Modified Solid Matrices Using X-ray Photoelectron Spectroscopy. *Langmuir* 2010; 26: 7299–7306.
- [29] Yang ZL, Li XR, Yang KW, et al. Amphotericin B-loaded poly(ethylene glycol)-poly(lactide) micelles: Preparation, freeze-drying, and in vitro release. *J Biomed Mater Res Part A* 2008; 85A: 539–546.
- [30] Bosnyak S, Jones ES, Christopoulos A, et al. Relative affinity of angiotensin peptides and novel ligands at AT₁ and AT₂ receptors. *Clin Sci* 2011; 121: 297–303.
- [31] de Gasparo M, Catt KJ, Inagami T, et al. International Union of Pharmacology. XIII. The angiotensin II receptors. *Pharmacol Rev* 2000; 52: 415–472.
- [32] Coates D. The angiotensin converting enzyme (ACE). *Int J Biochem Cell Biol* 2003; 35: 769–773.
- [33] Jiang W, Kim BYS, Rutka JT, et al. Nanoparticle-mediated cellular response is size-dependent. *Nat Nanotechnol* 2008; 3: 145–150.
- [34] Hennig R, Pollinger K, Tessmar J, et al. Multivalent targeting of AT₁ receptors with angiotensin II-functionalized nanoparticles. *J Drug Target* 2015; 23: 681–689.
- [35] Ballermann BJ, Skorecki KL, Brenner BM. Reduced glomerular angiotensin II receptor density in early untreated diabetes mellitus in the rat. *Am J Physiol* 1984; 247: F110–F116.
- [36] de Gennes PG. Polymers at an interface; a simplified view. *Adv Colloid Interface Sci* 1987; 27: 189–209.
- [37] Dos Santos N, Allen C, Doppen A-M, et al. Influence of poly(ethylene glycol) grafting density and polymer length on liposomes: Relating plasma circulation lifetimes to protein binding. *Biochim Biophys Acta - Biomembr* 2007; 1768: 1367–1377.
- [38] Abe K, Higashi K, Watabe K, et al. Effects of the PEG molecular weight of a PEG-lipid and cholesterol on PEG chain flexibility on liposome surfaces. *Colloids Surfaces A Physicochem Eng Asp* 2015; 474: 63–70.

- [39] Wang S, Dormidontova EE. Selectivity of Ligand-Receptor Interactions between Nanoparticle and Cell Surfaces. *Phys Rev Lett* 2012; 109: 238102.
- [40] Eisenthal R, Danson MJ, Hough DW. Catalytic efficiency and k_{cat}/K_M : a useful comparator? *Trends Biotechnol* 2007; 25: 247-249.
- [41] York SJ, Arneson LS, Gregory WT, et al. The rate of internalization of the mannose 6-phosphate/insulin-like growth factor II receptor is enhanced by multivalent ligand binding. *J Biol Chem* 1999; 274: 1164-71.
- [42] Poon Z, Chen S, Engler AC, et al. Ligand-Clustered "Patchy" Nanoparticles for Modulated Cellular Uptake and In Vivo Tumor Targeting. *Angew Chemie Int Ed* 2010; 49: 7266-7270.
- [43] Dai Q, Walkey C, Chan WCW. Polyethylene Glycol Backfilling Mitigates the Negative Impact of the Protein Corona on Nanoparticle Cell Targeting. *Angew Chemie Int Ed* 2014; 53: 5093-5096.
- [44] Dai Q, Wilhelm S, Ding D, et al. Quantifying the Ligand-Coated Nanoparticle Delivery to Cancer Cells in Solid Tumors. *ACS Nano* 2018; 12: 8423-8435.
- [45] Boucrot E, Saffarian S, Massol R, et al. Role of lipids and actin in the formation of clathrin-coated pits. *Exp Cell Res* 2006; 312: 4036-48.
- [46] Liu H, Liu Y, Liu S, et al. Clathrin-mediated endocytosis in living host cells visualized through quantum dot labeling of infectious hematopoietic necrosis virus. *J Virol* 2011; 85: 6252-62.
- [47] Erickson HP. Size and shape of protein molecules at the nanometer level determined by sedimentation, gel filtration, and electron microscopy. *Biol Proced Online* 2009; 11: 32-51.
- [48] Homo sapiens type-1 angiotensin II receptor - Protein - NCBI, <https://www.ncbi.nlm.nih.gov/protein/?term=Homo+sapiens+type-1+angiotensin+II+receptor> (accessed 19 February 2019).
- [49] Baudin B, Timmins PA, Drouet L, et al. Molecular weight and shape of angiotensin-I converting enzyme. A neutron scattering study. *Biochem Biophys Res Commun* 1988; 154: 1144-1150.
- [50] Huynh NT, Roger E, Lautram N, et al. The rise and rise of stealth nanocarriers for cancer therapy: Passive versus active targeting. *Nanomedicine* 2010; 5: 1415-1433.

Chapter 4 - Supporting Information

The Effect of Ligand Mobility on the Cellular Interaction of Multivalent Nanoparticles

1 Polymer modification

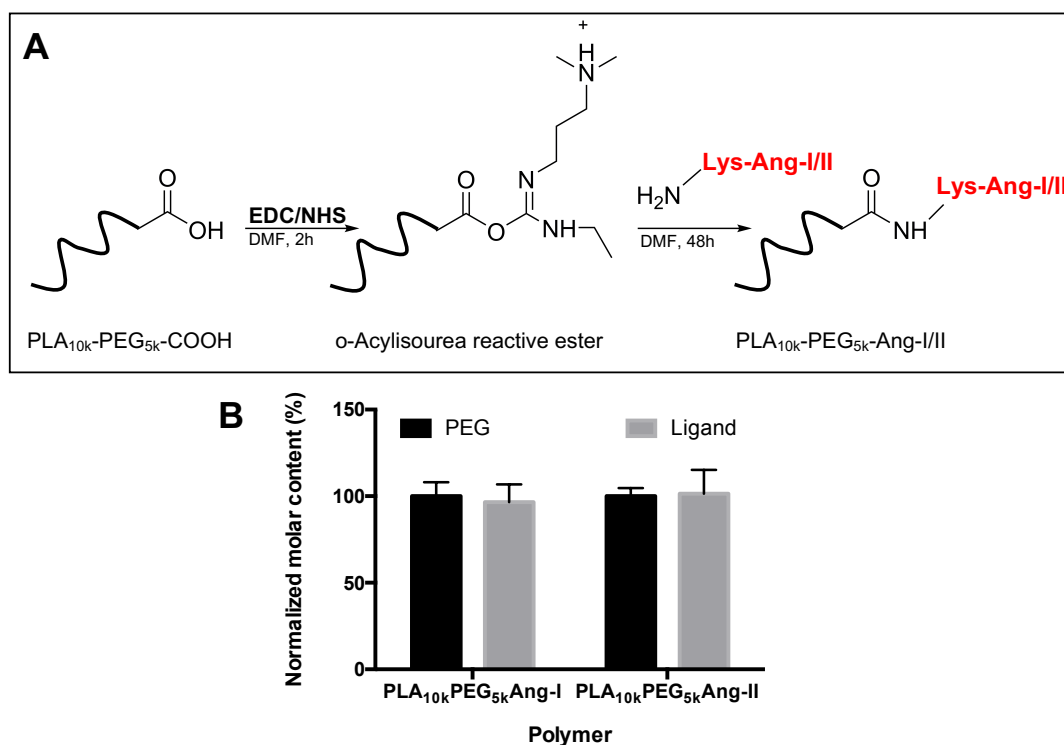


Figure S1. Polymer modification with angiotensin derivatives. (A) Lys-Ang-I/II is coupled to COOH-PEG_{5k}-PLA_{10k} through EDC/NHS chemistry. (B) Quantification of the molar content of PEG and ligand shows complete polymer modification.

2 Ligand density

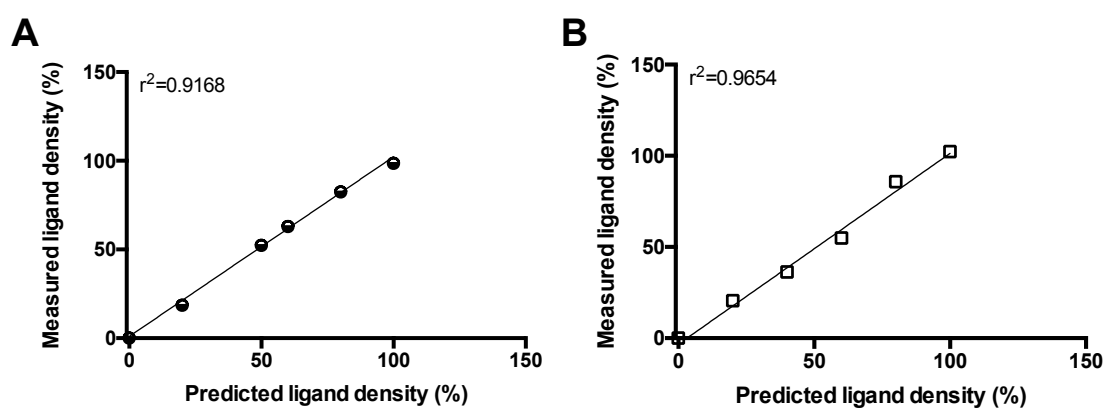


Figure S2. Theoretical ligand density and quantified normalized molar ligand and PEG content on the (A) NP_{2/510}Ang-II and (B) NP_{5/510}Ang-II corona.

3 AT1R-binding

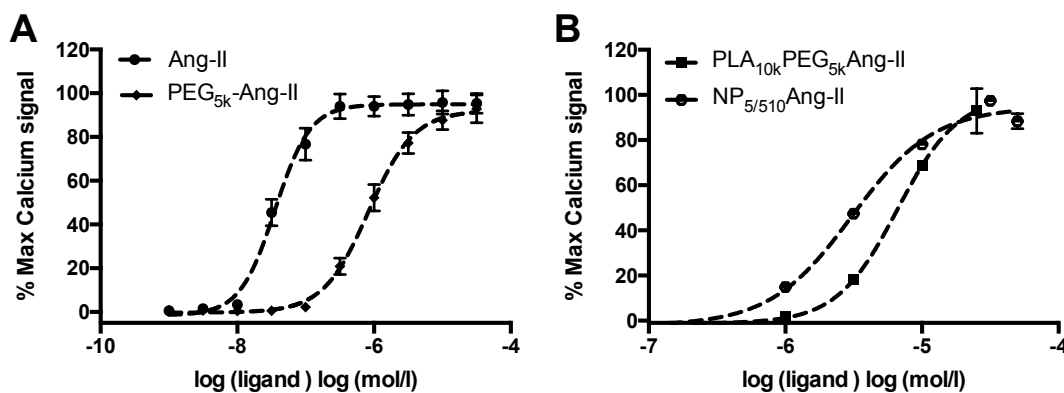


Figure S3. Affinity of polymer- and particle-bound Ang-II towards the AT1R analyzed by intracellular calcium measurements. Dose-response curve of free and PEGylated Ang-II (PEG_{5k}-Ang-II) (A) and block copolymer- (PLA_{10k}-PEG_{5k}-Ang-II) or particle-(NP_{5/510}Ang-II) bound Ang-II (B). Affinity of the free ligand (EC₅₀ = 36.3 ± 7.5 nM) decreases after binding to PEG_{5k} (EC₅₀ = 837.04 ± 94.0 nM). A further affinity loss is suffered when the Ang-II is coupled to a COOH-PEG_{5k}-PLA_{10k} (EC₅₀ = 6.7 ± 1.4 μM). The preparation of particles with 20% of Ang-II modified COOH-PEG_{5k}-PLA_{10k} polymer significantly increases ($p < 0.05$) the affinity of the particle-bound ligand to EC₅₀ values of 3.0 ± 0.1 μM. Results are presented as mean ± SD of at least n = 3 measurements.

4 Ligands per NP

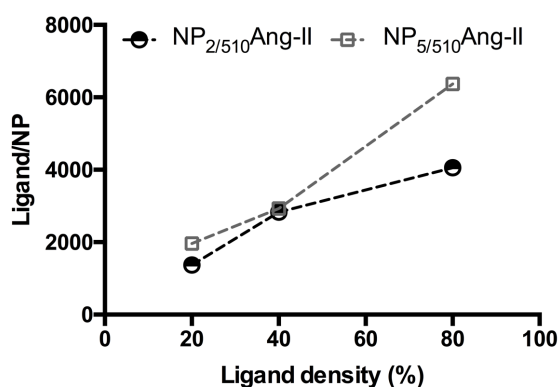


Figure S4. Ligand number on the NPs surface of NP_{2/510}Ang-II and NP_{5/510}Ang-II depending on the ligand density. When increasing amounts of Ang-II- PEG_{5k}-PLA_{10k} are used in the formulations, the ligand number per particle raises.

5 Protein corona formation on NPs

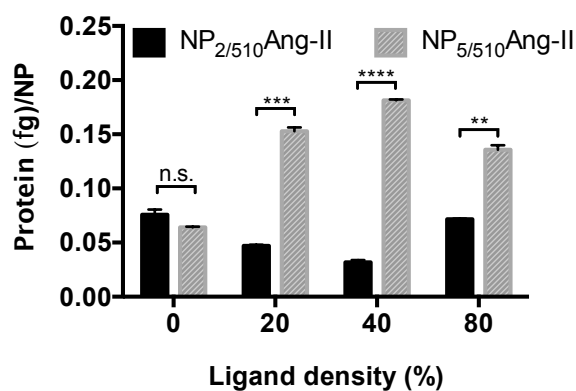


Figure S5. Serum protein adsorption on NP_{2/510} and NP_{5/510} functionalized with low (20%), medium (40%) or high (80%) amounts of Ang-II. NPs (0.65 mg mL⁻¹) were incubated with 50% fetal calf serum (v/v) for 1 hour at 37 °C. Afterwards, they were pelleted *via* two centrifugation steps (20,000 g for 1 hour) with a washing step with 1 mL water in between. Particles were resuspended (0.3 mg mL⁻¹) in 10% DPBS (v/v) and the protein adsorption quantified using a Micro BCA™ protein assay kits after the manufacturer's instructions and normalized to the particle number. Control particles with no ligands carrying either 5k or 2k PEG chains showed comparable serum protein adsorption. For functionalized particles, rigid NP_{5/510} depicted significantly higher protein adsorption compared to their flexible counterparts (NP_{2/510}) due the ligand entanglement in the long polymer chains in the flexible NPs resulting in an increased particle shielding by the polymer shell. Results are presented as mean ± SD of at least n = 3 measurements. Levels of statistical significance are indicated as **p ≤ 0.005, ***p ≤ 0.0005, and ****p ≤ 0.0001. n.s.: non-significant.

6 Uptake inhibition with EXP3174

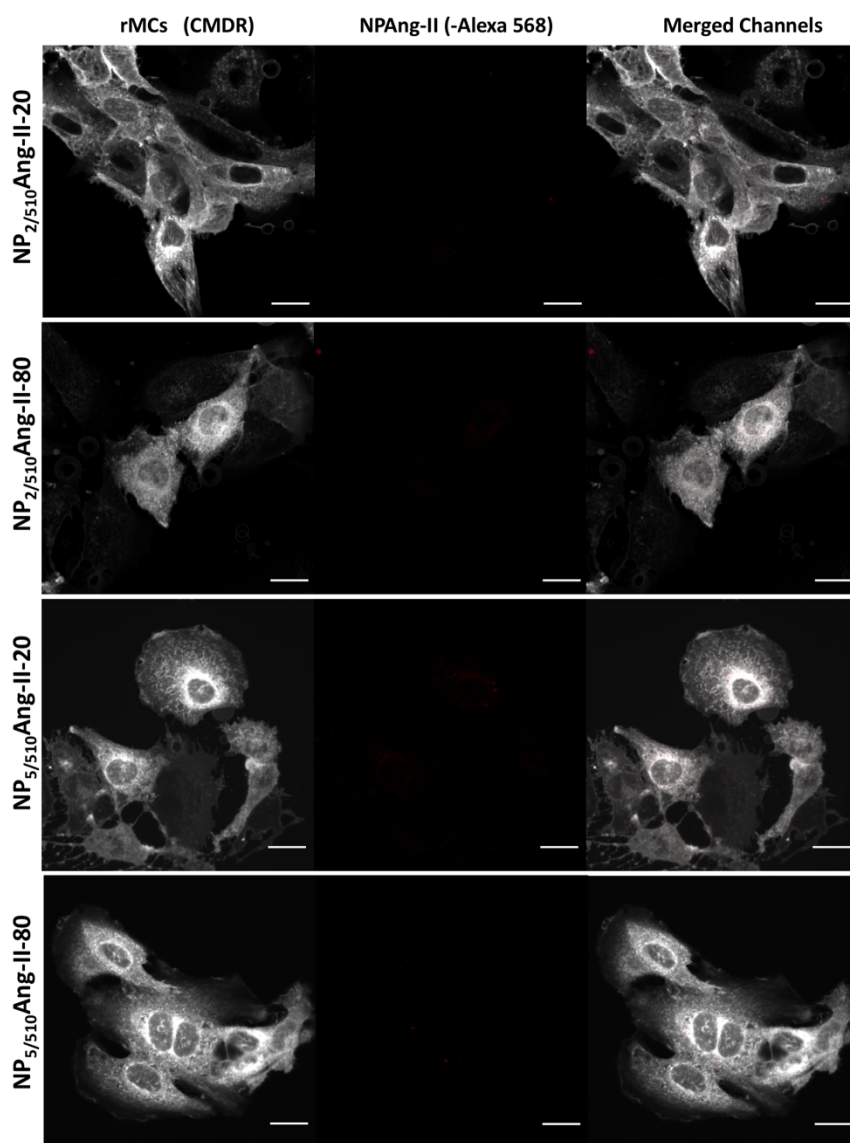


Figure S6. Uptake inhibition of NP_{2/510}Ang-II and NP_{5/510}Ang-II with 20 or 80% ligand density by 30 min pre-incubation of rMCs with EXP3174, an AT1R antagonist, analyzed by CLSM. Scale bar 20 μ m.

7 Uptake inhibition with Captopril

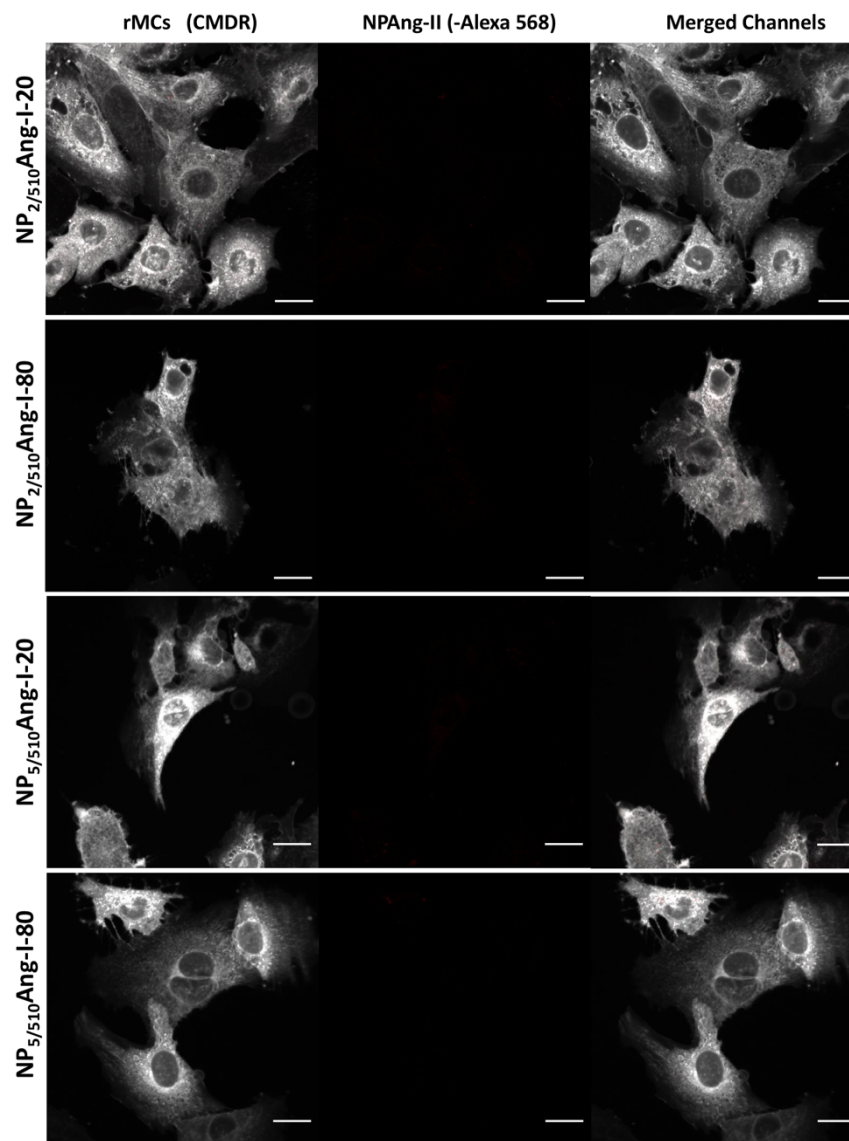


Figure S7. Uptake inhibition of NP_{2/510}Ang-I and NP_{5/510}Ang-I with 20% or 80% ligand density by 30 min pre-incubation of rMCs with captopril, an ACE inhibitor, analyzed by CLSM. Scale bar 20 μ m.

8 Distance between PEG chains

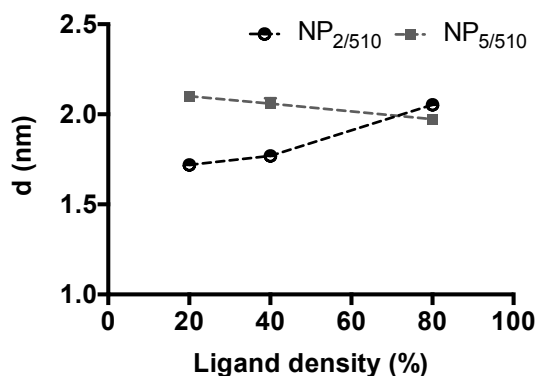


Figure S8. Calculated distance between the total PEG chains (d) on the surface of NP_{2/510} and NP_{5/510}.

9 Michaelis Menten kinetics of Ang-I bearing NPs

Table S1.

Samples	NP ₂₁₀			NP ₅₁₀		
Ligand density (%)	20	40	80	20	40	80
Km (μM)	12.3 ± 4.5	13.1 ± 1.7	9.9 ± 0.8	20.6 ± 5.1	20.2 ± 3.3	11.9 ± 1.4
Km-PNC (nM)	51.7 ± 18.8	48.8 ± 6.3	17.1 ± 1.4	183.6 ± 45.9	92.3 ± 15.2	24.6 ± 2.9
Vmax (pmol min ⁻¹)	88.5 ± 18.4	103.35 ± 5.1	95.7 ± 7.0	150.7 ± 70.9	113.8 ± 12.3	86.1 ± 9.3

Km: Michaelis Menten constant determined based on the ligand concentration; Km-PNC: Michaelis Menten constant determined based on the NP concentration; Vmax: maximum velocity.

10 Parameters used for the determination of the distances between PEG chains

Table S2.

Samples	NP ₂₁₀			NP ₅₁₀		
	20	40	80	20	40	80
Ligand Density (%)						
dh (nm)	62.13 ± 0.27	71.59 ± 0.35	72.06 ± 0.45	77.40 ± 0.99	79.70 ± 1.04	86.72 ± 0.83
Mw NMP (Da)	5097	5097	5097	5097	5097	5097
Mw LMP (Da)	2142	2142	2142	2142	2142	2142
f NMP	0.56	0.42	0.14	0.56	0.42	0.14
f LMP	0.14	0.28	0.56	0.14	0.28	0.56
S NMP (nm ²)	2.91 ± 0.02	6.14 ± 0.06	16.57 ± 0.2	4.32 ± 0.11	8.33 ± 0.22	15.30 ± 0.29
S LMP (nm ²)	11.63 ± 0.1	6.14 ± 0.06	4.14 ± 0.05	17.30 ± 0.45	8.33 ± 0.22	3.83 ± 0.07
S TP (nm ²)	2.33 ± 0.02	2.45 ± 0.02	3.31 ± 0.04	3.46 ± 0.09	3.33 ± 0.09	3.06 ± 0.06
ds (nm)	1.92 ± 0.01	2.80 ± 0.01	4.59 ± 0.03	2.35 ± 0.03	3.26 ± 0.04	4.41 ± 0.04
D (nm)	3.85 ± 0.02	2.80 ± 0.01	2.30 ± 0.01	4.69 ± 0.06	3.26 ± 0.04	2.21 ± 0.02
Ds (nm)	3.85 ± 0.02	2.80 ± 0.01	2.30 ± 0.01	2.10 ± 0.01	2.06 ± 0.03	1.97 ± 0.02
d (nm)	1.72 ± 0.01	1.77 ± 0.01	2.05 ± 0.01	2.10 ± 0.01	2.06 ± 0.03	1.97 ± 0.02

(dh) hydrodynamic diameter of the NPs determined through DLS measurements; (f) mass fraction of PEG in the blends of PEG-PLA; (S) surface that each PEG chain occupies on the NP; (ds) distance between NMPs; (D) distance between LMPs; (Ds) distance between the LMPs and the next same-length polymer; (d) distance among the total PEG chains.

Chapter 5

Nanoparticles Mimicking Viral Cell Recognition Strategies are Superior Transporters into Mesangial Cells

Published in *Advanced Science*

2020, 20 (2), 1900427

This chapter was published as: S. Maslanka Figueroa, D. Fleischmann, S. Beck, P. Tauber, R. Witzgall, F. Schweda and A. Goepferich, *Adv. Sci.* 2020, 1903204, doi:10.1002/advs.201903204

Abstract

Poor availability in the tissue of interest due to adverse physicochemical properties is a frequent cause of drug failure. While nanotechnology has developed a plethora of nanocarriers for drug transport, their ability to unequivocally identify cells of interest remains moderate. Viruses are the ideal nanosized carriers as they are able to address their embedded nucleic acids with high specificity to their host cells. Here it is reported that particles endowed with a virus-like ability to identify cells by three consecutive checks have a superior ability to recognize mesangial cells *in vivo* compared to conventional nanoparticles. Mimicking the initial viral attachment followed by a stepwise target cell recognition process leads to a 5- to 15-fold higher accumulation in the kidney mesangium and extensive cell uptake compared to particles lacking one or both of the viral traits. These results highlight the relevance that the viral cell identification process has on specificity and its application on the targeting strategies of nanomaterials. More so, these findings pave the way for transporting drugs into the mesangium, a tissue that is pivotal in the development of diabetic nephropathy and for which currently no efficient pharmacotherapy exists.

1 Introduction

Myriads of nanomaterials have been developed over recent years as carriers for drug therapy or diagnostics. To outfit them with the ability to identify target cells with sufficient specificity *in vivo*, ligands that bind to cellular receptors have been tethered to their surfaces [1, 2]. However, simply following this old paradigm [3] increased nanomaterial's avidities [4] but turned out to be insufficient for unequivocal cell identification [5]. Not even nanoparticles (NPs) that present several different ligands for hetero-multivalent binding [6] are able to distinguish between different cells types. Viruses in contrast, are NPs with ultimate target cell specificity that make use of a consecutive multistep process for cell identification [7, 8]. We recently showed that mimicking the sequential recognition strategy of influenza A virus, supplied nanomaterials with sufficient specificity to discern sharply between co-cultured target and off-target cells *in vitro* [9]. However, a close-up comparison with the way how viruses interact with cells made clear that the latter execute consecutive identification steps that had not been implemented into the former to date. They resemble 'if-then-else' elements in computer programming [10] that deserved more attention for the design of NPs. Especially the initial step of viral attachment to cell membranes, which does not result in particle uptake [11] but increases virus particle density on the cell surface and aids receptor recruitment is missing in contemporary NP design strategies. More so, this initial adhesion to glycolipids and glycoproteins [12] or specific receptors [13] was found to be essential for viral infectivity [14, 15].

It was, therefore, the goal of this study to investigate if nanomaterials outfitted with virus-mimetic cell identification mechanisms could be addressed to a tissue of profound therapeutic interest *in vivo* and if they were superior to materials following conventional design criteria. We chose the kidney as a target organ, since it holds different compartments made up of various cell types with distinct functions. Among them, we selected mesangial cells (MCs) a highly relevant target of drug therapy due to their crucial role in the maintenance of the integrity of the glomerular filter [16] and their severe impairment in several pathologies, such as mesangioproliferative glomerulonephritis and, more importantly, diabetic nephropathy (DN) [17, 18]. DN entails an enormous public health burden as it affects more than 50% of 425 million diabetic patients worldwide [19]. It is the leading cause of end-stage renal disease that can only be treated by dialysis or organ transplantation [20]. Even though a number of drugs hold great promise to inhibit pathomechanisms, such as MC proliferation and extracellular matrix overproduction in kidney glomeruli [17, 21], they suffer from poor mesangial availability. DN therapy could, therefore, be revisited for a number of compounds if a nanoparticulate drug transporter was available that was selectively and sufficiently taken up by MCs *in vivo*. Even though early reports had shown that 70

Chapter 5: Nanoparticle Mimicking Viral Cell Recognition Strategies

± 25 nm particles were most efficiently [22] penetrating the glomerular capillaries' 80-100 nm endothelial fenestrations [23], they are subject to mesangial clearance [24] and hence inadequate for drug delivery purposes if they do not specifically recognize and enter MCs. Therefore, we regarded MCs as an ideal target of paramount medical relevance for investigating if there was a benefit of outfitting NPs with a viral mechanism of cell identification.

We designed particles that carried EXP3174, an angiotensin-II type 1 receptor (AT1R) ligand, in the NP corona to mediate receptor attachment (Figure 1). As a G protein-coupled receptor (GPCR) antagonist, it has the advantage that binding cannot trigger cellular NP uptake [25], but only membrane binding [26] and thus prevents particle uptake by off-target cells that only carry the AT1R. For the second recognition criterion we outfitted the particles with the ability to probe cell surfaces for the presence of angiotensin converting enzyme (ACE) which recognizes the proligand angiotensin-I (Ang-I) in the particle corona and converts it to the active ligand angiotensin-II (Ang-II). As a third recognition step, Ang-II binds to the AT1R and, as an agonist, triggers cell uptake of particles upon receptor binding [25]. The whole process of target cell recognition can best be illustrated with a flow chart (Figure S1).

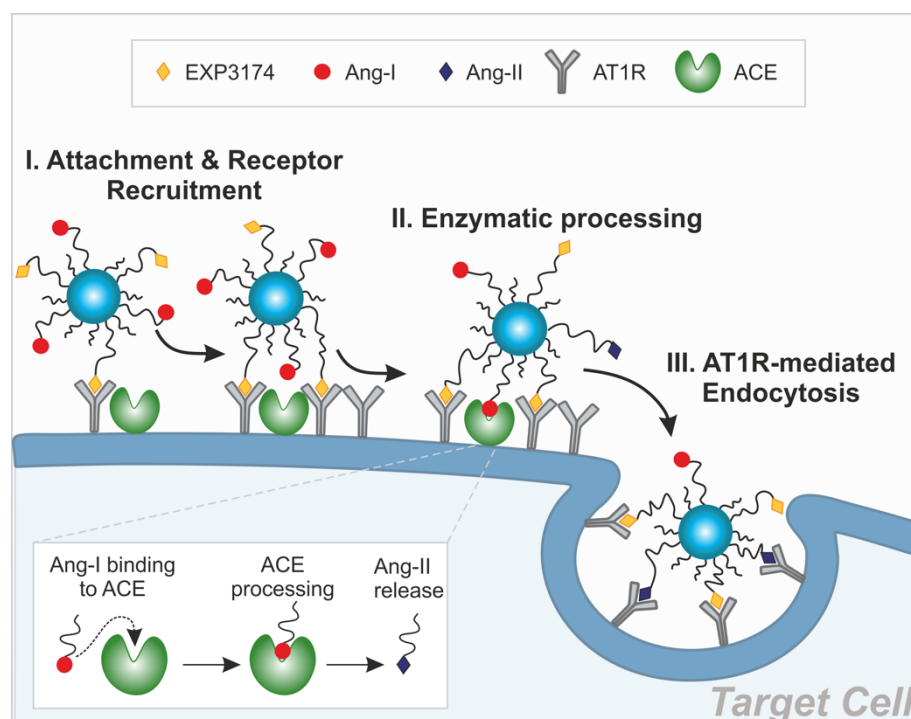


Figure 1. Virus-mimetic attachment and target cell recognition. NPs carrying EXP3174 and Ang-I on their corona (NPEXPAng-I) attach to the cell membrane through EXP3174-mediated AT1R-binding. Specific recognition is triggered through enzymatic Ang-I processing and Ang-II-mediated internalization [9].

We examined the particles for their target receptor avidity and target-cell specificity *in vitro*. Additionally, we assessed how the simultaneous presentation of two ligands addressing the same receptor, an antagonist promoting cell membrane binding, and an agonist, supporting cellular internalization, would affect the NPs ability to mediate cellular uptake. Lastly, we investigated if particles with such a virus-mimetic triple recognition strategy were superior to conventional NPs or particles mediating only either the viral attachment or stepwise internalization for reaching MCs *in vivo*.

2 Materials and Methods

2.1 Materials

Carboxylic-acid, Boc-amine- or methoxy-functionalized poly(ethylene glycol) PEG (2000 and 5000 Da) were purchased from JenKem Technology USA Inc. (Allen, TX, USA). Lysine N-modified Ang-I and Ang-II (Lys-Ang-I and Lys-Ang-II) (purity > 98%) were purchased from Genscript (Piscataway, NJ, USA). EXP3174 and captopril were obtained from Santa Cruz Biotechnology (Dallas, TX, USA). Fura-2AM was purchased from Life Technologies (Carlsbad, CA, USA). DPBS, Lipofectamine 2000, TAMRA-amine, Pierce BCA Assay kit, CellMask™ Deep Red Plasma Membrane Stain (CMDR), CellTracker™ Deep Red (CTDR) and Green (CTG) were purchased from Thermo Fisher Scientific (Waltham, MA, USA). Hoechst 33258 was obtained from Polysciences Inc. (Warrington, PA, USA). Integrin- α 8 goat antibody was purchased from R&D Systems (Minneapolis, MN, USA). Cy2-anti-goat secondary antibody was obtained from Jackson Immuno Research Labs (PA, USA). CXN2-HA-AT1R-YFP was a gift from Yusuke Ohba (Addgene plasmid #101659; <http://n2t.net/addgene:101659>; RRID: Addgene_101659). All other materials and reagents in analytical grade were obtained from Sigma Aldrich (Taufkirchen, Germany).

2.2 Cell Culture

Rat MCs (rMCs) were kindly gifted by Prof. Dr. Armin Kurtz (Institute of Physiology, University of Regensburg). NCI-H295R (CRL-2128) and HeLa (CCL-2) cells were purchased from ATCC. All three cell lines were cultured in RPMI1640 medium supplemented with 10% fetal bovine serum (FBS) (Biowest, Nuaille, France), insulin-transferrin-selenium, and 100 nM hydrocortisone. HK-2 cells were purchased from ATCC (CRL-2190) and maintained in DMEM-F12 (1:1) medium supplemented with 10% FBS. rMCs expressing YFP-tagged AT1R (pAT1R-rMCs) were obtained by transfecting rMCs with a plasmid encoding the AT1R with a YFP-tag (CXN2-HA-AT1R-YFP) using Lipofectamine 2000 after the manufacturer's instructions. pAT1R-

rMCs were cultured in RPMI1640 medium supplemented with geneticin (600 $\mu\text{g mL}^{-1}$).

2.3 Polymer preparation

PEG-poly(lactic acid) (PLA) block-copolymers were synthesized after Qian et. al [27] with slight modifications as previously described by our group [9, 28]. For the preparation of Ang-I-modified polymers, COOH-PEG_{5k}-PLA_{10k} (14 μmol) was activated with 1-ethyl-3-(3-dimethylaminopropyl)carbodiimide (EDC) and N-hydroxysuccinimide (NHS) (350 μmol) in N,N-Dimethylformamide (DMF) for 2 h. Afterwards, 2-mercaptoethanol (863 μmol) was added (20 minutes), prior to the dropwise addition of N,N-Diisopropylethylamine (DIPEA) (66 μmol) and Lys-Ang-I (17 μmol). After 48 h, the resulting polymer was diluted in ultrapure water (DMF concentration below 10%) and dialyzed using a 6-8 kDa molecular weight cut-off regenerated cellulose dialysis membrane over 24 h. For EXP3174-modified polymer preparation, EXP3174 (96.4 μmol) was activated with N,N'-Dicyclohexylcarbodiimide (DCC) and NHS (96.4 μmol) in DMF for 2 hours. Afterwards resulting urea byproducts were removed by centrifugation (5 minutes, 12,000 g) and filtration with a 0.2 μm Rotilabo PTFE syringe filter. NH₂-PEG_{5k}-PLA_{10k} (27.6 μmol) in DMF and DIPEA (1.7 mmol) were added to the activated ligand and reacted over 20 h. The ligand-modified polymer was purified by precipitation in ice cold 1:5 (v/v) diethyl-ether:methanol and dialysis against 10% ethanol in 10 mM borate buffer (pH 8.5) over 24 h followed by dialysis against ultrapure water over 24 h using a 6-8 kDa molecular weight cut-off regenerated cellulose dialysis membrane. Ligand-modified block-copolymers were lyophilized over 72 h prior to ligand-coupling confirmation (Figure S2). Polymer characterization was performed through ¹H-NMR using a Bruker Avance II 400 spectrometer (Bruker BioSpin GmbH, Rheinstetten, Germany) (Figure S9-S14) and high-performance liquid chromatography (HPLC), using an Agilent Infinity 1260 HPLC (Agilent Technologies GmbH, Waldbronn, Germany) (Figure S15).

For particle detection, TAMRA-amine (for CLSM) and CF6467-amine (for flow cytometry and *in vivo* experiments) were covalently coupled to carboxylic acid-terminated 13.4 kDa PLGA prior to particle preparation as previously described by our group [29].

2.4 NP preparation and characterization

PEG-PLA block-copolymers and 13.4 kDa poly(lactic-co-glycolic acid) (PLGA) were mixed at a 70:30 mass ratio to a final concentration of 10 mg mL⁻¹ in acetonitrile (ACN).

For ligand-modified particles COOH-PEG_{2k}-PLA_{10k} and ligand-modified polymers were mixed accordingly so that 20% of the polymers making up the NP-structure were modified with Ang-I (NPAng-I) or/and EXP3174 (NPEXP and NPEXPAng-I, respectively). NPs were prepared *via* bulk nanoprecipitation of polymer mixtures in vigorously stirring 10% Dulbecco's phosphate buffered saline (DPBS) (v/v) (pH 7.4) to a final concentration of 1 mg mL⁻¹. Particles were stirred for 2 h and concentrated by ultracentrifugation using a 30-kDa molecular weight cutoff Microsep advance centrifugal device (Pall Life Sciences) for 20 minutes at 756 g.

Size and ξ -potential of the resulting particles were determined in 10% phosphate buffered saline (PBS) (v/v) at a constant temperature of 25 °C using 1 mg mL⁻¹ or 3.5 mg mL⁻¹ concentrations, respectively, with a ZetaSizer Nano ZS (Malvern Instruments) [9, 28]. Quantification of particle PEG concentration was performed using a colorimetric iodine complexing assay [30] and correlated with the gravimetric NP content determined *via* lyophilization as we previously described [29]. The molar particle concentration was calculated from the particle mass determined through the colorimetric iodine complexing assay, the particle density (1.25 g cm⁻³) [31] and the hydrodynamic diameter of the NPs obtained through DLS measurements assuming a spherical particle shape. Ang-I concentration on the particle corona was quantified using a Pierce BCA assay kit, after the manufacturer's instructions, and a FLUOstar Omega microplate reader (BMG Labtech). EXP3174 concentration was determined fluorometrically ($\lambda_{\text{ex}}=250$ nm and $\lambda_{\text{em}}=370$ nm) using a LS-5S fluorescence plate reader (PerkinElmer).

2.5 Intracellular calcium measurements

The AT1R interaction of the different NP formulations was assessed through a ratiometric Fura-2 Ca²⁺ chelator method [32] as previously described by our group [9, 26] using AT1R positive rMCs [9]. To determine the particle avidity and ligand affinity for the AT1R, Fura-2-loaded-rMC in suspension (45 μ L \approx 90,000 cells) were incubated with different samples (10 μ L) (NPs or free ligands ranging from 1-300 μ M ligand-based concentration) for 30 minutes. Afterwards, cells were stimulated with Lys-Ang-II (45 μ L = 300 nM) and the resulting calcium signal immediately recorded for 1 minute using a FLUOstar Omega microplate reader with 340/20 nm and 380/20 nm excitation and 510/20 nm emission bandpass filters. To determine the kinetics of the AT1R interaction the same procedure was used, but the samples (10 μ M ligand concentration) were incubated for different time periods (5-320 minutes) with the cells.

2.6 Enzyme kinetic measurement

The Michaelis-Menten kinetics were determined as we previously described [9]. In order to rule out the interference of the EXP3174 ligand on NPEXPang-I under the experimental conditions used, NPEXP were used as a control (Figure S3). The K_m for particle- and ligand based- concentrations, K_{cat} and K_{cat}/K_m were obtained using GraphPad Prism 6.0.

2.7 Cellular distribution of NPs

In order to determine the cellular distribution of the different particle formulations (Figure 4), pAT1R-rMCs were seeded into 8-well μ -slides (Ibidi, Graefelfing, Germany) (10,000 cells per well) and incubated over 24 h. Then they were incubated with pre-warmed NP-solutions (0.2 mg mL^{-1}) in Leibovitz medium (LM) supplemented with 0.1% bovine serum albumin (BSA) for 15, 45 or 90 minutes. Afterwards, the NPs were discarded, and the cells washed thoroughly with DPBS prior to cell staining with 1x CMDR for 5 minutes and fixation with 4% paraformaldehyde (PFA) in DPBS for 10 minutes. Confocal images were acquired using a Zeiss LSM 700 microscope with the focal plane set at $1.4 \mu\text{m}$ using the Zen Software (Carl Zeiss Microscopy). For particle uptake and binding inhibition cells were preincubated with free EXP3174 (1 mM) prior to particle addition. Images were analyzed using Fiji software [33]. Particle uptake through flow cytometry was performed as previously described by our group [9]. In short, rMCs were seeded in 24-well plates at a density of 30,000 cells per well and incubated for 48 h ($37 \text{ }^\circ\text{C}$). Prewarmed NP-solutions (0.7 mg mL^{-1} in LM with 0.1% BSA) were added to the cells, after washing them with DPBS, and incubated for 45 minutes. To confirm the uptake specificity, cells were incubated with 1 mM of captopril and/or EXP3174 for 30 minutes prior to particle addition. Afterwards, particle solutions were discarded, and the cells washed thoroughly with DPBS, trypsinized and centrifuged ($2 \times, 200 \text{ g}$ 5 minutes, $4 \text{ }^\circ\text{C}$). NP-associated cell fluorescence was analyzed in DPBS using a FACS Calibur cytometer (Becton Dickinson). Fluorescence was excited at 633 nm and recorded using a 661/16 nm bandpass filter. The population of viable cells was gated using Flowing software 2.5.1. (Turku Centre for Biotechnology) and the geometric mean of the NP-associated fluorescence was analyzed.

2.8 NP target cell specificity

To assess the NP uptake in different cells lines through flow cytometry rMCs, HK-2 and HeLa cells were seeded out in 24-well plates at a density of 30,000, 50,000 or

100,000 cells per well, respectively and incubated over 48 h. Afterwards pre-warmed NP-solutions (0.7 mg mL⁻¹ in LM with 0.1% BSA) were added on top of the cells and processed as described above. The particle specificity in co-culture of target and off-target cells was investigated through confocal laser scanning microscopy (CLSM) and flow cytometry analysis as previously described by our group [9].

2.9 NP kidney distribution *in vivo*

The experimental procedures on animals were carried out according to the national and institutional guidelines and were approved by the local authority (Regierung von Unterfranken, reference number: 55.2-2532-2-329). As model animals 10-week-old female NMRI-mice (Charles River Laboratories, Sulzfeld, Germany) were used. The different NP formulations (NPEXPAng-I, NPAng-I, NPEXP and NPMeO) (120 nM NPs \approx 10 mg mL⁻¹ NPs) were injected (100 μ L) *via* the vena jugularis after anesthesia with isoflurane inhalation and buprenorphine (0.1 mg kg⁻¹) (n = 6 for each NP sample). Additionally, the free dye used to fluorescently label the particles (CF647) was injected (100 μ L) in the same concentration contained in a particle sample (50 μ M). After 5 minutes a blood sample was collected *via* i.v. puncture while mice were still under anesthesia. After 1 h of particle circulation mice were anaesthetized with ketamine/xylazine, a final blood sample was collected, and they were killed through perfusion fixation with 4% PFA. The kidneys were harvested and cut transversally. They were cryoprotected by incubation in phosphate buffer (0.1 M pH 7.4) supplemented with 18% sucrose and 1% PFA overnight. Afterwards, they were frozen in liquid nitrogen-cooled 2-propanol (-40 °C) and embedded in Tissue Tek® O.C.T.™ Compound (Sakura Finetek). Kidneys were cut into 5 μ m cryosections using a CryoStar NX70 cryostat (Thermo Fisher Scientific) and transferred onto Superfrost™ plus glass slides. Cell nuclei were stained with DAPI (12.5 μ g mL⁻¹ in DPBS) prior to imaging using an Axiovert 200M (Zeiss) fluorescence microscope and Zen System Software 2017 (Zeiss). Images of the whole kidney were acquired using a 10x objective. For glomerular fluorescence quantification images were taken using a 40x objective (an average of 120 glomeruli per sample for n=6 mice per NP sample) and analyzed using Fiji Software [33]. For better visualization the lookup table “Red Hot” was applied to the particle-associated fluorescence. The area of each glomerulus was quantified, and the fluorescent area gated. Then, the integrated fluorescence density of each gated area was quantified and correlated to the whole glomerulus area. In order to compare the particle-associated fluorescence of the inner and outer cortex, the cortex was divided into two equal sections and the glomerular fluorescence analyzed as described above.

2.10 Immunohistochemistry

To assess the glomerular localization of NPs, 5 μm kidney cryosections were washed for 5 minutes consecutively with DPBS, DPBS supplemented with 0.1% sodium dodecyl sulfate (SDS), and DPBS prior to 10 minute-blockage with 5% BSA in DPBS supplemented with 0.04 % Triton-X (m/v). Sections were washed again with DPBS (5 minutes) and incubated overnight with the primary polyclonal goat anti-Integrin- $\alpha 8$ antibody (1:200 in DPBS with 0.5% BSA and 0.004 Triton-X (m/v)) at 4 °C. Then, they were washed for 5 minutes in DPBS and incubated for 1 h with the Cy2-anti-goat secondary antibody (1:400) and DAPI (12.5 $\mu\text{g mL}^{-1}$) in DPBS supplemented with 0.5% BSA and 0.04% Triton-X at r.t. light protected. Cryosections were washed with DPBS and ultrapure water before they were mounted using Dako Faramount Mounting Medium (Agilent Technologies) and analyzed using a Zeiss LSM 700 microscope and Fiji software, as described above.

2.11 Statistics

Statistical analysis was performed using GraphPad Prism Software 6.0. Student t tests (Figure 3C, 5A/C-D, 7B) or two-way ANOVA with a Sidak's (Figure 3D, 5B, 7C) or Turkey's (Figure 3F) multiple comparison test were employed to evaluate statistical significance. Levels of statistical significance and "n" numbers for each experiment are indicated in the text and figure legends.

3 Results and Discussion

3.1 Block-copolymers allow for a virus-mimetic particle design

For the development of virus-mimetic NPs we coupled the ligands EXP3174 and Ang-I, to PEG_{5k}-PLA_{10k} block copolymers (Figure S2), which were blended with PLGA for NP manufacturing *via* bulk nanoprecipitation [34] rendering particles with sufficient stability *in vivo* [35]. Such NPs are known for their excellent biocompatibility and highly tunable composition (Figure 2). The remaining, non-functionalized polymers were carboxylic acid-ended PEG-PLA with a shorter 2k PEG and a 10k PLA block (COOH-PEG_{2k}-PLA_{10k}) (Figure 2A). By modifying the polymers with ligands prior to NP preparation, the ligand density can be precisely controlled. Particles were prepared such that 20% of their PEG chains were decorated with Ang-I and an additional 20% with EXP3174 (NPEXPAng-I) (Figure 2B). The ligand density was kept at a 40% maximum to avoid steric hindrance among ligands and non-specific interactions [36]. As a control, ligand-free methoxy-PEG-terminated particles (NPMEO) and particles carrying either 20% Ang-I or EXP (NPAng-I and NPEXP, respectively) were

assembled (Figure 2A). By combining long ligand-carrying polymers with shorter non-functionalized polymers for particle preparation, the size of the NPs could be kept under 80 nm (Figure 2C) to endow particles with the ability of passing through the endothelial fenestrations of mesangial capillaries [37]. Carboxylic acid terminated block copolymers were selected as a filler that provides an overall negative particle charge ideal to avoid non-specific electrostatic adsorption to the negative cell membranes [38] (Figure 2D).

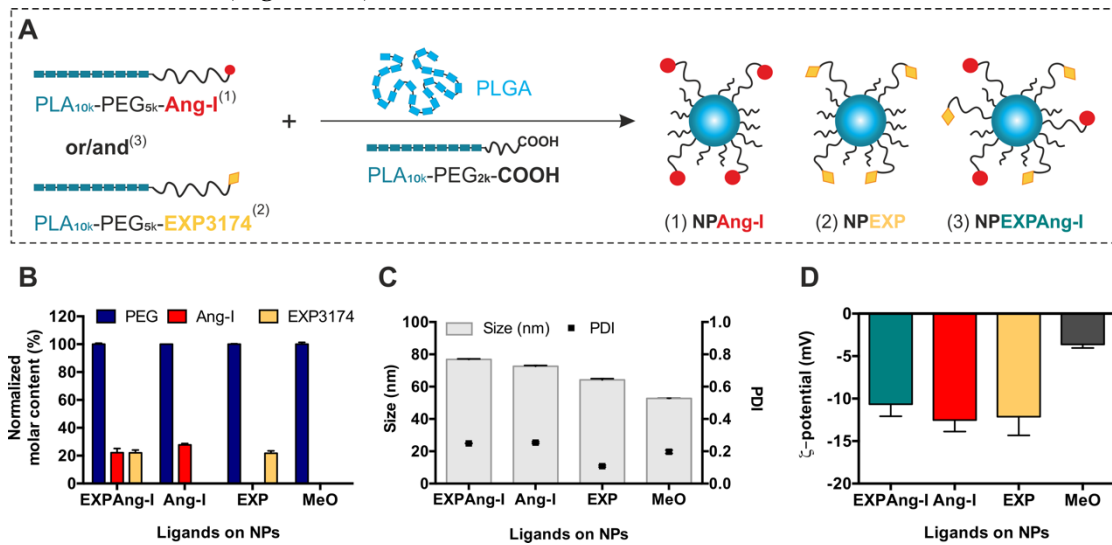


Figure 2. NP characterization. (A) Assembly of ligand-decorated NPs. (B) Molar ligand content of different NP species normalized to the PEG content, (C) size and polydispersity index (PDI) and (D) ζ -potential of the resulting NP formulations. Results are presented as mean \pm SD of at least $n = 3$ measurements.

3.2 NPs recognize target receptors *in vitro*

Particle avidity for the target receptor, which mediates primary attachment and subsequent internalization, was investigated using calcium mobilization assays (Figure 3), since the stimulation or silencing of the Gq-coupled AT1R with an agonist or antagonist results in a cytosolic Ca^{2+} influx or its suppression, respectively [39]. To that end, target-positive rMCs [9] were incubated with varying concentrations of either free ligands or NP-formulations prior to stimulation with Ang-II and recording the resulting calcium signal. As depicted in Figure 3A, control experiments with free EXP3174 and Ang-II revealed a high affinity of both compounds for the AT1R in the low nanomolar range (IC_{50} values of 0.6 ± 0.4 and 1.5 ± 0.1 nM, respectively) which is in accordance with literature values [40]. Ang-I displays a lower affinity (IC_{50} 0.9 ± 0.6 μM), as the receptor binding and activation occurs only after enzymatic conversion to Ang-II by ACE present on the cell membrane. The coupling of ligands to linkers leads to an affinity loss that is compensated by the high avidity multivalent binding of

Chapter 5: Nanoparticle Mimicking Viral Cell Recognition Strategies

several receptors simultaneously [26] (Figure 3B-C). NPAng-I show a lower avidity for the AT1R (IC₅₀ of 9.4 ± 0.4 nM) than NPEXP (IC₅₀ of 0.4 ± 0.1 nM), as their primary interaction is with the ACE. Nevertheless, particle binding of Ang-I leads to a significant decrease in IC₅₀ values compared to the free ligand due to a facilitated enzymatic cleavage at the NP-interface [41] and the subsequent multivalent binding. NPEXP in contrast, had avidities that were of the same order of magnitude as for the free ligand. Interestingly, particles that carried both ligands, NPEXPAng-I, showed a cooperative effect with respect to receptor interaction, as they had significantly higher avidity for the AT1R (IC₅₀ of 0.2 ± 0.09 nM) than either of the particles carrying only one type of ligand (Figure 3C). This proves that the ligands do not hinder each other's interaction, which was a point of great concern, as after Ang-I enzymatic activation to Ang-II both ligands target the same receptor in a simultaneous agonistic and antagonistic manner. NPMeO confirmed that the assay was ligand-specific, as they did not elicit any response due to their lack of functionalization (Figure 3B).

To assess kinetics of cell/particle interactions, intracellular calcium measurements were performed over a 5.5-hour period. The extent to which they could silence calcium signaling triggered by the present free agonist served as a measure for the completeness to which the respective particles had bound *via* their ligands to the AT1R in the cell surface at different time points (Figure 3D). Particles carrying only Ang-I on their surface displayed a slow receptor binding since they initially need to be activated by the cell membrane-bound ACE to Ang-II carrying particles before they can interact with the AT1R. The receptor binding reached a maximum at about 40% after 1-hour incubation, which remained constant over the assay's duration. This points towards a fast internalization of the particles once a certain number of proligand is activated. Once Ang-II on the particle surface binds to a receptor, the particles are rapidly internalized (as they have picomolar AT1R avidities [9]) which indicates that not all proligands may need to be activated for NP internalization to occur. This phenomenon is avoided when adding EXP3174 as an attachment factor on the particle surface. A very fast and complete receptor blockage occurs after only 5 minutes of particle incubation (for NPEXPAng-I and NPEXP alike). The AT1R inhibition is maintained over almost the whole measurement and descends to about 80% at the last time points, probably due to receptor upregulation and recycling [42]. The attachment by EXP3174 to the cell membrane slows down the recognition process and enables a higher Ang-I to Ang-II activation that can more efficiently bind to the AT1R. Comparing NPEXPAng-I and NPEXP there is a significantly higher initial AT1R inhibition of NPEXPAng-I which evens out after 45 minutes. This is probably due to the combined effect of the two ligands which leads to a higher avidity for the AT1R, as seen previously (Figure 3C).

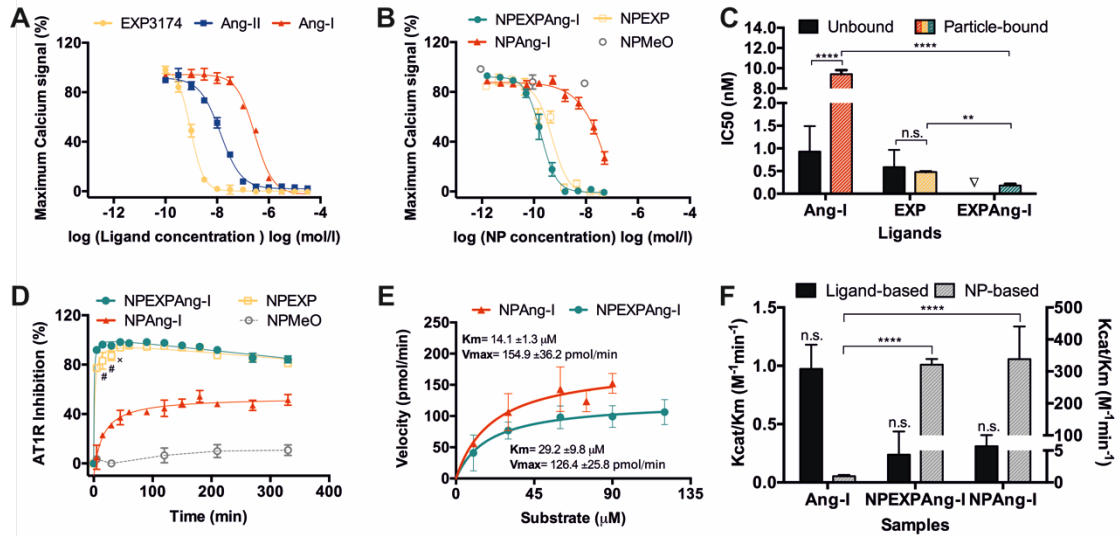


Figure 3. *In vitro* interaction with AT1R and ACE. Interaction of ligand-decorated NPs with their target AT1R (A)-(D) and ACE (E)-(F) determined by intracellular calcium measurements. (A) Ligand affinity and (B) particle avidity for the AT1R. (C) IC₅₀ values for the free and particle-bound ligands. (D) Kinetic measurement of the AT1R inhibition by ligand-decorated particles. (E) Michaelis-Menten kinetics of NPEXPAng-I and NPAng-I. (F) Specificity constant (Kcat/km) for the free and particle-bound Ang-I calculated based on ligand and NP concentration. Results are presented as mean \pm SD of at least $n = 3$ measurements. Levels of statistical significance are indicated as ** $p \leq 0.01$, **** $p \leq 0.0001$ and # $p \leq 0.0001$ and $\times \leq 0.001$ comparing the AT1R inhibition of NPEXP and NPEXPAng-I at different time points. n.s.: non-significant.

A prerequisite for particle internalization is the ability of ACE to activate Ang-I to Ang-II. Therefore, we investigated the enzyme kinetics for NPEXPAng-I, to determine whether the presence of the antagonist on the particle surface would hinder the enzymatic reaction. A soluble form of ACE was incubated for varying time periods with different particle concentrations and the resulting Ang-II on the NP corona was quantified running calcium mobilization assays. The interference of the EXP3174 ligand in the assay was assessed by measuring the signal inhibition exhibited by NPEXP (Figure S3). The Michaelis Menten constant (K_m) determined for both NPAng-I and NPEXPAng-I (Figure 3E), resulted in values that were of the same order of magnitude as for the free ligand [9, 43] for both particle formulations. Additionally, we determined the catalysis constant (Kcat) to calculate the specificity constant (Kcat/ K_m) which is a useful indicator for comparing the affinity of different substrates for the same enzyme [44] (Figure 3F). The enzymatic activation of Ang-I on the NPEXPAng-I corona was not significantly different from the one on NPAng-I, indicating that ACE is not sterically hindered by the additional ligand EXP3174. Furthermore, the Kcat/ K_m value calculated based on the ligand concentration was equal for free and particle-bound Ang-I. More so, when Kcat/ K_m is calculated based on the NP concentration the bound ligand is a significantly better substrate for the enzyme, which is a result of the binding of several ligand molecules on the particle surface to various enzyme molecules (Figure 3F).

3.3 Virus-mimetic NPs are target-cell specific

After the particle interaction with their individual targets had been successfully established, the next step was to determine if NPs carrying an antagonist as well as an agonist on their corona would still trigger internalization by their target cells, and if so, if the uptake ensued from a specific ligand-receptor interaction. As antagonists do not cause AT1R-mediated endocytosis [26, 45] and agonists do [9, 46], we investigated *via* CLSM the cellular localization of NPEXPAng-I in pAT1R-rMCs. As shown in Figure 4, NPEXPAng-I-associated fluorescence was found inside the cells. It increased with higher incubation times and strongly colocalized with the AT1R fluorescence. This points towards a specific particle uptake, mediated by the AT1R.

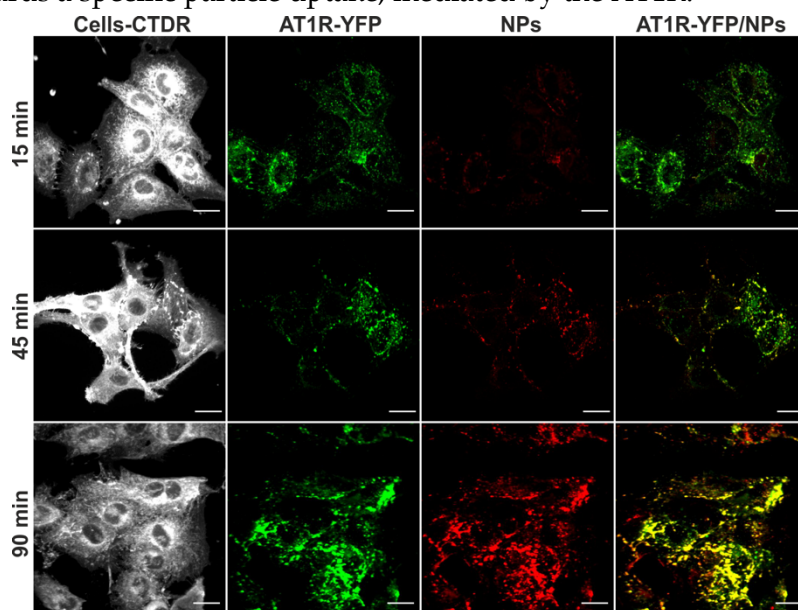


Figure 4. Cellular localization of NPEXPAng-I. NPEXPAng-I (red) are internalized in target cells (white) transfected with a YFP-tagged AT1R (green) (pAT1R-rMCs) at different incubation times. Scale bar 20 μ m.

However, particles carrying only the antagonist (NPEXP) were not internalized by the cells and located mostly on the cellular surface (Figure S4A), which is in accordance with previous findings with EXP3174 and other antagonist-decorated particles [26, 45]. But still, the particle fluorescence also colocalized with the receptor fluorescence, demonstrating a receptor-mediated attachment. As NPAng-I were also internalized by the cells (Figure S4B), the enzymatically created Ang-II seems to mediate the cellular uptake of NPEXPAng-I. Interestingly, there was a rearrangement of the receptors on the cellular membrane with increasing incubation times (Figure 4), from a more diffuse and uniform cell membrane distribution (15 minutes) to a more concentrated clustering (90 minutes), which strongly colocalized with the NP fluorescence. This is additional evidence that the uptake is mediated by the AT1R, as the activation of receptors that are internalized *via* clathrin-coated pits, such as the GPCR like the AT1R,

promotes receptor clustering [47, 48]. For NPEXP a receptor rearrangement on the cell membrane also occurred, which is a result of a multivalent receptor binding promoted by receptor movement on the cellular surface. Once NPEXP attach to a receptor on the cell membrane, their lack of internalization can lead to receptor-particle mobility on the cell membrane, and further receptor binding [49]. NPMs were not taken up by the cells (Figure S4C), confirming that a specific targeting mechanism is essential to mediate a high cellular internalization.

Overall, we could demonstrate that the presence of an attachment-mediating antagonistic ligand linked to the particle corona does not hinder subsequent particle internalization. More so, the inclusion of an additional ligand on the particle surface compensated the targeting loss due to steric hindrance of the Ang-I ligand by the addition of a higher number of long polymer chains (Figure S5). To further confirm the particle specificity and ligand-mediated internalization, the cells were pre-incubated for 30 minutes prior to particle addition with free EXP3174 or captopril, an ACE inhibitor, which resulted in a suppression of the particle-associated fluorescence analyzed by flow cytometry (Figure 5A) and CLSM (Figure S6).

As the simultaneous presentation of two ligands on a particle surface can lead to more off-target interactions, we examined the particle internalization in different cell lines by flow cytometry (Figure 5B). HeLa cells, which do not express ACE and only express minor AT1R levels [9, 45] showed a low particle uptake, which was non-specific as it could not be suppressed by captopril or EXP3174. On the contrary, rMCs and HK-2 cells expressing both the targets [9] were able to take up the particles, shown by the much higher particle-associated cell fluorescence. The internalization was also mediated by the activated proligand binding to the AT1R, as the preincubation of cells with captopril or EXP3174 significantly suppressed the cell fluorescence. This is a great indicator of particle specificity for their target cells. Nevertheless, when NPs enter the body, they are presented simultaneously with target and off-target cells. Therefore, we investigated if our NPEXP_{Ang-I} were able to differentiate between them when presented simultaneously. Target cells (rMCs) were seeded together with an excess of off-target NCI-H295R or HeLa cells, which both lack the ACE and express high and low AT1R levels, respectively [9, 45]. They were incubated with the different NP formulations and investigated for particle-associated fluorescence through flow cytometry (Figure 5C-D). NPEXP_{Ang-I} showed outstanding target cell specificity, as they accumulated significantly more in target rMCs. The specificity is conferred by Ang-I as NP_{Ang-I} showed also low accumulation in both off-target cells. On the contrary, NPEXP bound to the cell surface to the same degree in rMCs as in NCI-H295R cells, which express high AT1R levels, demonstrating that a simple one-step recognition process is not enough to confer particle selectivity. CLSM images

Chapter 5: Nanoparticle Mimicking Viral Cell Recognition Strategies

confirmed our flow cytometry findings (Figures 5E and Figure S7), were NPEXPAng-I- and NPAng-I fluorescence (red) was mostly associated with target rMCs (green) and not in off-target HeLa or NCI-H295R cells (white), while NPEXP fluorescence was found in both rMCs and AT1R-expressing NCI-H295R cells. Taken all together, these results demonstrate that the NPEXPAng-I uptake is receptor-mediated and that the initial cell attachment through the EXP3174 ligand does not reduce the particle specificity for the target cells conferred by the virus-mimetic recognition process.

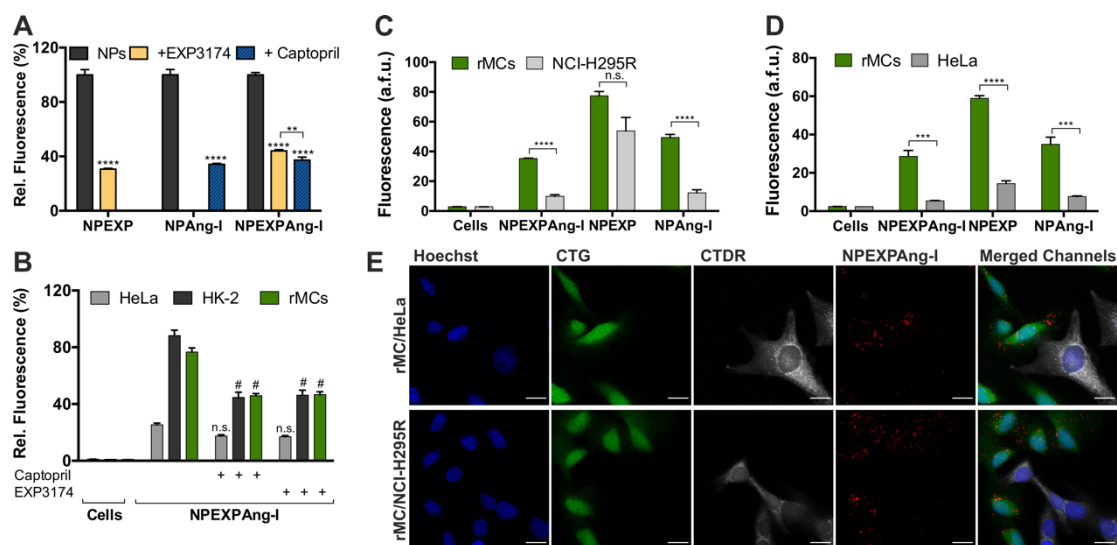


Figure 5. Uptake specificity of virus-mimetic NPEXPAng-I. (A) Ligand-mediated internalization of NPEXPAng-I, NPAng-I and NPEXP in rMCs inhibited by free EXP3174 and captopril. (B) Uptake of NPEXPAng-I in AT1R and ACE positive rMCs and HK-2 cells and AT1R and ACE negative HeLa cells. Specificity of particle uptake in co-culture of target rMCs with off-target (C) NCI-H295-R cells or (D) HeLa cells analyzed *via* flow cytometry. (E) CLMS images of particle uptake (red) in green-stained (CTG) rMCs (green) in co-culture with deep red-stained (CTDR) off-target HeLa or NCI-H295R cells (white). Scale bar 20 μ m. Results are presented as mean \pm SD of at least $n = 3$ measurements. Levels of statistical significance are indicated as ** $p \leq 0.01$, *** $p \leq 0.001$, **** $p \leq 0.0001$ and as # $p \leq 0.0001$ comparing the uptake of NPs in cells with and without captopril or EXP3174 inhibition. n.s.: non-significant.

3.4 Virus-mimetic NPs target MCs *in vivo*

Since the complementary targeting ability of both ligands on NPEXPAng-I and the particle specificity was demonstrated *in vitro* the next step was to determine whether the viral recognition principle would lead to a higher *in vivo* MC accumulation. To that end, targeted (NPEXPAng-I, NPAng-I and NPEXP) (Figure 1A) and non-targeted (NPMeO) particle formulations were injected into NRMI mice and cryosections of the kidneys examined for particle-associated fluorescence (Figure 6 and Figure S8A). As depicted in Figure 6, NPEXPAng-I fluorescence could be found homogeneously over all glomeruli in the kidney section, with no fluorescence in other kidney structures,

such as the tubuli. On the contrary, for NPMeO almost no NP fluorescence could be detected in the kidney sections. This demonstrates that simple size-dependent targeting is not enough to achieve a particle accumulation in MCs and NPMeO are probably cleared out of the mesangium due to their lack of specific cellular interaction. More so, NPEXP which are targeted NPs but not able to mediate cellular internalization also depicted very little glomerular fluorescence (Figure S8A), demonstrating that particle uptake is fundamental to achieve a high MC accumulation. Furthermore, NPEXPAng-I showed a much stronger and homogeneous glomerular distribution than NPAng-I, which lack the attachment factor (Figure S8A), demonstrating that *in vivo* an enhanced target cell recognition principle is highly advantageous.

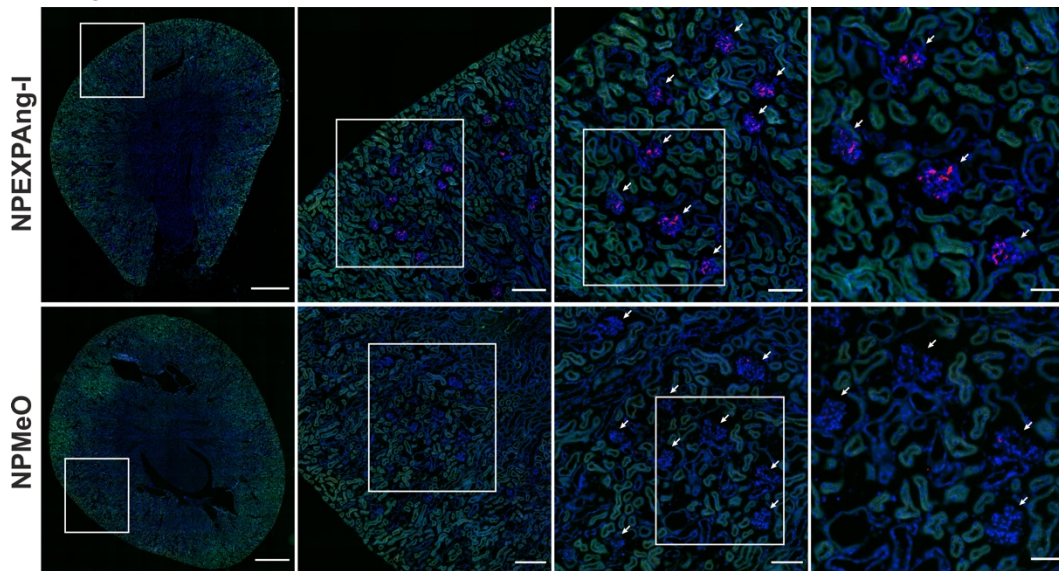


Figure 6. Distribution of NPEXPAng-I and NPMeO in mice kidney. Glomeruli are indicated with white arrows. Blue: DAPI staining of cell nuclei; green: tissue autofluorescence; red: NP-associated fluorescence. From left to right squared out regions are shown as magnifications. Scale bars left to right 900, 200, 100 and 50 μm .

In order to quantitatively assess the NP-associated fluorescence and better distinguish the differences among the different particle formulations, images of the glomeruli were taken at higher magnifications (Figure 7A). Quantitative analysis of the glomerular fluorescence yielded a 15-fold higher fluorescence for virus-mimetic particles with enhanced recognition mechanism (NPEXPAng-I) compared to non-targeted control particles (NPMeO), which showed only small fluorescence spots in some glomeruli. Additionally, NPEXPAng-I displayed significantly higher accumulation than one-ligand targeted particles (7- and 5-fold higher than NPEXP and NPAng-I, respectively) (Figure 7B). That the detected fluorescence was particle-associated, was confirmed by the kidney distribution of the free dye used for particle labelling (CF647), which showed strong tubular but no glomerular fluorescence (Figure S8B), as due to its small

Chapter 5: Nanoparticle Mimicking Viral Cell Recognition Strategies

size it can be freely filtrated. To assess the NP glomerular distribution the fluorescence of the glomeruli in the outer and inner cortex was compared (Figure 7C). For all particle formulations there were no significant differences among the two populations. This indicates that the particles are distributed homogeneously in the glomeruli of the entire kidney cortex, which is an indispensable prerequisite for the treatment of glomerular-associated diseases. Finally, as besides MCs there are other cells in the glomerulus which could have internalized the NPs, a specific antibody-staining of MCs using integrin- $\alpha 8$ as a marker was performed to ascertain that the particles accumulated in MCs. As depicted in Figure 7D, the NPEXPAng-I fluorescence localized inside the antibody-stained MCs, confirming that our particles were able, not only to reach the glomerular mesangium, but also to be taken up by MCs.

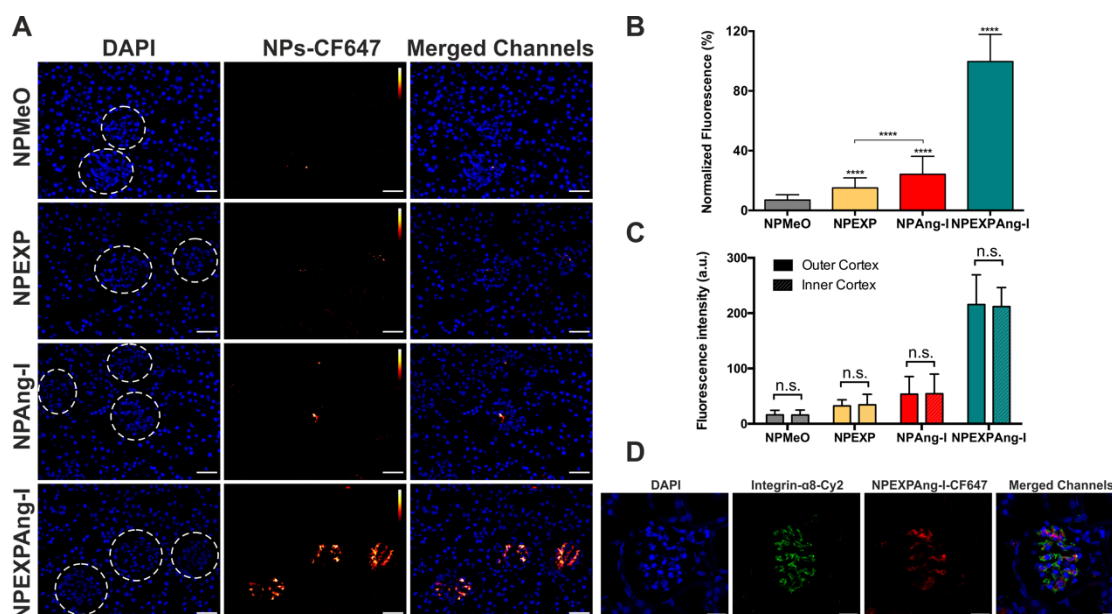


Figure 7. Assessment of the NP-associated fluorescence detected in kidney glomeruli analyzed through fluorescence microscopy. (A) Images of kidney glomeruli (dotted circles) of mice treated with the different particle formulations. Scale bar 40 μm . (B) Quantitative analysis of the complete glomerular NP-fluorescence. (C) Comparison of the particle-associated fluorescence in the glomeruli of the outer and inner cortex. (D) Glomerular localization of NPEXPAng-I determined *via* CLSM and Integrin- $\alpha 8$ -staining of MCs. Scale bar 20 μm . Results in (C) and (D) are presented as mean \pm SD of at least $n = 120$ glomeruli fluorescent measurements of $n = 6$ mice per NP sample. Levels of statistical significance are indicated as **** $p \leq 0.0001$. n.s.: non-significant.

Taken together these results clearly show that size-mediated targeting is a necessary prerequisite to reach the mesangium, but insufficient to achieve particle accumulation in MCs. NP internalization seems to be imperative to avoid mesangial clearance, which explains that particles lacking this trait (NPMeO and NPEXP) lead to the lowest glomerular fluorescence. Implementing a virus-mimetic recognition principle (NPAng-I) increases NP specificity and results in particle uptake which in turn leads

to a higher MC-accumulation. However, facilitating the target cell recognition *via* an initial virus-like cell attachment (NPEXPAng-I) significantly enhances the NP's targeting potential, a result of a combined effect of the two ligands, as shown by the *in vitro* studies. Furthermore, the enhanced functionalization of NPEXPAng-I does not lead to a decrease in the particle blood residence. Generally, NPs are coated with polymers such as PEG, which increase their circulation time [50] and decrease plasma protein adsorption [51]. A positive effect, which is usually counteracted by ligand functionalization, as off-target cells expressing the targeted receptors can bind and interfere with the NPs. Nevertheless, quantification of the plasma NP fluorescence one hour after injection showed that NPEXPAng-I remained in circulation to the same extent as non-targeted NPMeO and significantly longer than the other targeted formulations (Figure S8C). This is probably due to a higher particle specificity resulting from a more complex cell recognition process. Overall, our results demonstrate that by closely mimicking the viral attachment and internalization and combining it with an optimal NP size we were able to develop NPs that target and accumulate in MCs.

The presented results are of immediate relevance for the delivery of drugs to MCs. Even though, previous studies found that nanomaterials enter the mesangium, they had been carried out mainly under pathological conditions [52–57], associated with an increased vascular permeability and inflammation [58]. This explains why the NPs that were used had diameters as big as 400 nm [59] which is far above the 80 nm size limit of endothelial fenestration permeability found under physiological conditions [22]. Even though such particles might be beneficial to deliver drugs to halt tissue damage once a certain disease state is established, they may not be useful to prevent its outbreak. In the initial phases of DN, for example, there are little morphological changes which can hinder mesangial particle deposition [60]. In contrast, the particles we suggest, would enable a high NP accumulation under physiological conditions which could be used to stop or slow down disease development in an early phase. As follow up experiments, it would be interesting to investigate how the particles behave in a diabetic animal model, where the target expression levels could vary. In this regard, a higher particle MC-accumulation would be expected due to an overexpression of ACE under diabetic conditions [61]. Another field of application could be the control of vascular endothelial growth factor type A regulation (VEGF-A) inside glomeruli. It has been shown that unphysiologically high or low VEGF-A levels can cause renal disease [62]. MCs could be used to balance these levels by recombinant VEGF-A production or antiangiogenic drugs.

Beyond these rather concrete therapeutic implications our findings also shed light on the need for a more rigorous NP design for cell identification *in vitro* and *in vivo*. NP biodistribution following systemic administration always entails a high material loss

to clearance organs, such as the liver and the spleen [63] which is also the fate of virus particles [64]. Since NPs are distributed in the organism typically by passive transport mechanisms, their appearance in a specific tissue is a matter of their physicochemical properties. However, the fraction of particles accumulating in a tissue can be increased if they are able to actively interact with the cells of interest. Thereby, it is not sufficient to outfit NPs with one or more ligands that bind to respective receptors to confirm a cell's identity. Our particles demonstrate quite clearly that viral strategies of a stepwise cell identification are more advantageous. More so, it is not enough to only mimic the sequential viral internalization (NPAng-I). Our results show that incorporating an additional attachment step (NPEXPAng-I) is necessary to increase the target tissue *in vivo* accumulation. This confirms that the viral attachment is not only essential for viral cell recognition but also for optimal nanomaterial targeting. Furthermore, performing the attachment through an antagonist for the same receptor that is responsible in a subsequent step for agonist-mediated particle uptake does not impede NP internalization.

For cell identification, receptors that belong to the family of GPCRs, such as the AT1R we used in this study, are of particularly high value since the consequences of a positive outcome of an individual cell check can be determined by choosing the type of ligand that is used for the explorative interaction [25]. Thus, by carefully selecting the targets we use for the interaction and the type of ligand, we can outfit particles with a logic that may allow for an identification of even more concealed target cells than we investigated in this study. An example could be local ocular applications in retinal tissue in which a particle would need to be able to distinguish between the more than 60 cell types that are present [65].

4 Conclusion

We could show that virus-mimetic NPs that triple check cell identity are subject to an enhanced NP accumulation in the targeted MCs *in vivo*. By combining an antagonistic ligand, mimicking initial cell attachment of viruses, with an enzyme mediated target cell recognition process, our particles had an outstandingly high *in vitro* target avidity together with an exceptional target cell specificity. We could also demonstrate that the simultaneous hetero-multivalent binding of a particle-tethered agonist and antagonist for the same GPCR leads to particle uptake which, to the best of our knowledge, has never been shown before. Overall, our results suggest that non-specific size-mediated passive targeting is not sufficient to achieve a satisfactory particle accumulation in MCs. Even traditional particle functionalization with a single ligand appears to be an insufficient approach. However, by mimicking the intricate multistep viral target cell

Conclusion

binding and recognition process we obtained particles that are able to identify and accumulate in MCs. This will open new options for the delivery of drugs for the treatment of renal diseases, such as DN for which we are lacking an efficient therapy.

References

- [1] Mammen M, Choi SK, Whitesides GM. Polyvalent interactions in biological systems: Implications for design and use of multivalent ligands and inhibitors. *Angew Chemie - Int Ed* 1998; 37: 2754–2794.
- [2] Weissleder R, Kelly K, Sun EY, et al. Cell-specific targeting of nanoparticles by multivalent attachment of small molecules. *Nat Biotechnol* 2005; 23: 1418–1423.
- [3] Ringsdorf H. Structure and Properties of Pharmacologically Active Polymers. *J Polym Sci Polym Symp* 1975; 153: 135–153.
- [4] Hong S, Leroueil PR, Majoros IJ, et al. The Binding Avidity of a Nanoparticle-Based Multivalent Targeted Drug Delivery Platform. *Chem Biol* 2007; 14: 107–115.
- [5] Wilhelm S, Tavares AJ, Dai Q, et al. Analysis of nanoparticle delivery to tumours. *Nat Rev Mater* 2016; 1: 1–12.
- [6] Modery-Pawlowski CL, Sen Gupta A. Heteromultivalent ligand-decoration for actively targeted nanomedicine. *Biomaterials* 2014; 35: 2568–2579.
- [7] Boulant S, Stanifer M, Lozach P-Y. Dynamics of virus-receptor interactions in virus binding, signaling, and endocytosis. *Viruses* 2015; 7: 2794–815.
- [8] Marsh M, Helenius A. Virus Entry: Open Sesame. *Cell* 2006; 124: 729–740.
- [9] Maslanka Figueroa S, Veser A, Abstiens K, et al. Influenza A virus mimetic nanoparticles trigger selective cell uptake. *Proc Natl Acad Sci* 2019; 116: 9831–9836.
- [10] Lloyd JW. *Foundations of Logic Programming*. Springer Berlin Heidelberg, 1987.
- [11] Wickham TJ, Mathias P, Cheresch DA, et al. Integrins $\alpha\beta 3$ and $\alpha\beta 5$ promote adenovirus internalization but not virus attachment. *Cell* 1993; 73: 309–319.
- [12] Grove J, Marsh M. The cell biology of receptor-mediated virus entry. *J Cell Biol* 2011; 195: 1071–82.
- [13] Smith AE, Helenius A. How viruses enter animal cells. *Science* 2004; 304: 237–42.
- [14] Doms RW. Basic Concepts: A Step-by-Step Guide to Viral Infection. In: *Viral Pathogenesis: From Basics to Systems Biology: Third Edition*. Elsevier, 2016, pp. 29–40.
- [15] Jones JC, Turpin EA, Bultmann H, et al. Inhibition of Influenza Virus Infection by a Novel Antiviral Peptide That Targets Viral Attachment to Cells. *J Virol* 2006;

- 80: 11960–11967.
- [16] Schlöndorff D, Banas B. The Mesangial Cell Revisited: No Cell Is an Island. *J Am Soc Nephrol* 2009; 20: 1179–1187.
- [17] Scindia YM, Deshmukh US, Bagavant H. Mesangial pathology in glomerular disease: targets for therapeutic intervention. *Adv Drug Deliv Rev* 2010; 62: 1337–1343.
- [18] Nguyen TQ, Goldschmeding R. The Mesangial Cell in Diabetic Nephropathy. In: *Diabetic Nephropathy*. Springer International Publishing, 2019, pp. 143–151.
- [19] International Diabetes Federation. IDF Diabetes Atlas. *IDF Diabetes Atlas, 8th Ed* 2017; 1–150.
- [20] Dronavalli S, Duka I, Bakris GL. The pathogenesis of diabetic nephropathy. *Nat Clin Pract Endocrinol Metab* 2008; 4: 444–452.
- [21] Kok HM, Falke LL, Goldschmeding R, et al. Targeting CTGF, EGF and PDGF pathways to prevent progression of kidney disease. *Nat Rev Nephrol* 2014; 10: 700–711.
- [22] Hang C, Choi J, Zuckerman JE, et al. Targeting kidney mesangium by nanoparticles of defined size. *Proc Natl Acad Sci U S A* 2011; 108: 6656–6661.
- [23] Luft FC, Aronoff GR, Evan AP, et al. Effects of moxalactam and cefotaxime on rabbit renal tissue. *Antimicrob Agents Chemother* 1982; 21: 830–5.
- [24] Elema JD, Hoyer JR, Vernier RL. The glomerular mesangium: Uptake and transport of intravenously injected colloidal carbon in rats. *Kidney Int* 1976; 9: 395–406.
- [25] Hild W, Pollinger K, Caporale A, et al. G protein-coupled receptors function as logic gates for nanoparticle binding and cell uptake. *Proc Natl Acad Sci U S A* 2010; 107: 10667–72.
- [26] Hennig R, Pollinger K, Vesper A, et al. Nanoparticle multivalency counterbalances the ligand affinity loss upon PEGylation. *J Control Release* 2014; 194: 20–27.
- [27] Qian H, Wohl AR, Crow JT, et al. A Strategy for Control of “Random” Copolymerization of Lactide and Glycolide: Application to Synthesis of PEG-b-PLGA Block Polymers Having Narrow Dispersity. *Macromolecules* 2011; 44: 7132–7140.
- [28] Abstiens K, Maslanka Figueroa S, Gregoritz M, et al. Interaction of functionalized nanoparticles with serum proteins and its impact on colloidal

Chapter 5: Nanoparticle Mimicking Viral Cell Recognition Strategies

- stability and cargo leaching. *Soft Matter* 2019; 15: 709–720.
- [29] Abstiens K, Gregoritz M, Goepferich AM. Ligand Density and Linker Length are Critical Factors for Multivalent Nanoparticle–Receptor Interactions. *Appl Mater Interfaces* 2019; 11: 1311–1320.
- [30] Childs CE. The determination of polyethylene glycol in gamma globulin solutions. *Microchem J* 1975; 20: 190–192.
- [31] Rabanel J-M, Faivre J, Tehrani SF, et al. Effect of the Polymer Architecture on the Structural and Biophysical Properties of PEG–PLA Nanoparticles. *ACS Appl Mater Interfaces* 2015; 7: 10374–10385.
- [32] Grynkiewicz G, Poenie M, Tsien RY. A New Generation of Ca²⁺ Indicators with Greatly Improved Fluorescence Properties*. *J Biol Chem* 1985; 260: 3440–3450.
- [33] Schneider CA, Rasband WS, Eliceiri KW. NIH Image to ImageJ: 25 years of image analysis. *Nat Methods* 2012; 9: 671–675.
- [34] Fessi H, Puisieux F, Devissaguet JP, et al. Nanocapsule formation by interfacial polymer deposition following solvent displacement. *Int J Pharm* 1989; 55: R1–R4.
- [35] Yang ZL, Li XR, Yang KW, et al. Amphotericin B-loaded poly(ethylene glycol)–poly(lactide) micelles: Preparation, freeze-drying, and in vitro release. *J Biomed Mater Res Part A* 2008; 85A: 539–546.
- [36] Angioletti-Uberti S. Exploiting Receptor Competition to Enhance Nanoparticle Binding Selectivity. *Phys Rev Lett* 2017; 118: 1–5.
- [37] Zuckerman JE, Davis ME. Targeting Therapeutics to the Glomerulus With Nanoparticles. *Adv Chronic Kidney Dis* 2013; 20: 500–507.
- [38] Verma A, Stellacci F. Effect of Surface Properties on Nanoparticle–Cell Interactions. *Small* 2010; 6: 12–21.
- [39] de Gasparo M, Catt KJ, Inagami T, et al. International Union of Pharmacology. XIII. The angiotensin II receptors. *Pharmacol Rev* 2000; 52: 415–472.
- [40] Sachinidis A, Ko Y, Weisser P, et al. EXP3174, a metabolite of losartan (MK 954, DuP 753) is more potent than losartan in blocking the angiotensin II-induced responses in vascular smooth muscle cells. *J Hypertens* 1993; 11: 155–162.
- [41] Johnson BJ, Russ Algar W, Malanoski AP, et al. Understanding enzymatic acceleration at nanoparticle interfaces: Approaches and challenges. *Nano Today* 2014; 9: 102–131.
- [42] Hein L, Meinel L, Pratt RE, et al. Intracellular Trafficking of Angiotensin II and

- its AT 1 and AT 2 Receptors: Evidence for Selective Sorting of Receptor and Ligand. *Mol Endocrinol* 1997; 11: 1266–1277.
- [43] Rice GI, Thomas DA, Grant PJ, et al. Evaluation of angiotensin-converting enzyme (ACE), its homologue ACE2 and neprilysin in angiotensin peptide metabolism. *Biochem J* 2004; 383: 45–51.
- [44] Eisenthal R, Danson MJ, Hough DW. Catalytic efficiency and k_{cat}/K_M : a useful comparator? *Trends Biotechnol* 2007; 25: 247–249.
- [45] Hennig R, Ohlmann A, Staffel J, et al. Multivalent nanoparticles bind the retinal and choroidal vasculature. *J Control Release* 2015; 220: 265–274.
- [46] Bkaily G, Sleiman S, Stephan J, et al. Angiotensin II AT 1 receptor internalization, translocation and de novo synthesis modulate cytosolic and nuclear calcium in human vascular smooth muscle cells. *Can J Physiol Pharmacol* 2003; 81: 274–287.
- [47] Liu AP, Aguet F, Danuser G, et al. Local clustering of transferrin receptors promotes clathrin-coated pit initiation. *J Cell Biol* 2010; 191: 1381–93.
- [48] Puthenveedu MA, von Zastrow M. Cargo Regulates Clathrin-Coated Pit Dynamics. *Cell* 2006; 127: 113–124.
- [49] Kolb RJ, Woost PG, Hopfer U. Membrane Trafficking of Angiotensin Receptor Type-1 and Mechanochemical Signal Transduction in Proximal Tubule Cells. *Hypertension* 2004; 44: 352–359.
- [50] Klibanov AL, Maruyama K, Torchilin VP, et al. Amphipathic polyethyleneglycols effectively prolong the circulation time of liposomes. *FEBS Lett* 1990; 268: 235–237.
- [51] Gref R, Lück M, Quellec P, et al. ‘Stealth’ corona-core nanoparticles surface modified by polyethylene glycol (PEG): Influences of the corona (PEG chain length and surface density) and of the core composition on phagocytic uptake and plasma protein adsorption. *Colloids Surfaces B Biointerfaces* 2000; 18: 301–313.
- [52] Liao J, Hayashi K, Horikoshi S, et al. Effect of Steroid-Liposome on Immunohistopathology of IgA Nephropathy in ddY Mice. *Nephron* 2001; 89: 194–200.
- [53] Suana AJ, Tuffin G, Frey BM, et al. Single Application of Low-Dose Mycophenolate Mofetil-OX7-Immunoliposomes Ameliorates Experimental Mesangial Proliferative Glomerulonephritis. *J Pharmacol Exp Ther* 2011; 337: 411–422.
- [54] Ito K, Chen J, Khodadadian JJ, et al. Liposome-mediated transfer of nitric oxide

Chapter 5: Nanoparticle Mimicking Viral Cell Recognition Strategies

- synthase gene improves renal function in ureteral obstruction in rats. *Kidney Int* 2004; 66: 1365–1375.
- [55] Gerald T, Waelti E, Huwyler J, et al. Immunoliposome Targeting to Mesangial Cells: A Promising Strategy for Specific Drug Delivery to the Kidney. *J Am Soc Nephrol* 2005; 16: 3295–3305.
- [56] Scindia Y, Deshmukh U, Thimmalapura P-R, et al. Anti- α 8 integrin immunoliposomes in glomeruli of lupus-susceptible mice: A novel system for delivery of therapeutic agents to the renal glomerulus in systemic lupus erythematosus. *Arthritis Rheum* 2008; 58: 3884–3891.
- [57] Morimoto K, Kondo M, Kawahara K, et al. Advances in Targeting Drug Delivery to Glomerular Mesangial Cells by Long Circulating Cationic Liposomes for the Treatment of Glomerulonephritis. *Pharm Res* 2007; 24: 946–954.
- [58] Satchell SC, Braet F. Glomerular endothelial cell fenestrations: an integral component of the glomerular filtration barrier. *Am J Physiol Physiol* 2009; 296: F947–F956.
- [59] Tomita N, Morishita R, Yamamoto K, et al. Targeted gene therapy for rat glomerulonephritis using HVJ-immunoliposomes. *J Gene Med* 2002; 4: 527–535.
- [60] Zuckerman JE, Gale A, Wu P, et al. siRNA Delivery to the Glomerular Mesangium Using Polycationic Cyclodextrin Nanoparticles Containing siRNA. *Nucleic Acid Ther* 2015; 25: 53–64.
- [61] Vidotti DB, Casarini DE, Cristovam PC, et al. High glucose concentration stimulates intracellular renin activity and angiotensin II generation in rat mesangial cells. *Am J Physiol Physiol* 2004; 286: F1039–F1045.
- [62] Eremina V, Sood M, Haigh J, et al. Glomerular-specific alterations of VEGF-A expression lead to distinct congenital and acquired renal diseases. *J Clin Invest* 2003; 111: 707–16.
- [63] Tsoi KM, MacParland SA, Ma X-Z, et al. Mechanism of hard-nanomaterial clearance by the liver. *Nat Mater* 2016; 15: 1212–1221.
- [64] Peng K-W, Frenzke M, Myers R, et al. Biodistribution of Oncolytic Measles Virus After Intraperitoneal Administration into IfnarTM-CD46^{Ge} Transgenic Mice. *Hum Gene Ther* 2003; 14: 1565–1577.
- [65] Masland RH. Cell Populations of the Retina: The Proctor Lecture. *Investig Ophthalmology Vis Sci* 2011; 52: 4581.

Chapter 5 - Supplementary Information

**Nanoparticles Mimicking Viral Cell
Recognition Strategies are Superior
Transporters into Mesangial Cells**

1 Target-cell recognition of virus-mimetic NPs

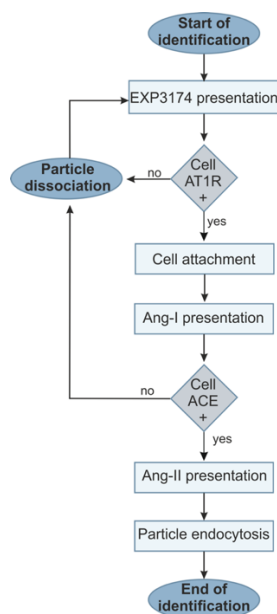
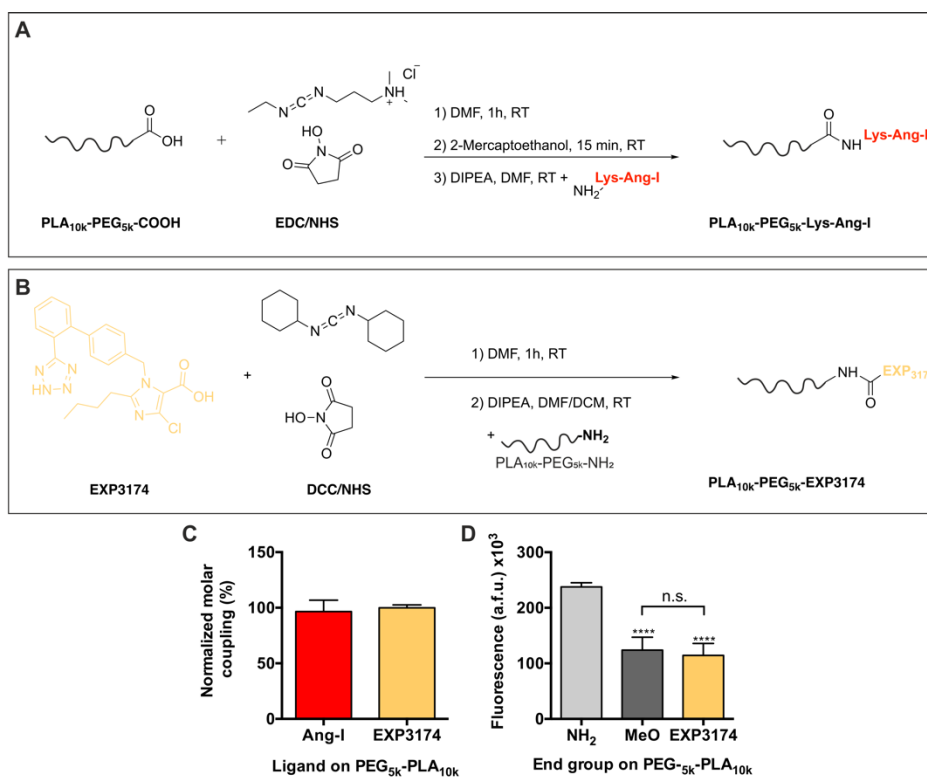


Figure S1. Flow chart. Exemplification of the triple target cell recognition of virus-mimetic NPs.

2 Polymer ligand modification



Chapter 5: Nanoparticles Mimicking Viral Cell Recognition Strategies

Figure S2. Ligand coupling to PEG-PLA block copolymers. (A) Lys-Ang-I and (B) EXP3174 were linked to carboxylic acid- or amine- ended PEG_{5k}-PLA_{10k} using EDC/NHS or DCC/NHS chemistry, respectively. (C) Complete polymer functionalization shown by the quantification of the molar ligand and PEG content. For that, polymers were solubilized in acetonitrile at a concentration of 40 mg mL⁻¹ and precipitated in stirring ultrapure water to create polymer micelles (final concentration 1 mg mL⁻¹). Coupled Ang-I was quantified using a Pierce BCA assay kit after the manufacturer's instructions using a FLUOstar Omega microplate reader (BMG Labtech). EXP3174 was fluorescently quantified at λ_{ex} =250 nm and λ_{em} =370 nm using a LS-5S fluorescence plate reader (PerkinElmer). (D) Absence of unreacted NH₂ polymer end groups on EXP3174-modified-polymer was determined using fluorescamine [1]. A Student's t-test was performed using GraphPad Prism 6.0 to assess statistical significance. Levels of statistical significance are indicated as ****p \leq 0.0001 comparing the fluorescence of MeO- and EXP3174- with NH₂-terminated PEG_{5k}-PLA_{10k}.

3 Maximum calcium signal and inhibition by NPEXP

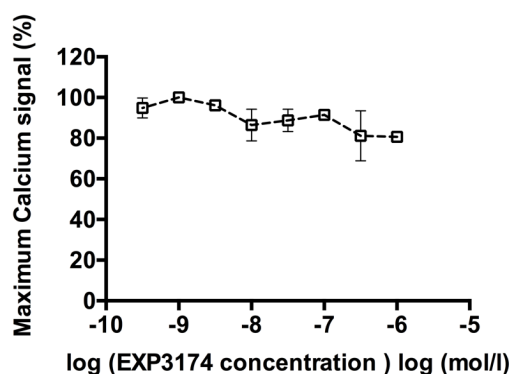


Figure S3. rMCs (90,000 cells per well) were stimulated simultaneously with Ang-II (400 nM) and NPEXP and the resulting intracellular calcium response measured immediately for 1 minute. At the used NPEXP concentrations, the EXP3174 ligand did not inhibit the agonist-triggered calcium signal during the assay duration. Therefore, the influence of EXP3174 on the Ang-II-measurement was considered negligible. Results are shown as mean \pm SD of at least n = 3 measurements.

4 Time-dependent NP uptake

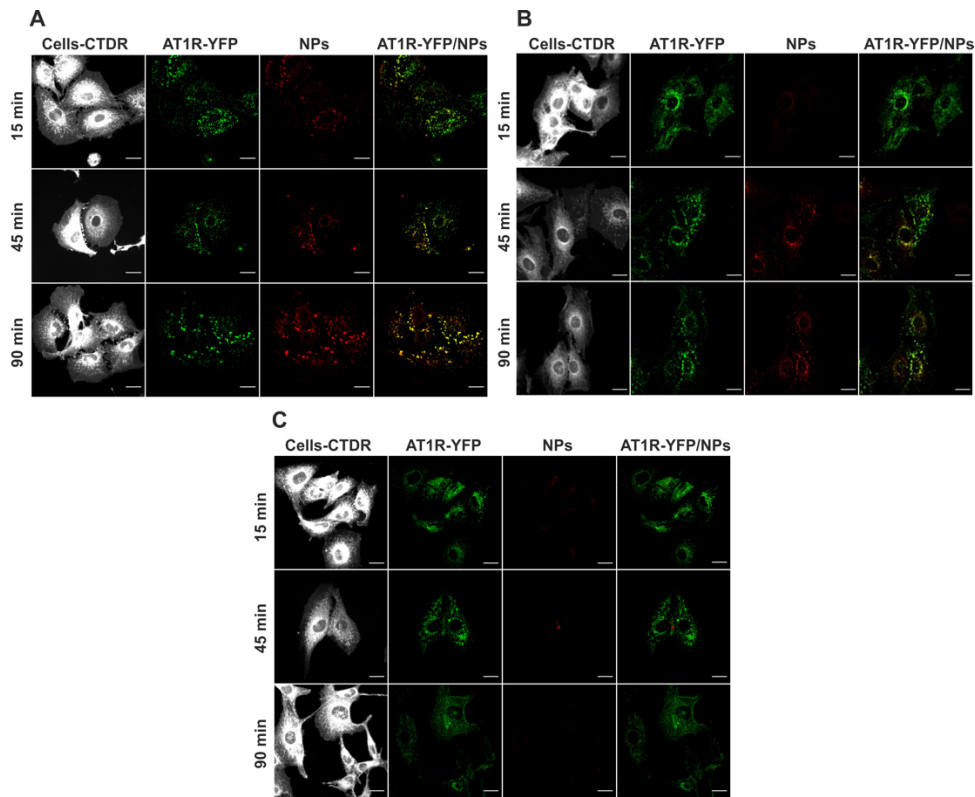


Figure S4. Uptake of different particle formulations over time in AT1R positive pAT1R-rMCs analysed through CLSM. (A) NPEXP are not internalized in the cell line and mostly locate on the cellular membrane and filipodia between cells forming big clusters over time. Receptor binding is shown by the colocalization of NP- and receptor- associated fluorescence. (B) NPAng-I are internalized by the cells as depicted by their cytoplasmic localization. (C) NPMeO do not associate with cells due to their lack of a tethered ligands enabling a specific targeting. White: cells; Green: AT1R-YFP; Red: NP-formulations. Scale bar 20 μ m.

5 Particle functionalization and steric hindrance

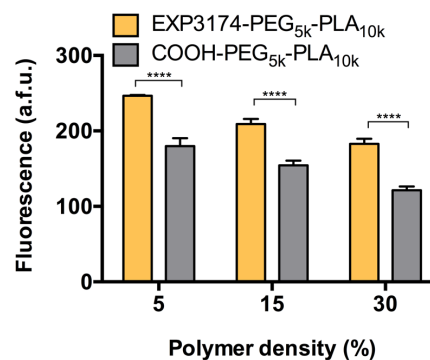


Figure S5. EXP3174 counterbalances the uptake decrease due to steric hindrance of the Ang-I ligand by long polymer chains on NPEXPAng-I. NPAng-I (grey) with 20% Ang-I density were prepared with

Chapter 5: Nanoparticles Mimicking Viral Cell Recognition Strategies

varying polymer densities of COOH-PEG_{5k}-PLA10k and analysed for their cellular uptake using flow cytometry. Concomitantly, NPEXPAng-I (yellow) were prepared with varying densities of EXP3174-PEG_{5k}-PLA10k to compare the effect of the second ligand on the steric hindrance of Ang-I. Functionalization of long polymer chains with EXP3174 on NPEXPAng-I counterbalanced the decreased uptake due to steric hindrance of the Ang-I ligand when adding non-functionalized long polymers, and significantly increased the particle internalization. Results are presented as mean \pm SD of at least $n = 3$ measurements. A 2-way ANOVA with Sidak's multiple comparisons test was performed using GraphPad Prism 6.0 to assess statistical significance. Levels of statistical significance are indicated as **** $p \leq 0.0001$.

6 Particle specificity

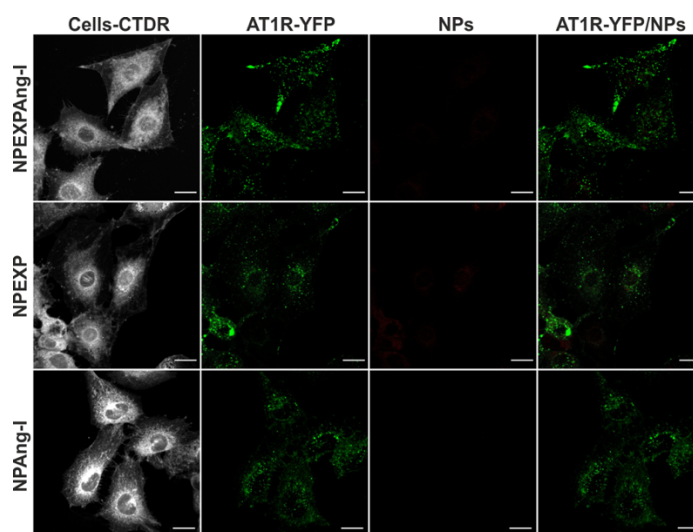


Figure S6. Specificity of the NP uptake analysed through CLSM. Cells were preincubated for 30 minutes with free EXP3174 prior to the addition of the different NP formulations (NPEXPAng-I, NPAng-I and NPEXP). Inhibition of the target receptor resulted in the suppression of the particle-associated fluorescence. Scale bar 20 μ m.

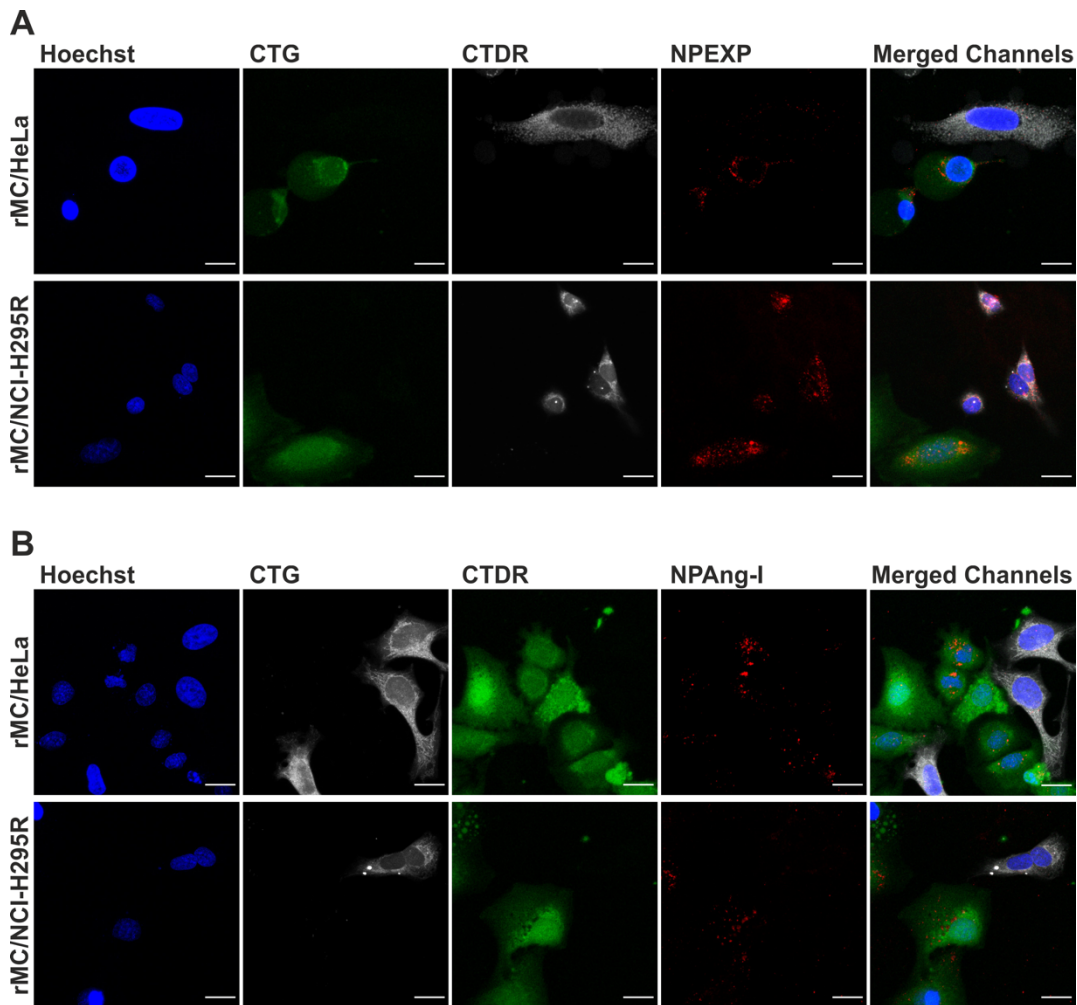


Figure S7. Uptake of (A) NPEXP and (B) NPAng-I in co-culture of target and off-target cells. NPEXP show accumulation in rMCs and NCI-H205R cells, as they both carry the AT1R. Contrary, the co-culture of rMCs and HeLa cells shows preferential accumulation of NPEXP in rMCs, as HeLa cells express only minor amounts of the receptor on the cell membrane. NPAng-I show a higher specificity as they accumulate in target rMCs, which carry the necessary equipment for their internalization (the ACE and the AT1R), over off-target cells lacking ACE (HeLa or NCI-H295R cells). Blue: cell nuclei; White: off-target cells (HeLa or NCI-H295R); Green: target cells (rMCs); Red: NPs. Scale bar 20 μ m.

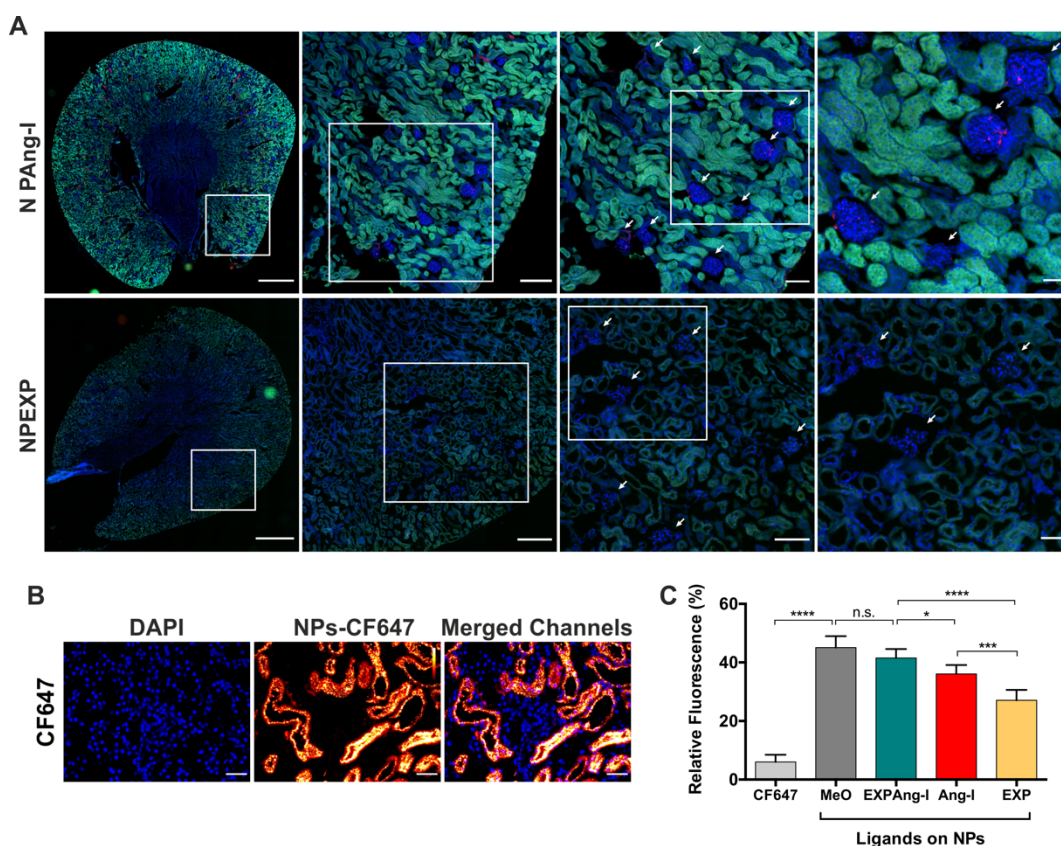
7 *In vivo* distribution of different NP formulations

Figure S8. *In vivo* distribution of different NP formulations. (A) Distribution of NPAng-I and NPEXP in mice kidneys. NPAng-I show low NP-associated fluorescence in the majority of glomeruli (white arrows) contrary to NPEXP which did not accumulate in this area. From left to right squared out regions are shown as magnifications. Scale bar from left to right 900, 200, 100 and 50 μ m. Blue: DAPI staining of cell nuclei; Green: tissue autofluorescence; Red: NPs. (B) Kidney distribution of the free CF647 dye used to label the NPs. Strong fluorescence could be detected in the tubular area, with no fluorescence in the glomeruli (white circle), as due to its low molecular size it can be freely filtrated. (C) Plasma residence of different NP-formulations after 1-hour circulation in NRMI mice normalized to the fluorescence measured 5 minutes after injection. NP-associated fluorescence in plasma was measured using a FLUOstar Omega microplate reader (BMG Labtech) with excitation and emission wavelengths of 640 and 680 nm, respectively. Fluorescence 1 hour after injection was correlated to the initial fluorescence 5 minutes after injection. Non-targeted NPs (NPMEO) show the highest blood circulation time due to the stealth effect conferred by the PEG-shell. This is matched by NPEXPAng-I even though ligands cover 40% of the NP surface, which usually decreases a particles stealth effect. They depict a significant higher fluorescence in plasma after 1 h compared to particles functionalized with only one ligand (NPAng-I and NPEXP). NPAng-I, which carry a specific two-step virus-mimetic recognition mechanism also show a significant superior blood residence than NPEXP, which represent commonly targeted NPs. As a control, the free dye used to label the particles (CF647) was injected into mice, which rapidly disappears from the blood circulation due to its free filtration. Results in c) are presented as mean \pm SD of at least $n = 6$ samples. A Student t test was performed using GraphPad Prism 6.0 to assess statistical significance. Levels of statistical significance are indicated as * $p \leq 0.05$, *** $p \leq 0.001$ and **** $p \leq 0.0001$. n.s.: non-significant.

8 Polymer characterization

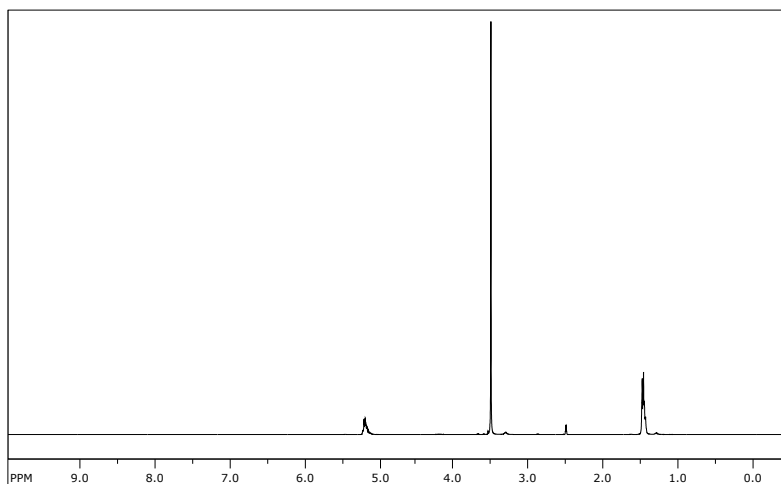


Figure S9. $^1\text{H-NMR}$ (DMSO- d_6 , 400 MHz) spectra of $\text{NH}_2\text{-PEG}_{5\text{k}}\text{-PLA}_{010\text{k}}$. δ (ppm): 1.44 ppm ($-\text{C}(\text{CH}_3)\text{H}-$), 2.50 ppm (solvent peak), 3.30 ppm ($\text{H}_3\text{COCH}_2\text{CH}_2-$), 3.49 ppm ($-\text{OCH}_2\text{CH}_2-$), 4.21 ppm ($-\text{OCH}_2\text{CH}_2\text{-O}(\text{CO})-$), 5.17 ppm ($-\text{C}(\text{CH}_3)\text{H}-$).

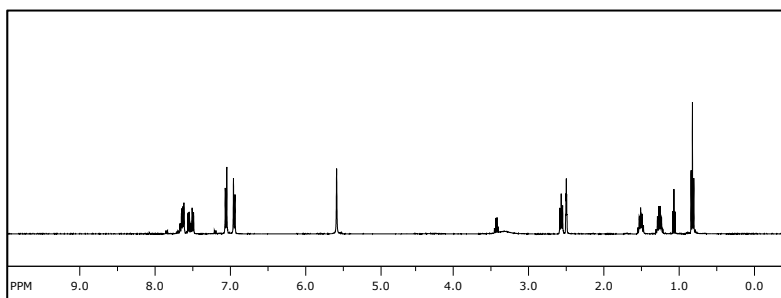


Figure S10. $^1\text{H-NMR}$ (DMSO- d_6 , 400 MHz) spectra of EXP3174. δ (ppm): 0.79 ppm ($-\text{CH}_3\text{CH}_2$), 1.25 ($\text{CH}_3\text{CH}_2\text{CH}_2$), 1.48 ($\text{CH}_2\text{CH}_2\text{CH}_2$), 2.50 (solvent peak), 2.56 ppm ($\text{CH}_2\text{CH}_2\text{CN}_2$), 5.45 ppm ($\text{NCH}_2\text{C}(\text{CH})\text{CH}$), 6.93 ppm ($=\text{CHC}(\text{H})=\text{CH}$), 7.05 ppm ($(=\text{CHC}(\text{H})=\text{CH})$), 7.51 ppm ($(=\text{CHC}(\text{H})=\text{CH})$), 7.98 ppm ($=\text{CHC}(\text{H})=\text{C}$).

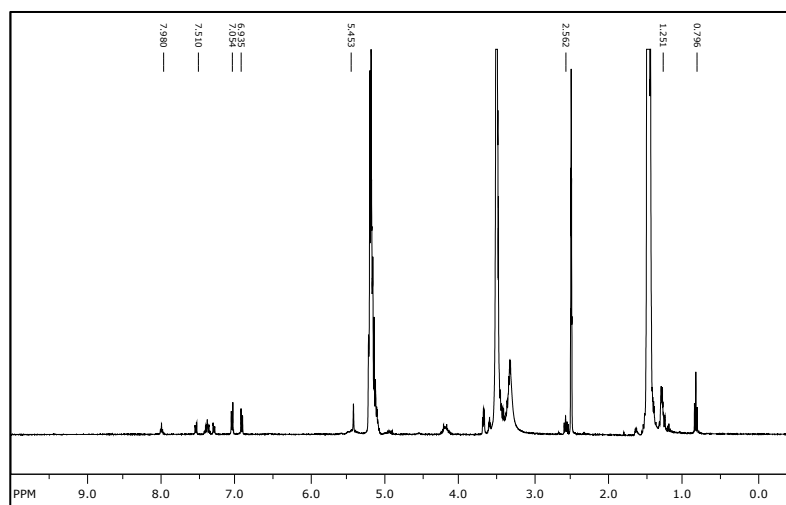


Figure S11. $^1\text{H-NMR}$ (DMSO- d_6 , 400 MHz) spectra of EXP3174-PEG $_{5k}$ -PLA $_{10k}$. Characteristic EXP3174 shifts (marked) confirm the successful coupling of EXP3174 to NH $_2$ -PEG $_{5k}$ -PLA $_{10k}$. δ (ppm): 0.79 ppm (-H $_3$ C-CH $_2$), 1.25 (H $_3$ C-CH $_2$ -CH $_2$), 1.44 ppm (-C(CH $_3$)H-), 1.48 (CH $_2$ CH $_2$ CH $_2$), 2.50 (solvent peak), 2.56 ppm (CH $_2$ CH $_2$ CN $_2$), 3.30 ppm (H $_3$ COCH $_2$ CH $_2$ -), 3.49 ppm (-OCH $_2$ CH $_2$ -), 4.21 ppm (-OCH $_2$ CH $_2$ -O(CO)-), 5.17 ppm (-C(CH $_3$)H-), 5.57 ppm (NCH $_2$ C(CH)CH), 6.93 ppm (=CHC(H)=CH), 7.05 ppm ((=CHC(H)=CH), 7.54 ppm ((=CHC(H)=CH), 7.65 ppm (=CHC(H)=C).

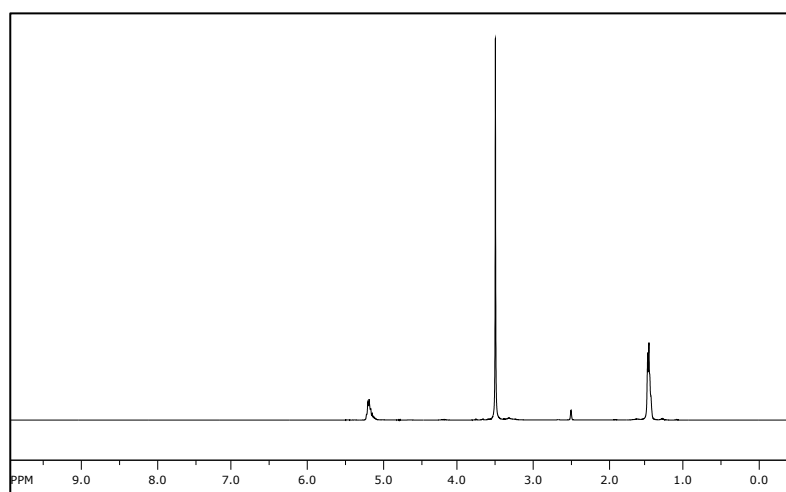


Figure S12. $^1\text{H-NMR}$ (DMSO- d_6 , 400 MHz) spectra of COOH-PEG $_{5k}$ -PLA $_{10k}$. δ (ppm): 1.46 ppm (-C(CH $_3$)H-), 2.50 ppm (solvent peak), 3.30 ppm (H $_3$ COCH $_2$ CH $_2$ -), 3.49 ppm (-OCH $_2$ CH $_2$ -), 4.19 ppm (-OCH $_2$ CH $_2$ -O(CO)-), 5.19 ppm (-C(CH $_3$)H-).

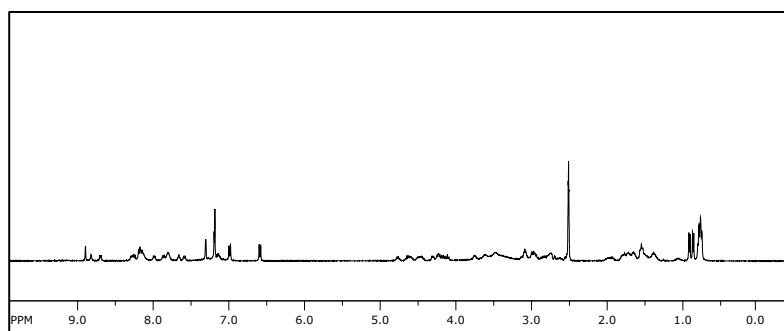


Figure S13. $^1\text{H-NMR}$ (DMSO- d_6 , 400 MHz) spectra of Lys-Ang-I. δ (ppm): 0.73 (-CH(CH₃)CH₃), 0.84 (CH₃-CH(CH₃)CHN), 2.50 (solvent peak), 6.59 ppm (=CHC(H)=CH), 7.20 ppm (=CHC(H)=CH), 8.20 ppm CO(NH)CH(CH₂)CO.

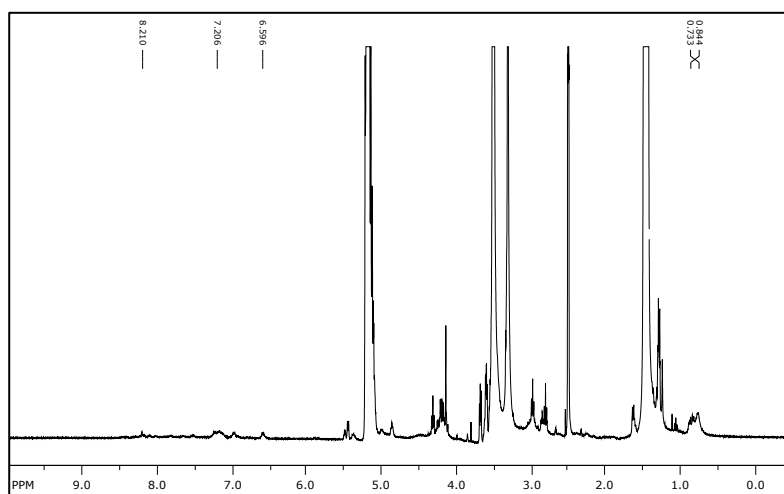


Figure S14. $^1\text{H-NMR}$ (DMSO- d_6 , 400 MHz) spectra of Ang-I- PEG_{5k}-PLA_{10k}. Characteristic Lys-Ang-I shifts (marked) confirm the successful coupling of Lys-Ang-I to COOH-PEG_{5k}-PLA_{10k}. δ (ppm): 0.73 (-CH(CH₃)CH₃), 0.84 (CH₃-CH(CH₃)CHN), 2.50 (solvent peak), 6.59 ppm (=CHC(H)=CH), 7.20 ppm (=CHC(H)=CH), 8.20 ppm CO(NH)CH(CH₂)CO.

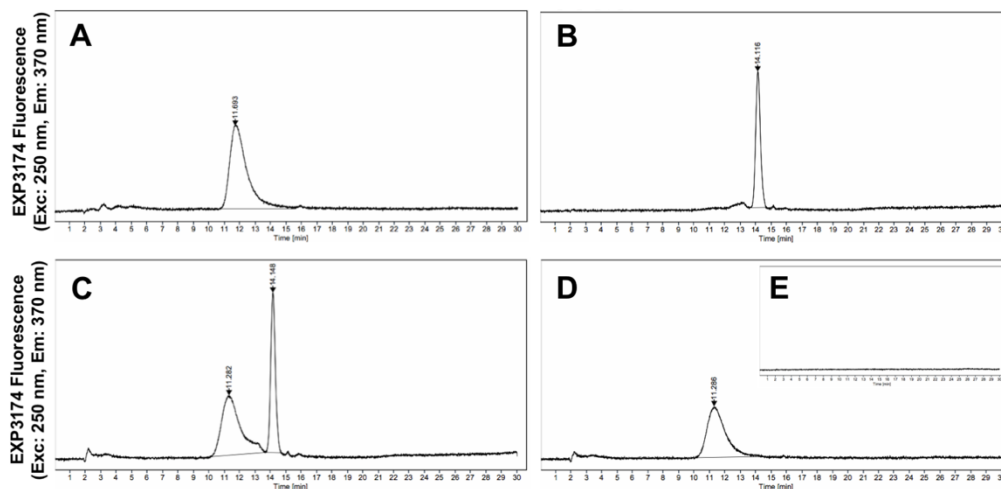


Figure S15. Coupling confirmation of EXP3174 to block copolymer PEG_{5k}-PLA_{10k}. An Agilent PLRP-S 4000A 8 μ m 150x4.6 mm column and an Agilent Infinity 1260 HPLC were used. Elution was obtained by using the following gradient of solvents A (Water/Acetonitrile (95/5) (v/v) with 0.1% TFA) and B (Acetonitrile/Water (95/5) (v/v) with 0.085% TFA): 75/25 (A/B) to 72/25 (A/B) in 5 minutes to 15/85 (A/B) in 30 minutes. Samples (10 μ L) were injected at a concentration of 10 μ M. The column was operated at 40 $^{\circ}$ C and a flow rate of 1 mL min⁻¹. EXP3174 fluorescence was excited at 250 nm and detected at 370 nm. HPLC chromatograms of (A) free EXP3174, (B) EXP-PEG_{5k}-PLA_{10k} (C), EXP-PEG_{5k}-PLA_{10k} mixed with free EXP3174, (D) COOH-PEG_{5k}-PLA_{10k} mixed with free EXP3174, and (E) COOH-PEG_{5k}-PLA_{10k}. (B) shows the absence of free EXP3174, proving the success of the purification procedure.

9 References

- [1] Smith RE, MacQuarrie R. A sensitive fluorometric method for the determination of arginine using 9,10-phenanthrenequinone. *Anal Biochem* 1978; 90: 246–255.

Chapter 6

Thermodynamic, Spatial and Methodological Considerations for the Manufacturing of Therapeutic Polymeric Nanoparticles

Published in *Pharmaceutical Research*

2020, 37 (3), 59

This chapter was published as: S. Maslanka Figueroa, D. Fleischmann, S. Beck and A. Goepferich, *Pharm. Res.* 2020, 37 (3), 59, doi: 10.1007/s11095-020-2783-4

Abstract

The purpose of this study is to evaluate fundamental parameters that dictate the effectiveness of drug loading. A model water-soluble drug lacking ionizable groups, pirfenidone (PFD), was encapsulated through nanoprecipitation in poly(ethylene glycol)-poly(lactic acid) (PEG-PLA)-poly(lactic-co-glycolic acid) (PLGA) NPs. Firstly, the thermodynamic parameters predicting drug-polymer miscibility were determined to assess the system's suitability. Then, the encapsulation was evaluated experimentally by two different techniques, bulk and microfluidic (MF) nanoprecipitation. Additionally, the number of molecules that fit in a particle core were calculated and the loading determined experimentally for different core sizes. Lastly, the effect of co-encapsulation of α -lipoic acid (LA), a drug with complementary therapeutic effects and enhanced lipophilicity, was evaluated. The thermodynamic miscibility parameters predicted a good suitability of the selected system. MF manufacturing enhanced the encapsulation efficiency by 60-90% and achieved a 2-fold higher NP cellular uptake. Considering spatial constrictions for drug encapsulation and increasing the size of the PLGA core the number of PFD molecules per NP was raised from under 500 to up to 2,000. More so, the co-encapsulation of LA increased the number of drug molecules per particle by 96%, with no interference with the release profile. In conclusion, thermodynamic, spatial and methodological parameters should be considered to optimize drug encapsulation.

1 Introduction

Nanoprecipitation [1], or solvent displacement, is a frequently used technique for the preparation of therapeutic polymer nanoparticles (NPs), as it is a simple, clean, and versatile approach [2]. More so, it enables drug encapsulation without requiring additional steps, such as covalently coupling the drug to structural particle components.

There are several elements that to some extent determine the success of a nanoprecipitation-mediated drug encapsulation, such as the physicochemical characteristics of the selected drug. As this technique involves the addition of a small volume of organic polymer phase into a large volume of aqueous phase, it has mostly been exploited for the encapsulation of lipophilic drugs that have little to no water solubility. Its application to water-soluble drugs is often inefficient, but can be improved to some extent by modulating the pH value of the water phase [3–5] or promoting electrostatic interaction with excipients [4]. Alternatively, some authors have resulted to modify the drug molecule itself [6], or released it from its salt form [2], for which doxorubicin is a common example [7]. However, these approaches are not universally applicable. For the former the presence of ionizable groups is a mandatory requirement and the latter may not be a feasible option due to the additional regulatory burdens associated with changing a drug's structure. More so, there is a lack of research regarding the encapsulation through nanoprecipitation of water-soluble molecules that lack the aforementioned criteria.

An additional element that has an impact on drug encapsulation is the thermodynamic compatibility, i.e. miscibility, of the drug and particle-forming polymers. Therefore, thermodynamic parameters such as the Flory-Huggins interaction parameter (χ_{sp}), or the solubility parameters (δ) are frequently used to assess drug-polymer miscibility [8]. However, there are other elements that can determine the successful encapsulation of a drug in a selected particle system, such as dimensional restrictions, the used nanoprecipitation method or the presence of a co-encapsulated drug molecule.

Therefore, the goal of this study was to encapsulate through nanoprecipitation a partially water-soluble drug lacking ionizable groups and evaluate different parameters dictating the drug loading.

As a drug model for our purposes we selected pirfenidone (PFD) (Figure 1). PFD is a small molecule drug, with a $\log P = 2.14$. Therefore, it would be initially considered a good candidate for encapsulation through nanoprecipitation. However, it is soluble in water up to 2 mg mL^{-1} , which is exceedingly high for this technique, due to the large volumes of water phase being used.

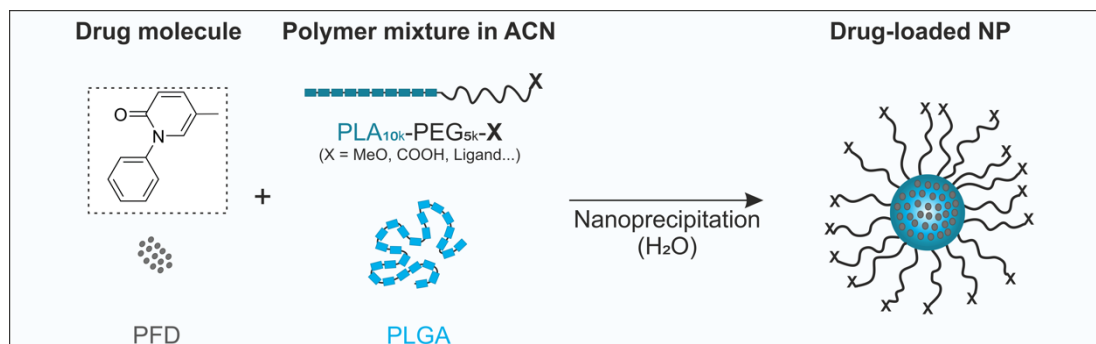


Figure 1. Encapsulation of PFD in block copolymer NPs. Particles are prepared through nanoprecipitation of organic mixtures of PEG-PLA, PLGA and the drug in aqueous medium.

PFD is an antifibrotic agent, approved for the treatment of idiopathic pulmonary fibrosis [9]. Additionally, recent studies showed its potential for the treatment of diabetic kidney disease [10, 11] and glomerulosclerosis [12]. However, it has a considerable plasma protein binding (50%) and fast elimination half-life (2.4 hours), which requires a large oral dose intake ($> 2 \text{ g day}^{-1}$) to achieve therapeutic effects [13]. This elevated daily intake prompts considerable gastrointestinal side effects which contribute to therapy discontinuation by a large number of patients [11, 14]. Therefore, it is an excellent candidate that would benefit from incorporation in a nanoparticulate system. Over the past years PFD has been encapsulated in PLGA NPs by the emulsion solvent evaporation method for the treatment of pulmonary fibrosis [15] and corneal wounds [16], in chitosan-alginate nanocarriers through the pre-gelation method for transdermal delivery [17] and in liquid crystalline nanoparticles [18]. However, it has never been encapsulated before by means of nanoprecipitation, which would considerably ease NP preparation and allow for simple cost-effective upscaling and reproducible results [19].

For our systematic investigation of the PFD encapsulation we relied on well-established poly(ethylene glycol)-poly(lactic acid) (PEG-PLA) block copolymer NPs [20] with a poly(lactic-co-glycolic acid) (PLGA)-stabilized core (Figure 1). Such particles are known for their good biocompatibility and highly tunable composition. Additionally, by modifying the PEG end-groups with ligands the particles can be targeted to receptors on the cellular membrane to increase their specificity [21]. To evaluate the suitability of our particle system for the encapsulation of PFD we firstly estimated the compatibility of PFD with the particle-forming polymers through the calculation of thermodynamic miscibility parameters. Then, we prepared the NPs through two different nanoprecipitation techniques, bulk and microfluidic (MF) manufacturing, and assessed the drug loading. More so, we investigated the influence of the two different approaches on the NP characteristics and their interaction at cellular level. Additionally, we evaluated the spatial constrain on drug loading by

calculating the number of molecules that can fit in a single NP core and experimentally determined the influence of this parameter by preparing particles with larger cores. Finally, we investigated the effect of introducing an additional drug molecule in the formulation, α -lipoic acid (LA), on PFD encapsulation.

2 Materials and Methods

2.1 Materials

Methoxy and carboxylic acid end-functionalized PEG (MeO-PEG_{5k}-OH and COOH-PEG_{5k}-OH) with a molecular weight of 5000 Da were purchased from JenKem Technology USA Inc. (Allen, TX, USA). PFD was obtained from MedChem Express (Sollentuna, Sweden). Dulbecco's phosphate-buffered saline (DPBS) was purchased from Thermo Fisher Scientific (Waltham, MA, USA). LA, PLGA with a molecular weight of 13.4 kDa, and all other reagents and chemicals in analytical grade were purchased from Sigma Aldrich (Taufkirchen, Germany). Ultrapure water for particle preparation was obtained from a Millipore Milli-Q water purification system (Billerica, MA, USA).

2.2 Compatibility of the drug and particle assembling polymers

To predict the miscibility of particle-forming polymers with either PFD or LA, different thermodynamic parameters were calculated. To that end, an ideal particle polymer distribution was assumed where PEG conforms the shell, PLGA the core, and PLA is situated at the core-shell interphase. The interference of concurring NP polymers in the miscibility was not taken into consideration. The total solubility parameters (δ) were obtained from literature values for the polymers (PEG (24.0 MPa^{1/2}) [22], PLA (22.0 MPa^{1/2}) [22] and PLGA (22.3 MPa^{1/2}) [23]), and calculated for PFD and LA using the partial solubility parameters after Kirevelen and Nijenhuis [24] determined by the group contributions methods using Equation 1-3. δ_d , δ_p , δ_h are the partial solubility parameters associated with the dispersion forces, the polar interactions and the hydrogen bonding components, respectively.

$$\delta_d = \sum \frac{F_{di}}{V} \quad (1)$$

$$\delta_p = \frac{(\sum F_{pi}^2)^{1/2}}{V} \quad (2)$$

$$\delta_h = (\sum \frac{E_{hi}}{V})^{1/2} \quad (3)$$

Chapter 6: Thermodynamic, Spatial and Methodological Considerations

The estimation of the molecular volume of PFD ($V = 119 \text{ cm}^3$) and LA ($V = 144 \text{ cm}^3$) was done by the group contribution methods after Fedors [25]. The total solubility parameters were determined using Equation 4 [24].

$$\delta^2 = \delta_d^2 + \delta_p^2 + \delta_h^2 \quad (4)$$

The differences in solubility parameters ($\Delta\delta$, $\Delta\delta_d$, $\Delta\delta_p$, $\Delta\delta_h$) were calculated by subtracting the polymer's from the drug's solubility parameter. The mixing enthalpy calculated from the total- or partial solubility parameters (ΔH_{MT} and ΔH_M , respectively) was determined according to Equation 5 [26] and 6 [27], where Φ_1 and Φ_2 and δ_1 and δ_2 represent the volume fractions and the solubility parameters of the drug and polymer, respectively.

$$\Delta H_{MT} = \phi_1\phi_2(\delta_{drug} - \delta_{polymer})^2 \quad (5)$$

$$\Delta H_M = \phi_1\phi_2[(\delta_{d1} - \delta_{d2})^2 + (\delta_{p1} - \delta_{p2})^2 + (\delta_{h1} - \delta_{h2})^2] \quad (6)$$

The Flory-Huggins interaction parameter (χ_{sp}) was calculated with the Hildebrand-Scatchard equation (Equation 7) using the obtained total solubility parameters.

$$\chi_{sp} = (\delta_1 - \delta_2)^2 \frac{V_{drug}}{RT} \quad (7)$$

2.3 Polymer synthesis

Block copolymers (PEG_{5k}-PLA_{10k}) with different PEG-end functionalization (MeO, or COOH) were synthesized after Qian et. al [28] with slight modifications as previously described by our group [29]. In brief, for the ring opening polymerization of cyclic 3,6-dimethyl-1,4-dioxane-2,5-dione (lactide), MeO-PEG_{5k}-OH and COOH-PEG_{5k}-OH were used as macroinitiators using 1,8-diazabicyclo[5.4.0]undec-7-ene (DBU) as a catalyst. As products, MeO-PEG_{5k}-PLA₁₀ and COOH-PEG_{5k}-PLA_{10k} were obtained, for non-targeted and targeted NP preparation, respectively (please refer to supplementary methods for ligand modification of the polymers).

2.4 Particle preparation *via* bulk or microfluidic nanoprecipitation

Block copolymer NPs were prepared through nanoprecipitation of PEG_{5k}-PLA_{10k} and PLGA_{13.4k} polymer mixtures. To that end, and if not indicated otherwise, PEG-PLA and PLGA were mixed at a 70:30 mass ratio in acetonitrile (ACN) to a final polymer concentration of 10 mg mL⁻¹ (1 mL). For drug-loaded particles, different amounts of PFD ranging from 25 µg to 10 mg (1-600-fold molar excess to PLGA) were added to the polymer mixture. Afterwards, for bulk nanoprecipitation, they were pipetted in

stirring sterile filtrated Millipore water (5 mL) at a 1:5 organic to aqueous phase ratio to a polymer concentration of 2 mg mL⁻¹.

For MF manufacturing, the particles were prepared using the NanoAssemblr™ Benchtop (Precision NanoSystems Inc, Vancouver, Canada). Process parameters were controlled using the NanoAssemblr™ controller software (v1.09). If not noted otherwise the particles were prepared at a total flow rate (TFR) of 2 mL min⁻¹ and a flow rate ratio (FRR) of 1:5 organic to water phase. To investigate the effect on drug loading of the different microfluidic parameters, the TFR (2-12 mL min⁻¹) and the FRR (1:1-1:10) were varied.

For both preparation techniques, immediately after preparation, particles were diluted to 20 mL with Millipore water and purified and concentrated through ultracentrifugation with a 30-kDa molecular weight cutoff Microsep advance centrifugal device (Pall corporation, NY, USA) at 959 g for 20 minutes. Purification from free or adsorbed drug was performed through thoroughly washing the NPs with Millipore water and ultracentrifugation, as described above (2x).

2.5 Particle characterization

The particle size was determined through dynamic light scattering (DLS) using a ZetaSizer Nano ZS. The device was equipped with a 633 nm He-Ne laser at a backscatter angle of 173 ° (Malvern Instruments GmbH, Lappersdorf, Germany). Measurements were performed at 25 °C using Millipore water as dispersing medium and a NP concentration of 1 mg mL⁻¹. The measurement position was set at 4.65 mm and the data was recorded with Malvern Zetasizer software 7.11 (Malvern Instruments, Worcestershire, United Kingdom).

The particle PEG content was determined using a colorimetric iodine complexing assay [30] as previously described by our group [29].

The NP mass concentration was determined gravimetrically after lyophilization and the PFD content was measured photometrically after particle disruption in ACN at 300 nm using a FLUOStar Omega microplate reader (BMG Labtech, Ortenberg, Germany). The NP molar concentration (PNC) was calculated using Equation 8 where m is the NP mass determined gravimetrically after lyophilization, ρ_{NP} is the density of the particles (1.25 g cm⁻³) [31], dh is the hydrodynamic diameter of the NPs determined through DLS, N_A is the Avogadro number, and V the volume of the samples.

$$PNC = \frac{m}{\rho_{NP} \frac{4}{3} \pi \left(\frac{dh}{2}\right)^3} \times \frac{1}{N_A V} \quad (8)$$

Chapter 6: Thermodynamic, Spatial and Methodological Considerations

The encapsulation efficiency (EE) was determined using Equation 9, where m_E is the quantified mass of entrapped drug, and m_T is the total mass of drug added initially to the formulation.

$$EE (\%) = \frac{m_E}{m_T} \times 100 \quad (9)$$

The loading capacity (LC) was determined through Equation 10, where M_T is the total mass of the particle formulation.

$$LC (\%) = \frac{m_E}{M_T} \times 100 \quad (10)$$

The number of drug molecules per NP was calculated by dividing the molar concentration of the drug by the molar concentration of the NPs determined as described above.

2.6 Determination of the spatial restriction of PFD loading

To determine the number of molecules that fit inside a NP, the volume of the particle core was estimated. To that end, the mean NP size was used as a starting point. For the calculation it was considered that the PLA is located at the core-shell interface and that the PLGA and PEG form the core and shell, respectively. To estimate the core size, first the conformation of the PEG on the particle surface was investigated using the Flory radius (R_F) [32]. When the distance between polymer chains on a particle surface is smaller than the R_F , they assume an extended brush conformation. Otherwise, they take a folded mushroom configuration. The R_F can be calculated using Equation 11, where α is the length of a PEG monomer (0.278-0.358 nm) [33] and N is the number of monomers in one molecule (each monomer has the molecular weight of 44 g mol⁻¹).

$$R_F = \alpha N^{\frac{3}{5}} \quad (11)$$

The surface (S) that is taken by the polymers on the particle surface can be calculated after Gref et. al [34] using Equation 12. M_{PEG} represents the molecular weight of the PEG, and f is the mass fraction of PEG in the PEG-PLA blends. The S can be used to determine the distance between polymers (D) on the particle surface using Equation 13 [34].

$$S = \frac{6 M_{PEG}}{dh N_A f \rho_{NP}} \quad (12)$$

$$D = 2 \left(\frac{S}{\pi} \right)^{\frac{1}{2}} \quad (13)$$

The length in nm of a PEG brush can be calculated by multiplying the monomer length $\alpha = 0.35$ nm by N . This value was subtracted twice from the dh of the NP to obtain the

diameter of the particle core (d_c). The volume of the core (V_{core}) was calculated assuming a spherical shape after Equation 14, where r_c is the calculated radius of the particle core ($d_c/2$).

$$V_{core} = \frac{4}{3}\pi r_c^3 \quad (14)$$

The estimation of the molecular volume of PFD ($V_{drug} = 0.2 \text{ nm}^3$) was conducted using the group contribution methods after Fedors [25]. The number of drug molecules that are able to fit inside a single particle core were calculated through Equation 15, assuming the maximal packing efficiency of poly-sized spheres (90%) [35], a spherical molecule shape and an even drug distribution among all the particles.

$$\text{Drug molecules per NP} = \frac{V_{core}}{V_{drug}} \times 0.9 \quad (15)$$

In order to prepare particles with increasing PLGA core sizes, the PLGA content of the formulations was increased. Particles with a PEG-PLA to PLGA mass ratio of 70:30, 60:40, 50:50 and 40:60 were prepared to a total final polymer concentration of 10 mg mL^{-1} , as described above. NPs were prepared through bulk nanoprecipitation and an initial PFD mass of $25 \text{ }\mu\text{g}$, as described above.

2.7 Co-encapsulation of LA

For the co-encapsulation of LA and PFD, the NPs were prepared as described above. LA and PFD were simultaneously added to the organic polymer mixture prior to particle preparation. The PFD to LA molar ratio was varied to determine the ideal particle composition. Additionally, the initial PFD amount was set to 2 mg and LA in a molar excess (ranging from 0.1 to 3.5) was added to the different formulations. As a control, NPs only encapsulating LA at the same concentrations added to the PFD-containing formulations were prepared. As an additional control the molar excess of LA added was replaced by the same molar excess of PFD. The PFD or LA content in the formulations was determined photometrically after particle lyophilization and disruption in ACN at 300 or 334 nm, respectively, using a FLUOStar Omega microplate reader (BMG Labtech, Ortenberg, Germany). The EE and number of drug molecules per particle was determined as described above.

2.8 *In vitro* release studies

The *in vitro* release of PFD was assessed through the dialysis bag method. To that end, NPs containing PFD (NP-PFD), or PFD and LA (NP-PFD/LA) were prepared at a 70:30 PEG-PLA to PLGA mass ratio and purified as described above. An initial PFD and LA

Chapter 6: Thermodynamic, Spatial and Methodological Considerations

mass of 2 mg and 4.5 mg, respectively, were used. The samples were adjusted to a final volume of 2 mL (60 mg mL⁻¹ NPs) and placed in a 3.5-5kDa molecular weight cut off Spectrum™ Spectra/Por™ 3 RC Dialysis Membrane (Spectrum Laboratories, Inc, Rancho Dominguez, CA, USA). The dialysis membrane was introduced in a 35 mL glass vial containing 27 mL of DPBS (pH 7.3) under sink conditions. Vials were kept in a 37 °C shaking water bath and 0.5 mL samples were taken at different time points and replaced with fresh pre-warmed buffer. As a control, particles with no encapsulated drug (NPMEO), and free drug (PFD, 2.2 mg) were used. The PFD concentration was quantified at 300 nm using a FLUOStar Omega microplate reader (BMG Labtech, Ortenberg, Germany).

2.9 Statistical analysis

Statistical analysis was performed using GraphPad Prism Software 6.0. Student's t-test (Figure 3 and Figure 5A) was employed to evaluate statistical significance. Levels of statistical significance and "n" numbers for each experiment are indicated in the text and figure legends.

3 Results and Discussion

3.1 Thermodynamic considerations for PFD encapsulation

A frequent approach to estimate the compatibility of a drug in a polymer is the calculation of their thermodynamic interactions. This approach has been used by several authors to select the most suitable polymers for encapsulating a certain drug or retroactively explain experimental outcomes [26, 27, 36–38]. Here, we assessed the thermodynamic miscibility of PFD and LA with either PEG, PLA or PLGA to determine the suitability of our particle system for the selected drug(s). As depicted in Equation 16, the thermodynamic miscibility of two substances is given by the free energy of mixing (ΔG_M), where ΔH_{MT} and ΔS_M are the enthalpy and entropy of mixing, respectively. If the ΔG_M is negative, the two substances are considered mutually soluble.

$$\Delta G_M = \Delta H_{MT} - T\Delta S_M \quad (16)$$

The mixing enthalpy (ΔH_M) per volume unit for each polymer-drug can be used as an indicator for the miscibility of two substances. It is given by Equation 5 after Hildebrand [26]. For its determination the volume fractions and the solubility parameters of the drug and polymer, Φ_1 and Φ_2 and δ_1 and δ_2 respectively, are considered.

The solubility parameters for some common drugs and polymers are reported in the literature [22, 23]. Otherwise they can be calculated after van Krevelen and Nijenhuis [24] using Equation 4 by combining the contribution of the partial solubility parameters associated with the dispersion forces (δ_d), the polar interactions (δ_p) and the hydrogen bonding components (δ_h). The total- and partial solubility parameters of PFD, LA and the particle-forming polymers are depicted in Table I.

Table I. Partial and total solubility parameters for the drugs (PFD and LA) and the particle-assembling polymers.

Component	δ_d	δ_p	δ_h	δ
PFD*	20.5	9.4	7.7	23.8
LA*	22.9	2.9	10.2	25.2
PEG#[22]	20.3	9.6	6.0	24.0
PLA#[22]	19.8	4.0	6.7	22.0
PLGA#[23]	17.4	9.1	10.5	22.3

obtained from literature#, calculated*.

The miscibility of two components is promoted when their solubility parameters have similar values and thus, ΔH_{MT} tends to 0. Therefore, the differences among solubility parameters of drug and polymer ($\Delta\delta$, $\Delta\delta_d$, $\Delta\delta_p$, and $\Delta\delta_h$) can also be used to predict miscibility [37] (Table II).

Table II. Calculated differences between the solubility parameters or polarity of PFD or LA and the particle-forming polymers.

Particle component	PFD				LA			
	$\Delta\delta_d$	$\Delta\delta_p$	$\Delta\delta_h$	$\Delta\delta_t$	$\Delta\delta_d$	$\Delta\delta_p$	$\Delta\delta_h$	$\Delta\delta_t$
PEG	0.2	-0.2	1.7	-0.2	2.6	-6.7	4.2	1.2
PLA	0.7	5.4	1.0	1.8	3.1	-1.1	3.5	3.2
PLGA	3.1	0.3	-2.8	1.5	5.5	-6.2	-0.3	2.9

However, as Liu et al. pointed out, Equation 5 does only take into consideration dispersion forces [27]. As an alternative, they proposed the determination of ΔH_M taking into account all forces of the interaction by using the partial solubility parameters, as depicted in Equation 6.

The most frequently used indicator to predict the miscibility of drug molecules with different polymers is the Flory-Huggins interaction parameter (χ_{sp}) [8]. It is given by the Hildebrand-Scatchard equation (Equation 7), which takes into account the total solubility parameters (δ) of the drug and polymer in combination with the molar volume of the drug (V_{drug}). A complete miscibility is achieved when χ_{sp} is < 0.5 [24] which requires a very near match of both solubility parameters of drug and polymer.

Chapter 6: Thermodynamic, Spatial and Methodological Considerations

The closer the χ_{sp} is to zero, the more favorable interactions between the two components, and thus the better compatibility of drug and polymer.

With the determined solubility parameters (δ , δ_d , δ_p , and δ_h) (Table I) and their differences ($\Delta\delta$, $\Delta\delta_d$, $\Delta\delta_p$, and $\Delta\delta_h$) (Table II), we calculated the mixing enthalpy (ΔH_{MT} or ΔH_M), and χ_{sp} in order to predict the miscibility of our drugs with the particle system (Figure 2).

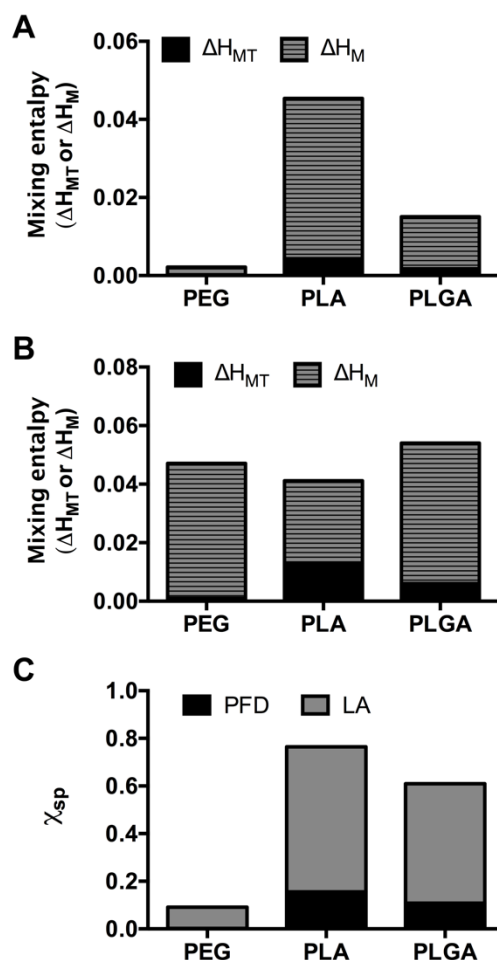


Figure 2. Prediction of the drug-polymer miscibility. Mixing enthalpy of the particle-assembling polymers and (A) PFD or (B) LA. (C) Flory-Huggins interaction parameter

Comparing the total solubility parameters (δ) (Table I), it is evident that all substances (drugs and polymers alike) have very similar values ranging between 22 - 25 MPa^{1/2}. This indicates a very good match for the selected drug and polymers, which is confirmed by the values of ΔH_{MT} and ΔH_M of the PFD- or LA-polymer mixtures (Figure 2). As pointed out by Liu et. al [27], the absolute values for ΔH_{MT} and ΔH_M differed. Furthermore, for the case of LA, a complete opposite tendency was seen (Figure 2B).

The ΔH_{MT} predicted a higher miscibility for PEG > PLGA > PLA, whereas the ΔH_M anticipated a better miscibility with PLA > PEG > PLGA. Nevertheless, the enthalpy values for all mixtures were very close to zero predicting good miscibility from a thermodynamic point of view.

As the most common used parameter to predict drug-polymer compatibility is the χ_{sp} , we also compared these values for the polymers composing our NPs. As depicted in Figure 2C, the χ_{sp} values predict total miscibility of PFD with all the polymers forming the particle with a predilection to PEG > PLGA > PLA. However, for LA it indicates low miscibility with PLGA and PLA, as $\chi_{sp} < 0.5$ only for PEG, disagreeing with the other estimated parameters. Overall, as suggested previously by other authors [27], the different parameters predicting drug-polymer miscibility varied in terms of the polymer which showed the highest miscibility. Nevertheless, except the χ_{sp} for the LA-PLA or LA-PLGA mixture, all the obtained values indicated thermodynamically favorable miscibility. In general, the highest miscibility for PFD is predicted to be with PEG, followed by PLGA and PLA (Figure S1A and Table S1). For LA the same trend in miscibility is to be expected (Figure S1B and Table S1).

As all determined parameters unanimously predict that PFD is very compatible with all the particle-forming polymers, we determined that the block copolymer PEG-PLA/PLGA particle system is an appropriate candidate for its encapsulation.

3.2 Influence of the nanoprecipitation technique on PFD loading

In order to experimentally investigate the encapsulation of PFD in PEG-PLA/PLGA block copolymer NPs, we evaluated two different manufacturing techniques, bulk or MF nanoprecipitation (Figure 3). To that end, PFD-polymer mixtures in ACN were precipitated into a water phase, either manually or with the assistance of a microfluidic device. The initial PFD addition was varied to determine its influence on the drug loading. The resulting particles were homogenous in terms of size with narrow polydispersity indexes (PDI) (Figure 3A) independent of the amount of drug added to the formulation. As frequently observed, MF manufacturing rendered particles about 15 nm smaller (~ 50 nm) compared to bulk nanoprecipitated particles (~ 65 nm). This is due to the fact that the MF mixing is faster than the time the particles need to nucleate, which does not occur during bulk nanoprecipitation [39].

For both methods an increase in initial drug concentrations reduced the EE (Figure 3B), which can be partially explained by an increase in mixing enthalpy with increasing volume fractions of drug (Figure S2). Interestingly, MF manufacturing achieved significantly higher EE, a phenomenon also described by other authors [40, 41]. As an additional advantage, MF preparation allows for a precise control over the

Chapter 6: Thermodynamic, Spatial and Methodological Considerations

manufacturing parameters, such as the TFR (Figure S3) and the FRR (Figure S4) which, in turn, permit drug loading optimization and a decrease in batch to batch variations. Furthermore, the resulting particles have the ideal size (~ 50 nm) for optimal NP-cell interaction [42] (Figure S5).

Despite the decrease in efficiency of the process with higher PFD amounts, the LC (Figure 3C) and number of drug molecules per particle (Figure 3D) increased with larger initial PFD additions. This is frequent for particles entrapping the drug during NP preparation [39], and is probably promoted in this particular case by the water solubility of PFD (~ 2 mg mL⁻¹). Interestingly, both methods achieved a comparable number of PFD molecules per particle, which is probably due to a larger number of smaller particles being produced by MF compared to bulk nanoprecipitation.

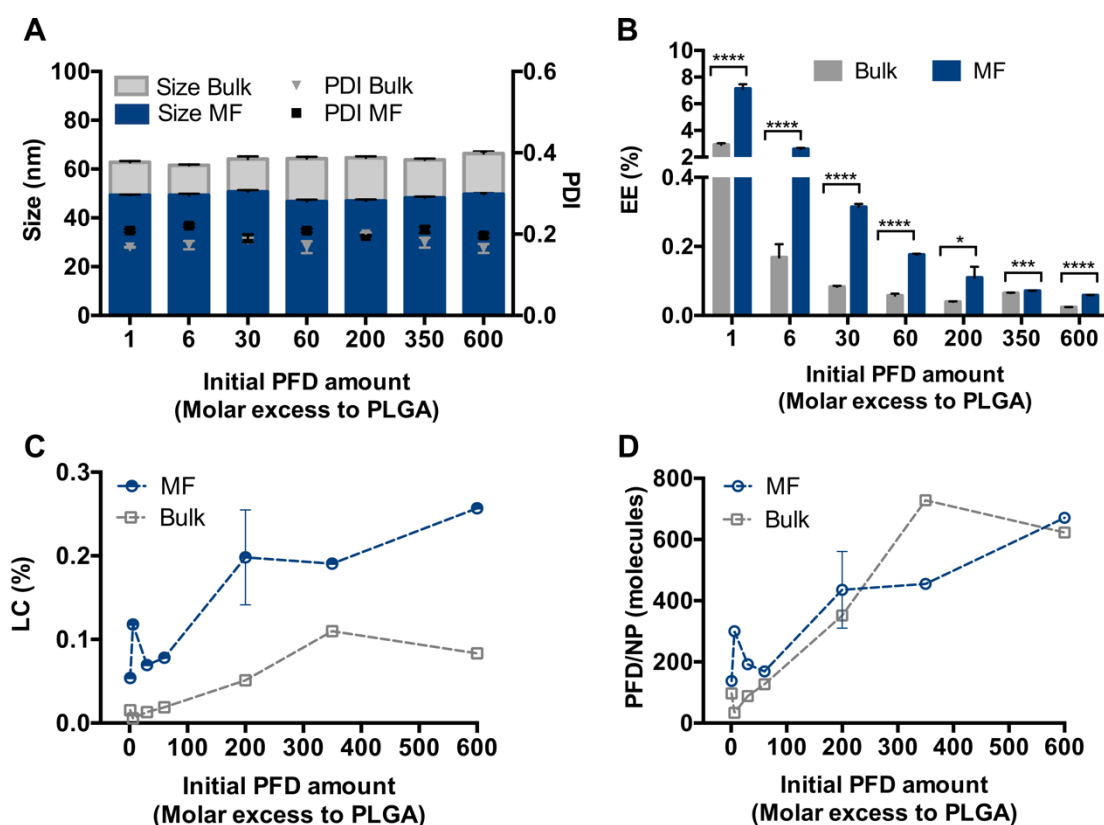


Figure 3. PFD encapsulation in block copolymer NPs through bulk and MF nanoprecipitation. Particle characterization in terms of (A) size and PDI, (B) Encapsulation Efficiency (EE) (C) Loading Capacity (LC) and (D) number of PFD molecules per particle. Results are shown as mean \pm SD of at least $n = 3$ measurements. Levels of statistical significance are indicated as * $p \leq 0.005$, *** $p \leq 0.001$, and **** $p \leq 0.0001$.

However, the low number of drug molecules that were being incorporated into the particle system (under 1000 molecules per NP) was quite surprising, considering the

high predicted miscibility of PFD with the particle-forming polymers (Figure 2). By those calculations, PFD displayed a very high compatibility with PEG. Therefore, part of the drug may end up in the particle's shell. However, during NP purification, this non-core-bound drug is washed out through the several purification steps, promoted by the water solubility of PFD, causing a lower than expected EE.

Overall, we could demonstrate that PFD encapsulation in block copolymer NPs is feasible by nanoprecipitation. Comparing both manufacturing techniques, it is apparent that MF is superior. Not only did it lead to a significantly higher EE than bulk nanoprecipitation, but this could be further enhanced up to 40% by adjusting the manufacturing parameters (Figure S3 and S4). More so, a higher cellular uptake was achieved by MF-nanoprecipitated particles (Figure S5) which is highly relevant for *in vitro* and *in vivo* applications.

3.3 Spatial limits on the drug encapsulation

Due to the low number of PFD molecules being incorporated in our particles (Figure 3), despite the high predicted miscibility with the selected polymers, we decided to estimate the number of drug molecules that would actually fit inside a single particle's core (Figure 4). For our determination we considered a particle structure as depicted in Figure 4A, where the PEG composes the shell, the PLGA forms the particle core, and the PLA is located at the core-shell interface. Given that after NP manufacturing, the particles are purified from drug that is free or entangled in the PEG shell through various washing and centrifugation steps, we considered that the particle-bound drug would mostly be located in the PLGA core. We speculated that the spatial constriction given by the core size would determine the number of PFD molecules that can be fitted inside the particle.

To determine the size of the core, the length of the PEG brush was calculated and subtracted from the overall particle diameter (~ 65 nm). To that end, we firstly determined the conformation of the PEG shell on the particle corona. For our NPs prepared at a 70:30 PEG-PLA to PLGA mass ratio, the PEG assumes an extended brush conformation. This corresponds to a length of approximately 30 nm (for a PEG with a molecular weight of ~ 4800 Da). This would leave a particle core of about 5 nm in diameter, which would allow for the encapsulation of about 200 PFD molecules per NP, assuming spherical shapes and 90% packing efficiency. It needs to be noted that this calculation does not take into consideration the space occupied by the core-forming PLGA itself. However, the value is in the same size-range of that was experimentally determined (Figure 3).

Chapter 6: Thermodynamic, Spatial and Methodological Considerations

Therefore, we hypothesized that the number of encapsulated molecules per particle could be improved by increasing the size of the PLGA core. To confirm these assumptions, particles with an increase in PLGA mass ratio were prepared. From the initial PEG-PLA to PLGA 70:30 mass ratio, we raised the PLGA fraction to 60:40, 50:50 and 60:60. As expected, the NPs increase in size in a linear manner from 60 to 120 nm (Figure 4B).

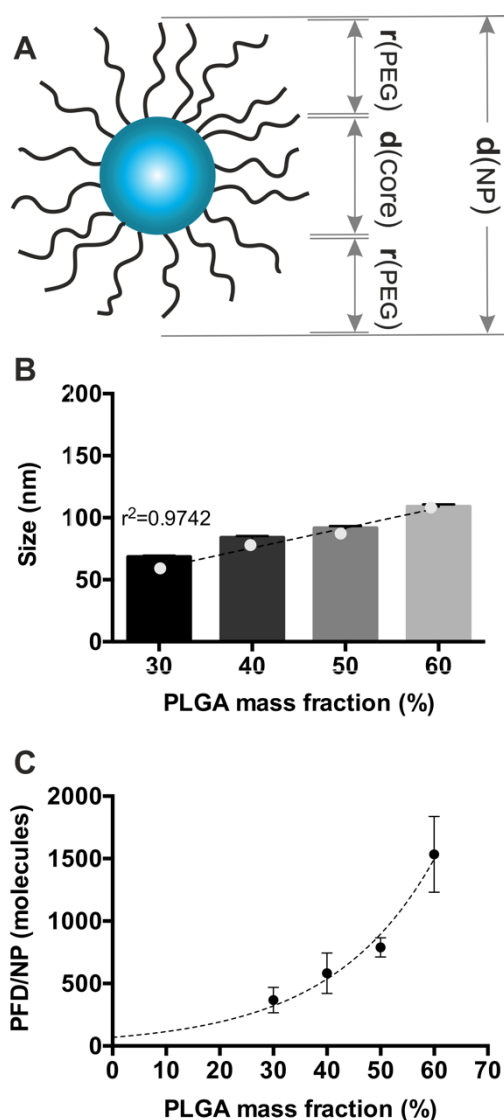


Figure 4. Core volume-dependent PFD encapsulation. (A) structure of a block copolymer NP. $d(\text{NP})$: particle diameter; $r(\text{PEG})$: PEG-brush radius; $d(\text{core})$: particle core diameter. (B) NP size and (C) PFD molecules per NP with increasing PLGA mass fraction. Results are shown as mean \pm SD of at least $n = 3$ measurements. Data in (B) and (C) are fitted with a linear and an exponential growth equation, respectively.

However, for all the formulations the PEG assumed a brush conformation (Table S2), indicating that the size increase was core-derived (Figure S6). More importantly, the number of PFD molecules per particle increased exponentially (Figure 4C), therefore confirming our theory that there is a spatial restriction for drug loading in a particle.

3.4 Co-encapsulation of LA and PFD in block copolymer NPs

Even though increasing the size of the PLGA core dramatically enhanced the number of PFD molecules per NP, for certain applications this may not be a feasible option. More so, the number of PFD molecules per NP did not reach the extent that would be expected from the linear size increase (Figure S7). This can be explained, on the one hand, by the volume that the PLGA takes up in the core by itself and which was not considered for the calculations. On the other hand, the high affinity of PFD to PEG may limit its core localization and promote a partial distribution among the NP shell. This PEG-associated PFD is removed during particle purification due to water solubility of the drug (2 mg mL^{-1}). However, a PEG shell is highly necessary for the *in vivo* applications of NPs, as it reduces protein adsorption [29, 34] and increases their blood residence [43].

As an alternative approach, we hypothesized that inclusion of an additional drug molecule, also compatible with PEG but highly water insoluble, would increase the number of PFD molecules per NP by limiting the PFD diffusion to the aqueous phase.

As a candidate we selected LA. It has a very poor water solubility (0.2 mg mL^{-1}), which is 10-times lower than for PFD (2 mg mL^{-1}). Additionally, as determined by the miscibility prediction (Figure 2), it is compatible with the particle forming polymers, especially with PEG. More so, at a therapeutic level it may show complementary effects to PFD as they both demonstrate positive antioxidative effects in doxorubicin-induced cardiac and renal toxicity [44] and oxidative liver damage [45].

To test our hypothesis, we prepared NPs encapsulating both PFD and LA (Figure 5). Initially we combined different PFD and LA ratios and examined the EE. As depicted in Figure 5A, a LA molar excess significantly increased the EE from 20% to 40%. We then maintained a constant PFD concentration and varied the formulation's LA content. Interestingly, an exponential increase/decrease in PFD molecules per NP was observed as LA content was increased/lowered (up to 25,000 PFD molecules per NP) (Figure 5B). When comparing the size of particles only incorporating LA with the ones encapsulating LA and PFD, there was only a 10 nm size difference (Figure 5C). Furthermore, the number of PFD molecules per NP reached with increasing LA addition could not be achieved by just increasing the initial PFD added to the formulations (Figure 5D), which reached a maximum of about 1,000 molecules per particle (dashed line in Figure 5B and 5D). This rising number of PFD molecules per

Chapter 6: Thermodynamic, Spatial and Methodological Considerations

NP can be explained by a decrease in mixing enthalpy with increasing amounts of LA, which may promote the miscibility of PFD with the particle-forming polymers (Figure S8). Additionally, the lower water solubility of LA and its interaction with PFD may promote a stronger particle binding of the latter. This is reinforced by the fact that the single encapsulation of LA, reaches a higher number of molecules per NP (Figure S9) compared to the individual PFD encapsulation.

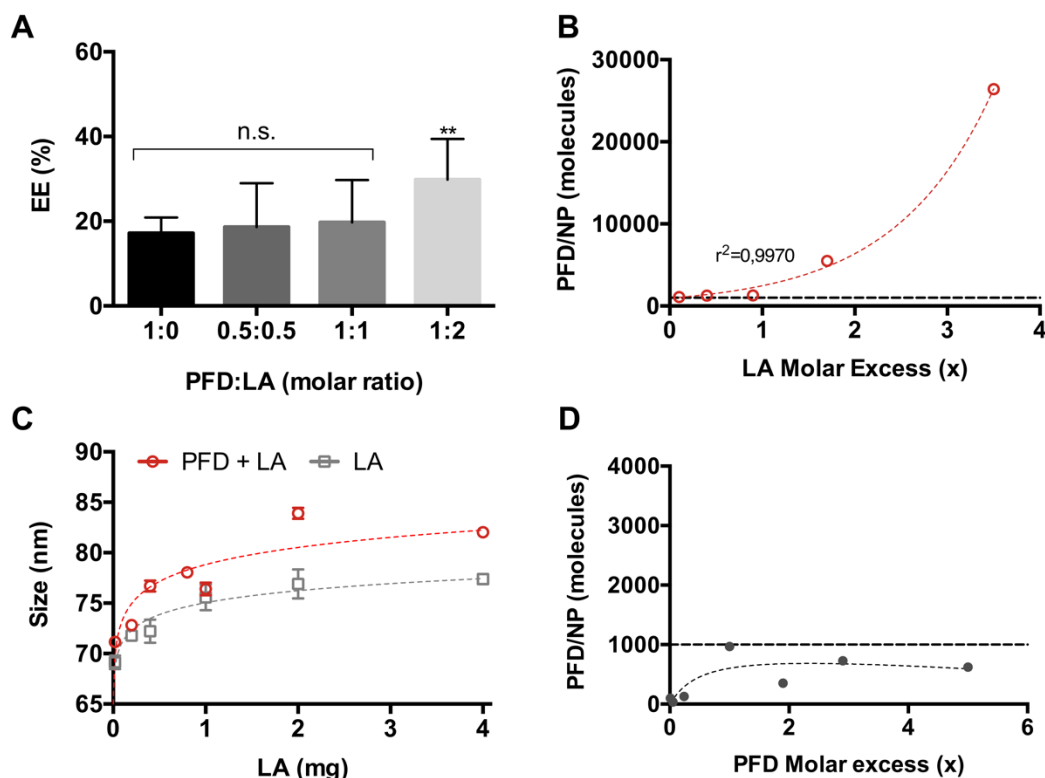


Figure 5. Co-encapsulation of LA and PFD in block copolymer NPs. (A) NPs prepared with varying PFD to LA molar ratios. (B) PFD molecules per particle and (C) size of NPs prepared with increasing LA amounts. (D) Maximum number of PFD molecules per particle at increasing initial PFD amounts. Results are shown as mean \pm SD of at least $n = 3$ measurements. Levels of statistical significance are indicated as $**p \leq 0.01$ and $*p \leq 0.05$ compared to NPs without LA, n.s.: non-significant. Data in (B) are fitted with an exponential growth equation. Data in (C) and (D) are fitted with a saturation curve.

However, the co-encapsulation of an additional drug molecule can raise concerns about its interference with the release profile of the original drug. Therefore, we investigated the PFD *in vitro* release from the different NP formulations using the dialysis bag method. To that end, NPs containing PFD (NP-PFD) or PFD and LA (NP-PFD/LA) were compared. As controls, the release profiles under the same conditions of drug-free particles (NPMeO) and free drug (PFD) were evaluated. As depicted in Figure 6, after 1 hour all of the free-drug was released from the dialysis membrane. At that time point, about 70% of the PFD was released from the NPs. The remaining 30%

of the particle-bound drug was released very slowly over the course of the next 5 hours. This fast release is probably due to the large surface area to volume ratio resulting from the small particle size. Additionally, the water-solubility of PFD may boost this effect. However, these results are in line with the release of other hydrophilic drugs prepared through nanoprecipitation, such as procaine hydrochloride from PLGA NPs [4]. Comparing the release profiles of NP-PFD and NP-PFD/LA it becomes apparent that both particle formulations show the same release curve. Therefore, we can conclude that the LA incorporation has no detrimental effects on the PFD release (Figure 6).

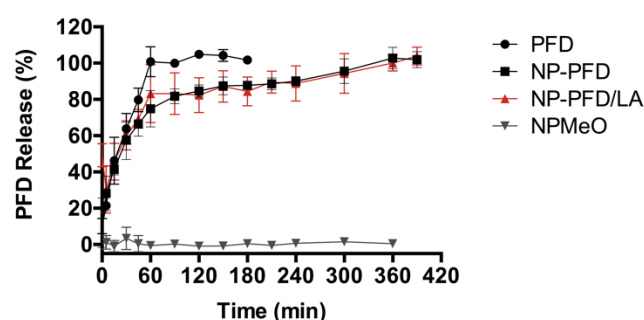


Figure 6. Release profile of PFD from block copolymer NPs. PFD: Free drug; NP-PFD: PFD-loaded NPs; NP-PFD/LA: PFD- and LA-loaded NPs; NPMEO: control, drug-free NPs. Results are shown as mean \pm SD of at least $n = 3$ measurements.

4 Conclusion

In this study we systematically examined the encapsulation of PFD, a water-soluble drug lacking ionizable groups, in block copolymer NPs through nanoprecipitation. We determined different thermodynamic parameters which predicted a good miscibility of the drug with the particle-forming polymers (PEG, PLA and PLGA) (Figure 2). We showed that the calculation of different parameters yielded slight differences among their predictions (Figure S1), which is in agreement with previous studies. More so, even though useful for selecting appropriate polymers for the drug encapsulation, they cannot be exclusively considered. We demonstrate that spatial constrictions regarding the particle's core size can also limit the number of molecules that can be encapsulated in polymer NPs (Figure 4) and by modulating them the number of encapsulated molecules can be increased. We experimentally assessed the EE, LC and number of encapsulated drug molecules per particle using two common nanoprecipitation techniques (Figure 3). Among them, we were able to demonstrate that MF manufacturing achieves significantly higher drug loading with the additional benefit

Chapter 6: Thermodynamic, Spatial and Methodological Considerations

of precise adjustment of the process parameters (Figure S3 and S4) and enhanced NP-cell interactions (Figure S5).

Lastly, we demonstrated how the encapsulation of an additional drug, LA, with similar polymer miscibility but lower water solubility is able to exponentially increase the number of PFD molecules per NP (Figure 5) without affecting the drug's release profile (Figure 6).

Overall our study demonstrates that the encapsulation of a water-soluble drug without ionizable groups is feasible when taking into consideration and adjusting the limits due to size constrictions and appropriately selecting the manufacturing method (MF vs bulk nanoprecipitation). More so, by considering the co-encapsulation of an additional appropriate molecule an additional increase in drug loading can be achieved.

References

- [1] Fessi H, Puisieux F, Devissaguet JP, et al. Nanocapsule formation by interfacial polymer deposition following solvent displacement. *Int J Pharm* 1989; 55: 1-4.
- [2] Almoustafa HA, Alshawsh MA, Chik Z. Technical aspects of preparing PEG-PLGA nanoparticles as carrier for chemotherapeutic agents by nanoprecipitation method. *Int J Pharm* 2017; 533: 275-284.
- [3] Barichello JM, Morishita M, Takayama K, et al. Encapsulation of Hydrophilic and Lipophilic Drugs in PLGA Nanoparticles by the Nanoprecipitation Method. *Drug Dev Ind Pharm* 1999; 25: 471-476.
- [4] Govender T, Stolnik S, Garnett MC, et al. PLGA nanoparticles prepared by nanoprecipitation: drug loading and release studies of a water soluble drug. *J Control Release* 1999; 57: 171-185.
- [5] Peltonen L, Aitta J, Hyvönen S, et al. Improved Entrapment Efficiency of Hydrophilic Drug Substance During Nanoprecipitation of Poly(l)lactide Nanoparticles. *AAPS PharmSciTech*; 5, https://www.ncbi.nlm.nih.gov/pmc/articles/PMC2784850/pdf/12249_2008_Article_51115.pdf (2004, accessed 15 May 2018).
- [6] Wang H, Xie H, Wu J, et al. Structure-Based Rational Design of Prodrugs to Enable Their Combination with Polymeric Nanoparticle Delivery Platforms for Enhanced Antitumor Efficacy. *Angew Chemie - Int Ed* 2014; 53: 11532-11537.
- [7] Yang Q, Tan L, He C, et al. Redox-responsive micelles self-assembled from dynamic covalent block copolymers for intracellular drug delivery. *Acta Biomater* 2015; 17: 193-200.
- [8] Thakral S, Thakral NK. Prediction of Drug-Polymer Miscibility through the use of Solubility Parameter based Flory-Huggins Interaction Parameter and the Experimental Validation: PEG as Model Polymer. *J Pharm Sci* 2013; 101: 2271-2280.
- [9] Kim ES, Keating GM. Pirfenidone: A Review of Its Use in Idiopathic Pulmonary Fibrosis. *Drugs* 2015; 75: 219-230.
- [10] RamachandraRao SP, Zhu Y, Ravasi T, et al. Pirfenidone Is Renoprotective in Diabetic Kidney Disease. *J Am Soc Nephrol* 2009; 20: 1765-1775.
- [11] Sharma K, Ix JH, Mathew A V., et al. Pirfenidone for diabetic nephropathy. *J Am Soc Nephrol* 2011; 22: 1144-1151.
- [12] Cho ME, Smith DC, Branton MH, et al. Pirfenidone slows renal function decline

Chapter 6: Thermodynamic, Spatial and Methodological Considerations

- in patients with focal segmental glomerulosclerosis. *Clin J Am Soc Nephrol* 2007; 2: 906–13.
- [13] George PM, Wells AU. Pirfenidone for the treatment of idiopathic pulmonary fibrosis. *Expert Rev Clin Pharmacol* 2017; 10: 483–491.
- [14] Bonella F, Wessendorf T, Costabel U. Clinical experience with pirfenidone for the treatment of idiopathic pulmonary fibrosis. *Eur Respir J*; 42, https://erj.ersjournals.com/content/42/Suppl_57/P3808.short (2013, accessed 8 December 2019).
- [15] Trivedi R, Redente EF, Thakur A, et al. Local delivery of biodegradable pirfenidone nanoparticles ameliorates bleomycin-induced pulmonary fibrosis in mice. *Nanotechnology* 2012; 23: 505101.
- [16] Chowdhury S, Guha R, Trivedi R, et al. Pirfenidone Nanoparticles Improve Corneal Wound Healing and Prevent Scarring Following Alkali Burn. *PLoS One* 2013; 8: e70528.
- [17] Abnoos M, Mohseni M, Mousavi SAJ, et al. Chitosan-alginate nano-carrier for transdermal delivery of pirfenidone in idiopathic pulmonary fibrosis. *Int J Biol Macromol* 2018; 118: 1319–1325.
- [18] Silva RO, Costa BL da, Silva FR da, et al. Treatment for chemical burning using liquid crystalline nanoparticles as an ophthalmic delivery system for pirfenidone. *Int J Pharm* 2019; 568: 118466.
- [19] Vauthier C, Bouchemal K. Processing and Scale-up of Polymeric Nanoparticles. *Pharm Res* 2008; 36: 1025–1058.
- [20] Xiao RZ, Zeng ZW, Zhou GL, et al. Recent advances in PEG-PLA block copolymer nanoparticles. *Int J Nanomedicine* 2010; 5: 1057–65.
- [21] Maslanka Figueroa S, Vesper A, Abstiens K, et al. Influenza A virus mimetic nanoparticles trigger selective cell uptake. *Proc Natl Acad Sci* 2019; 116: 9831–9836.
- [22] Adamska K, Voelkel A, Berlińska A. The solubility parameter for biomedical polymers—Application of inverse gas chromatography. *J Pharm Biomed Anal* 2016; 127: 202–206.
- [23] Schenderlein S, Lück M, Müller BW. Partial solubility parameters of poly(D,L-lactide-co-glycolide). *Int J Pharm* 2004; 286: 19–26.
- [24] van Krevelen DW, te Nijenhuis K. Properties of polymers. Their correlation with chemical structure; their numerical estimation and prediction from additive group contributions. In: *Endeavour*. 2009, pp. 1–987.

-
- [25] Fedors RF. A Method for Estimating Both the Solubility Parameters and Molar Volumes of liquids. *Polym Eng Sci* 1974; 14: 147–154.
- [26] Li Y, Taulier N, Rauth AM, et al. Screening of Lipid Carriers and Characterization of Drug-Polymer-Lipid Interactions for the Rational Design of Polymer-Lipid Hybrid Nanoparticles (PLN). *Pharm Res* 2006; 23: 1877–1887.
- [27] Liu J, Xiao Y, Allen C. Polymer–drug compatibility: A guide to the development of delivery systems for the anticancer agent, ellipticine. *J Pharm Sci* 2004; 93: 132–143.
- [28] Qian H, Wohl AR, Crow JT, et al. A Strategy for Control of “Random” Copolymerization of Lactide and Glycolide: Application to Synthesis of PEG- b -PLGA Block Polymers Having Narrow Dispersity. *Macromolecules* 2011; 44: 7132–7140.
- [29] Abstiens K, Maslanka Figueroa S, Gregoritz M, et al. Interaction of functionalized nanoparticles with serum proteins and its impact on colloidal stability and cargo leaching. *Soft Matter* 2019; 15: 709–720.
- [30] Childs CE. The determination of polyethylene glycol in gamma globulin solutions. *Microchem J* 1975; 20: 190–192.
- [31] Rabanel J-M, Faivre J, Tehrani SF, et al. Effect of the Polymer Architecture on the Structural and Biophysical Properties of PEG–PLA Nanoparticles. *ACS Appl Mater Interfaces* 2015; 7: 10374–10385.
- [32] de Gennes PG. Polymers at an interface; a simplified view. *Adv Colloid Interface Sci* 1987; 27: 189–209.
- [33] Kreuzer HJ, Wang RLC, Grunze M. Single molecule force spectroscopy by AFM indicates helical structure of poly(ethylene-glycol) in water Related content Effect of stretching on the molecular conformation of oligo (ethylene oxide): a theoretical study Stretching of single polymer strands: *New J Phys* 1999; 1: 6.1–6.11.
- [34] Gref R, Lück M, Quellec P, et al. ‘Stealth’ corona-core nanoparticles surface modified by polyethylene glycol (PEG): influences of the corona (PEG chain length and surface density) and of the core composition on phagocytic uptake and plasma protein adsorption. *Colloids Surfaces B Biointerfaces* 2000; 18: 301–313.
- [35] Kansal AR, Torquato S, Stillinger FH. Computer generation of dense polydisperse sphere packings. *J Chem Phys* 2002; 117: 8212–8218.
- [36] Hancock BC, York P, Rowe RC. The use of solubility parameters in pharmaceutical dosage form design. *Int J Pharm* 1997; 148: 1–21.

Chapter 6: Thermodynamic, Spatial and Methodological Considerations

- [37] Greenhalgh DJ, Williams AC, Timmins P, et al. Solubility parameters as predictors of miscibility in solid dispersions. *J Pharm Sci* 1999; 88: 1182-1190.
- [38] Latere Dwan'Isa JP, Rouxhet L, Pr eat V, et al. Prediction of drug solubility in amphiphilic di-block copolymer micelles: The role of polymer-drug compatibility. *Pharmazie* 2007; 62: 499-504.
- [39] Kamaly N, Xiao Z, Valencia PM, et al. Targeted polymeric therapeutic nanoparticles: design, development and clinical translation. *Chem Soc Rev* 2012; 41: 2971.
- [40] Liu Z, Fontana F, Python A, et al. Microfluidics for Production of Particles: Mechanism, Methodology, and Applications. *Small* 2019; 1904673.
- [41] Karnik R, Gu F, Basto P, et al. Microfluidic Platform for Controlled Synthesis of Polymeric Nanoparticles. *Nano Lett* 2008; 8: 2906-2912.
- [42] Jiang W, Kim BYS, Rutka JT, et al. Nanoparticle-mediated cellular response is size-dependent. *Nat Nanotechnol* 2008; 3: 145-150.
- [43] Klibanov AL, Maruyama K, Torchilin VP, et al. Amphipathic polyethyleneglycols effectively prolong the circulation time of liposomes. *FEBS Lett* 1990; 268: 235-237.
- [44] Giri SN, Ali Al-Bayati M, Du X, et al. Amelioration of doxorubicin-induced cardiac and renal toxicity by pirfenidone in rats. *Cancer Chemother Pharmacol* 2004; 53: 141-150.
- [45] Macias-Barragan J, Caligiuri A, Garc a-Banuelos J, et al. Effects of alpha lipoic acid and pirfenidone on liver cells antioxidant modulation against oxidative damage. *Rev Med Chil* 2014; 142: 1553-64.

Chapter 6 – Supporting Information

Thermodynamic, Spatial and Methodological Considerations for the Manufacturing of Therapeutic Polymer Nanoparticles

1 Drug-polymer miscibility

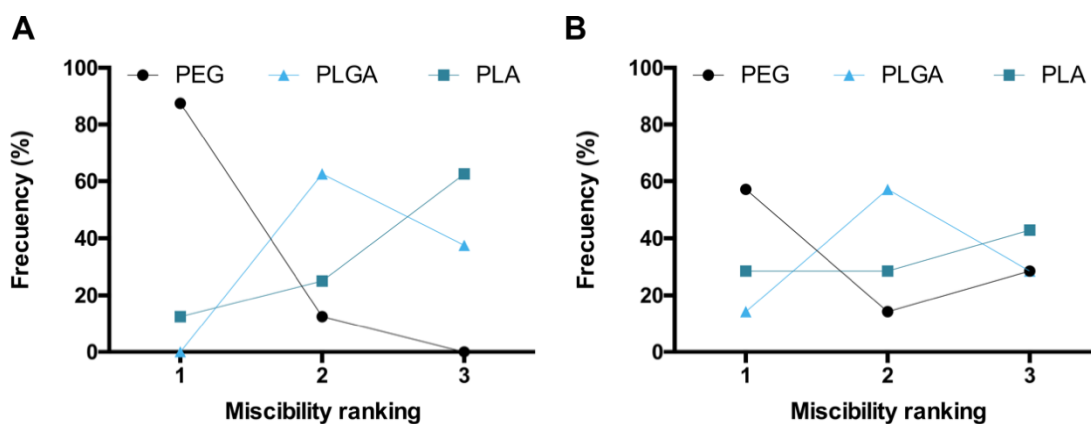


Figure S1. Ranking of the (A) PFD- and (B) LA polymer miscibility determined by the calculation of 7 predicting parameters ($\Delta\delta$, $\Delta\delta_d$, $\Delta\delta_p$, $\Delta\delta_{lv}$, ΔH_{MT} , ΔH_M , and χ_{sp}). The majority of the calculated parameters indicate the highest miscibility of PFD and LA with PEG (80% or 50% of the considered parameters, respectively), followed by PLGA (65% or 60%) and PLA (65% or 45%). For each parameter's individual miscibility prediction please see Table SI.

2 Mixing enthalpy

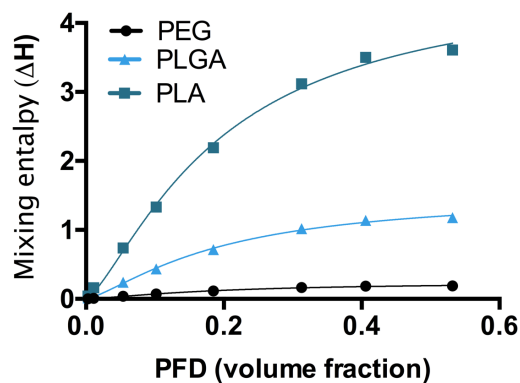


Figure S2. Mixing enthalpy of PFD with PEG, PLA or PLGA at increasing drug volume fractions. At increasing PFD volume fractions, the miscibility with the different particle-assembling polymers decreases.

3 Influence of the microfluidic manufacturing parameters

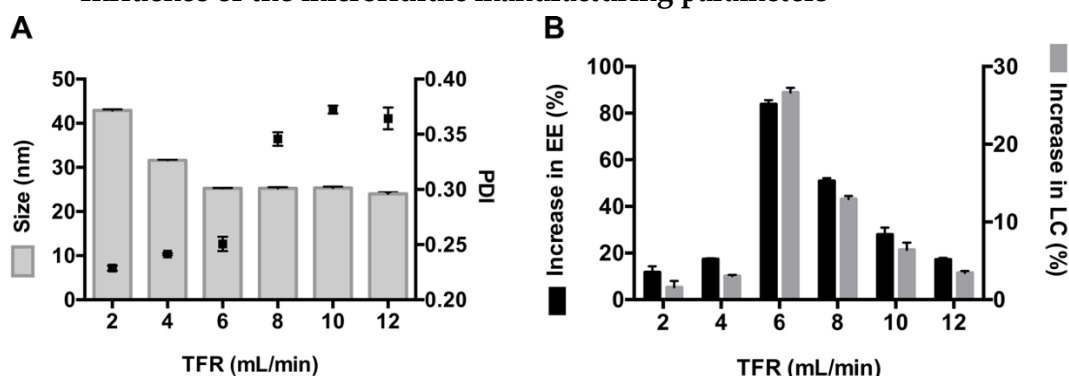


Figure S3. Effect of the total flow rate (TFR) during MF manufacturing on (A) particle characteristics (size and PDI) and (B) increase in EE and LC in block copolymer NPs. Increasing the TFR decreases the overall particle size. However, at TFR > 8 mL min⁻¹, the PDI of the resulting NPs drastically increases, due to particle instability and aggregation. A TFR of 6 mL min⁻¹ achieves the highest enhancement of the EE compared to NPs prepared *via* bulk nanoprecipitation. A deviation from this TFR results in a lower enhancement of the EE.

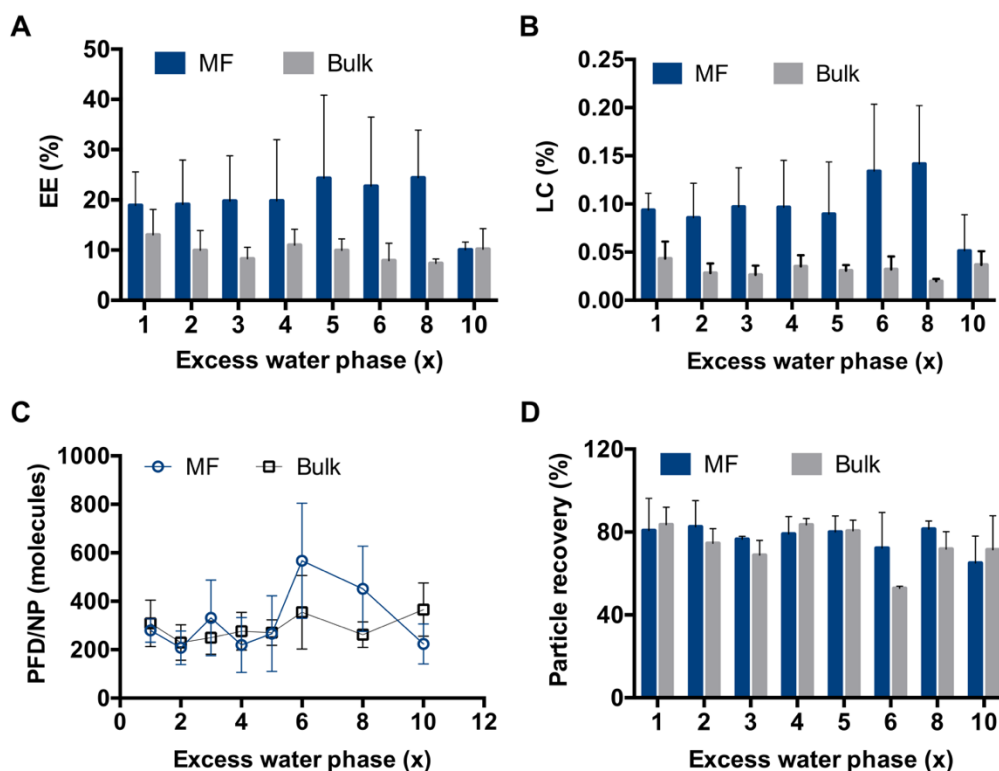


Figure S4. Influence of the flow rate ratio (FRR) during nanoprecipitation on PFD loading in block copolymer NPs. (A) EE, (B) LC, (C) number of molecules per particle, and (D) particle recovery after preparation and purification. Particles were prepared *via* bulk nanoprecipitation or MF manufacturing (TFR of 2 mL min⁻¹). Independent of the organic to water phase ratio, MF manufacturing achieves and enhanced PFD EE and LC, compared to bulk nanoprecipitation. The number of PFD molecules per particle

is similar due to a higher number of smaller-sized particles rendered by the MF technique. Particle recovery at the different parameters used is equivalent for both nanoprecipitation techniques.

4 Influence of the manufacturing technique on the cellular interaction

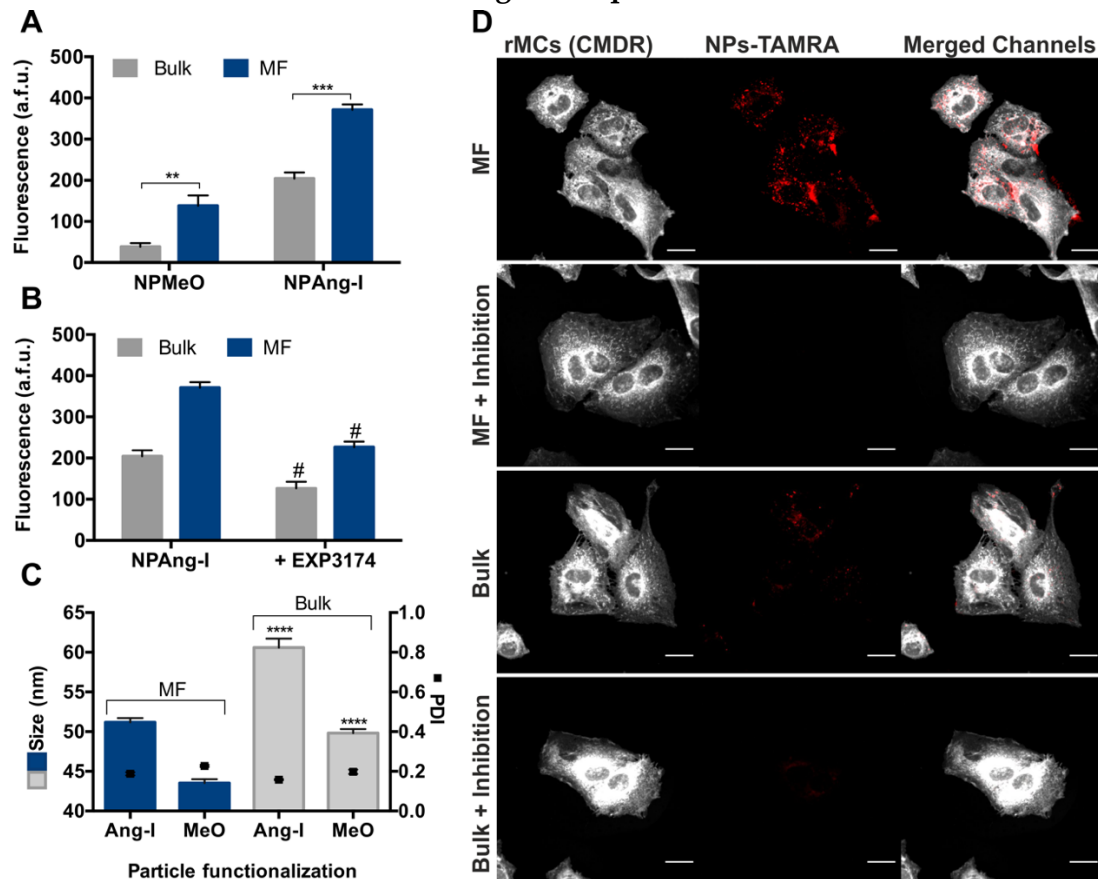


Figure S5. Cellular interaction of NPs prepared through microfluidic or bulk nanoprecipitation. (A) Uptake of Angiotensin-I-targeted (NPAng-I) [1] and methoxy-terminated non-targeted (NPMeO) particles in target rat mesangial cells (rMCs) analyzed through flow cytometry. (B) Specificity of the uptake shown by its suppression by EXP3174. (C) Particle size. (D) Cellular interaction of NPAng-I analyzed through CLSM. Scale bar 20 μ m. Cells stained with a cell membrane stain (CMDR) and are displayed in white. NPs were prepared using a TAMRA-labelled fluorescent PLGA [1, 2] and are displayed in red. Levels of statistical significance are **** $p \leq 0.0001$, *** $p \leq 0.001$ and ** $p \leq 0.01$, or # $p \leq 0.01$ comparing cells treated with NPs or NPs and EXP3174. Results are shown as mean \pm SD of at least $n = 3$ measurements. A Student's t-test was used to assess statistical significance. The enhanced cellular uptake of MF-manufactured NPs can be explained due to their smaller size, which falls in the ideal range for NP-cell interplay [3] (50 nm). More so, due to rapid MF mixing, the number of hydrophilic-end groups that get buried due to polymer adsorption on the particle surface is reduced [4], which can enhanced ligand-mediated targeting.

5 Spatial considerations on drug loading

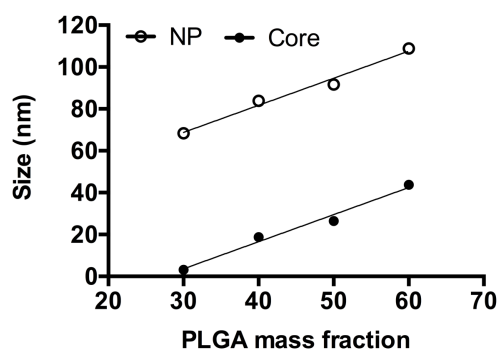


Figure S6. Size of NPs and their core in dependence with the PLGA mass fraction.

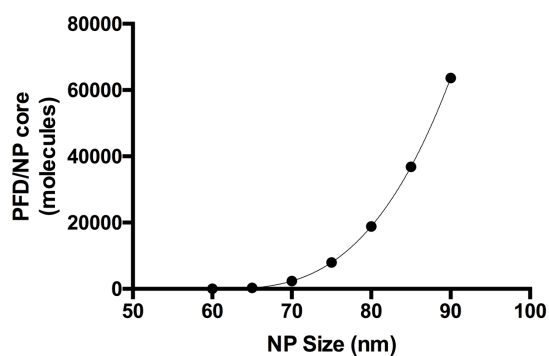


Figure S7. Theoretical number of PFD molecules per NP core calculated in dependence with the particle size. Data are fitted with a third order polynomial equation.

6 Influence of the LA co-encapsulation on the PFD loading

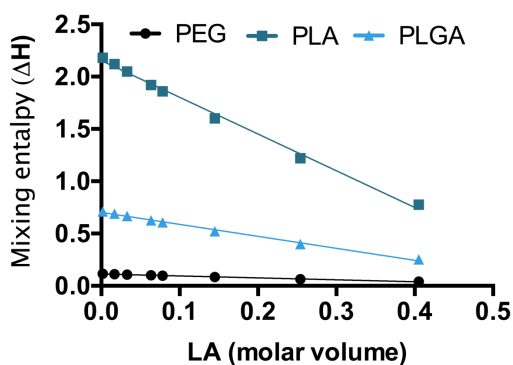


Figure S8. Mixing enthalpy of PFD and the particle forming polymers with increasing volume fractions of LA. A higher volume fraction of co-encapsulating drug, LA, decreases the mixing enthalpy of PFD with the particle-forming polymers. Data are fitted with a linear equation.

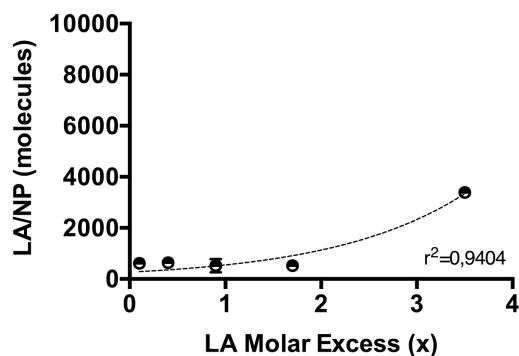


Figure S9. Number of LA molecules encapsulated per NP in dependence with the initially added LA.

7 Comparison of the different miscibility prediction parameters

Table S1

Parameters	Miscibility of PFD and Polymers	Miscibility of LA and Polymers
δ	PEG > PLGA > PLA	PEG > PLGA > PLA
δ_d	PEG > PLA > PLGA	PEG > PLA > PLGA
δ_p	PEG > PLGA > PLA	PLA > PLGA > PEG
δ_h	PLA > PEG > PLGA	PLGA > PLA > PEG
ΔH_M	PEG > PLGA > PLA	PLA > PEG = PLGA
ΔH_{MT}	PEG > PLGA > PLA	PEG > PLGA > PLA
χ_{sp}	PEG > PLGA > PLA	PEG > PLGA > PLA

8 PEG conformation on the particle surface

Table S2

PEG:PLGA (Mass Ratio)	S (nm ²)	D (nm)	RF	Conformation
70:30	3.78 ± 0.25	2.19 ± 0.07	5.87	Brush
60:40	3.48 ± 0.15	2.10 ± 0.05	5.87	Brush
50:50	3.65 ± 0.34	2.15 ± 0.10	5.87	Brush
60:40	3.72 ± 0.30	2.18 ± 0.09	5.87	Brush

S: surface each PEG chain occupies on the particle surface; D: distance between PEG chains; RF: Flory radius.

9 Supplementary Methods

9.1 Cell culture

The cells used in this study were cultured at 37 °C and 5% CO₂. Rat mesangial cells (rMCs) were a kind gift of Prof. Dr. Armin Kurtz (Institute of Physiology, University Regensburg, Regensburg, Germany). They were cultured in RPMI 1640 medium

Chapter 6: Thermodynamic, Spatial and Methodological Considerations

supplemented with 10% fetal bovine serum (Biowest, Nuaille, France) and insulin-transferrin-selenium (Life Technologies, Carlsbad, CA, USA) and 100 nM hydrocortisone. They were used as target cells in uptake experiments as their expression of the target structures was shown in previous studies of our group [1, 5].

9.1 Preparation of NPs for cellular uptake experiments

To evaluate the cellular interaction of NPs prepared through MF and bulk nanoprecipitation, methoxy-ended NPs (NPM_{EO}) and targeted NPs were prepared. As target moiety we selected a targeting system that we previously developed for highly specific cell recognition [1]. To that end, Angiotensin-I-functionalized particles were prepared (NP_{Ang-I}) for which Lysine-terminated Angiotensin-I (Lys-Ang-I) (Genscript, Piscataway, NJ, USA) was coupled to a carboxylic-acid terminated PEG-PLA (COOH-PEG_{5k}-PLA_{10k}) using Ethyl-3-(3-dimethylaminopropyl)carbodiimide (EDC)/N-Hydroxysuccinimide (NHS) chemistry, as previously described [1]. In short, the polymer was activated with a 25-fold molar excess of EDC/NHS for 2 hours in N,N-Dimethylformamide (DMF) prior to addition of 60-fold excess 2-mercaptoethanol for 20 minutes. Afterwards, a 1.2-fold and 5-fold molar excess of Lys-Ang-I in DMF and Diisopropylethylamine (DIPEA), respectively, were added to the activated polymer and left to react over 48 hours. The Lys-Ang-I-modified polymer (Ang-I-PEG_{5k}-PLA_{10k}) was purified *via* dialysis using a 6-8 kDa molecular weight cut-off regenerated cellulose dialysis membrane over 24 hours.

Targeted particles were prepared in the same manner as non-functionalized NPs, as described in the methods section of the main text using bulk or MF manufacturing. A 70:30 mass ratio of PEG-PLA to PLGA was used with 20% of the PEG-PLA being Ang-I-PEG_{5k}-PLA_{10k}. To ensure particle detection, a covalently fluorescently labelled PLGA (TAMRA-PLGA and CF647-PLGA for microscopy and flow cytometry experiments, respectively) was used for particle preparation, as described previously by our group [1, 2]. Particle characterization was performed as described in the main text method section.

9.2 Cellular interaction of NPs

To assess the cellular internalization of particles prepared using different manufacturing techniques (bulk nanoprecipitation vs MF preparation) through confocal scanning laser microscopy (CLSM), rMCs were seeded at a density of 10,000 in 8-well Nunc Lab Tech™ II Chamber Slide™ systems (Thermo Fisher Scientific, Waltham, MA, USA). Cells were incubated for 24 hours before pre-warmed particle

solutions at a concentration of 50 $\mu\text{g mL}^{-1}$ in Leibovitz Medium (LM) supplemented with 0.1% bovine serum albumin (BSA) were added on top of them. After a 45-minute incubation period, the NP solution was discarded, and the cells washed with pre-warmed DBPS. The cells were stained with Cell Mask™ deep red (CMDR) plasma membrane stain (Thermo Fisher Scientific, Waltham, MA, USA) (1x) for 5 minutes at room temperature. After an additional washing step with Dulbecco's Phosphate Buffered Saline (DPBS), the cells were fixed with 4% paraformaldehyde (PFA) in DPBS for 10 minutes. Cells were washed with DPBS and imaged, using a Zeiss Axiovert 200 microscope with an LSM 510 laser-scanning device. A 63x Plan- Apochromat (NA 1.4) objective was used. To excite the NP and cell fluorescence 543 nm and 633 nm He-Ne lasers were used, respectively. A 560-615 bandpass and a 650 longpass filter were used to record the NP- and cell-associated fluorescence. To assess uptake specificity, cells were preincubated for 30 minutes with 1 mM EXP3174 (Santa Cruz Biotechnology, Dallas, TX, USA), as previously described [1], prior to particle addition.

For flow cytometry analysis cells were seeded in 30,000 cells per well in 24-well plates (Corning, Corning, NY, USA) and incubated for 48 h. Afterwards, NP solutions at a concentration of 50 $\mu\text{g mL}^{-1}$ in LM supplemented with 0.1% BSA were added to the cells for 45 minutes. After the incubation, the NPs were discarded, and the cells washed with pre-warmed DPBS. Next, they were trypsinized and washed twice through centrifugation (200 g, 5 minutes). The cells were resuspended in ice-cold DPBS and analyzed using a CyFlow Space flow cytometer (Sysmex Partec GmbH, Goerlitz, Germany) and FloMax software. The particle-associated fluorescence was excited using a 638 nm red diode laser and recorded with a 675/30 bandpass filter. Data analysis was performed using Flowing software (Turku Centre for Biotechnology, Finland) by gating the population of viable cells and evaluating the geometrical mean fluorescence. Graph PadPrism 6.0 (GraphPad Software Inc., CA, USA) was used to assess statistical significance.

10 References

- [1] Maslanka Figueroa S, Veser A, Abstiens K, et al. Influenza A virus mimetic nanoparticles trigger selective cell uptake. *Proc Natl Acad Sci* 2019; 116: 9831–9836.
- [2] Abstiens K, Maslanka Figueroa S, Gregoritz M, et al. Interaction of functionalized nanoparticles with serum proteins and its impact on colloidal stability and cargo leaching. *Soft Matter* 2019; 15: 709–720.
- [3] Jiang W, Kim BYS, Rutka JT, et al. Nanoparticle-mediated cellular response is size-dependent. *Nat Nanotechnol* 2008; 3: 145–150.

Chapter 6: Thermodynamic, Spatial and Methodological Considerations

- [4] Karnik R, Gu F, Basto P, et al. Microfluidic Platform for Controlled Synthesis of Polymeric Nanoparticles. *Nano Lett* 2008; 8: 2906–2912.
- [5] Hennig R, Pollinger K, Tessmar J, et al. Multivalent targeting of AT₁ receptors with angiotensin II-functionalized nanoparticles. *J Drug Target* 2015; 23: 681–689.

Chapter 7

Summary and Conclusion

1 Summary

Conventional therapies frequently entail severe side effects that stem from their systemic administration. More so, promising drug candidates often fail during clinical studies due to lack of patient compliance when adverse effects become unbearable. Therefore, a considerable effort has been made to develop nanoparticulate carrier systems to improve the efficacy of pharmacotherapies. Viruses have long served as inspiration to achieve this purpose (**Chapter 1**). They possess several traits from which a nanomaterial-mediated therapy would profit enormously. They are able to overcome complex biological barriers, such as the blood-brain barrier or the mucus barrier, and thus, distribute to compartments of difficult access. More so, they can evade clearance by the immune system and escape endosomal pathways after cellular internalization. Especially their ability to enter cells with superior specificity would tremendously improve the efficacy of nanotherapies. This precise capacity to differentiate between cells relies on the unique interaction of viral surface ligands with cellular receptors [1]. In an effort to imitate this trait, nanoparticles (NPs) are frequently decorated with ligands to target receptors overexpressed under diseased states. Even though this design strategy has been extensively applied, it fails to endow nanomaterials with the much-needed target specificity. Compared to the initial dose of non-functionalized NPs that reaches a target tissue (0.7%), ligand-decoration achieves only a moderate improvement by 0.2% [2]. This lack of success can be partially explained by the fact that the targeted receptors can be ubiquitously found under physiological conditions. But, more importantly, current strategies fail to accurately imitate the viral host-cell interaction. One of the major elements that differentiates the NP and viral cell recognition is the complexity of the process. In comparison to the one-step receptor binding performed by conventional NPs, viruses undergo a sequential multistep receptor binding process [3]. When an influenza A virus-inspired two-step enzyme-mediated recognition strategy is implemented on NPs, the particles are endowed with the ability to discern with high specificity between target mesangial cells (MCs) and off-target cells *in vitro* (**Chapter 3**). The use of an angiotensin converting enzyme (ACE)-cleavable proligand, angiotensin-I (Ang-I), enables the first recognition step. When ACE is present on the cell membrane, it transforms Ang-I to angiotensin-II (Ang-II) on the NP surface. The subsequent angiotensin-II type 1 receptor (AT1R)-binding confirms cell identity and triggers internalization. Due to the high number of tethered ligands, the particles display a high avidity for their targets. More so, when presented simultaneously with cells with diverging expression patterns of ACE and AT1R they preferentially accumulate in cells that have both of the targets on their surface, even when off-target cells outweigh them in number.

An additional element that leads to the unsatisfactory results of targeted nanomaterials is an incomplete knowledge of the elements influencing multivalent interactions.

Chapter 7: Summary and Conclusion

Multivalent NP-cell interactions are not only determined by the expression levels of the targeted receptor but are also highly dependent on the NP design. However, ligands are frequently frivolously tethered to the surface of particles, leading to inconsistent and contradictory results. In this regard, ligand mobility on the particle corona is an insufficiently explored parameter that highly determines the way that particles behave after cell contact (**Chapter 4**). When ligands are tethered to long linker chains and the remaining polymer chains composing the particle surface are kept shorter, the ligand mobility on the particle surface increases. More so, despite increased initial shrouding of the ligands, the avidity of mobile particles for the targeted remains in the same range as for “rigid” particles following conventional design criteria. Furthermore, an increased ligand mobility promotes particle internalization after cellular contact, which cannot be matched by higher NP functionalization.

Since NP formulations are optimized *in vitro*, their performance *in vivo* is frequently much inferior. One of the causes being that nanomaterials face additional obstacles they were not subjected to under controlled *in vitro* settings, such as different flow conditions or the formation of a protein corona. These obstacles limit their cellular targeting abilities and therefore lead to poor therapeutic outcomes. Even though a two-step viral cellular recognition process enables an elevated *in vitro* target cell specificity, looking at the viral host-cell interaction it is apparent that a crucial step is missing. Viruses initiate cell contact through an initial attachment step, that aids particle accumulation on the cellular surface and receptor recruitment for subsequent identification steps [3]. This viral attachment can be mimicked with synthetic NPs by functionalizing them with an additional ligand that does not mediate particle internalization, such as the AT1R antagonist losartan carboxylic acid (EXP3174) [4, 5] (**Chapter 5**). Combination of EXP3174 and Ang-I on the surface of NPs leads to a complementary effect of both ligands regarding their avidity for the AT1R. More so, after activation of Ang-I to Ang-II by cell membrane-bound ACE, particle internalization is still effective. Using this tree-step viral cellular interaction strategy leads to a 5- to 15-fold higher target mesangial cell accumulation than NPs lacking one or both of the viral traits, respectively.

Even if an ideal delivery system is available, difficulties in drug loading can limit its therapeutic efficacy. Therefore, a systematic evaluation of the parameters determining drug encapsulation is of paramount importance (**Chapter 6**). Pirfenidone (PFD) is an antifibrotic drug with promising potential for the treatment of MCs in the context of diabetic nephropathy [6]. More so, it would enormously profit from a targeted delivery due to the enormous side effects derived from its systemic administration [7]. However, due to its elevated water solubility and lack of ionizable groups its encapsulation in polymer NPs through nanoprecipitation can be a challenge. By

regarding thermodynamic miscibility parameters, the suitability of a polymeric carrier system can be evaluated. Additionally, the drug loading can be optimized by selecting a suitable nanoprecipitation method. Microfluidic manufacturing enhanced the PFD encapsulation efficiency in polymer NPs by 60-90% with the additional advantage of a precise control over the manufacturing parameters. More so, by considering spatial constrictions the number of PFD molecules per particle can be dramatically raised. Alternatively, the co-encapsulation of a drug with complementary activity, like α -lipoic acid (LA) can exponentially increase the PFD molecules incorporated without interfering with their release profile.

Altogether this experimental data illustrates the powerful tools that a virus-mimetic NP design is for the development of nanocarriers with the ability to specifically identify and accumulate in a desired target cell. More so, it highlights the importance of apparently small design parameters, such as ligand mobility or considerations regarding drug loading, for the precise optimization of targeted therapeutic nanomaterials.

2 Conclusion

This work has elucidated important foundations for the improvement of targeted nanomaterial design. Especially for the specific identification and drug delivery to mesangial cells, which are highly involved in the development and progression of diabetic nephropathy. One of the major problems NPs face up to date is the insufficient target cell specificity. In this regard valuable inspiration for the particle design can be drawn from viruses. The implementation of a two-step heteromultivalent Influenza A-virus-inspired recognition process endows particles with an utmost specificity *in vitro*. The additional implementation of the viral attachment through an antagonistic ligand, tremendously augments the particle *in vivo* target cell interaction and accumulation. In this regard, an enhanced ligand mobility is of paramount importance to promote successful multivalent interactions that lead to a fruitful cellular uptake. More so, a systematical consideration of thermodynamic, methodological and spatial constrictions determining drug loading are the fundamentals of surmounting the challenges of the incorporation of hydrophilic drugs, such as PFD, in polymer NPs through nanoprecipitation. Taken all together, the newly gained understanding of the design of targeted nanomaterials has enormous potential to improve current shortcomings and develop new platforms for the treatment of MCs during their involvement in severe and highly prevalent diseases, such as diabetic nephropathy.

3 References

- [1] Grove J, Marsh M. The cell biology of receptor-mediated virus entry. *J Cell Biol* 2011; 195: 1071–82.
- [2] Wilhelm S, Tavares AJ, Dai Q, et al. Analysis of nanoparticle delivery to tumours. *Nat Rev Mater* 2016; 1: 1–12.
- [3] Boulant S, Stanifer M, Lozach P-Y. Dynamics of virus-receptor interactions in virus binding, signaling, and endocytosis. *Viruses* 2015; 7: 2794–815.
- [4] Hild W, Pollinger K, Caporale A, et al. G protein-coupled receptors function as logic gates for nanoparticle binding and cell uptake. *Proc Natl Acad Sci U S A* 2010; 107: 10667–72.
- [5] Hennig R, Pollinger K, Veser A, et al. Nanoparticle multivalency counterbalances the ligand affinity loss upon PEGylation. *J Control Release* 2014; 194: 20–27.
- [6] RamachandraRao SP, Zhu Y, Ravasi T, et al. Pirfenidone is renoprotective in diabetic kidney disease. *J Am Soc Nephrol* 2009; 20: 1765–75.
- [7] Sharma K, Ix JH, Mathew A V., et al. Pirfenidone for diabetic nephropathy. *J Am Soc Nephrol* 2011; 22: 1144–1151.

Appendix

Abbreviations

Abz-FRK(Dnp)-P	O-aminobenzoic acid-phenylalanyl-arginine-lysine (2,4-dinitrophenyl)-proline
ACE	Angiotensin converting enzyme
ACN	Acetonitrile
Ang-I	Angiotensin-I
Ang-II	Angiotensin-II
AT1R	Angiotensin-II type 1 receptor
BBB	Blood-brain barrier
BSA	Bovine serum albumin
CAR	Coxsackie and adenovirus receptor
CEA	Carcionembryonic agent
CLSM	Confocal laser scanning microscopy
CMDR	CellMask™ deep red plasma membrane stain
CPPs	Cell penetrating peptides
CTG	CellTracker™ green
CTDR	CellTracker™ deep red
<i>D</i>	Distance between LMPs
<i>ds</i>	Distance between NMPs
<i>Ds</i>	Distance between LMPs and the next same-length polymer
DBU	1,8-diazabicyclo[5.4.0]undec-7-ene
DIPEA	N,N-Diisopropylethylamine
DPBS	Dulbeco's phosphate buffered saline

Appendix

DMF	N,N-Dimethylformamide
DMTMM	4-(4,6-Dimethoxy-1,3,5-triazin-2-yl)-4-methylmorpholinium chloride
DN	Diabetic nephropathy
DOX	Doxorubicin
DV	Dengue virus
EDC	1-Ethyl-3-(3-dimethylaminopropyl)carbodiimide
EGFR	Epidermal growth factor receptor
EGTA	Ethylene glycol-bis(2-aminoethylether)-N,N,N',N'-tetraacetic acid
EXP3174	Losartan carboxylic acid
FA	Folic acid
FBS	Fetal bovine serum
χ_{sp}	Flory-Huggins interaction parameter
FRR	Flow rate ratio
GAGS	Glycosaminoglycans
GPCRs	G protein-coupled receptors
HA	Hyaluronic acid
HBV	Hepatitis B virus
HCV	Hepatitis C virus
HES	Hydroxyethyl starch
HIV	Human immunodeficiency virus
HV	Herpes virus
HSV	Herpes simplex virus
IC50	Half maximal inhibitory concentration
ITS	Insulin-Transferrin-Selenium
LA	Lipoic acid
LM	Leibovitz medium
LMPs	Ligand-modified polymers

Abbreviations

LRP-1	Lipoprotein receptor-related protein-1
Lys-Ang-I	Lysine N-modified Angiotensin-I
Lys-Ang-II	Lysine N-modified Angiotensin-II
MCs	Mesangial cells
MES	2-(N-morpholino) ethanesulfonic acid
MF	Microfluidic
ΔH_{MT}	Mixing enthalpy from the total solubility parameters
ΔH_M	Mixing enthalpy from the partial solubility parameters
MMPs	Matrix metalloproteinases
NHS	N-Hydroxysuccinimide
NMPs	Non-modified polymers
NPs	Nanoparticles
PDI	Polydispersity index
PEG	Poly(ethylene glycol)
PEI	Polyethyleneimine
PFD	Pirfenidone
PLA	Poly(lactic acid)
PLGA	Poly(lactic-co-glycolic acid)
PTX	Paclitaxel
RABV	Rabies virus
ROS	Reactive oxygen species
RVG	Rabies virus glycoprotein
R_F	Flory radius
δ	Solubility parameter
TAMRA	Tetramethylrhodamine
TF	Transferrin
TfR	Transferrin Receptor
TFR	Total flow rate

Curriculum Vitae

Personal Information

Name: Sara Maslanka Figueroa
Date of birth: 11th of December 1992
Place of birth: Ourense, Galicia (Spain)
Nationality: Spanish / German

Scientific education and work experience

04/2016 – 03/2020 **PhD Candidate/Research Assistant**
Department of Pharmaceutical Technology,
University of Regensburg

04/2016 – 03/2020 **Structured doctorate program**
Graduate school ChemPharm
Faculty of Chemistry and Pharmacy,
University of Regensburg

10/2016 **Licensure as Pharmacist in Germany**

02/2016 **Licensure as Pharmacist in Spain**

09/2015 – 02/2016 **Clinical Pharmacy Intern**
University Hospital Ourense (Spain)

02/2015 – 02/2016 **Diploma Thesis**
Department of Microbiology and Parasitology,
University Santiago de Compostela.

"Parasitosis in international adoptions" supervised by Prof.
Dr. Ma Teresa Santamarina Fernández

09/2014 – 02/2015

Research Internship

Department of Pharmaceutical Technology,
University of Regensburg

09/2014 – 02/2015

Pharmacy Studies / Erasmus scholarship

University of Regensburg

09/2010 – 02/2016

Pharmacy Studies

University Santiago de Compostela

School Education

06/2010

University access exam

CIUG (Comisión Interuniversitaria de Galicia)

09/2008 – 06/2010

High school Diploma/ A levels

IES as Lagoas, Ourense

09/1996 – 06/2008

Primary and Secondary School

Colexio Guillelme Brown, Ourense

Scientific Awards

11/2019

Innovation Award

BioPark, Regensburg

07/2019

Great Scientific Communication Award

CRS Annual meeting & exposition, Valencia

Peer-reviewed publications

1. Abstiens Kathrin, Maslanka Figueroa Sara, Gregoritzka Manuel, Goepferich Achim. Interaction of functionalized nanoparticles with serum proteins and its impact on colloidal stability and cargo leaching. *Soft Matter* 2019, 15:709-720
2. Maslanka Figueroa Sara, Veser Anika, Abstiens Kathrin, Fleischmann Daniel, Beck Sebastian, Goepferich Achim. Influenza A Virus Mimetic Nanoparticles Trigger Selective Cell Uptake. *Proceedings of the National Academy of Sciences (PNAS)* 2019, 116 (20):9831-9836 (**Chapter 3**)
3. Maslanka Figueroa Sara, Fleischmann Daniel, Beck Sebastian, Goepferich Achim. The Effect of Ligand Mobility on the Cellular Interaction of Multivalent Nanoparticles. *Macromolecular Bioscience* 2020, 20 (2):1900427 (**Chapter 4**)
4. Maslanka Figueroa Sara, Fleischmann Daniel, Beck Sebastian, Goepferich Achim. Thermodynamic, Spatial and Methodological Considerations for the Manufacturing of Therapeutic Polymer Nanoparticles. *Pharmaceutical Research* 2020, 37 (3): 59 (**Chapter 6**)
5. Maslanka Figueroa Sara, Fleischmann Daniel, Beck Sebastian, Tauber Philipp, Witzgall Ralph, Schweda Frank, Goepferich Achim. Nanoparticles Mimicking Viral Cell Recognition Strategies are Superior Transporters into Mesangial cells. *Submitted for publication* (**Chapter 5**)

List of Publications

Conference abstracts

1. S. Maslanka Figueroa, A. Goepferich. Tailoring the particle corona composition modulates the cellular interaction of multivalent-binding nanoparticles. *CRS Annual Meeting & Exposition*, Valencia, Spain, 2018.
2. D. Fleischmann, S. Maslanka Figueroa, A. Goepferich. Hetero-multivalent block-copolymer nanoparticles show enhanced mesangial cell selectivity in an in vitro co-culture assay. *CRS Annual Meeting & Exposition*, Valencia, Spain, 2018.
3. S. Maslanka Figueroa, D. Fleischmann, A. Goepferich. Virus-mimetic multistep-binding nanoparticles for enhanced target-cell specificity. *6th Galenus Workshop*. Würzburg, Germany, 2018.
4. S. Maslanka Figueroa, D. Fleischmann, A. Goepferich. Virus-mimetic nanoparticles for enhanced target-cell specificity. *DPhG Jahrestagung*, Hamburg, Germany, 2018.
5. D. Fleischmann, S. Maslanka Figueroa, A. Goepferich. Enhanced cell recognition of heteromultivalent nanoparticles using a biomimetic approach. *DPhG Jahrestagung*, Hamburg, Germany, 2018.
6. S. Maslanka Figueroa, D. Fleischmann, A. Goepferich. Strategies for Enhancing the Target Specificity and Affinity of Nanomaterials. *Biomaterials International*, Tokyo, Japan, 2018.
7. S. Maslanka Figueroa, K. Abstiens, D. Fleischmann, A. Goepferich. Angiotensin-I decorated nanoparticles target mesangial cells after enzymatic activation. *11th World Meeting on Pharmaceutics Biopharmaceutics and Pharmaceutical Technology*, Granada, Spain, 2018.

Acknowledgements

First and foremost, my deepest gratitude goes to Prof. Dr. Achim Göpferich for giving me the opportunity to be part of his research group and entrusting me with this exciting project. I thank him for his dedicated guidance and enthusiasm that inspired me to continuous growth. I also thank him for enabling my participation in several national and international conferences. I am deeply grateful for our scientific conversations, which were always fruitful and stimulating. His incomparable ability to put things in a new light always encouraged me to be creative. For this I am deeply thankful.

Furthermore, I want to express my sincerest gratitude to Prof. Dr. Frank Schweda for his invaluable guidance as my graduate school mentor and during our research cooperation. I thank him for the opportunity to be a part of his research group, surrounded by exceptional people. His profound expertise provided extremely helpful scientific input for my work and facilitated my continuous learning. I also thank him for his truthful nature and the always productive meetings that made me truly enjoy our time working together. I am also deeply thankful to Dr. Philip Tauber for his vital support with the animal experiments.

I express my deep gratitude to all my former and present colleagues in the research group of Pharmaceutical Technology. I am truly thankful for the exceptional work atmosphere they created and making my time in Regensburg so memorable. In this regard, a special “thank you” goes out to the following colleagues:

Dr. Anika Vesper, Dr. Manuel Gregoritz and Dr. Kathrin Abstiens for their scientific guidance during my first year at the work group.

Sebastian Beck, the best lab mate one could wish for, for the great work atmosphere, our daily chats and his friendship.

My project partner Daniel Fleischmann, for his like-minded work style and the great time I had during our always successful cooperations.

Heike Lehr, for her our fantastic conversations, our yoga adventures and our friendship, which I truly value.

More so, I thank all three of them for being great conference buddies

Stefanie Thalhauser, for always being supportive and a superb companion at our mutual conference visits.

Monika Stahl, and Marilena Bohley for our cheerful chats and their great camaraderie, especially during the supervision of the practical courses.

Moritz Graf, for his infinite kindness and unmatched ability to always have an open ear for problems.

Christian Ziegler, for creating a very enjoyable and laid back work atmosphere.

Oliver Zimmer and Jonas Groner, for the entertaining conversations, especially during our lunch breaks.

Furthermore, I thank Eva Wrobel for her outstanding organization skills and her caring nature.

I am truly grateful for the excellent technical assistants I had the pleasure to work with during my time at the university. I especially would like to thank Viktoria Messmann for her assistance with the polymer synthesis and Andrea Blaimer for her proficient support of the practical courses. Both of them I thank for our harmonious early morning chats. I thank Renate Liebl for introducing me in the fascinating world of the cell culture. I am extremely grateful to Robert Götz for his great support during our animal experiments. I further thank Uwe de Vries for his assistance with the confocal laser microscope.

The German Research Foundation (DFG) is acknowledged for providing financial support for my project.

I thank my former university friends from the University of Santiago de Compostela for our yearly meet ups, with no remanence of time passing and their constant support during my time in Regensburg.

A very special thanks goes to Pablo, for his loving support. I thank you for you ever lasting positivity and your unrestricted trust in me.

And last, but not least, I want to thank my family, without whom this would not have been possible, for their constant encouragement, support, and unconditional love.

Declaration in lieu of oath

I hereby declare that I have completed the dissertation presented without the impermissible help of third parties, without the use of resources other than those indicated, and that any data and concepts stemming directly or indirectly from other sources are indicated with citations to the literature.

No further persons were involved with the creation of the contents of the dissertation presented. In particular, I have not made use of the assistance of a doctoral consultant or other person in return for payment. No-one has received payment in kind either directly or indirectly for work which is associated with the content of the dissertation submitted.

The dissertation has not been submitted in the same or similar form to another examining authority, neither in Germany nor abroad.

Regensburg, 16.03.2020

.....

(Sara Maslanka Figueroa)

